

# Project L.O.R.A.X.

## A New Spin on Aerial Wildfire Detection

AE3200 Design Synthesis Exercise - Final Report Draft  
Group 13: Swarm of Rotating Cylindrical Wing Drones



# Project L.O.R.A.X.

A New Spin on Aerial Wildfire Detection

by

## Group 13: Swarm of Rotating Cylindrical Wing Drones

Kilian Seibl (5059755)

David Peeters (5505291)

Jan Franquesa Monés (5522595)

Martijn Spaans (5562872)

Tom Spaans (5554829)

Junxiang Qi (5680263)

Rein Viegiers (5688116)

Isaac Pietro Doyle (5746477)

Twan Kok (5341612)

Django van der Plas (5556465)

**Tutor** B. Remes

**Coaches** A. Hassanein, F. Vaccari

**Timeframe** Q4 2024/2025

**Faculty** Faculty of Aerospace Engineering, Delft

**Cover  
Style**

Created by Django van der Plas  
TU Delft Report Style, with modifications by Daan Zwaneveld and  
Kilian Seibl



# Acknowledgements

On behalf of the entire team, we would like to thank our tutors and coaches, Bart Remes, Francesco Vaccari, and Abdelrahman Hassanein. Their support, practical assistance, and expert guidance were instrumental to the successful completion of this project.

Additionally, we are grateful to Marija Popovic for her crucial insights into swarming strategy and swarming diagrams, which greatly enhanced our understanding. Our sincere thanks also go to Nathaniel P. Stebbins Dahl for his exceptional knowledge in flight dynamics, Simulink, and control theory, which provided essential theoretical and practical foundations for our work. Finally, we would like to thank Ewoud Smeur for his valuable contributions to control theory discussions and for his thoughtful feedback during our midterm and final presentation .

# Changelog

*Table 1: Document Version History*

Date	Version	Changes
18/06/2025	v1.0	Initial draft
26/06/2025	v1.1	General grammar, phrasing, and typo corrections throughout the report; updated numerous cross-references from placeholders to final values; removed specific table references in the Technical Risk Assessment summary in <a href="#">chapter 1</a> to improve readability; in <a href="#">chapter 6</a> , updated mitigation strategies for TR-TEC-14 (Jamming of the rails) and revised the risk description and mitigation for TR-SAF-01 (Drone crashing); Improved Free Body Diagram in <a href="#">chapter 8</a> ; restructured <a href="#">section 9.1</a> by merging the 'Stall Angle of Attack' subsection into the 'Assumptions' subsection; improved figures in <a href="#">section 9.4</a> ; in <a href="#">chapter 10</a> , completed sections by filling in placeholder data regarding swarming configurations and mothership path planning, and converted code logic from <a href="#">Figure 10.9</a> from pseudocode to flow diagram; corrected and clarified the servo motor torque calculation in <a href="#">section 11.4</a> , adding <a href="#">Equation 11.8</a> and <a href="#">Figure 11.19</a> for better explanation; moved the Internal Link Budget table from the Final Budgets chapter to the Electronics section in <a href="#">chapter 11</a> ; updated the Bill of Materials for the launcher in <a href="#">chapter 12</a> with revised component weights; in the Requirements Compliance Matrix ( <a href="#">Table 15.1</a> ), added a detailed explanation for the compliance status of requirement STK02-MIS20; A thermal management estimate was added for the main airframe in <a href="#">chapter 12</a> ; Redid the recommendations and improved the conclusion section in <a href="#">chapter 17</a> ; redesigned the Functional Flow Diagram ( <a href="#">section 17.2</a> ) and Functional Breakdown Structure ( <a href="#">section 17.2</a> ) for improved clarity; and added a new source to the bibliography for aeroacoustics and cited it in <a href="#">section 11.3</a> .; Updated the market analysis to include a market overview ( <a href="#">section 3.1</a> ).

# Nomenclature

## Abbreviations

Abbreviation	Definition	Abbreviation	Definition
2D	2 Dimensional	IR	InfraRed
3D	3 Dimensional	ISA	International Standard Atmosphere
6DoF	6 Degrees of Freedom	KV	Motor Constant
AI	Artificial Intelligence	L/D	Lift to Drag Ratio
AoA	Angle of Attack	L.O.R.A.X.	Lightweight Observational Rotating Autonomous X-Zylo
APC	Advanced Precision Composites	LiPo	Lithium Polymer (Battery Type)
API	Application Programming Interface	LQR	Linear-Quadratic Regulator
B2B	Business-to-Business	LSE	Low-Speed External (clock)
B2G	Business-to-Government	MATLAB	MATrix LABoratory
BEC	Battery Eliminator Circuit	MDO	Multidisciplinary Design Optimisation
BOM	Bill of Material	MIMO	Multiple-Input Multiple-Output
BVLOS	Beyond Visual Line of Sight	ML	Machine Learning
CAD	Computer-Aided Design	MMOI	Mass Moment of Inertia
CCK	Complementary Code Keying	MODIS	Moderate Resolution Imaging Spectroradiometer
CCW	Counter-Clockwise	MOI	Moment of Inertia
CD	Drag Coefficient	MPC	Model Predictive Control
CDR	Critical Design Review	MUX	Multiplexer
CFD	Computational Fluid Dynamics	NACA	National Advisory Committee for Aeronautics
CG	Centre of Gravity	NASA	National Aeronautics and Space Administration
CL	Lift Coefficient	OpenVSP	Open Vehicle Sketch Pad
COTS	Commercial Off-The-Shelf	PID	Proportional-Integral-Derivative
CP	Centre of Pressure	PLA	Polylactic Acid
CW	Clockwise	RANS	Reynolds-Averaged Navier-Stokes
DfD	Design for Disassembly	RoC	Rate of Climb
DoD	Depth of Discharge	ROS	Rate of Spread
DoF	Degrees of Freedom	RPM	Revolutions Per Minute
DRC	Design Rule Check	RTC	Real-Time Clock
EASA	European Union Aviation Safety Agency	SBC	Single Board Computer
EKF	Extended Kalman Filter	SORA	Specific Operations Risk Assessment
ESC	Electronic Speed Controller	SPI	Serial Peripheral Interface
EVA	Ethylene-Vinyl Acetate	SWIR	Short-Wave Infrared
FPC	Flex Printed Circuit	TIA	Transimpedance Amplifier
GPS	Global Positioning System	TRL	Technology Readiness Level
GSD	Ground Sample Distance	UAV	Unmanned Aerial Vehicle
HSE	High-Speed External (clock)	V&V	Verification & Validation
HSI	High-Speed Internal (clock)	VIIRS	Visible Infrared Imaging Radiometer Suite
I <sup>2</sup> C	Inter-Integrated Circuit	VLM	Vortex Lattice Method
IMU	Inertial Measurement Unit	VTOL	Vertical Take-Off and Landing

## Symbols

Symbol	Definition	Unit	Symbol	Definition	Unit
Latin Symbols					
$a, b$	Semi-minor and semi-major axes of fire ellipse	[m]	$C_p$	Pressure coefficient	[-]
$C_D$	Drag coefficient	[-]	$C_Q$	Torque coefficient	[-]
$C_L$	Lift coefficient	[-]	$C_T$	Thrust coefficient	[-]
$C_{M_y}$	Pitching moment coefficient	[-]	$D$	Drag force or Propeller diameter	[N] or [m]
$E$	Energy	[W·h]	$F$	Force	[N]
$I$	Moment of inertia or Electric current	[kg·m <sup>2</sup> ] or [A]	$J$	Advance ratio	[-]

Continued on next page...

Symbol	Definition	Unit	Symbol	Definition	Unit
$K$	Spring coefficient	[N/m]	$L$	Lift force or Angular momentum	[N] or [kg·m <sup>2</sup> /s]
$M$	Moment	[N·m]	$m$	Mass	[kg]
$n$	Propeller rotational speed	[Hz]	$P$	Power	[W]
$p$	Normal load or Spin rate	[N] or [rad/s]	$Q$	Torque	[N·m]
$r$	Radius	[m]	$Re$	Reynolds number	[-]
$S$	Surface area	[m <sup>2</sup> ]	$T$	Thrust or Temperature	[N] or [°C]
$t$	Thickness or Time	[m] or [s]	$V$	Velocity	[m/s]
$W$	Wind speed	[km/h]			
Greek Symbols					
$\alpha$	Angle of Attack (AoA)	[°]	$\beta$	Sideslip angle	[°]
$\Delta$	Change or difference in a quantity	[-]	$\eta$	Efficiency	[-]
$\theta$	Pitch angle	[°]	$\mu$	Coefficient of friction	[-]
$\nu$	Poisson's ratio	[-]	$\rho$	Density	[kg/m <sup>3</sup> ]
$\sigma$	Stress	[Pa]	$\tau$	Torque	[N·m]
$\phi$	Spin angle	[°]	$\Omega, \omega$	Angular velocity or spin rate	[rad/s] or [Hz]

## Subscripts

Subscript	Description	Subscript	Description
aero	Pertaining to aerodynamics	p	Pertaining to precession
ambient	Ambient condition	pack	Pertaining to the battery pack
B	Body frame	peak	Peak or maximum value
battery	Pertaining to the battery	prop	Pertaining to propulsion
body	Pertaining to the drone body	r	Radial direction
carriage	Pertaining to the movable carriage	ref	Reference value
cruise	Value at cruise condition	s	Pertaining to spin
E	Inertial (Earth) frame	shaft	Pertaining to the motor shaft
elec	Pertaining to electrical systems	strut	Pertaining to the strut
flame	Pertaining to the flame	total	Total or combined value
g	Pertaining to gravity	travel	Pertaining to travel distance
ic	Interference value	$\theta$	Tangential direction
motor	Pertaining to the motor	$\infty$	Freestream condition

# 1 Executive Overview

The L.O.R.A.X. project aims to design a swarm of rotating cylindrical wing drones for efficient large-area scanning, overcoming the limitations of conventional methods. Inspired by the X-ZyLo toy, the project's main objective is broken down into six distinct goals: proving the feasibility of the rotating pipe-shaped wing design and its implementation in an autonomous drone; simulating the controllability of a single drone with a single actuator controlling thrust, stability and control; demonstrating its imaging capabilities; simulating swarming operations with 10 nodes for better mission performance; demonstrating the ability to be deployed from a mothership; and ensuring the design meets sustainability benchmarks.

## Market Analysis

The L.O.R.A.X. drone swarm is designed to address the growing need for real-time wildfire mapping with a scalable, cost-effective, and versatile solution. The stakeholder map identifies key groups such as the design team, customers, and academic institutions, highlighting their roles and influence in the project's success. A SWOT analysis shows strong potential for market entry due to the drone's modular design, swarming capabilities, and low unit cost. However, challenges remain in development complexity and regulatory uncertainty.

Compared to existing wildfire mapping systems, L.O.R.A.X. offers a unique balance of fast area coverage (6 km<sup>2</sup>/min), good resolution (0.67 m/pixel), and real-time data at a significantly lower cost (€16,705 per swarm of ten) than traditional UAVs and manned aircraft. Its swarm design allows flexibility and fault tolerance, making it suitable for a variety of missions beyond firefighting, such as environmental monitoring and search and rescue.

The business model focuses on partnerships with research labs, sensor manufacturers, and public agencies. Revenue is generated through drone sales, software licensing, and support services. With a unit price around €1000 and a modular payload system, L.O.R.A.X. aims to become a reliable and adaptive tool for modern wildfire response and environmental monitoring operations.

## Technical Risk Assessment

The Technical Risk Assessment for the L.O.R.A.X. drone project is presented in [chapter 6](#), which is essential for meeting the reliability requirements. The assessment identifies risks across technical, financial, organisational, mission, safety, sustainability, and ethical domains, each evaluated for probability and impact. Mitigation strategies are proposed for each identified risk, with their effects quantified by changes in probability and impact scores. The effectiveness of these strategies is visually demonstrated through pre-mitigation and post-mitigation risk maps, which show a significant reduction in overall risk. While most risks are reduced to acceptable levels, critical risks that remain after the mitigation, such as potential simulation inaccuracies (TR-TEC-05) and mothership failure (TR-TEC-19) are highlighted and discussed for future mitigation.

## Trade-Off Summary

Several design options were explored for both the drone control system and payload to support wildfire mapping. The final configuration uses a pair of counter-rotating propellers combined with a spring mechanism to shift the drone's centre of gravity. This setup provides strong turning ability, good stability, and reliable performance during flight, while remaining relatively simple to build and integrate.

For the payload, the selected combination includes a visual camera for confirming fire events and an infrared photodiode for detecting them. This setup offers wide area coverage, dependable detection, and effective confirmation, while keeping weight, power use, and cost at reasonable levels.

## Flight Characteristics

### Aerodynamics

[section 9.1](#) details the aerodynamic characterization of the novel L.O.R.A.X. drone, a critical step in its design. Key design parameters, including an aspect ratio of 2 and the NACA63(3)018 airfoil, were established based on efficiency and component integration needs, cruising at a velocity of 20 m/s and 6° angle of attack. Aerodynamic coefficients were primarily derived using OpenVSP's Panel Method, validated against experimental data, showing acceptable lift prediction (10% error imposed) and a conservative (overestimated) drag.

Significant assumptions were necessary due to the unique rotating annular wing configuration. RANS CFD simulations provided qualitative insights, indicating stall delay with increasing spin rates up to 10 Hz, but a counterin-

tuitive lift reduction at very high spin (30 Hz), Additionally, significant drag reduction at high angles of attack with high spin rates was observed. As the RANS simulation was not validated, these trends were not implemented. Stall behaviour was modelled by interpolating experimental data, and strut interference drag was estimated using Hoerner's[18] empirical relations. It was also found that due to the interaction of the propeller wake with the inner surface of the annular wing, a significant deviation in the pressure distribution compared to when there were no propellers was found.

The final aerodynamic forces listed in Table 1.1 are found by performing the aerodynamic analysis for each isolated component. These components were the annular wing and the struts. The aerodynamic forces found for these components were then imposed with the assumed errors, and together with the interference drag due to the strut junctions, the final aerodynamic forces for the L.O.R.A.X. drone were found.

### Propulsion Subsystem

The propulsion subsystem for the L.O.R.A.X. drone was designed to meet specific performance criteria, including a total cruise thrust of 0.6 N, a 10-minute flight duration, and precise spin torque control for its annular wing. The APC 4.1x4.1E<sup>1</sup> and 4.1x4.1EP<sup>2</sup> propellers were selected due to available performance data, good efficiency, and suitable size/pitch for the target cruise speed of 20 m/s. For the motor, the E-flite Park 250 (2200KV)<sup>3</sup> was chosen for its 2S LiPo compatibility, ability to deliver 6.5 W mechanical shaft power per motor at a cruise RPM of 10,820, and sufficient torque for rapid spin-up. Performance analyses confirmed its suitability for both cruise (55% efficiency, 1.6A draw per motor) and launch (26.6 W shaft power at 45% efficiency), operating well within its limits. The propeller model utilises thrust and torque coefficients dependent on the advance ratio for simulation.

### Power Subsystem

The power subsystem is central to the drone's endurance and unique CG-shifting control mechanism. The LPHD4525035 LiPo cell<sup>4</sup> was chosen, configured as a 2S3P (7.4 V, 750 mA-h) battery pack. This distributed arrangement of six cells (two per strut) optimises the drone's mass moment of inertia and CG placement, while balancing movable mass for control authority against battery capacity. This configuration provides sufficient energy (5.55 W-h) for an estimated flight time exceeding 10.86 minutes at a cruise power of 27.6 W (including 4 W for auxiliaries) and can safely deliver the peak launch current of 9.03 A, staying within its 15 C continuous discharge limit (11.25 A). A FlexPCB manages power distribution, voltage regulation, and includes safety features like a fuse and voltage monitoring.

### Stability & Control

Stability and control are heavily influenced by the drone's rapid spin, providing gyroscopic stabilisation that allows flight even if the centre of pressure (CP) shifts ahead of the centre of gravity (CG). The control system addresses the complex Multiple-Input Multiple-Output (MIMO) nature of the drone by using contra-rotating propellers to decouple spin rate from thrust. A cascaded control architecture is employed, with an inner Proportional-Integral (PI) loop regulating roll rate and an outer Proportional-Integral-Derivative (PID) loop controlling pitch rate. An input mixer translates throttle and differential (roll) commands into individual motor outputs, with saturation handling. Controller gains were heuristically tuned for stable performance.

### Flight Dynamics

Flight characteristics are significantly affected by the spring coefficient of the carriage, which tunes the relationship between pitch, airspeed, and climb rate; the drone was trimmed for zero climb rate at a 6° pitch angle. Steady-state flight analysis showed varying yaw rates depending on pitch, with increased yaw at higher angles of attack (stall), a property utilised for rotation manoeuvres. However, straight flight inherently involves some precession. The drone does not meet the 30°/s manoeuvring requirement, a deviation deemed acceptable as

**Table 1.1:** Aerodynamic Characteristics of the L.O.R.A.X. Drone. Twin values indicate upper and lower error bounds.

Forces	Value	Unit
$V_{\text{cruise}}$	20.00	m/s
$\alpha_{\text{cruise}}$	6.00	°
$L_{\text{cruise}}$	[2.2478, 2.7474]	N
$D_{\text{cruise}}$	0.4452	N
$M_{y,\text{cruise}}$	[-0.0628, -0.0377]	N·m
$L/D_{\text{cruise}}$	[5.0490, 6.1712]	-
$(x_{cp}/c)_{\text{cruise}}$	0.1990	-

<sup>1</sup>apcprop.com, 4.1x4.1E, 2024. Available at: <https://www.apcprop.com/product/4-1x4-1e> (accessed 23/06/2025).

<sup>2</sup>apcprop.com, 4.1x4.1EP, 2024. Available at: <https://www.apcprop.com/product/4-1x4-1ep> (accessed 23/06/2025).

<sup>3</sup>FlyBrushless.com, E-flite Park 250 Performance Data, 2024. Available at: <https://www.flybrushless.com/motor/view/238> (accessed 12/06/2025).

<sup>4</sup>lipolbattery.com, LPHD4525035, 2024. Available at: <https://www.lipolbattery.com/high%20rate%20discharge%20lithium%20polymer%20battery.html> (accessed 22/06/2025).

stability in gusts is prioritised over high agility, given the concept's limitations. Rotation manoeuvres involve inducing a controlled deep stall to achieve higher yaw rates, though this results in altitude loss.

## Swarming Performance

chapter 10, "Swarming Performance," comprehensively details the L.O.R.A.X. drone swarming and communication strategy for early wildfire detection and continuous monitoring over a 10 km<sup>2</sup> forest area, aiming to overcome the limitations of traditional satellite approach by providing superior spatial and temporal resolution. To evaluate the swarming behaviour, a robust fire model was incorporated into the simulation, featuring two active hotspots, each covering 10 to 20 acres. The simulation represents a 10 km<sup>2</sup> area divided into a grid of 10 m×10 m cells.

Hotspot temperature intensity is represented on a 0-1 scale, mapping to realistic temperatures (e.g., 1.0 for 1100°C at the fire front) and incorporating exponential cooling dynamics. Fire spread is modelled using an ellipsoidal shape influenced by wind speed, with the Forward Rate of Spread (ROS) linked to wind conditions to demonstrate dynamic growth.

Central to the mission is a "detect-confirm" payload strategy: detector drones utilise Teledyne BFS visual cameras at 270 m altitude, capturing imagery for a simulated enhanced YOLOv5 machine learning model that probabilistically generates initial risk maps and uncertainty maps. Subsequently, confirmatory drones, equipped with Hamamatsu IR photodiodes operating at 70 m, provide precise temperature measurements to verify hotspots and enhance the fidelity of the overall intensity map; these IR sensors aid in estimating the drones' roll state.

Path planning for the L.O.R.A.X. drone system is shaped by its unique constraints: linear deployment from a mothership, a < 2 km communication range, and limited yaw control that restricts manoeuvrability. To address these, an outward-segmented Archimedes spiral was chosen for detection, optimising area coverage while minimising altitude loss and turn inefficiency.

The mothership uses a path optimisation strategy to maintain proximity to all drones post-deployment. For hotspot confirmation, a k-means clustering and Mixed Integer Linear Programming (MILP) approach solves the multi-agent Travelling Salesman Problem. Active fire monitoring reuses this adaptive algorithm with real-time updates. Simulation results guided the selection of a 6-detector, 4-confirmator configuration, balancing coverage speed and robustness across varying fire conditions.

Effective communication is essential for this coordination, with data (payload/GPS) flowing from drones to the mothership for AI processing and map generation, then back to the swarm as optimised waypoints, and simultaneously to a ground station. A detailed link budget analysis confirms that the chosen Wi-Fi system can reliably transmit the required 3.96 Mbps of image data over 1 km with a 10 dB margin. A mesh network is employed between the drones to allow for the relaying of this signal, increasing range. The chapter concludes by acknowledging the fundamental feasibility of the system while identifying avenues for future optimisation, including swarming configurations, advanced image compression, and novel spin-independent antenna designs.

## Detailed Implementation

### Structural Characteristics

To ensure the L.O.R.A.X. drone can handle the required loads during operation, a structural analysis was performed. Beginning with an airframe analysis that considered point loads from batteries and struts, as well as hoop stresses from rotation, using the previously determined airframe geometry. Various materials like PLA, PP, balsa wood, Carbon Fibre Epoxy, and Aluminium 6061 were compared for the airframe, with EVA CF65 foam ultimately chosen due to its lightweight properties (45.67g estimated mass) and ease of manufacturing, despite its lower strength compared to metals or composites; hoop stresses for EVA were calculated and found to be well within limits. For the three struts connecting the motor to the airframe, off-the-shelf 4mm diameter carbon fibre rods were chosen for their thinness, hollowness, and structural rigidity. These struts were designed to withstand motor torque and guide cables. An airfoil shape (Eppler 863) was added around the struts to reduce drag.

### Electronics

The L.O.R.A.X. drone electronics architecture uses a dual-MCU setup:

- **STM32F411** on the MainPCB handles high-frequency IMU (ICM20948 @1125 Hz) state estimation.
- **STM32F405** on the FlexPCB manages control, communication (ESP8266), and peripheral sensors.

Key sensors:

- **GPS:** Omnidirectional antenna, 1 Hz update rate was found to be sufficient.

- **Barometer:** BMP180 via I2C (to be upgraded to BMP390).
- **IMU (ICM20948):** 9-axis (accel, gyro, mag), 1125 Hz for gyro/accel, 100 Hz for mag.

Sensor fusion is handled by an Extended Kalman Filter (EKF), tuned based on pose estimation feedback. Spin rate estimation is limited by gyroscope saturation (34.9 rad/s specification).

Three custom PCBs were developed:

- **FlexPCB:** Core avionics
- **MainPCB:** Dedicated IMU processing.
- **IrPCB:** Demonstration board for IR sensing.

Recommendations include:

- Improve DRC setup in Altium and verify connector strain relief.
- Upgrade IMU for better spin estimation or incorporate IR-based methods.
- Integrate sensor fusion with the flight controller model for full validation.

## Noise estimation

A noise assessment confirmed that the drone operates well within the required limits, with sound levels significantly below rural background noise. The analysis focused on the propeller system, the main source of noise, and showed a wide safety margin against the 35 dB requirement at 150 metres.

Even without accounting for shielding effects, the results demonstrate that the drone is exceptionally quiet. This makes it highly suitable for use in noise-sensitive environments.

## Launch System

The in-air launch unit system consists of a PVC tube mounted and clamped on the mothership. The swarm of drones will be launched sequentially from the tube, one after the other in a line. Once it is time for a drone to be launched, the front propeller is brought to full power, translating the drone towards the launch point. At the launch point, there are 3 wheel system arms that lock the drone in position without constraining its rotation. This allows each drone to speed up to 7 [Hz] before its launch, by using the power of its motor. Once the drone is ready to be launched, one servomotor connected to a Raspberry Pi Zero retracts the wheel system by rolling a PLA gear system formed by one central ring gear and four pulley gears. [Appendix G](#) shows a technical drawing for the full assembly.

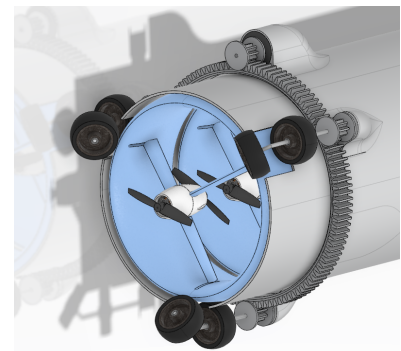


Figure 1.1: Rendered visualisation of the in-air unit launch system

The results from this design enabled the calculation of the required torque to spin the wheels, leading to the selection of the final Servo Motor. Moreover, the system has been proven to be structurally resistant to the applied loads. Nevertheless, some recommendations for a future system update could be made, which mainly aim to ensure that the wheels do not obstruct the orientation of the drones during launch through a more detailed study, and to develop the computer system that communicates with the servo motor. Finally, the overall dimensions of this subsystem are 250 mm x 250 mm x 1100 mm

## Final Design

For this section, technical drawings were made for both an individual drone node and the launch system (which are reported in [Appendix F](#) and [Appendix G](#), respectively). The final assembly of the drone can be divided into various groups.

- **Wingframe group:** it includes the airframe made of foam, together with the rail system for the carriage and a tight-fit cutout for the infrared camera, visual camera, flexible PCB, and 2 Electronic Speed Controllers. Moreover, holes were fitted from the leading edge to the trailing edge to enable forced airflow cooling of the electronic systems.
- **Carriage Group:** it consists of the Motor mount group (mentioned below), and 3 airfoil struts. The Carriage group comprises all the components that move along the centreline of the drone node to change the total CG location. The final results for the masses and CG locations are shown in [Table 1.2](#).
  - **Motor mount group:** it is a subset of the Carriage Group. It includes 2 motors, 2 propellers, the main PCB, a front mount and a back mount. These latter two mounts and the main PCB are screwed from

the back to the front with M2 self-supported screws.

The final masses of each subsystem were computed from the CAD and summarised in a final budget. Next to that, a final power budget and internal link budget were set up. After this, contingencies of 5% and 10% were applied to the mass and power budget, respectively, for the next design phase.

*Table 1.2: CG shift data results for the carriage system*

Component	Mass [kg]	Most fore CG position relative to the chord]	Most aft CG position relative to the chord	Total CG shift
Moving Carriage System	0.120	-13.10%	21.40%	34.50%
Fixed Wing Body	0.12	41.76%	41.76%	0%
Complete Assembly	0.237	13.98%	31.45%	17.47%

## Cost Breakdown

In [chapter 14](#), a thorough breakdown of the development cost of the L.O.R.A.X. is presented. The prices of all components and materials are listed per subsystem, and an estimate for variable cost was made. The development cost of a single node was estimated to be €1.65k, and the cost of a 10-node swarm, including the launcher, was estimated to be €16.7k. To cover uncertainty, a 10% contingency was added to each of the subsystems. Furthermore, a 30% contingency was added to the variable cost as these were found to be hard to predict. With contingencies, the total cost of one 10-node swarm would range between €15.1k and €19.9k, staying within the required budget of €20k. Finally, the operational costs were considered, as there was a requirement for this. However, it was concluded that there was too little time to properly set up an entire operational structure, which made it impossible to predict the operational cost. Thus, it was concluded that the operational cost would be estimated in the upcoming design phases.

## Operations

The operational aspects of the L.O.R.A.X. drone system are discussed in [chapter 13](#). It first presents the architecture of a typical mission, which includes pre-mission phases (fire suspicion, mapping request, mothership deployment), mission execution (swarm deployment, area scanning, fire detection and reporting, movement to retrieval zone), and end-of-mission tasks (drone retrieval, maintenance, and reuse). The chapter also discusses operational characteristics, such as the target reliability for individual drones and the swarm, and the advantages of the single-actuator design for maintainability. The main conclusion was that due to the novel design, extensive testing would need to be done to properly quantify the reliability.

A significant focus was placed on sustainability. Project sustainability involves material selection, energy-efficient design, and Design for Disassembly (DfD) to promote recycling at end-of-life. Operational sustainability is achieved through post-mission drone retrieval. Social sustainability considerations include minimising harm to people and wildlife during operations and ensuring a safe manufacturing environment.

## Verification & Validation

The Verification and Validation (VV) approach for the L.O.R.A.X. drone is detailed in [chapter 15](#), beginning with a Requirements Compliance Matrix ([Table 15.1](#)). This matrix serves as a tool for tracking each requirement's compliance status (Pass/Fail/TBD) and its corresponding verification method (Analysis, Demonstration, Inspection, Simulation, or Test). The Feasibility Analysis following identifies that regulatory constraints, specifically Open Category drone limits, are currently unmet, requiring reclassification into EASA's 'Specific' category. Requirements relying on future production/testing are flagged as TBD.

Then, a Sensitivity Analysis is conducted to evaluate the system's robustness to design uncertainties:

- Mass sensitivity focuses on airframe mass variations with aspect ratio changes, showing a limited margin before exceeding the 250g limit.
- Flight performance sensitivity reveals low yaw rate responsiveness with pitch variation, affecting manoeuvrability.

- Cost sensitivity highlights vulnerability to increased manufacturing time, which could raise costs significantly.

Software V&V is performed for OpenVSP, RANS simulations, and the Flight Dynamics Model, ensuring modelling correctness, solver stability, and some validation against literature and trends.

Subsystem V&V covers sensors, swarming logic, flight time, structure, and propulsion. Methods include specification checks, simulations, lab tests, and hardware measurements.

Together, these efforts validate the system's core capabilities while identifying critical areas for future testing and refinement.

## Development

[chapter 16](#) outlines the future development for the L.O.R.A.X. project, starting with a conceptual project design and development plan that visualises phases from detailed design iteration, to testing, production, client delivery, mission deployment, and finally, end-of-life disassembly or recycling. After a conceptual manufacturing and integration plan, methods for manufacturing methods are specified. These consist of methods such as CNC lathing, EVA foam for the annular wing, 3D printing for motor fairings, wire cutting foam for strut fairings, and stamping aluminium for the rail system.

# Table of Contents

<b>Nomenclature</b>	<b>3</b>
<b>1 Executive Overview</b>	<b>1</b>
<b>2 Project Overview</b>	<b>9</b>
2.1 Project Objectives . . . . .	9
<b>3 Market Analysis</b>	<b>10</b>
3.1 Market Overview . . . . .	10
3.2 Stakeholder Map . . . . .	11
3.3 SWOT Analysis . . . . .	11
3.4 Competitive Analysis in Sector . . . . .	12
3.5 Business Model Canvas . . . . .	13
<b>4 Functional Analysis</b>	<b>15</b>
<b>5 Requirements</b>	<b>16</b>
<b>6 Technical Risk Assessment</b>	<b>20</b>
6.1 Risks and Mitigation . . . . .	20
<b>7 Trade-Off Summary</b>	<b>24</b>
<b>8 Unified Simulation</b>	<b>26</b>
8.1 Simulation Architecture . . . . .	26
8.2 Flight Dynamics Module . . . . .	27
<b>9 Flight Characteristics</b>	<b>30</b>
9.1 Aerodynamic Characteristics . . . . .	30
9.2 Propulsion Subsystem . . . . .	39
9.3 Power Subsystem . . . . .	43
9.4 Stability & Control . . . . .	45
9.5 Flight Dynamics . . . . .	51
<b>10 Swarming Performance</b>	<b>54</b>
10.1 Map Modelling of Forest Fires . . . . .	55
10.2 Payload . . . . .	58
10.3 Path Planning . . . . .	63
10.4 Communications . . . . .	66
<b>11 Detailed Design</b>	<b>70</b>
11.1 Structural Characteristics . . . . .	70
11.2 Electronics . . . . .	73
11.3 Noise Estimation . . . . .	81
11.4 Launching System . . . . .	82
<b>12 Final Design</b>	<b>86</b>
12.1 Drone Final Assembly . . . . .	87
12.2 Hardware/Software Diagram . . . . .	90
12.3 Final Budgets . . . . .	91
<b>13 Operations</b>	<b>93</b>
13.1 Operations and Logistics . . . . .	93
13.2 Operational Characteristics . . . . .	94
13.3 Sustainability . . . . .	94
<b>14 Cost Breakdown</b>	<b>96</b>
14.1 Materials . . . . .	96
14.2 Propulsion . . . . .	96
14.3 Electronics & Power . . . . .	96
14.4 Payload . . . . .	97
14.5 Launch System . . . . .	97
14.6 Variable Costs . . . . .	97

---

14.7 Total Cost Budget . . . . .	98
14.8 Operational Costs . . . . .	98
<b>15 Verification &amp; Validation</b>	<b>99</b>
15.1 Requirements Compliance Matrix . . . . .	99
15.2 Sensitivity Analysis . . . . .	102
15.3 Software Verification & Validation . . . . .	103
15.4 Subsystem Verification & Validation . . . . .	105
<b>16 Development</b>	<b>109</b>
16.1 Project Design and Development Plan . . . . .	109
16.2 Manufacturing and Integration Plan . . . . .	109
<b>17 Conclusion &amp; Recommendations</b>	<b>111</b>
17.1 Achievements . . . . .	111
17.2 Recommendations . . . . .	112
<b>A Functional Flow Diagram</b>	<b>115</b>
<b>B Functional Breakdown Structure</b>	<b>118</b>
<b>C Gantt Chart</b>	<b>119</b>
<b>D PCB Schematic</b>	<b>119</b>
<b>E Experimental Data for Aerodynamic Coefficients</b>	<b>123</b>
<b>F Drone Node Technical Drawing</b>	<b>123</b>
<b>G Launch Unit Technical Drawing</b>	<b>126</b>

## 2 Project Overview

The goal of the *swarm of rotating cylindrical wing drones* project is to design a new type of drone that, in a swarm, can scan large areas effectively. Conventional terrain mapping methods are rather expensive and limited to specific resolution angles, mostly being able to map 2D projected surfaces. To overcome these hurdles, this report discusses the design of the “*Lightweight Observational Rotating Autonomous X-Zylo*” or L.O.R.A.X. drone swarm.

The L.O.R.A.X. drone concept is based on the flight principles of X-ZyLo toy<sup>1</sup>. The team used Nils Wagner’s paper on the flight characteristics of the X-ZyLo [36] as a basis for the research and design of the L.O.R.A.X. drone.

A key finding of this project is the fundamental trade-off that must be made between gyroscopic stability and manoeuvring agility, inherent in such a rotating cylindrical wing drone. This report demonstrates that, while high manoeuvring rates are not feasible, the resulting stability provides a robust platform for the intended swarming and mapping operations.

### 2.1. Project Objectives

As stated in the project guide, the main objective of this project is to design a swarm of rotating cylindrical wing drones, optimised to scan large areas efficiently.

In this section, the given objective is broken down into six clear, distinct objectives. The objectives are meant to set clear targets for each phase of the project and will help to assess whether or not the outcomes of each phase are in line with the stakeholder expectations. Next to that, they also form a basis for the verification and validation process.

- **Prove the feasibility of a rotating pipe-shaped wing:** Assess the aerodynamic performance of a cylindrical shape and the stability characteristics of a rotating cylinder. Determine the feasibility of implementing the wing design in an unmanned aerial vehicle.
- **Simulate the controllability of a single drone node in different flight conditions:** Develop a control system that uses a single actuator to manage propulsion, spin-induced gyroscopic stabilisation, and directional control. Develop a control model that proves directional stability during wind gusts.
- **Demonstrate the imaging capabilities of each drone node:** Show that the swarm can scan an area of 10 km<sup>2</sup> with a 360° field of view and a resolution of at least 1 m<sup>2</sup>.
- **Simulate swarming operations to optimise mission performance:** Develop a swarming simulation for 10 drone nodes, show that it can scan a large area more effectively than a single drone.
- **Demonstrate drone deployment capabilities:** Show that the drones can be deployed from a mother ship. Simulate a deployment sequence that starts from the mother ship and ends when the drones are in swarming formation.
- **Prove that the drone design meets sustainability benchmarks:** Include sustainable design choices throughout the project where possible (e.g., recyclable/biodegradable material). Show that the system is optimised to have minimal energy consumption.

---

<sup>1</sup>CalCoast Toys, X-ZyLo. Available at: <https://www.wmctoys.com/products/x-zylo/x-zylo-ultra> (accessed 18/06/2025).

## 3 Market Analysis

This chapter analyses the current market drone and firefighting market, and how the product is expected to perform in the wildfire mapping market, and who the relevant stakeholders are that must be satisfied accordingly. An Overview of the market is discussed in [section 3.1](#). Then the stakeholder map is presented in [Figure 3.1](#) as well as the SWOT analysis in [Table 3.1](#). The performance of relative competition is better analysed in [Table 3.3](#) to show how the product places itself among its competition, together with a Business model canvas of the product in [section 3.5](#).

### 3.1. Market Overview

The proposed system, an autonomous swarm of cylindrical rotating drones for forest fire monitoring and detection, targets the rapidly growing intersection of aerial robotics and environmental protection. The global drone industry is experiencing significant growth, valued at approximately 13.86 billion dollars in 2023, with forecasts projecting expansion to over 65.25 billion by 2032 <sup>1</sup>, driven by applications in agriculture, public safety, and environmental monitoring. Within this broader context, wildfire detection has emerged as a critical use case due to the rising frequency and severity of forest fires globally. <sup>2</sup>

Climate change intensifies wildfire risks through prolonged droughts, higher average temperatures, and erratic weather patterns. These conditions have created urgent demand for rapid, scalable, and intelligent monitoring systems capable of covering vast and often inaccessible terrain such as nature reserves. Traditional manned surveillance methods and stationary sensor networks (towers) are increasingly viewed as insufficient due to their limited responsiveness and high operational costs. In contrast, drone-based systems, particularly autonomous swarms, can offer dynamic coverage, real-time data collection, and reduced human risk. The forest fire detection technology market alone is projected to exceed 1.2 billion dollars by 2030, with UAV platforms contributing a significant share <sup>3</sup>.

Key technological trends are accelerating adoption. Advances in swarm robotics, edge computing, and thermal imaging enable drones to operate cooperatively and autonomously, even in GPS-denied or visually obstructed environments like dense forest. Furthermore, increasing government support for Beyond Visual Line of Sight (BVLOS) operations, especially in unpopulated areas, lowers regulatory barriers for wide-area deployments. Initiatives by the European Union <sup>4</sup> and U.S. Federal Aviation Administration (FAA) <sup>5</sup> are creating favourable conditions for autonomous drone services in emergency response and environmental monitoring.

Sustainability is also a key driver. Wildfires contribute significantly to carbon emissions and biodiversity loss, and public pressure is mounting for agencies to adopt eco-efficient and non-invasive monitoring technologies. Swarm drones, with their low environmental footprint and adaptability, are well-positioned to meet these societal and ecological expectations.

---

<sup>1</sup>Fortune Business Insights, Drone Market Size, Share & Industry Analysis, last updated June 09 2025. Available at: <https://www.fortunebusinessinsights.com/commercial-drone-market-102171> (accessed 12/06/2025).

<sup>2</sup>NASA, Wildfires and Climate Change, last updated May 28 2025. Available at: <https://science.nasa.gov/wildfires-and-climate-change> (accessed 12/06/2025).

<sup>3</sup>Verified Market Research, Forest Wildfire Detection System Market Size And Forecast (2025), <https://www.verifiedmarketresearch.com/product/forest-wildfire-detection-system-market/>, (accessed 12/06/2025).

<sup>4</sup>European Commission, U-space and Drone Regulations, 2023. Available at: [https://transport.ec.europa.eu/news-events/news/new-eu-rules-dedicated-airspace-drones-enter-force-2023-01-26\\_en](https://transport.ec.europa.eu/news-events/news/new-eu-rules-dedicated-airspace-drones-enter-force-2023-01-26_en) (accessed 12/06/2025).

<sup>5</sup>Federal Aviation Administration (FAA), BVLOS ARC Final Report, 2023. Available at: [https://www.faa.gov/regulations\\_policies/rulemaking/committees/documents/index.cfm/document/information/documentID/5424](https://www.faa.gov/regulations_policies/rulemaking/committees/documents/index.cfm/document/information/documentID/5424) (accessed 12/06/2025).

## 3.2. Stakeholder Map

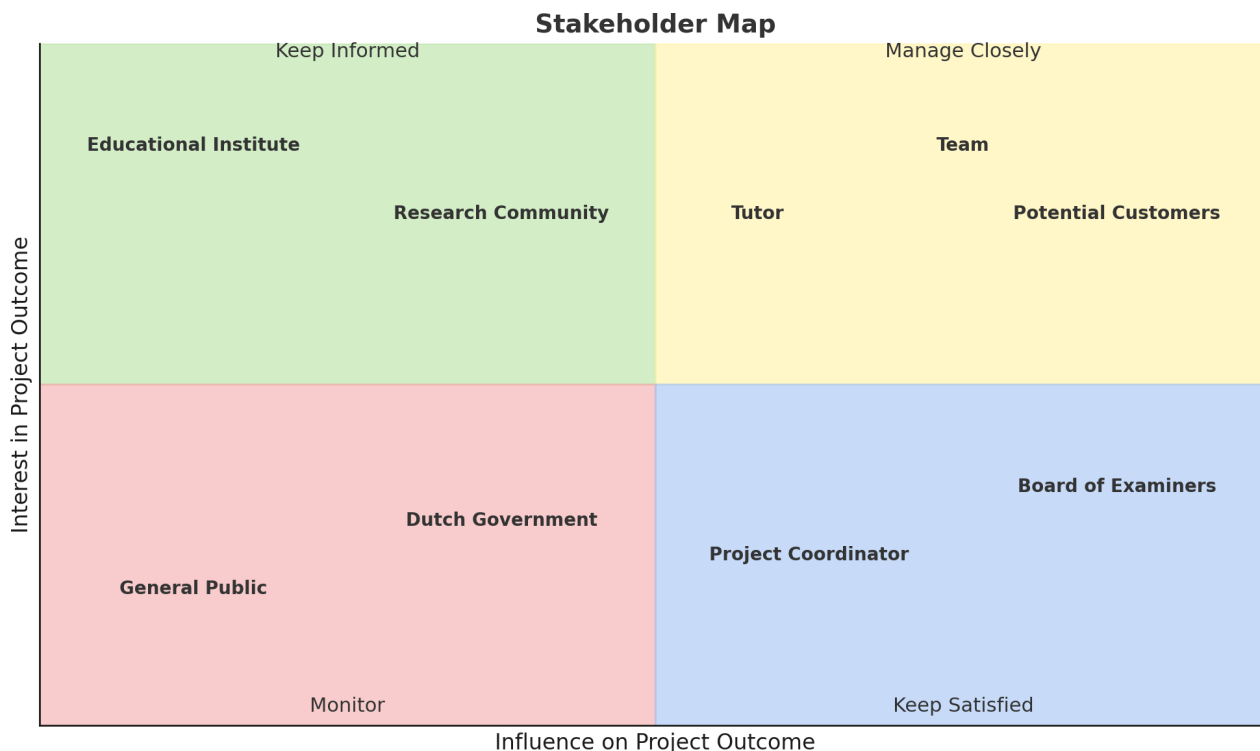


Figure 3.1: Stakeholder map concerning the Rotating cylindrical drone swarm

Figure 3.1 is the stakeholder map that categorises stakeholders based on two key dimensions: their interest in the project outcome and their influence on the project outcome. In the first quadrant (keep informed), which includes stakeholders like the educational institute (TU Delft) and the wider research community. These groups are highly interested in the project's results, due to academic and developmental alignment, but they do not significantly affect decision-making. In the second quadrant (manage closely), the team, tutor and potential customers are identified as stakeholders. These stakeholders are both influential and deeply invested in the project's success. Their input, feedback and approval are crucial, so they must be closely managed through constant interaction and collaboration. This quadrant typically contains the core team and key external beneficiaries. Next, in the third quadrant (monitor), the general public and the Dutch government are included. While these entities have limited influence and relatively low direct interest in the project's specific outcome, they may become more relevant due to regulatory or public engagement reasons. Lastly, in the fourth quadrant (keep satisfied), the project coordinator and the board of examiners are included. Although they may not be actively engaged with day-to-day developments, their decisions and evaluations carry substantial weight. Keeping them satisfied involves strategic reporting, occasional meetings, and ensuring their expectations are met without overloading them with detail.

## 3.3. SWOT Analysis

An important tool to perform the market analysis on the product is a SWOT analysis. The strengths, weaknesses, opportunities and threats arising from the market are analysed to give better insight into how the product can be placed optimally on the market. This is shown in Table 3.1.

As shown by the SWOT Analysis, there is ample room to place the product within the market. The projected cost and environmental impact of the project are of prime importance to keep low to competitively place itself within the sector. There will, however, be challenges in the product development process due to the novelty of the idea and therefore the complexity of the task. This will lead to high development costs due to significant verification and validation required for the product.

The versatility of the product due to its swarm nature allows it to be able to scan different areas with multiple types of sensors simultaneously, and these sensors can easily be interchanged to allow for versatile application of the drones not only in wildfire mapping but also in: Autonomous monitoring (e.g. precision farming, pollution detection, wildlife conservation), search and rescue operations and military applications, according to Alqudsi

Et al.[4]. The general opportunities in the Firefighting Drone Market are also projected to be very large, with a rapidly growing market described in section 3.4 alongside development and integration with AI and ML algorithms to improve swarming capabilities further. The rapidly increasing risk of wildfires due to poor forest management and global warming is also a cause for a large need in the sector.

Table 3.1: SWOT Analysis of Product-Market

SWOT Analysis: Swarm of Cylindrical Drones for Wildfire Mapping	
<b>Strengths</b>	<b>Weaknesses</b>
<ul style="list-style-type: none"> <li>- Unique product on the market with potential of capturing a new market</li> <li>- Low projected cost per item</li> <li>- Versatile platform which can have a modular payload to accommodate different sensors</li> <li>- Fast projected manufacturing time</li> <li>- Scalability and fault tolerance due to the swarm nature - Simplicity, low number of potential failure points</li> </ul>	<ul style="list-style-type: none"> <li>- Reliability unproven compared to traditional fixed-wing UAVS and quad-copters</li> <li>- Risk of novel concept implementation</li> <li>- High development cost due to high verification and validation requirements</li> <li>- Not a standalone product - reliance on mothership for operation</li> <li>- Limited range compared to larger UAVS</li> </ul>
<b>Opportunities</b>	<b>Threats</b>
<ul style="list-style-type: none"> <li>- Emerging markets for micro-UAV + swarming application</li> <li>- Collaborations with research institutes</li> <li>- Integration with AI and ML technologies with swarming algorithms</li> <li>- Rapidly increasing number of wildfires due to global warming</li> </ul>	<ul style="list-style-type: none"> <li>- Potential competing designs if proven successful</li> <li>- Rapid advancement of technology is causing possible redundancy of product</li> <li>- Legal and Regulatory hurdles</li> </ul>

### 3.4. Competitive Analysis in Sector

To assess the competitiveness of the proposed fire-mapping drone swarm system, a comparative analysis was conducted against existing fire detection and mapping solutions. This includes another UAV platform being the AVY Aera<sup>6</sup>, a fixed-wing VTOL drone produced by a Dutch startup for mapping purposes, representing direct competition in the Dutch market. Other fire-mapping systems considered are from satellite Imaging<sup>7</sup>, the OV-10A Bronco manned aircraft operated by CAL FIRE<sup>8</sup>, and the Ground-based Towers ALERTCalifornia<sup>9</sup> uses across California. Defining performance indicators such as cost, scanning area and resolution are compared. The results, summarised in Table 3.3, provide a basis for positioning the system within the market and refining functional requirements to meet cost-effectiveness and performance expectations.

Table 3.3: Competitive analysis of fire mapping solutions

System	Scanning (km <sup>2</sup> /min)	Area	Resolution (m/pixel)	Estimated Cost (EUR)	Data Latency (mins)
L.O.R.A.X. Drone Swarm	6		0.67	16,705	Real-time
Satellite Imaging (MODIS, VIIRS, Landsat)	» 1		30-1000	» 10 <sup>6</sup>	30-60
Manned Aircraft (CalFire OV-10A Bronco)	Observed area		Naked-eye	480,000 base + high operating costs	Real-time
Fixed-wing Single-Node UAV (Avy Aera)	< 1		0.25	85,000-120,000	Real-time
Ground-Based Towers (ALERTCalifornia)	14,657 per node		N/A	» 10 <sup>4</sup>	Real-time

<sup>6</sup>Avy Aera Brochure 2025, <https://avy.eu/technology>, (accessed 16/06/2025).

<sup>7</sup>NASA FIRMS Fire Map. Available at: <https://firms.modaps.eosdis.nasa.gov/map/#d:24hrs;@0.5,-3.9,3.3z> (accessed 16/06/2025)

<sup>8</sup>CAL FIRE Aviation Program. Available at: <https://www.fire.ca.gov/what-we-do/fire-protection/aviation-program> (accessed 16/06/2025)

<sup>9</sup>ALERTCalifornia Technology Overview. Available at: <https://alertcalifornia.org/technology/> (accessed 16/06/2025)

The L.O.R.A.X. drone swarm offers a unique combination of real-time hotspot mapping, high-resolution imaging (0.67 m/pixel), and fast area coverage (6 km<sup>2</sup>/min) at a competitive cost of €16,705, making it a scalable solution for tactical wildfire intelligence.

Manned aircraft like the OV-10A Bronco have extremely high cost (€480,000+ base cost) and rely on visual observation without onboard sensors, offering no data transmission and exposing human crews to risk. Satellite systems (e.g., MODIS, VIIRS) and ground-based networks like ALERTCalifornia towers excel at wide-area detection but lack the precision and update rate needed to guide firefighting teams to precise hotspots.

Compared to UAVs like the Avy Aera (cost: €85,000–€120,000, coverage: <1km<sup>2</sup>/min, resolution: 0.25 m/pixel), the L.O.R.A.X. swarm delivers broader, faster coverage at significantly lower cost. While Avy provides high accuracy, its single-node design limits its coverage compared to the swarm configuration proposed.

### 3.5. Business Model Canvas

The business centres around developing and deploying a swarm of low-cost, rotating cylindrical-wing drones designed for forest fire detection. These drones are equipped with thermal and visual sensors and coordinated through swarm algorithms, enabling scalable, redundant coverage of large forest areas. Their modular payload system allows for real-time smoke and fire detection while remaining lightweight and cost-effective at around €1000 per unit.

Key partners include sensor manufacturers, aerospace research labs, forestry departments, environmental monitoring agencies, and drone software developers. These partners support the development, testing, and deployment of the drones. Internally, the main activities involve designing and manufacturing the drones, developing the swarm coordination software, integrating detection payloads, conducting field tests in forest environments, and offering ongoing maintenance and support services.

The business relies on critical resources such as drone hardware and software intellectual property, custom swarm algorithms, sensor packages, and access to assembly and testing facilities. Deployment partnerships and pilot programs with public agencies help validate and promote the solution.

Customer relationships are maintained through technical support, operator training, custom payload development, and long-term fleet maintenance. The product reaches customers, mainly government agencies, forestry services, and environmental organisations through direct B2G and B2B sales, scientific conferences, specialised drone expos, and an online monitoring platform.

Revenue comes from the sale of individual drones, bundled swarm solutions, maintenance contracts, software licensing, and integration services tailored to customer needs. Costs are driven by research and development, materials sourcing, software and hardware production, testing, certification, and user training.

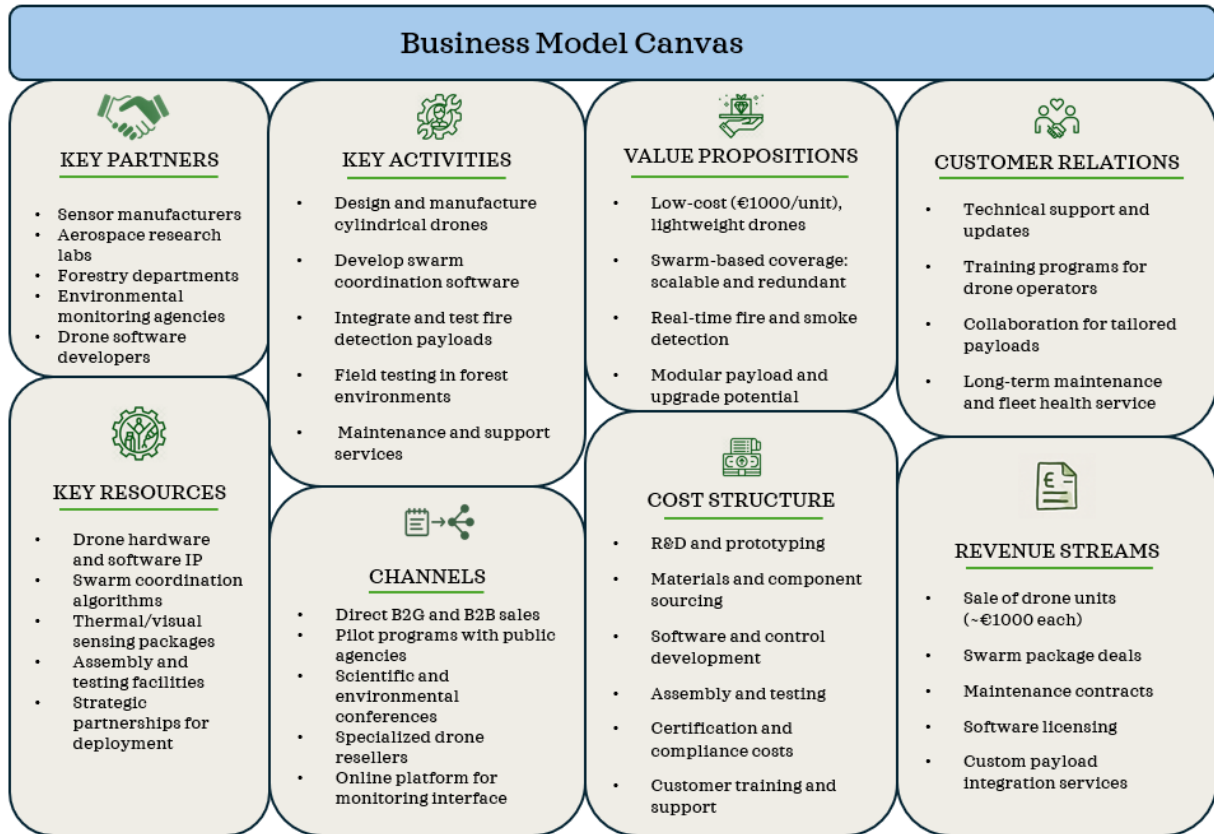


Figure 3.2: Business model canvas of LORAX, format is coherent to the Cambridge Enterprise template.

## 4 Functional Analysis

To derive proper system and subsystem requirements, it was necessary to inspect and analyse the functions that the system shall perform. Hence, a functional flow diagram for the L.O.R.A.X. project was made, and is presented in the [Appendix A](#). The diagram shows a time-dependent flow of all the functions to be performed. It shows a general overview of the project planning, followed by the mission, and ending with the system disposal (as shown in the green boxes). Furthermore, the first-level functions that are mainly related to the mission itself are then extended to second and third-level functions, with orange and grey boxes, respectively.

Note that three high-level functions show strong coupling, these being swarm control, single-node flight, and measurements. They happen simultaneously and require constant input from each other. For the swarm to be controlled, the drones must first be deployed and achieve stable flight independently, and then the drone nodes need to be able to adjust their flight path based on the swarm control. Changes in drone dynamics are then used as input to calculate the desired swarm flight path. Furthermore, the swarm control is also dependent on the measurements taken by the swarm, as these show different conclusions on detected hotspots, which influence the decision of the node distribution.

After setting up the functional flow diagram, the blocks were organised into a functional breakdown structure, seen in [Appendix B](#). Here, the functions under "Perform Mission" are segmented with added levels of detail. Note that this diagram has no time dependency. Each block has a unique identifier that is coherent with those of the functional flow diagram.

## 5 Requirements

This chapter goes over the requirements driving the design, development, and operation of the L.O.R.A.X. drone. Three categories of requirements are defined: stakeholder, mission and system requirements. Table 5.1 holds the abbreviations for the categorisation of the requirements, whereas Table 5.2 explains the abbreviations used to describe the verification methods. In Table 5.3, the stakeholder and mission requirements are discussed.

Table 5.1: Priority Abbreviations for categorisation of the requirements

Abbreviation	Meaning
Ky	Key requirement
K	Killer requirement
D	Driving requirement

Table 5.2: Verification Method Abbreviations used for the requirements

Abbreviation	Meaning
A	Analysis
I	Inspection
D	Demonstration
T	Testing
S	Simulation

Table 5.3: Stakeholder and Mission Requirements

ID	Requirement Text	Priority	Rationale/Source	Verification
<b>STK Level (Stakeholder Requirements)</b>				
STK01	The system shall provide the primary customer (e.g., Firefighting Agencies) with a more effective and rapidly deployable wildfire monitoring solution compared to current methods.	Ky	Market Analysis, User Need	A
STK02	The system shall operate with minimal negative environmental impact, addressing societal and regulatory expectations.	Ky	Market Analysis, Sustainability Driver	A
STK03	The system shall operate safely and in full compliance with applicable airspace and drone regulations (e.g., EASA).	D	Market Analysis, EASA/FAA	A, I
STK04	The project shall be developed successfully within the academic, time, and resource constraints defined by the Design Synthesis Exercise.	D	DSE Context	I
STK05	The system shall represent a cost-effective solution in terms of acquisition and operation for potential end-users.	D	Market Analysis, User Need	A
STK06	The system shall be designed so it can be easily adapted for uses beyond wildfire mapping.	Ky	Market Analysis	A
<b>MIS Level (Mission Requirements)</b>				
<i>High-Level Mission Goals</i>				
STK01-MIS01	The Swarm System shall perform effective autonomous wildfire mapping over a designated area.	Ky	Derived from STK01	S, D
STK05-MIS02	The Swarm System shall operate within defined economic constraints.	D	Derived from STK05, STK04	A
STK03-MIS03	The Swarm System shall operate safely according to regulations.	D	Derived from STK03, STK01	A, I
STK02-MIS04	The Swarm System shall meet sustainability goals addressing societal and regulatory expectations.	Ky	Derived from STK02, STK03	A, T, I
STK04-MIS05	The Swarm System development shall adhere to specified DSE process constraints.	D	Derived from STK04	I, A
STK06-MIS29	The Swarm System Mission shall support operational scenarios utilising different, interchangeable sensor payloads.	Ky	Derived from STK06	A, D
<i>Detailed Mission Capabilities &amp; Constraints (Original User Req. Mapping)</i>				
STK01-MIS06	Each drone node shall have a minimum flight time of 10 [min].	D	UR-PE-1; Flows from STK01-MIS01	T, S
STK01-MIS07	The mission shall utilise a main mother-ship for drone node launch.	Ky	UR-PE-2; Flows from STK01-MIS01	I
STK01-MIS89	Each drone shall not stall, compromising controllability, due to a gust of 5 m/s	D	Flows from STK01-MIS01	S, T
STK01-MIS10	The system shall provide a mothership-drone communication range of at least 1 [km] line of sight.	D	UR-PE-5; Flows from STK01-MIS01	T, A
STK01-MIS11	The swarm shall scan an area of at least 10 [km <sup>2</sup> ].	D	UR-PE-6; Flows from STK01-MIS01	S, A
STK01-MIS12	Each drone node shall detect hotspots of at least 1 [m <sup>2</sup> ].	D	UR-PE-7; Flows from STK01-MIS01	S, T
STK01-MIS13	Each drone node shall determine an average hotspot temperature of at least [110] [°C].	Ky	UR-PE-8; Flows from STK01-MIS01	TBD

Continued on next page...

Table 5.3: Stakeholder and Mission Requirements – Continued

ID	Requirement Text	Priority	Rationale/Source	Verification
STK01-MIS14	Each drone node actuator shall provide thrust, control, and torque.	D	UR-PE-9; Flows from STK01-MIS01	A, I
STK03-MIS15	The system shall comply with EASA Open Category A1/C0 regulations for civil drones.	D	UR-SR-1; Flows from STK03-MIS03	I, A
STK03-MIS16	Each drone node shall have a minimum reliability of [95] [%] for a mission.	Ky	UR-SR-2; Flows from STK03-MIS03	TBD
STK03-MIS17	The integrated swarm network shall have a minimum reliability of at least [99] [%].	Ky	UR-SR-3; Flows from STK03-MIS03	TBD
STK02-MIS18	Each drone node shall produce zero nitrogen oxide emissions during operation.	Ky	UR-SU-1; Flows from STK02-MIS04	A, I
STK02-MIS19	Each drone node flying over 150 [m] shall emit a maximum noise level of 35 [dB] at ground level.	Ky	UR-SU-2; Flows from STK02-MIS04	A, T
STK02-MIS20	Each drone node operating above 150 [m] altitude shall not be spotted by civilians.	Ky	UR-SU-3; Flows from STK02-MIS04	A, I
STK03-MIS21	Each drone node weight shall not exceed 250 [g].	D	UR-EB-1; Flows from STK03-MIS03	I, T
STK03-MIS22	The system communication shall comply with European datalink requirements (EASA Art. TCO.205).	D	UR-EB-2; Flows from STK03-MIS03	I, A
STK05-MIS23	The drone node design shall be suitable for mass production.	D	UR-EB-3; Flows from STK05-MIS02	A, I
STK01-MIS24	The swarm shall be launched from an in-air launch unit.	D	UR-EB-4; Flows from STK01-MIS01	A, I
STK05-MIS25	The mission total acquisition cost (10 nodes + launch unit) shall be under 20000 [€].	D	UR-CB-1; Flows from STK05-MIS02	A
STK05-MIS26	The mission operational cost shall be lower than 1000 [€/hour].	Ky	UR-CB-2; Flows from STK05-MIS02	A

Then, the system-level requirements are explained in Table 5.4. The table has an additional column for the requirement type and category. Three main requirement types are distinguished: Operational, Functional and Constraints, where constraints are restrictions in the degree of freedom for providing a solution. In addition, the Rationale/Source column explains the relation to the respective mission requirement as well as the ID from the requirement discovery tree (RDT).

Table 5.4: System Requirements

ID	Requirement Text	Type	Category	Rationale/Source	Verification
<b>SYS Level (System Requirements)</b>					
<i>RDT 1.1.1 Launch Drone Swarm</i>					
STK01-MIS07-SYS01	The system shall launch drone nodes from a mothership.	Operational	Structure, Nav&Ctrl	Flows from MIS07, MIS24; RDT 1.1.1.1	S, D, T
STK01-MIS06-SYS02	The system shall ensure drone nodes achieve stable flight after launch.	Functional	Nav&Ctrl, Structure	Flows from MIS06; RDT 1.1.1.2	S, T
<i>RDT 1.1.2 Operate Drone Swarm Autonomously</i>					
STK01-MIS06-SYS03	The system (each drone node) shall maintain stable and controllable flight in expected operational conditions.	Functional	Nav&Ctrl, Propulsion	Flows from MIS06; RDT 1.1.2.1	S, T
STK01-MIS06-SYS39	The system (each drone node) shall maintain continuous rotation about its primary axis during flight to provide gyroscopic stability.	Functional	Propulsion, Structure, Nav&Ctrl	Flows from STK01-MIS06-SYS03; Project Premise	T, S, A, I
STK01-MIS11-SYS04	The system shall coordinate the movement and actions of 10 drone nodes as a swarm.	Functional	Nav&Ctrl (Swarm)	Flows from MIS11; RDT 1.1.2.2	S, D
STK01-MIS11-SYS05	The system shall enable drone nodes to execute predefined or dynamically assigned flight paths.	Operational	Nav&Ctrl (Swarm)	Flows from MIS11; RDT 1.1.2.3	S, D
STK01-MIS06-SYS06	The system (each drone node) shall operate continuously for a minimum of 10 minutes.	Functional	Power, Propulsion	Flows from MIS06; RDT 1.1.2.4	T, S
<i>RDT 1.1.3 Scan Area of Interest</i>					
STK01-MIS11-SYS07	The system (swarm) shall scan a total area of at least 1 [km <sup>2</sup> ] within the mission duration.	Functional	Payload, Nav&Ctrl (Swarm)	Flows from MIS11; RDT 1.1.3.1	S, A
STK01-MIS12-SYS08	The system (each drone node) shall achieve 360-degree sensing coverage around its spin axis.	Functional	Payload, Structure	Flows from MIS12; RDT 1.1.3.2; System Desc.	A, I
<i>RDT 1.1.4 Detect Wildfire Hotspots</i>					
STK01-MIS12-SYS09	The system (each drone node) shall detect thermal hotspots of at least 1 [m <sup>2</sup> ] size.	Functional	Payload	Flows from MIS12; RDT 1.1.4.1	S, T

Continued on next page...

Table 5.4: System Requirements – Continued

ID	Requirement Text	Type	Category	Rationale/Source	Verification
STK01-MIS13-SYS10	The system (each drone node) shall measure hotspot temperatures of at least [110] [°C].	Functional	Payload	Flows from MIS13; RDT 1.1.4.2	TBD
<i>RDT 1.1.5 Manage Data &amp; Communication</i>					
STK01-MIS12-SYS11	The system (each drone node) shall acquire data from its onboard sensor(s).	Functional	Payload, Power	Flows from MIS12; RDT 1.1.5.1	S, T
STK01-MIS12-SYS12	The system (mothership/nodes) shall process sensor data to identify hotspots and locations.	Functional	Nav&Ctrl, Payload	Flows from MIS12; RDT 1.1.5.2	S, A
STK01-MIS10-SYS13	The system shall facilitate data transmission between drone nodes and the mothership.	Functional	Nav&Ctrl (Comm)	Flows from MIS10; RDT 1.1.5.3	S, T
STK01-MIS10-SYS14	The system shall maintain radio communication link (line of sight) up to at least 1 [km] range.	Functional	Nav&Ctrl (Comm)	Flows from MIS10; RDT 1.1.5.4	T, A
<i>RDT 1.1.6 Perform Manoeuvres</i>					
STK01-MIS14-SYS17	Any actuator added to the system (a drone node) shall simultaneously provide propulsion, gyroscopic stability, and control.	Functional	Propulsion, Nav&Ctrl	Flows from MIS14; RDT 1.1.6.3	A, I, S
STK01-MIS14-SYS18	The drone shall not stall due to a gust of 5 m/s	Functional	Propulsion, Nav&Ctrl	Flows from MIS14; RDT 1.1.6.3	A, I, S
<i>RDT 1.2.1 Adhere to Resource Constraints</i>					
STK05-MIS25-SYS18	The system (10 nodes + launch unit) total procurement cost shall be below 20000 [€].	Constraint	Project Mgmt	Flows from MIS25; RDT 1.2.1.1	A
STK05-MIS26-SYS19	The system operational cost shall be below 1000 [€/hour].	Constraint	Project Mgmt	Flows from MIS26; RDT 1.2.1.2	A
STK04-MIS27-SYS20	The system (drone nodes) shall be simulated using a parametric simulator supporting aero/dynamic coupling.	Constraint	Nav&Ctrl, Aero	Flows from MIS27; RDT 1.2.1.3	I, S
STK04-MIS28-SYS21	The system simulation environment shall support controller development and swarming algorithm optimisation.	Constraint	Nav&Ctrl (Swarm)	Flows from MIS28; RDT 1.2.1.3	I, S
STK04-MIS05-SYS22	The system shall be developed within the DSE project timeframe (approx. 10 weeks).	Constraint	Project Mgmt	Flows from MIS05; RDT 1.2.1.4	I
<i>RDT 1.2.2 Ensure Safety &amp; Reliability</i>					
STK03-MIS15-SYS23	The system (each drone node) shall comply with EASA Open Category A1/CO mass and operational limits.	Constraint	Structure, Nav&Ctrl	Flows from MIS15; RDT 1.2.2.1	I, A
STK03-MIS21-SYS24	The system (each drone node) maximum take-off mass shall not exceed 250 [g].	Constraint	Structure	Flows from MIS21; RDT 1.2.2.2	I, T
STK03-MIS16-SYS25	The system (each drone node) shall achieve a minimum reliability of [95] [%] for each mission.	Constraint	All	Flows from MIS16; RDT 1.2.2.3	TBD
STK03-MIS17-SYS26	The system (swarm network) shall achieve a combined mission reliability of [99] [%].	Constraint	Nav&Ctrl (Swarm)	Flows from MIS17; RDT 1.2.2.4	TBD
STK03-MIS15-SYS27	The system shall be designed to minimise risk of harm to people or property during operation.	Constraint	Structure, Nav&Ctrl	Flows from MIS15/MIS03; RDT 1.2.2.5	A, I
<i>RDT 1.2.3 Meet Sustainability Requirements</i>					
STK02-MIS18-SYS28	The system (each drone node) propulsion shall produce zero NOx emissions.	Constraint	Propulsion	Flows from MIS18; RDT 1.2.3.1	A, I
STK02-MIS19-SYS29	The system (each drone node) noise emission at 150 [m] altitude shall not exceed 35 [dB] at ground level.	Constraint	Propulsion, Aero	Flows from MIS19; RDT 1.2.3.2	A, T
STK02-MIS20-SYS30	The system (each drone node) shall have a low visual signature to minimise spotting by civilians above 150 [m] alt.	Constraint	Structure	Flows from MIS20; RDT 1.2.3.3	A, I
STK06-MIS06-SYS33	The system (drone node) shall provide a standardised mechanical interface for sensor payload attachment and detachment.	Constraint	Structure, Payload	Flows from MIS29; RDT 1.2.3.4	I, D
STK06-MIS06-SYS34	The system (drone node) shall provide a standardised electrical interface for powering interchangeable sensor payloads.	Constraint	Power, Payload	Flows from MIS29; RDT 1.2.3.4	I, T
STK06-MIS06-SYS35	The system (drone node) shall provide a standardised data interface for communication with interchangeable sensor payloads.	Constraint	Nav&Ctrl (Comm), Payload	Flows from MIS29; RDT 1.2.3.4	I, T
STK06-MIS06-SYS36	The system's flight control and navigation functions shall remain operational and within performance specifications regardless of the specific compliant sensor payload installed.	Constraint	Nav&Ctrl	Flows from MIS29; RDT 1.2.3.4	S, T
STK06-MIS06-SYS37	The system software architecture shall support the integration of different sensor payload driver modules compliant with the defined interfaces.	Functional	Nav&Ctrl (Software)	Flows from MIS29; RDT 1.2.3.4	A, S

Continued on next page...

Table 5.4: System Requirements – Continued

ID	Requirement Text	Type	Category	Rationale/Source	Verification
STK06-MIS06-SYS38	The system design shall accommodate variations in mass and centre of gravity resulting from interchangeable sensor payloads within [0.02][kg] and [0.01][m] limits without compromising flight stability.	Constraint	Structure, Nav&Ctrl	Flows from MIS29; RDT 1.2.3.4	A, S
<i>RDT 1.2.4 Comply with Engineering &amp; Operational Constraints</i>					
STK03-MIS22-SYS31	The system communication shall comply with European datalink regulations (Art TCO.205).	Constraint	Nav&Ctrl (Comm)	Flows from MIS22; RDT 1.2.4.1	A, I
STK05-MIS24-SYS32a	The system design shall maximise the use of Commercial-Off-The-Shelf (COTS) components where performance and other requirements permit.	Constraint	All (Design Choice)	Flows from MIS24; RDT 1.2.4.2	I, A
STK05-MIS24-SYS32b	The system assembly design shall minimise the number of unique parts and distinct assembly operations.	Constraint	Structure, Manuf.	Flows from MIS24; RDT 1.2.4.2	A, I
STK05-MIS24-SYS32c	The materials selected for primary structural components shall be suitable for high-volume manufacturing processes (e.g., injection moulding, stamping) where feasible.	Constraint	Structure, Manuf.	Flows from MIS24; RDT 1.2.4.2	A, I

## 6 Technical Risk Assessment

To meet the 95% drone node reliability and 99% swarm network reliability requirements, stated in [chapter 5](#), a detailed risk assessment is performed. This assessment will identify potential risks that could compromise the success, safety, or efficiency of the L.O.R.A.X. drone swarm mission. Additionally, various measures are taken to mitigate the probability and impact of these risks. First, [section 6.1](#) describes the different risks and the mitigation strategies. [subsection 6.1.1](#) then shows the effect on the risk map after the mitigation.

### 6.1. Risks and Mitigation

A highly detailed risk assessment approach is used to identify any risk that could potentially harm the mission of the L.O.R.A.X. drone. This section describes the identified risks, followed by their mitigation strategy. These may be found in [Table 6.1](#)

The risks are divided into different categories, namely: Technical (TEC), Financial (FIN), Organisational (ORG), Mission (MIS), Safety (SAF), Sustainability (SUS), and Ethical (ETH). Each risk has its unique identifier, probability score, and impact score. The identifier is made up of 'Technical Risk (TR)-Category-Number'. A risk has its own probability and impact score, suggesting how likely the risk is to happen and what the magnitude of the impact is. The probability score is scaled according to *Likely (4)*, *Possible (3)*, *Unlikely (2)* and *Rare (1)*. The impact score is scaled using *Negligible (1)*, *Marginal (2)*, *Moderate (3)*, *Critical (4)* and *Catastrophic (5)*.

Followed by the risks are the mitigation strategies belonging to each risk. These mitigation strategies are set up in a way that the risk is reduced to an acceptable level. In [Table 6.1](#), these strategies are followed by their effect on the scores. Also, the responsible role is assigned to each risk.

*Table 6.1: Risk Assessment*

ID	Risk Description	Prob.	Impact	Mitigation Strategy	Prob. $\Delta$	Impact $\Delta$	Responsible
TR-TEC-01	Inaccurate results from the Aerodynamic simulation, leading to under- or overestimation of the aerodynamic performance	4	4	Validate with experimental results, state the assumptions made, and apply errors.	-2	-1	Simulation Engineer
TR-TEC-02	Inaccurate stall model in simulation leading to wrong flight envelope limits	3	4	Implement the stall behaviour of experimental results and limit the flight envelope to a value lower than the predicted stall.	-1	-2	Simulation Engineer
TR-TEC-03	Component failure on PCB (short circuit, open circuit, degradation)	2	4	Run detailed and careful DRC (design rule check) to ensure the components' placement is optimal.	-1	0	Electrical Control Engineer
TR-TEC-04	Overheating of components on PCB leading to failure	2	4	Allow airflow into the PCB where it is placed	-1	-3	Electrical Control Engineer/Structures Engineer
TR-TEC-05	Control simulation differs too much from reality, leading to unpredictable behaviour of the L.O.R.A.X. drone	3	5	Verify simulation by performing numerous tests	-1	0	Control Simulation Engineer
TR-TEC-06	Propeller detachment	2	3	Perform pre-flight checks	-1	0	Propulsion Engineer
TR-TEC-07	Failure in propulsion system causes uncontrollability	2	3	Test the system to its limits	-1	0	Propulsion Engineer
TR-TEC-08	Motor failure	2	3	Plan for regular maintenance	-1	0	Propulsion Engineer
TR-TEC-09	Inaccurate C.G. estimation results in a not big enough C.G. shift	2	4	Perform precise C.G. measurements in CATIA	-1	-1	Propulsion Engineer
TR-TEC-10	Failure in battery results in no power	2	3	Analyse how far the drone can glide without battery	0	-1	Electrical Control Engineer
TR-TEC-11	Due to the battery overheating, the structure catches fire	2	5	Implement ducts in the structure for cooling	-1	-1	Electrical Control Engineer
TR-TEC-12	Premature battery degradation leading to reduced flight time	2	3	Factor in degradation when planning mission endurance	-1	-1	Electrical Control Engineer
TR-TEC-13	A mass imbalance results in structural failure due to the rotational speed	3	4	Equally distribute the mass along the annular wing	-2	-1	Structures Head

*Continued on next page...*

Table 6.1: Risk Assessment – Continued

ID	Risk Description	Prob.	Impact	Mitigation Strategy	Prob. Δ	Impact Δ	Responsible
TR-TEC-14	Jamming of the rails of the C.G. shift system makes the C.G. shift inoperable	2	3	Apply lubricant during regular maintenance. If CP is in front of CG, a stable deep stall is achieved to safely land. If CP is behind the CG, the drone pitches down straight into the ground.	-1	-1	Structures Head
TR-TEC-15	Sensor failure	3	5	Diversify the sensor types used, apply protective enclosures and EMI shielding for payload components, perform rigorous testing on a spinning rig, and by flight testing.	-1	-2	Payload engineer
TR-TEC-16	Noise in the sensor leads to inaccurate state estimation	3	4	Appropriate tuning and filtering of the sensor data	-1	0	Payload engineer
TR-TEC-17	Failure of the visual camera causes no fire detection	3	4	More drones	0	-2	Swarm engineer
TR-TEC-18	Failure of the infrared camera causes no fire detection	3	4	More drones	0	-2	Swarm engineer
TR-TEC-19	Systematic loss of communication across the swarm due to mothership-side failure. Leading to total mission failure.	3	5	Set reliability requirement for mothership design	-1	0	Swarm engineer
TR-TEC-20	Failure in the communication link between a single drone and the mothership reduces swarm effectiveness.	2	4	Mesh network applied to intercommunicate between drones	0	-2	Swarm engineer
TR-TEC-21	Incorrect flight path distribution results in ineffective swarming paths	1	3	Areas of uncertainty are observed by the drones such that all the area is covered	0	-1	Swarm engineer
TR-TEC-22	Inaccurate swarming model results in mission failure	2	5	Validate the swarm model by performing smaller scaled flights	-2	0	Swarm engineer
TR-FIN-01	Inaccurate cost breakdown results in budgetary overruns	1	4	Include contingency in the budget	0	-1	Financial manager
TR-FIN-02	Fluctuations in price of parts (e.g., chips, batteries) result in unforeseen higher costs	3	2	Secure long-term agreements on pricing with supplier	-2	0	Financial manager
TR-FIN-03	Unexpected malfunctioning of parts demand replacement, increasing the costs	2	3	Develop an agreement with the supplier on free-of-charge replacement when malfunctioning component	0	-2	Financial manager
TR-FIN-04	Unexpected drone crashes demand full drone replacement for a fully operable swarm	3	4	Create budget for testing the crash survivability	-1	-1	Financial manager
TR-ORG-01	Not enough drones are loaded in the mothership	2	3	Develop a pre-mission setup	-1	0	Project Risk manager
TR-ORG-02	Mistakes in production plan results in delays	3	3	Have an experienced production engineer check the plan	-1	0	Project Risk manager
TR-ORG-03	Unavailable materials results in delays	3	2	Maintain close contact with supplier	-1	0	Project manager
TR-ORG-04	Issues with the supplier result in unavailable components	2	3	Find other suppliers	-1	-1	Financial manager, Structures Head
TR-MIS-01	Drone deployment failure results in reduced operational capacity	3	3	Ensure sufficient spacing and clear exit trajectory to minimise physical interference	-1	0	Structures Head
TR-MIS-02	Unsuccessful swarm deployment results in mission failure	3	5	Staggered launch sequence to prevent cascading inter-drone interaction failures.	-2	0	Swarm engineer
TR-MIS-03	Drone collision with another drone results in reduced operational capacity	1	4	Have back-up drones available on the mothership	0	-2	Project manager
TR-MIS-04	Drone collision with environment results in reduced operational capacity	3	3	Map the terrain and adjust the flight height accordingly	-2	0	Swarm engineer

Continued on next page...

Table 6.1: Risk Assessment – Continued

ID	Risk Description	Prob.	Impact	Mitigation Strategy	Prob. Δ	Impact Δ	Responsible
TR-MIS-05	Data acquisition failure results in no fire detection	3	5	Use different drones with different sensors	-1	-2	Payload engineer
TR-SAF-01	Drone crashing resulting in forest fire	2	5	Use of foam to create some form of foam packaging	0	-2	Risk manager
TR-SAF-02	Drone flying into pedestrian	2	5	Operate in unpopulated areas	-1	0	Risk manager
TR-SAF-03	Drone colliding with infrastructure (e.g., power lines, communication towers) results in damage	2	4	Map the terrain and adjust the flight height accordingly	-1	0	Swarm engineer
TR-SAF-04	Drone experiences bird strike	2	4	Have back-up drones available on the mothership	0	-2	Project manager
TR-SAF-05	Cyberattack on the swarm leads to intentional misuse	2	5	Make the communication links encrypted	-1	0	Payload engineer
TR-SUS-01	High energy consumption leads to a large carbon footprint	3	3	Use renewable energy	0	-2	Sustainability manager
TR-SUS-02	Failure of systems leads to undesired replacements	3	4	Design for easy repair	-1	-2	Sustainability manager
TR-SUS-03	Unrecoverable drones lead to waste in the environment	3	4	Apply GPS to a drone such that it is recoverable	0	-2	Sustainability manager
TR-SUS-04	Noise pollution from the swarm affects wildlife	2	4	Perform a noise measurement	-1	0	Sustainability manager
TR-ETH-01	Swarm used for purposes beyond the mission (e.g., military, surveillance, commercial data mining)	3	4	Establish ethical guidelines and acceptable use policies	-1	0	Risk manager

### 6.1.1. Risk Maps

To provide an overview of how the risks are mitigated, pre-mitigation and post-mitigation risk maps are constructed. These can be found in Table 6.2 and Table 6.3.

Table 6.2: Pre-mitigation Risk Map

	Negligible	Marginal	Moderate	Critical	Catastrophic
Likely				TR-TEC-01	
Possible		TR-FIN-02 TR-ORG-03 TR-MIS-01	TR-TEC-02 TR-ORG-02 TR-MIS-04 TR-SUS-01	TR-TEC-02, TR-TEC-13 TR-TEC-16, TR-TEC-17 TR-TEC-18, TR-FIN-04 TR-SUS-01, TR-SUS-02 TR-SUS-03, TR-ETH-01	TR-TEC-05 TR-TEC-15 TR-TEC-19 TR-MIS-02 TR-MIS-05 TR-SAF-05
Unlikely			TR-TEC-06, TR-TEC-07 TR-TEC-08, TR-TEC-10 TR-TEC-12, TR-TEC-14 TR-FIN-03, TR-ORG-01 TR-ORG-04, TR-SUS-04	TR-TEC-03 TR-TEC-04 TR-TEC-09 TR-TEC-20 TR-FIN-03 TR-SAF-03	TR-TEC-11 TR-TEC-22 TR-SAF-01 TR-SAF-02 TR-SAF-04
Rare			TR-TEC-21	TR-FIN-01 TR-MIS-03	

Table 6.3: Post-Mitigation Risk Map

	Negligible	Marginal	Moderate	Critical	Catastrophic
Likely					
Possible	TR-SUS-01	TR-TEC-17 TR-TEC-18 TR-SUS-03			
Unlikely	TR-FIN-03	TR-TEC-02 TR-TEC-10 TR-TEC-20 TR-FIN-03 TR-ORG-03 TR-SAF-01 TR-SAF-04 TR-SUS-02	TR-TEC-01 TR-TEC-15 TR-FIN-04 TR-ORG-02 TR-MIS-01 TR-MIS-05	TR-TEC-16 TR-ETH-01	TR-TEC-05 TR-TEC-19
Rare	TR-TEC-04 TR-TEC-21	TR-TEC-12 TR-TEC-14 TR-FIN-02 TR-ORG-04 TR-MIS-03	TR-TEC-06, TR-TEC-07 TR-TEC-08, TR-TEC-09 TR-TEC-13, TR-FIN-01 TR-ORG-01, TR-MIS-04	TR-TEC-03 TR-TEC-11 TR-SAF-03 TR-SUS-04	TR-TEC-22 TR-MIS-02 TR-SAF-02 TR-SAF-03

From Table 6.2 and Table 6.3, it can be seen how the risks are shifted more to the bottom left, lowering the probability and impact as much as possible. The risks having the most impact on the mission are **TR-TEC-05** and **TR-TEC-19**. To reduce the risk of **TR-TEC-05**, a more accurate simulation has to be obtained. Reducing the impact should consist of performing more verification and validation, and ultimately, having flight tests in a secure and safe area. The **TR-TEC-19** risk cannot be mitigated further, as a mothership failure is something that cannot be designed for. However, being aware of this possible failure is an important factor in the overall reliability of the mission.

## 7 Trade-Off Summary

The following chapter gives an overview of the designs considered for trade-off, as well as the method and reasoning for selecting the final configuration. Firstly, the method used for selecting between different control configurations is covered. Then, an overview of the different design configurations considered for the trade-off is given. Finally, the choices made in the trade-off are summarised.

The trade-off was performed with a qualitative approach. The relevant parameters were ranked from 1 to 5 using relative weights, the final scores were evaluated, and the design with the best score was selected. For the control system, a lot of emphasis was put on the control and agility and system performance, and endurance. Since they are key to successful mission completion and improved performance. For the payload sensor configuration, the most emphasis was put on detection and confirmation capability, since it is the key performance indicator of the mission.

During the trade-off, a selection was performed between 4 different control designs.

- The **Contra-Rotating Spring Pusher** uses a spring to shift its centre of gravity to provide a control torque to the L.O.R.A.X. (This concept is the contra-rotating concept with an extra spring to shift the CG of the drone).
- The **Contra-Rotating** design uses pure gyroscopic precession and spin rate modulation to provide a yaw rate to the drone
- The **Distributed Fan** design uses multiple rotors to spin up the drone, using sinusoidal power modulations in the rotors, the system can provide control torques in specified directions.
- The **Off-Axis** design uses the same control principle as the distributed fan but only includes a single propeller
- The **Swashplateless** design uses variable pitch propeller blades, which are actuated by pulses in the motor's rpm, to increase the angle of attack for certain parts of the rotation. Resulting in a thrust differential and therefore a control torque.

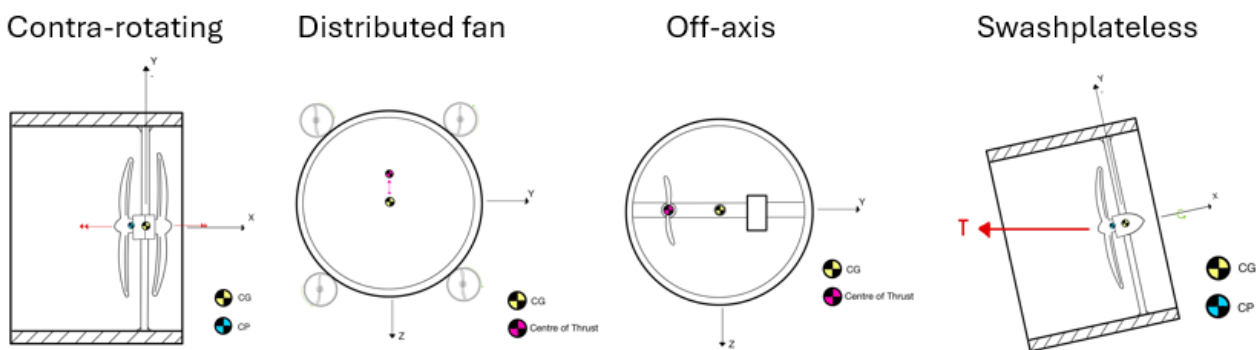


Figure 7.1: Design options of the rotating cylindrical wing drone.

The payload sensor types considered for the trade-off are as follows

- Infra-red camera
- Visual Camera
- Infra-red photodiode
- Pulsing Lidar
- Smoke detector

The chosen design uses two counter-rotating propellers along with a spring-based pushing mechanism. This setup provides good control, especially in turning, which is important for adjusting direction quickly during flight. While it is a bit more complex than using a single motor, the extra motor greatly improves the system's ability to rotate without adding too much cost or difficulty in building. Other options, like the simple spring pusher, gave longer flight times but were slower to turn. Designs such as the swashplateless system or distributed fans were

either harder to control or more complicated to build and operate. In the end, the counter-rotating spring pusher offered the best mix of control, reliability, and ease of integration.

For the payload, the selected combination is a visual camera for confirming fires and an infrared photodiode for detecting them. This setup covers a large area and is able to confirm fire events with good accuracy. It is not too heavy, doesn't use too much power, and is reasonably priced. Other options, like using a thermal camera, were lighter and cheaper but couldn't handle fast spinning well. LiDAR-based setups worked at high spin rates but were very expensive and used a lot of power, and could not operate at a reasonable altitude. Using a smoke sensor had a good detection range but poor confirmation performance. The visual and infrared setup provided a good balance between coverage, reliability, and practicality for real-world use.

## 8 Unified Simulation

The design of the L.O.R.A.X. is rather challenging, as a lot of its subsystems are strongly linked; decisions in one subsystem can very strongly influence all other subsystems. This is true for most aerospace projects, but can be very strongly observed in the L.O.R.A.X.

To address this, a Simulation-Based Design approach was used. This means simulations are not just applied for validating the final design, but to actively guide and drive design choices throughout the development process. This methodology also naturally aligns with some core principles of Multidisciplinary Design Optimisation (MDO), an engineering field focused on systematically optimising complex systems where various disciplines interact. Though the L.O.R.A.X. wasn't fully optimised using MDO in this phase, it certainly would be a promising possibility for improvement for future work.

### 8.1. Simulation Architecture

One of the key requirements for the L.O.R.A.X. project was the development of a unified simulation capable of encapsulating the complete behaviour of both the individual drone and the overall swarm. This unified simulation is structured around the following interconnected modules, as illustrated in [Figure 8.1](#).

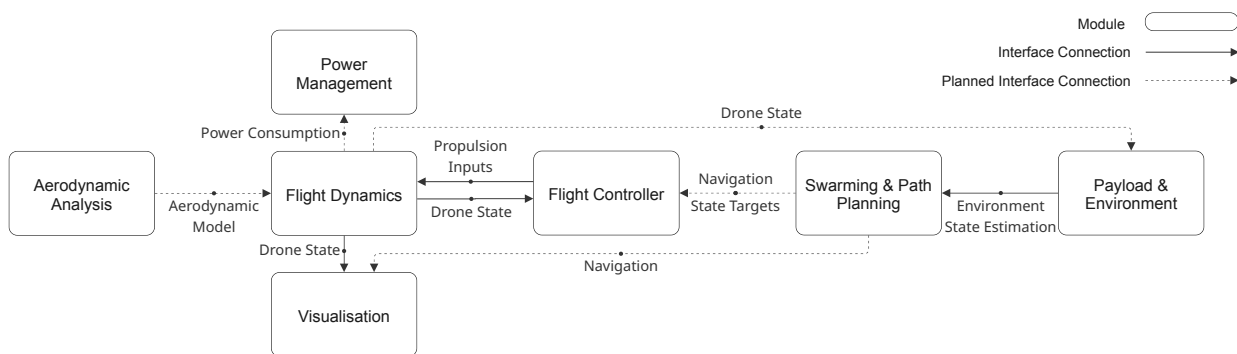


**Figure 8.1:** Architecture of the unified simulation used as backbone for the L.O.R.A.X. design process. This diagram illustrates the (planned) interconnected modules and their data flows.

- Aerodynamic Analysis Module:** Generates a simplified aerodynamic coefficient model for the L.O.R.A.X. drone based on Panel method analysis. This model is then supplied to the Flight Dynamics Module.
- Flight Dynamics Module:** Provides a high-fidelity, 6 Degrees of Freedom (6DoF) dynamic flight simulation, predicting the L.O.R.A.X. drone's behavior. It incorporates the simplified aerodynamic model from the Aerodynamic Analysis Module, along with gravity, propulsion, and rigid body dynamics. Its output, which represents the drone's state, is used for the Flight Controller and Swarming & Path Planning Modules.
- Flight Controller Module:** Processes navigation targets from the Swarming & Path Planning Module and generates control inputs for the Flight Dynamics Module's propulsion subsystem, enabling the drone to achieve a desired flight path.
- Power Management Module:** Analyses power consumption throughout a mission and tracks the drone's battery state.
- Payload & Environment:** Provides a state estimation of the mission environment and the drone's payload.
- Visualisation Module:** Generates visual representations of the drone in flight, including various graphs and a 3D representation based on the drone's state. While current capabilities include these visualisations, future improvements are planned to include a rendered 3D representation using Unreal Engine.

In [section 8.2](#), the flight dynamics module will be further discussed. In the subsequent chapters, the remaining modules will be discussed in more detail. Finally, the detailed design is discussed in [chapter 11](#).

MathWorks' Simulink [21] was selected as the primary programming environment for the unified simulation. Simulink offers advantages over alternative languages, such as Python, for modelling dynamic, time-dependent flight simulators, primarily due to its visual block diagram environment, which effectively represents system dynamics. Furthermore, it simplifies the modelling of continuous-time systems by providing pre-implemented

solver logic, allowing a direct focus on physical modelling rather than low-level programming. The built-in libraries and dynamic solvers are specifically tailored for physical and control systems, which significantly speeds up development.

## 8.2. Flight Dynamics Module

The approach to model the flight dynamics of the drone was based on P.H. Zipfel's *Modeling and Simulation of Aerospace Vehicle Dynamics* [43]. This book describes how to use Tensor Flight Dynamics, which provides a coordinate-system-independent framework ideal for describing complex motion. It provides a framework for simulating the flight dynamics of the L.O.R.A.X. The remainder of this section will be based on Zipfel's work.

### 8.2.1. Reference Frames

In any flight dynamics simulation, the definition and application of reference frames are crucial. For the L.O.R.A.X. drone, this is particularly important due to its spinning motion.

For the flight dynamics, three reference frames were used. They can also be seen in [Figure 8.2](#).

- Inertial Frame  $E$
- Body Frame  $B$
- Non-Spinning Body Frame  $B'$

For this simulation, a flat-earth assumption was used as the speeds of the drone are very small. According to Zipfel [43], even hypersonic missiles can still assume flat-earth, so it was decided that for the L.O.R.A.X., which flies at a speed of 20 m/s, this would be sufficient.

The Non-Spinning Body Frame ( $B'$ ) is a less commonly used frame that is especially used for spin-stabilised missiles. Just like such a missile, the L.O.R.A.X. is a spin-stabilised vehicle. Its advantage is its capability to isolate the drone's spin from its primary body axes. This simplifies aerodynamic analysis significantly.

For instance, the lift vector can be consistently defined as pointing upwards relative to this frame. In contrast, within a conventional Body Frame ( $B$ ), the lift vector would appear to constantly rotate, complicating its representation. By decoupling the spin, the non-spinning reference frame allows aerodynamic forces, like lift, to be defined in a manner more similar to conventional, non-spinning aircraft.

To achieve this, a parameter is added called the spin-angle  $\varphi$ , which is equivalent to roll in regular aircraft, but it is given a different name to prevent confusion. The body frame is rotated along the x-axis with the spin-angle. The drone spins around this axis with a spin-rate  $p$ .

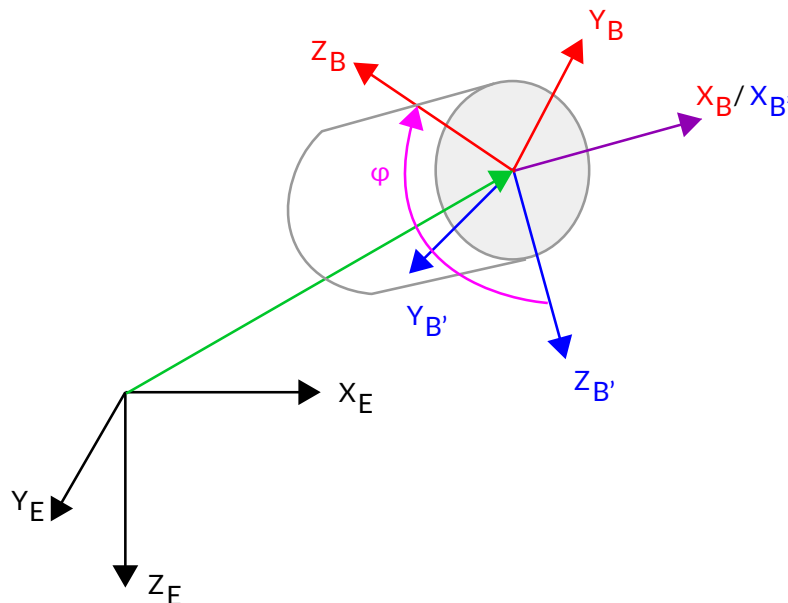


**Figure 8.2:** The figure illustrates the reference frames used in the simulation. The frames are: inertial Earth frame  $E$ , the spinning body frame  $B$  fixed to the object, and the non-spinning body frame  $B'$ . The non-spinning frame shares its  $X_{B'}$  axis with the body's  $X_B$  axis and its origin with the body frame, but it does not roll with the body. The angle  $\varphi$  represents the roll (spin) of the body frame relative to the non-spinning frame.  $Y_{B'}$  is aligned with the horizon, and  $Z_{B'}$  will be pointing downwards (but still swivels with pitch  $\theta$ ).

### 8.2.2. Equations of Motion

It was decided to use a 6 Degrees of Freedom (6DoF) rigid body set of equations of motion. This is one of the highest fidelity sets of equations flight dynamics can offer. This is necessitated by the highly coupled behaviour of the L.O.R.A.X.'s pitch, yaw and spin. In this model, inertia is considered time-varying (non-constant), but its time derivative is neglected. This simplification is justified because, while the drone's inertia does change as the spring moves, the effect of this derivative on the overall dynamics is incredibly small.

A derivation of the equations of motion is beyond the scope of this report, as it is very lengthy and will not provide additional benefit. Its detailed derivation can be found in Zipfel's book, and an overview can be found in the midterm report. A version with quaternions for the kinematic equations was used as the version with Euler angles has a risk of reaching a singularity.

These equations of motion for a rigid body are already implemented in Simulink's Aerospace Blockset<sup>1</sup>. This Commercial Off-The-Shelf (COTS) solution offers the advantage of being already verified, reducing development time. This block takes body-fixed forces and moments as input and outputs the drone's state, including position, velocity, attitude (as quaternions as well as Euler angles), and body rates. To make this block work with the non-spinning body frame ( $B'$ ), a transformation matrix is applied to all forces entering the block.

Initially, an attempt was made to implement a set of equations in the non-spinning reference frame. This proved to be quite challenging and would require more time to develop, which was beyond the time budget of this project. The downside of having a spinning body-fixed frame is that linearisation is significantly harder, and the numerical solution of the resulting equations becomes more challenging due to increased stiffness.

### 8.2.3. External Forces

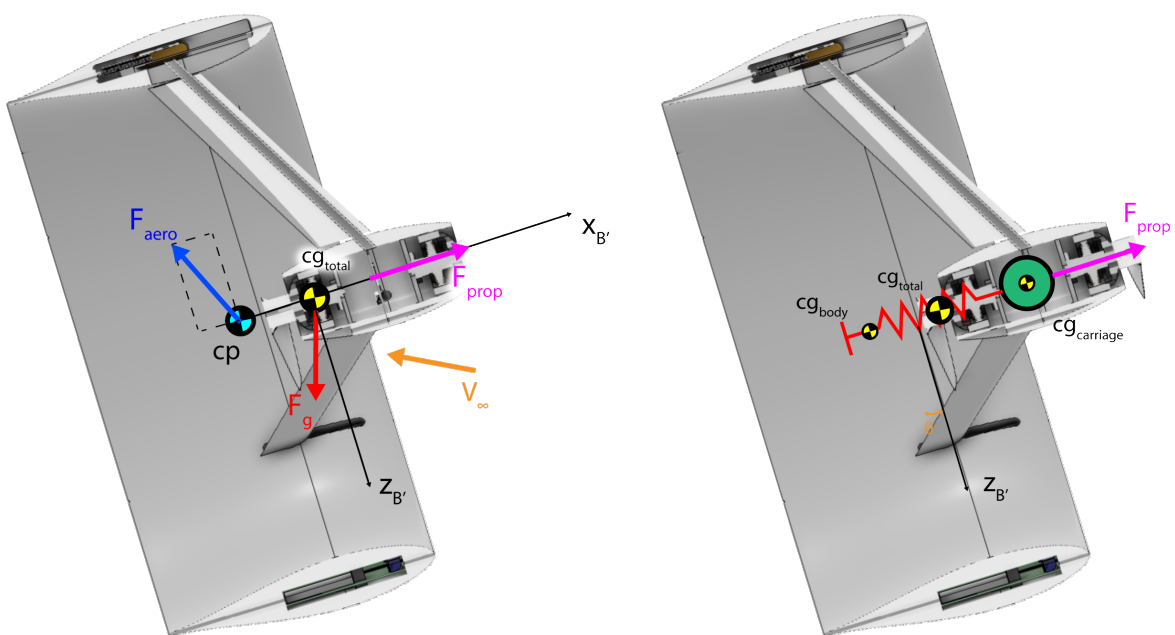
Figure 8.3 shows the Free Body Diagram of the L.O.R.A.X. drone. It consists of two parts: the body and the carriage. The struts, batteries and all moving parts are assumed to be part of the carriage. It is assumed that all aerodynamic forces act on the body and that the carriage movement does not add significant aerodynamic forces. This was assumed as the carriage does not move very significantly compared to the rest of the body. The carriage is attached to the body using a spring with spring coefficient  $K$ , and the force acting on the carriage comes from the propulsion system. The propulsion system is assumed to be aligned with the  $X_{B'}$  axis.

Gravity acts on the total Centre of Gravity (CG). The total centre of gravity gets calculated as a combination of the CG of the body and the carriage. The gravity vector will point down in the inertial frame. Finally, the Aerodynamic forces act on the Centre of Pressure (CP). Because there is a distance between the CG and the CP, there is a moment arm that creates a torque around the CG. If the CG is in the CP, which is possible due to the moving carriage, there will be no torque.

The aerodynamic force and propulsion force will be more extensively discussed in section 9.1 and section 9.2 respectively. The results of the flight simulation will also be shown in chapter 9.

---

<sup>1</sup><https://www.mathworks.com/help/aeroblks/6dofquaternion.html>, Accessed on 16-06-2025



(a) This free body diagram depicts the external forces acting on the drone, which consists of a body and a carriage. The reference axes shown are the non-spinning body axes ( $B'$ ). Aerodynamic forces ( $\vec{F}_{aero}$ ) are assumed to act at the body's centre of pressure (CP). The gravitational force ( $\vec{F}_g$ ) acts at the total centre of gravity. The propulsive force ( $\vec{F}_{prop}$ ) acts through the carriage's centre of gravity ( $CG_{carriage}$ ).  $\vec{V}_{\infty}$  indicates the freestream velocity.

(b) This figure shows the location of the total centre of gravity ( $CG_{carriage}$ ). The carriage is connected to the body via a spring.  $CG_{total}$  is a combination of the body's centre of gravity ( $CG_{body}$ ) and the carriage's CG. The angle  $\theta$  represents the pitch attitude of the body.

Figure 8.3: These diagrams show the forces acting on the L.O.R.A.X.

## 9 Flight Characteristics

This chapter discusses the unique flight characteristics of the L.O.R.A.X. drone, a critical aspect of its design and mission performance. Its behaviour in flight is a result of the combination of various subsystems, which are discussed in detail: aerodynamics (section 9.1), propulsion (section 9.2), power management (section 9.3), and stability and control (section 9.4). Finally, these elements will then be implemented in the flight dynamics module, which provides an extensive understanding of the drone's overall flight performance. This is discussed in section 9.5.

### 9.1. Aerodynamic Characteristics

Due to the unique design of the L.O.R.A.X. drone, the aerodynamic characteristics are unique by themselves as well. Little research has been performed on the aerodynamics of a rotating annular wing, offering the possibility to become pioneers for this configuration. This chapter describes how the aerodynamic coefficients are obtained. First, the design choices are discussed and justified. This is followed by stating the assumptions made. Next, the OpenVSP software validation is explained. Then, the aerodynamic coefficients are described and elaborated upon. Additionally, the link to the unified simulation of the aerodynamic analysis module is discussed.

#### 9.1.1. Design Choices

As a starting point for the drone design, the aspect ratio, defined as diameter over chord, was chosen. From earlier experiments by Fletcher [14], it was seen that higher aspect ratios generate lift more efficiently, as shown in Appendix E. An aspect ratio of 2 was found to have sufficient space along the chord for the spring system, while still generating lift efficiently. Furthermore, the NACA63(3)018 airfoil was selected, as this allows for components, such as batteries and wires, to be fitted inside the airframe. The optimal cruise velocity, 20 m/s, is found using an iterative process, led by a trade-off between the endurance and manoeuvrability, as discussed in section 9.5. In this section it is also discussed how the cruise Angle of Attack is chosen to be  $6^\circ$ , as this ensures a sufficient amount of climb rate in a straight line. From the chosen aspect ratio and the lifting equation, the reference surface area equals  $0.02 \text{ m}^2$ . The final parameters may be found in Table 9.1.

Table 9.1: Aerodynamic Parameters

Parameter	Value	Unit
Aspect Ratio	2	-
Airfoil	NACA63(3)0618	
$V_{\text{cruise}}$	20.00	m/s
$\alpha_{\text{cruise}}$	6.00	$^\circ$
$S_{\text{ref}}$	0.02	$\text{m}^2$
Diameter	0.2	m
Chord	0.1	m

#### 9.1.2. Assumptions

As the L.O.R.A.X. drone is a novel concept, there is limited information on the aerodynamics of a rotating cylindrical drone. Studies have been done on the physics of an annular wing, but not in combination with the wing rotating. Therefore, certain assumptions have to be made to attain an accurate estimation for the aerodynamic performance of the L.O.R.A.X. drone.

##### Rotational Drag

While the primary analysis focuses on lift, axial drag, and pitching moments, the rotation of the annular wing naturally induces an aerodynamic torque due to skin friction. In earlier design stages with a single propeller, accurately estimating this rotational drag was critical for determining a passively achieved steady-state body spin rate. With the current contra-rotating propeller configuration, however, the L.O.R.A.X. drone possesses active control over its body spin rate via differential torque/thrust.

The magnitude of this inherent rotational drag torque can still be estimated using established empirical correlations for rotating cylinders, as detailed by Childs [8]. The fundamental expression for the torque  $T_q$  on a cylindrical surface is given by:

$$T_q = C_{mc} \frac{1}{2} \pi \rho \Omega^2 d^4 L \quad (9.1)$$

For the L.O.R.A.X. annular wing, approximated as two thin cylindrical surfaces (inner and outer) with effective radius  $R_o$  and length  $L_c$ , the total drag torque is:

$$T_{q,\text{annulus}}(\Omega) \approx C_{mc}(\Omega) \pi \rho \Omega^2 R_o^4 L_c \quad (9.2)$$

The moment coefficient  $C_{mc}$  is a function of the rotational Reynolds number,  $Re_\omega = (\rho \Omega R_o^2) / \mu$ , and for turbulent flow (which is expected for the operational spin rates, as  $Re_\omega(\Omega) \approx 1121.88 \Omega \gg 60$  for  $\Omega > 0.05 \text{ rad/s}$  with

$R_o = 0.1$  m), it is typically determined iteratively from an empirical correlation such as:

$$\frac{1}{\sqrt{C_{mc}}} = -0.8572 + 1.250 \ln \left[ Re_\omega(\Omega) \sqrt{C_{mc}} \right] \quad (9.3)$$

Using the L.O.R.A.X. parameters ( $R_o = 0.1$  m,  $L_c = 0.1$  m,  $\rho = 1.225$  kg/m<sup>3</sup>,  $\mu = 1.789 \cdot 10^{-5}$  Pa · s), for a typical operational spin rate of  $\Omega \approx 44$  rad/s (approximately 7 Hz), the rotational Reynolds number is  $Re_\omega \approx 49,400$ . Iteratively solving for  $C_{mc}$  yields a value of approximately 0.0103. This results in an estimated total rotational drag torque on the annulus of:

$$T_{q,annulus}(\Omega \approx 44 \text{ rad/s}) \approx 0.0023 \text{ N} \cdot \text{m} \quad (9.4)$$

This value is very small and practically negligible. The contra-rotating propulsion system provides substantial differential torque authority. Therefore, the assumption regarding rotational dynamics is that *the desired body spin rate is actively commanded and maintained by the flight control system through differential propeller torque*. The control system is assumed to possess sufficient authority to overcome this inherent aerodynamic rotational drag and to modulate the spin rate as required for flight stability and manoeuvring. Consequently, a precise, independent characterization of this passive rotational drag within the primary OpenVSP aerodynamic model is deemed less critical than the design and validation of the spin rate control loop itself. This allows the main aerodynamic analysis to focus on the forces and moments directly relevant to the non-rotating or quasi-steady aspects of flight, with spin dynamics managed by active control.

### Trends from the RANS Simulation

To better understand complex aerodynamic phenomena, particularly those induced by the annular wing's rotation which may not be fully captured by inviscid panel methods like those in OpenVSP, qualitative Computational Fluid Dynamics (CFD) simulations using a Reynolds-Averaged Navier-Stokes (RANS) approach were performed. These trends are not used for direct quantitative inputs into the primary aerodynamic model but serve to inform the assumptions made and highlight potential deviations in this special application.

#### Lift Characteristics

The primary OpenVSP model, being inviscid, does not inherently account for boundary layer effects modified by surface rotation. RANS simulations (Figure 9.1) indicate that at lower spin rates (up to  $\Omega = 10$  Hz), the lift curve slope ( $dC_L/d\alpha$ ) changes at higher angles of attack compared to the non-rotating case. For instance, the RANS non-rotating case shows a reduced lift slope beyond  $\alpha \approx 10^\circ$ , while the  $\Omega = 10$  Hz case maintains a more consistent slope up to  $\alpha = 17.5^\circ$ . This suggests that the OpenVSP model's use of a single, effectively non-rotating lift curve is a simplification. It is assumed that such spin-induced modifications are either secondary for the primary flight regime or are encompassed within the general error margins applied to OpenVSP lift predictions. The RANS-predicted lower  $C_L$  at very high spin rates ( $\Omega = 30$  Hz) further supports an assumption that such extreme rates are outside the aerodynamically optimal envelope considered for the OpenVSP model.

#### Drag Characteristics

The OpenVSP panel method primarily predicts induced drag, with viscous and form drag components (and their modification by spin) relying on empirical additions or assumptions. RANS trends for drag (Figure 9.2) offer qualitative insight. For spin rates  $\Omega = 0$  Hz to 10 Hz, RANS  $C_D$  increases typically with  $\alpha$ . A notable RANS prediction is the significant  $C_D$  reduction at very high spin ( $\Omega = 30$  Hz) and high  $\alpha$  (e.g., at  $\alpha = 17.5^\circ$ ). This phenomenon is not captured by the standard OpenVSP approach. Thus, the assumption is that the OpenVSP drag estimates, which are generally conservative, serve as an adequate upper bound, particularly as such high-spin drag reduction regimes are not intended operational states. The RANS-indicated slightly higher  $C_D$  at  $\alpha = 0^\circ$  for  $\Omega = 30$  Hz may also point to spin effects on skin friction not resolved by OpenVSP.

#### Magnus Force and Pressure Distribution

Standard panel methods like OpenVSP do not directly compute Magnus forces for arbitrary rotating bodies. However, the RANS simulations qualitatively confirm its presence for the L.O.R.A.X. configuration. The predicted Magnus force (Figure 9.3) and the asymmetric pressure distributions for the spinning case (Figure 9.4) versus the non-spinning case (Figure 9.5) illustrate this rotational effect. Notably, the RANS pressure distribution for the spinning case suggests the resultant Magnus force vector has both lateral and vertical (lift-contributing) components.

Despite these observations, a key simplifying assumption for the current L.O.R.A.X. flight dynamics model (FDM) is the *neglect of the Magnus force in its entirety (both lateral and lift components)*. This decision is driven by the need for model simplification at this development stage, reliance on the strong gyroscopic stabilization inherent to the design to counteract unmodeled lateral forces, and an assessment that the primary aerodynamic forces (lift and drag from OpenVSP) are dominant for the current scope. While the RANS simulations highlight a physical effect, its full incorporation was deemed beyond the immediate project resources. This neglect represents an acknowledged simplification and an area for potential future model refinement.

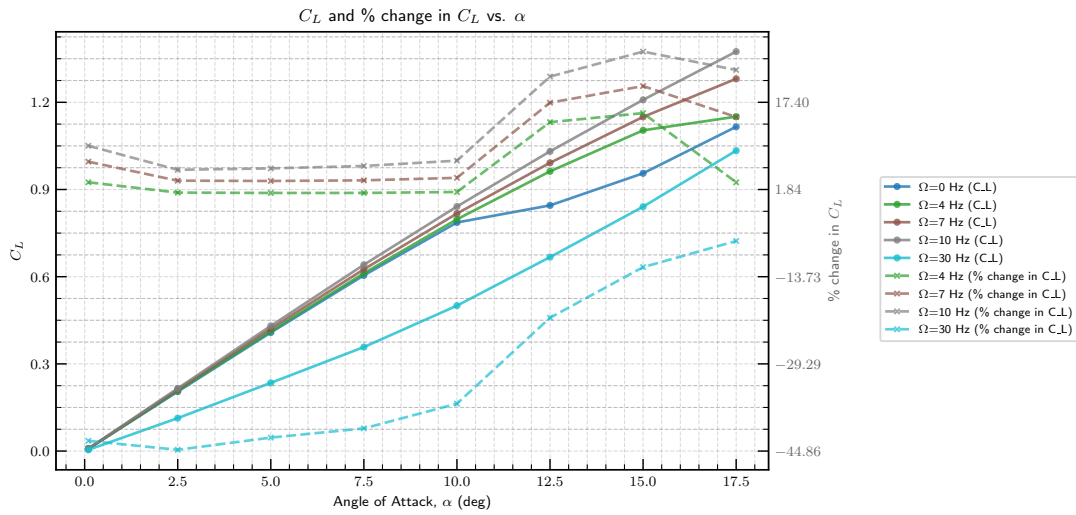


Figure 9.1: Lift coefficient ( $C_L$ ) vs. angle of attack ( $\alpha$ ) for various annulus spin rates ( $\Omega$ ). The left axis displays absolute  $C_L$  values, while the right axis indicates the percentage difference relative to the non-rotating ( $\Omega = 0$  Hz) case.

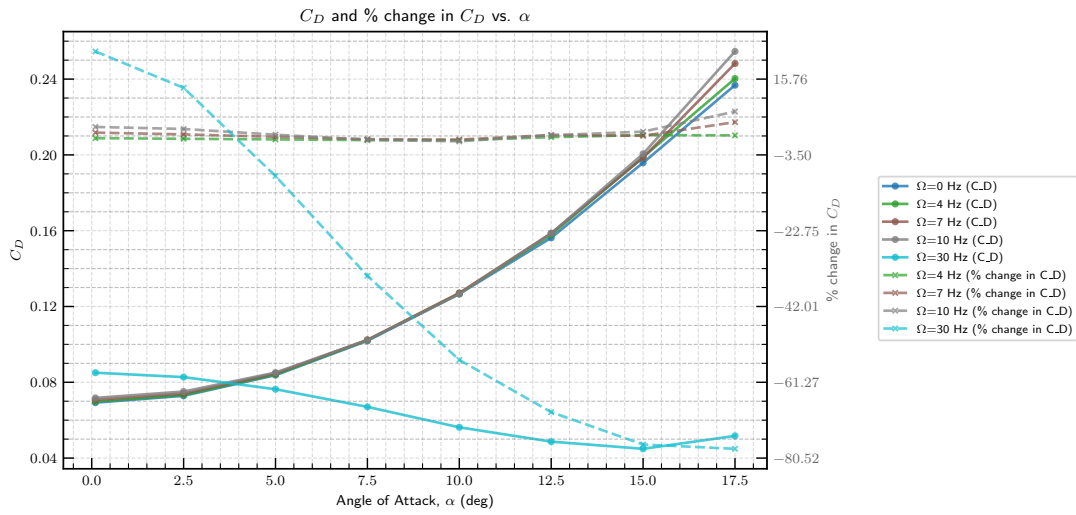


Figure 9.2: Drag coefficient ( $C_D$ ) vs. angle of attack ( $\alpha$ ) for various annulus spin rates ( $\Omega$ ). The left axis shows absolute  $C_D$ , while the right axis shows the percentage difference relative to the non-rotating ( $\Omega = 0$  Hz) case.

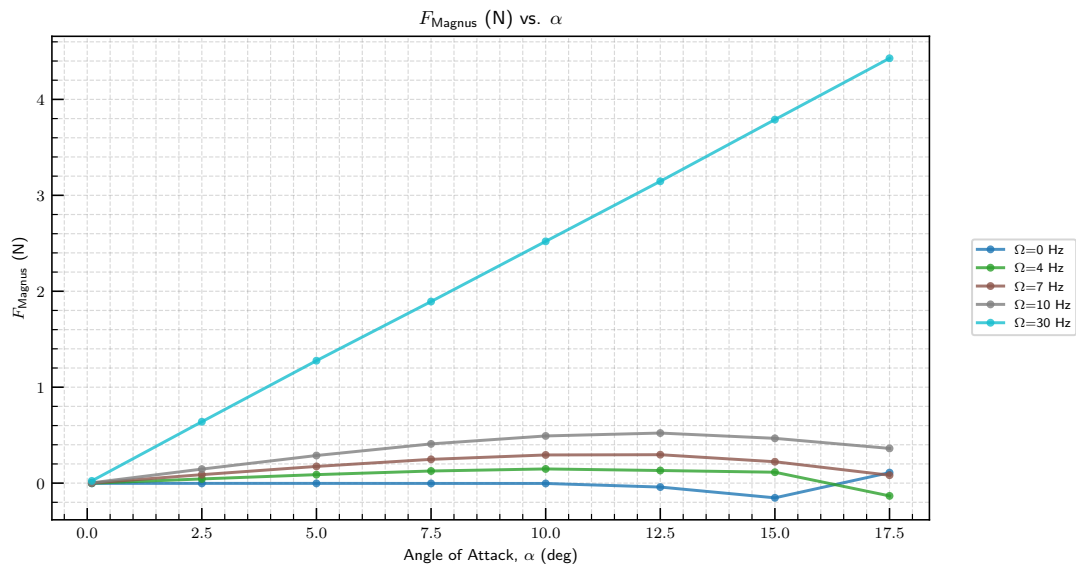


Figure 9.3: Magnus force in Newtons vs.  $\alpha$  for various spin rates ( $\Omega$ ).

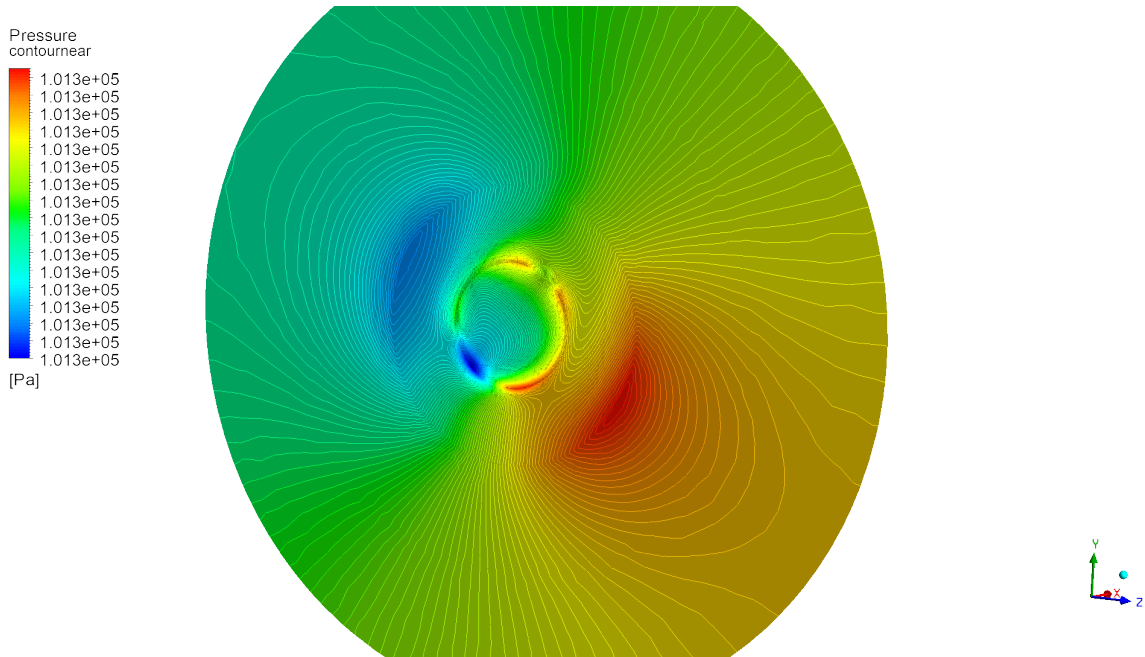


Figure 9.4: Pressure contours 1 cm behind the trailing edge.  $\Omega = 7 \text{ Hz}$ ,  $\alpha = 17.5^\circ$ . Note: the axis convention is inconsistent with the flight dynamics model. The simulation uses X in flow direction, Y up and Z out the left side of the drone.

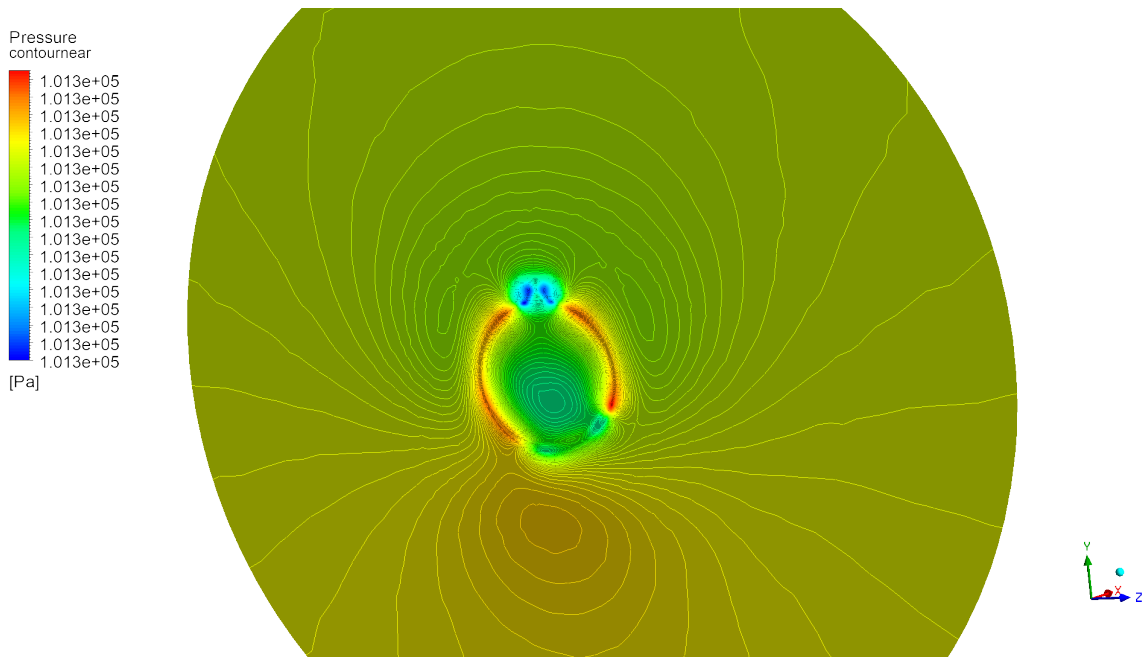


Figure 9.5: Pressure contours 1 cm behind the trailing edge.  $\Omega = 0 \text{ Hz}$ ,  $\alpha = 17.5^\circ$ . Note: the axis convention is inconsistent with the dynamics model. The simulation uses X in flow direction, Y up and Z out the left side of the drone.

### Interference Drag Wing-Strut

To account for the interference drag, both at the junction between the annular wing and its struts, and at the junction between the central hub and these same struts, a relation has to be found that approximates these contributions. Hoerner [18] describes such a relation. He has found an empirical relation for the interference drag originating at the junction of wings or struts with a plane wall, which can be seen in Figure 9.6. To use relation for the L.O.R.A.X. drone, the annular wing is assumed to be a straight flat plate. Similarly, the surface of the hub at the strut junction will be approximated as a local plane wall.

Hoerner defines Equation 9.5, which bases the drag coefficient on the chord area.

$$C_{Dc} = \Delta D / qc^2 = 0.8(t/c)^3 - 0.0003 \tag{9.5}$$

For the Eppler 863 strut airfoil ( $t/c = 0.357$ ) that is used,  $C_{Dc} = 0.036$ . For the conditions that the L.O.R.A.X. drone is operating at (Sea level,  $V = 20 \text{ m/s}$ ), the extra drag for one wing-strut junction will equal approximately

$1.127 \cdot 10^{-3}$  N. Assuming a similar  $t/c$  ratio and local flow conditions at the hub-strut junction, a comparable drag value would be expected for each hub-strut junction.

This obtained value can only be used by imposing an error interval, based on the assumptions and the uncertainty of the empirical relation. Assuming the annular wing is a flat plate does not accurately predict how the flow at the junction will behave. The strut intersects the wing where there's a strong pressure gradient, as opposed to the flat plate correlation used. This difference, therefore, causes a non-negligible deviation from the model. To account for this, an error of 60% is imposed. The curvature will bring a less significant error, as the annular ring is rather thin. Together with the fact that an empirical relation is used, the total error that will be added to the computed drag for the strut junction interference drag is 100%. Due to the struts aligning with the flow when the L.O.R.A.X. drone is rotating, it is assumed that the interference drag for a wing-strut junction remains the same when the drone is rotating. Also, it must be noted that due to this design choice the strut does not touch the annular wing or hub, as can be seen in Figure 11.3. The conservative error of 100% is therefore well chosen. For each wall-strut junction, the added drag will be a total of  $2.253 \cdot 10^{-3}$  N when taking the errors into account. It is suggested that the actual interference drag of a strut junction should be analysed with the use of a wind tunnel experiment for further research.

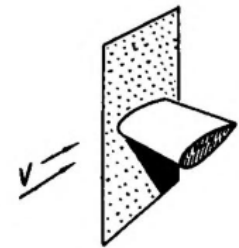
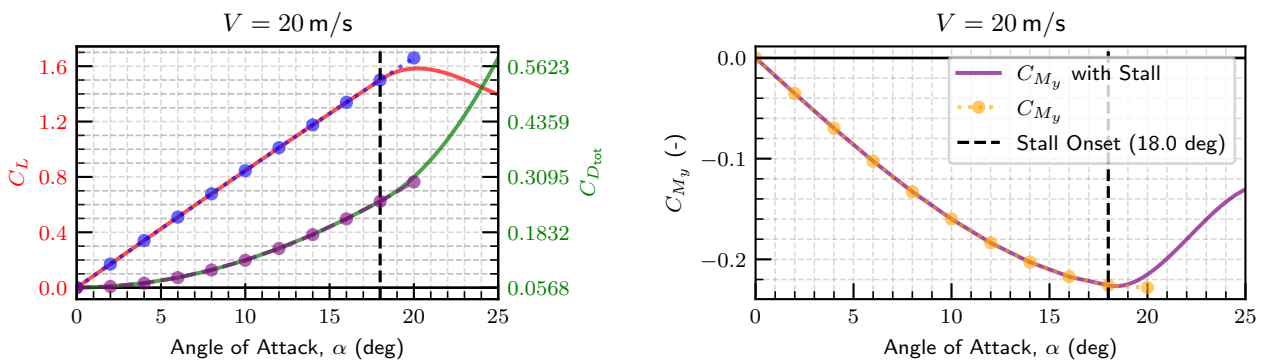


Figure 9.6: Visual representation of the flat plate-strut geometry found in Fluid-Dynamic Drag [18]. For the L.O.R.A.X. drone, the flat plate in the figure is either the annular wing or hub, and the wing represents the strut.

### Stall Angle of Attack

The stall angle of attack is difficult to estimate without the proper experimental data. Therefore, a relation that tries to reproduce the experimental results from Fletcher [14] is established. In his wind tunnel experiments, the aerodynamic coefficients of five annular wings with different aspect ratios were measured. The results may be found in Appendix E. From Appendix E, the stall angle of attack for the L.O.R.A.X. drone is assumed to be  $18^\circ$ . This is an approximation made by interpolating between the stall angles of attack of the wings with an aspect ratio of 1.5 and 3. The stall behaviour from the experimental data is then applied similarly, as can be seen in Figure 9.7.



(a) Lift and drag coefficient data for the annular wing with an AR of 2 simulated for  $V = 20$  m/s,  $\rho = 1.225$  kg/m<sup>3</sup> and  $Re = 135359$  obtained using the panel method. The red line represents the lift coefficient, and the green line is the drag coefficient. The dashed lines are the original data, which are compared with the thick lines that represent the data after the stall implementation.

(b) Moment coefficient data for the annular wing with an AR of 2 simulated for  $V = 20$  m/s,  $\rho = 1.225$  kg/m<sup>3</sup> and  $Re = 135359$  obtained using the panel method.

Figure 9.7: Stall behaviour plots for different aerodynamic coefficients.

### Propeller-Wing Interference

The propellers will accelerate the mass flow within the annular wing. Due to the lower pressure over the bottom part of the inner wing, the lift will be increased. However, this will be exactly the other way around for the top part of the inner wing, as the velocity is increased here as well. In the analysis, the propellers were changed to disks to increase the computation time. For an angle of attack equal to zero, the net change in lift will be zero. This is shown in Figure 9.8a, where the pressure distribution difference of the two configurations over the lower and upper wing is shown.

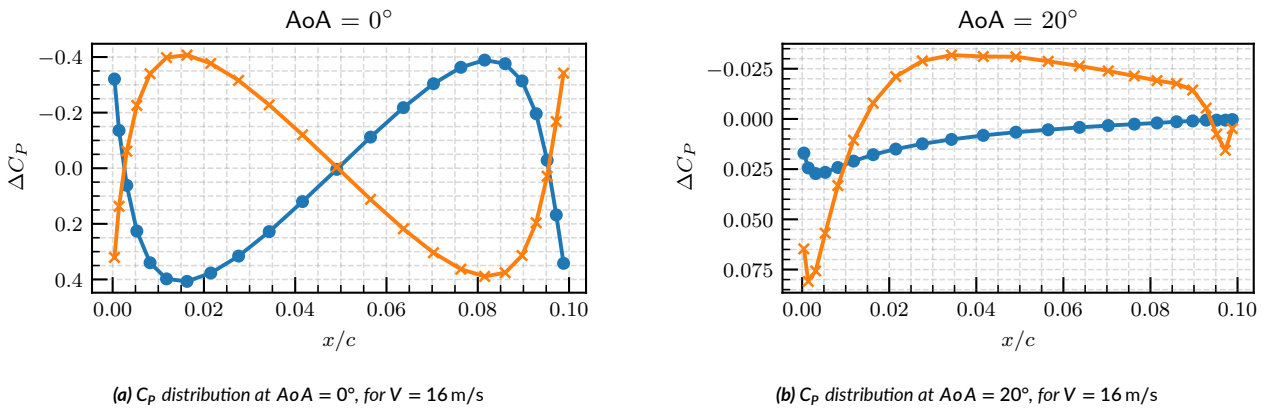


**Figure 9.8:** The pressure distribution difference between the configuration with the propellers on and with the propellers off, for the lower and upper wing along the chord. The orange line depicts the pressure distribution difference of the upper wing, and the blue line represents the same but for the lower wing of the L.O.R.A.X. drone.

As expected, the pressure distribution is increased over the lower wing when the propellers are added, and lowered over the upper wing. These cancel out perfectly, resulting in a net change in lift of zero. However, whenever the angle of attack changes, the pressure distribution in the annular wing changes. For  $Y = 0$ , the axis through the axis of the wing, this is shown in Figure 9.8b. This graph confirms how the pressure distribution over the lower wing is increased and decreased over the upper wing when the propellers are turned on. The net pressure distribution difference is positive, meaning that at the  $Y = 0$  slice, the lift is increased. However, the overall lift coefficient decreases by 1% for this angle of attack when the propellers are turned on. It is therefore assumed that the propeller has a more complex effect on the spanwise distribution than what is observed only at the  $Y = 0$  slice. However, as there is no major change in the lift coefficient, it is deemed sufficient for the aerodynamic simulation to analyse it without the propeller. For future research, it is recommended to analyse the pressure distribution around the entire annular wing to understand how the propeller slipstream interacts with the annular wing.

### 9.1.3. OpenVSP Validation

The OpenVSP software is used to create the geometry of the L.O.R.A.X. drone. Its inviscid solver, VSPAero, was validated against Fletcher's annular airfoil experiments, performed at Mach 0.13 and for a range of Reynolds numbers [14]. Using VSPAero's VLM and Panel Method via its Python API, an annular wing with an aspect ratio of 1.5 was analysed. Lift and drag coefficient errors, compared to experimental data, are presented in Figure 9.9. The presented errors suggest that although the VLM has a better computational time, the panel method is chosen for its higher accuracy. To ensure fidelity in the obtained results, an error of 10% will be imposed on the lift. The drag is always overestimated by the panel method. It is therefore assumed that the 40% error from the experimental results is already the upper bound. Therefore, the obtained drag from the panel method will not require any further upward adjustment as it is already conservative enough.

### 9.1.4. Aerodynamic Coefficient Model

The aerodynamic analysis module works in the following way. First, the isolated components will be analysed utilising the VSPAero solver integrated in the OpenVSP software. This VSPAero solver offers two solver options: the Vortex Lattice Method and the Panel Method. Both are inviscid solving methods, with a distinct difference between them.

The VLM reduces the body down to the camber line, whereas the panel method represents the body with surface panels. The panel method will be utilised for performing the aerodynamic analysis due to the lower error, as discussed in subsection 9.1.3. The number of wake nodes, wake iterations, and far field distance of the wake are set to 256, 5, and 10 times the span length as suggested by Even [13]. He executed a wake refinement study for the VSPAero simulation settings, where he found these settings to perform well while having a relatively low error. He also found that a span- and chordwise panel distribution of 24 and 48, respectively, was deemed a sufficiently dense mesh for the panel method. Therefore, these parameters will be used for the

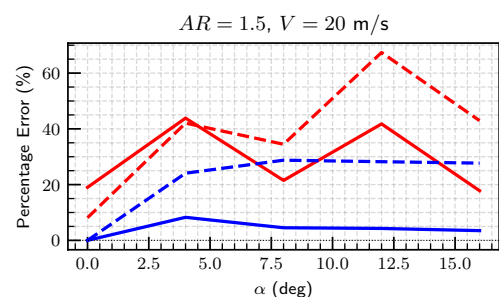


**Figure 9.9:** This figure shows the percentage errors of the VLM and panel method predictions for the lift and drag coefficient in comparison with experimental data obtained by Fletcher [14]. The thick lines are the results from the panel method, and the dashed lines are the VLM results. The red lines depict the drag coefficient errors, whereas the blue lines represent the lift coefficient errors.

aerodynamic analysis of the components.

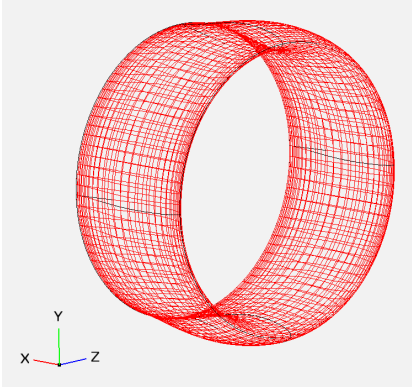


Figure 9.10: Geometry of the annular wing created in OpenVSP.

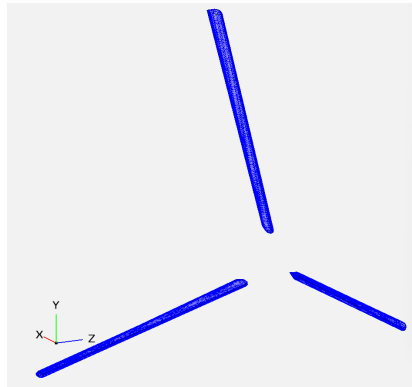


Figure 9.11: Geometry of the struts, created in OpenVSP.

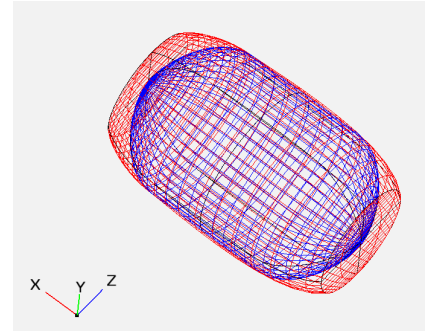


Figure 9.12: Geometry of the hub (blue) and the adjusted hub (red), created in OpenVSP.

### Isolated Annular Wing

To determine the aerodynamic performance of the annular wing, it has to be constructed in the OpenVSP software. The geometry may be found in Figure 9.10. The parameters, as discussed in subsection 9.1.1, are used for the analysis. For the given  $V_{cruise}$  and chord, the  $Re$  is estimated to be 135359. Due to the axisymmetric body of the annular wing, a sideslip angle  $\beta$  of  $20^\circ$  will be assumed to be the same as an angle of attack of  $20^\circ$  as the body has the same angle relative to the flow. Only the lift force will act perpendicular to the original lift force. For this analysis, it is deemed sufficient to only evaluate the annular wing for different angles of attack. The lift, drag, and moment coefficient graphs can be found in Figure 9.7 in subsection 9.1.2. The drag polar is found in Figure 9.13. The highest  $L/D$  is found at  $AoA = 10^\circ$ , equalling 7.0854.

At the chosen  $AoA_{cruise}$ , the  $L/D$  equals 6.4080. The lift is estimated to be 2.4976 N, and by implementing the error found during the validation for the lift, it ranges from 2.2478 N to 2.7474 N. The drag is estimated to be 0.3898 N. Considering the panel method's tendency to overestimate drag by up to 40% (as noted in subsection 9.1.3), this value is likely at the upper bound of the actual drag. Another error will therefore not be imposed on the drag. The moment is predicted to be  $-0.0502$  N/m, which is a nose-down pitching moment for the defined axis system in OpenVSP. As no validation has been done on the accuracy of the pitching moment calculated by the panel method in the VSPAero solver, an error of 25% is imposed. Therefore, the moment will be between  $-0.0628$  N·m and  $-0.0377$  N·m. An important parameter for the L.O.R.A.X. drone determined by the aerodynamic coefficients is the location of the centre of pressure. The centre of pressure determines the magnitude of the effect of the applied C.G. shift.

### Isolated Struts

To continue with the aerodynamic analysis of the L.O.R.A.X. drone, the performance of the struts is studied. The geometry created in OpenVSP may be found in Figure 9.11. The root and tip of a strut had to be rounded to avoid sharp edges in the panel method. Due to this change in the geometry, an error of 20% will be induced in the aerodynamic coefficients. As the struts, due to the twist, align with the flow when rotating, it is sufficient to analyse them at  $AoA = 0^\circ$ . For the analysis, again, a span- and chordwise panel distribution is 24 and 48, respectively. The chord length of the struts is 0.011 m, giving a Reynolds number of 14890. Using these conditions, the drag was estimated to equal 0.0349 N. Applying the error defined earlier, the drag becomes 0.0419 N. This amounts to 10.74% of the annular wing drag at  $AoA = 0^\circ$ . The total interference drag due to the six strut junctions is 64.53% of the strut drag. This seems reasonable, as Hoerner [18] describes how the drag coming from a strut intersection can be as great as the total drag coming from a strut section having a span of 10 times its chord. As the junctions in the L.O.R.A.X. drone are not truly strut-strut intersections, it gives a good indication of how the interference drag can be a substantial part of the strut drag. The moment coming from the struts is estimated to be  $7.136 \cdot 10^{-4}$  N·m. As this number is only 1% of the moment of the annular wing, it is neglected for further analysis.

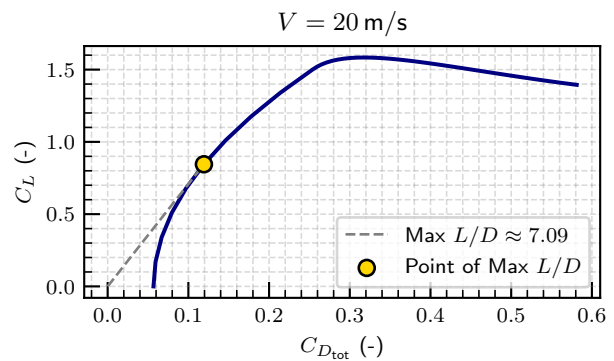


Figure 9.13: Drag polar of the annular wing simulated for  $V = 20$  m/s,  $\rho = 1.225$  kg/m<sup>3</sup> and  $Re = 135359$ .

### Isolated Hub

An aerodynamic analysis of the hub is also performed. First, the original geometry was created in OpenVSP. However, due to the flat leading and trailing edges, the VSPAero solver had problems with this geometry. An adjustment had to be made to the geometry to ensure smooth edges. This can be seen in [Figure 9.12](#), where the leading and trailing edge geometry has been altered. Instead of a flat edge, a point was created such that there are no sharp edges. For the hub analysis, after using the panel method as the inviscid flow solver, an estimated drag of  $4.7 \cdot 10^{-5}$  N was found at  $AoA = 6^\circ$  for  $V_{cruise}$ . Even with an error of 100% for the adjusted geometry, this drag is deemed to be insignificant when compared to the drag of the annular wing. Therefore, the hub will not need any further research, and the drag will not be taken into account for the L.O.R.A.X. drone.

### L.O.R.A.X. Drone

To determine the aerodynamic performance of the system, all the forces of the isolated components are added together. Also, the interference drag discussed in [subsection 9.1.2](#) is added to these components. The whole L.O.R.A.X. drone was also analysed, however, due to the solution not converging, this approach was not used. Nevertheless, adding up the aerodynamic performance of the isolated annular wing and struts, for  $AoA = 6^\circ$ , and also taking into account 6 strut junctions, the total drag is estimated to be 0.4452 N. This drag includes the upper-bound errors. The lift and moment equal the lift and moment solely from the annular wing, due to the struts and hub not contributing to these forces. The total lift of the L.O.R.A.X. drone will therefore range 2.2478 N to 2.7474 N. The moment ranges from  $-0.0628$  N·m and  $-0.0377$  N·m. The location of the centre of pressure of the L.O.R.A.X. drone is shown in [Figure 9.14](#), showcasing how the centre of pressure moves forward when the angle of attack is increased. The final data for cruise can be found in [Table 9.2](#). The final aerodynamic coefficients are found in [Figure 9.15](#).

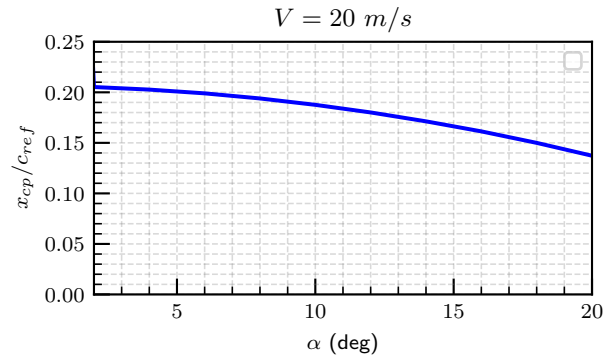
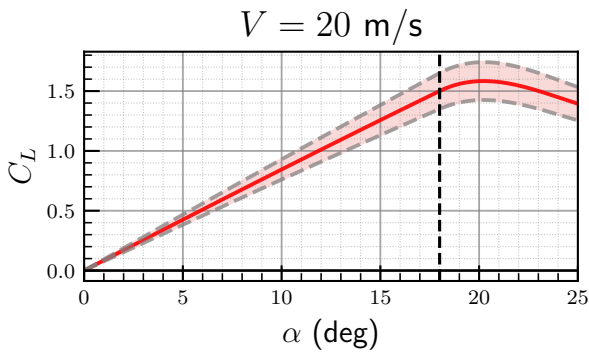


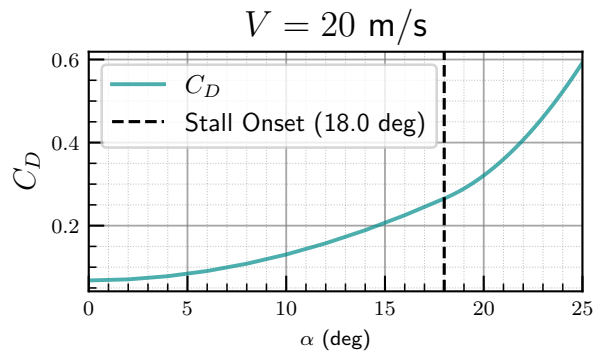
**Figure 9.14:** Centre of pressure location along the chord of the L.O.R.A.X. drone for  $V = 20$  m/s,  $\rho = 1.225$  kg/m<sup>3</sup> and  $Re = 135359$ .

**Table 9.2:** Aerodynamic Forces of the L.O.R.A.X. Drone. Double values indicate lower and upper error bounds.

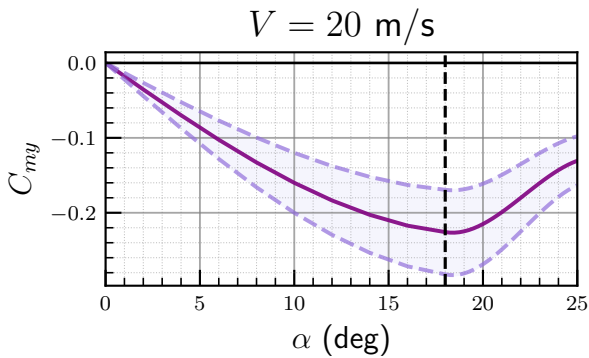
Forces	Value	Unit
$V_{cruise}$	20.00	m/s
$\alpha_{cruise}$	6.00	°
$L_{cruise}$	[2.2478, 2.7474]	N
$D_{cruise}$	0.4452	N
$M_{y,cruise}$	[-0.0628, -0.0377]	N·m
$L/D_{cruise}$	[5.0490, 6.1712]	-
$(x_{cp}/c)_{cruise}$	0.1990	-



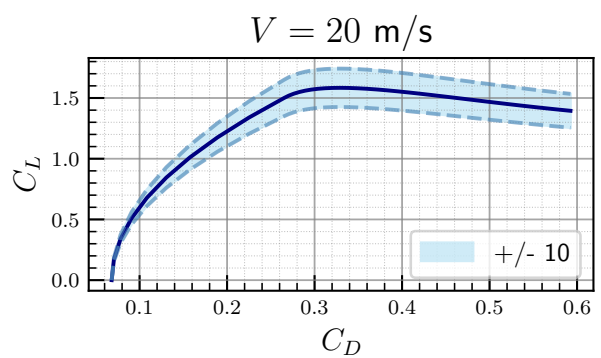
(a) This image showcases the lift coefficient vs. the angle of attack. The red interval describes the 10% error interval imposed on the results.



(b) This image showcases the drag coefficient vs. the angle of attack.



(c) This image showcases the moment coefficient vs. the angle of attack. The purple interval describes the 25% error interval imposed on the results.



(d) This image showcases the drag polar. The blue interval is the error interval imposed on the lift coefficient results.

Figure 9.15: Aerodynamic characteristics of the L.O.R.A.X. drone

### Simulation Implementation

To integrate the aerodynamic performance of the L.O.R.A.X. drone into the overall system simulation, a workflow was established to connect OpenVSP with the Simulink environment. This was done by using OpenVSP's Python API to construct the VSPAero solver in the Python environment.

The process can be seen in Figure 9.16

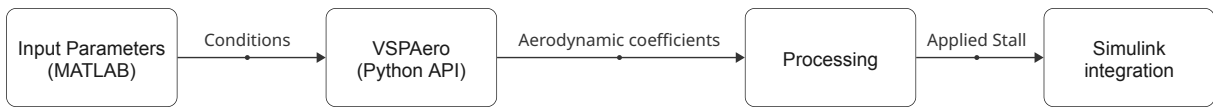


Figure 9.16: Block Diagram of the flow of the aerodynamic simulation.

This process allows for the coefficients to be precomputed, such that the simulations can be run without performing a new aerodynamic analysis for every run.

### 9.1.5. Recommendations

To obtain accurate results for the aerodynamics of the L.O.R.A.X. drone, it is highly advised to perform wind tunnel tests. Not only to obtain the coefficients, but also to fully understand what happens when the propellers and the drone itself are rotating. From the performed wind tunnel tests, it is then possible to validate the RANS simulation by comparing forces and moments, both for static and rotating test cases. This model would then give enough confidence for further research into the aerodynamics of a rotating annular wing. It is also recommended to determine the optimal twist distribution of the struts necessary to counteract the rotational flow induced by the propeller slipstream to improve aerodynamic efficiency.

## 9.2. Propulsion Subsystem

This section details the selection process for the L.O.R.A.X. drone's motor and propeller combination, driven by key mission and performance requirements. While cost is a secondary consideration, it may inform choices between components with similar performance.

### Design Requirements

The operational parameters and constraints for the propulsion system are summarized in Table 9.3. A conservative average thrust of 0.3 N per motor is assumed for initial sizing and power estimation, accommodating the need for differential torque/thrust to maintain and control spin.

Table 9.3: Propulsion Subsystem Design Requirements

Parameter	Requirement/Constraint
<b>Total Cruise Thrust</b>	Approx. 0.6 N to overcome drag at 20 m/s cruise velocity (see section 9.1).
<b>Thrust Distribution</b>	Differential thrust capability to maintain annular wing spin; average of 0.3 N per motor assumed for cruise sizing.
<b>Flight Duration</b>	Minimum 10 minutes (STK01-MIS06).
<b>Battery System</b>	Nominal 7.4 V (2S LiPo), operating range ~7.0 to 8.4 V (see section 9.3). Primary driver for motor KV selection.
<b>Spin Torque</b>	Sufficient reaction torque for rapid body spin-up at launch and potential spin reversal. Granular control for precise spin rate during steady flight.

### 9.2.1. Propeller Selection

Efficient conversion of motor power to thrust is critical. The propeller selection focuses on maximising efficiency while meeting performance parameters.

#### Launch/Spin-up and Cruise Phase

Rapid drone body spin-up is necessary at launch or during hard manoeuvres for gyroscopic stabilisation. This is achieved by operating one motor at maximum achievable torque (second motor off/minimal RPM), with its reaction torque accelerating the body. The dual propellers use a contra-rotating, push-pull configuration to largely cancel net reaction torque during symmetric thrust, allowing precise spin rate control via induced torque imbalances.

#### Propeller Interaction Assumption

A simplifying assumption is made for this preliminary design: the rear propeller operates as if in undisturbed air, with performance based on isolated characteristics. While the rear propeller in a contra-rotating system operates in the front propeller's slipstream (accelerated, rotational flow), detailed modelling (CFD or specialised codes) is beyond initial sizing scope. Studies suggest potential efficiency gains (5-8%) for the rear prop from swirl recovery [23], but turbulence and non-uniform inflow also play roles. Assuming isolated performance is likely slightly conservative or optimistic depending on these complex interactions but allows use of standard propeller data for initial motor sizing. This will be revisited in later design phases.



Figure 9.17: APC 4.1x4.1E Propeller

#### Selected Propellers: APC 4.1x4.1E and 4.1x4.1EP

The APC 4.1x4.1E two-blade propeller (Figure 9.17) and its reverse-rotation pusher version (4.1x4.1EP for the rear motor) were selected due to:

- **Detailed Performance Data:** Essential for accurate predictions. Data<sup>1</sup> includes thrust, power, torque, and efficiency across various RPMs/advance ratios. (Pusher performance is assumed identical to tractor).
- **Efficiency:** Two-blade propellers generally offer higher propulsive efficiency over multi-blade equivalents, crucial for endurance, at the cost of slightly higher noise[26].
- **Size/Pitch Suitability for Cruise (20 m/s):**
  - A 4.1-inch diameter suits the drone's size/mass (200 mm diameter, 250 g max), balancing thrust and disk loading, with ~50 mm tip clearance to the annulus.

<sup>1</sup>APC Propellers, 4.1x4.1E Performance Data, 2025. Available at: [https://www.apcprop.com/files/PER3\\_41x41E.dat](https://www.apcprop.com/files/PER3_41x41E.dat) (accessed 10/06/2025).

- A 4.1-inch pitch optimises for the 20 m/s cruise speed and low thrust needs. Higher pitch is efficient at higher speeds; lower pitch for static thrust [11].
- Figure 9.21 shows the propeller operates near peak efficiency at cruise.

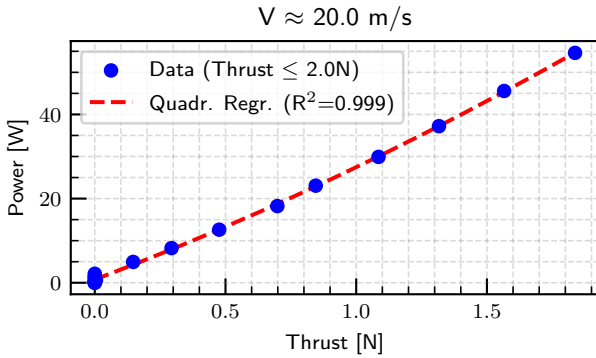


Figure 9.18: Shaft Power vs. Thrust (APC 4.1x4.1E,  $V \approx 20$  m/s).

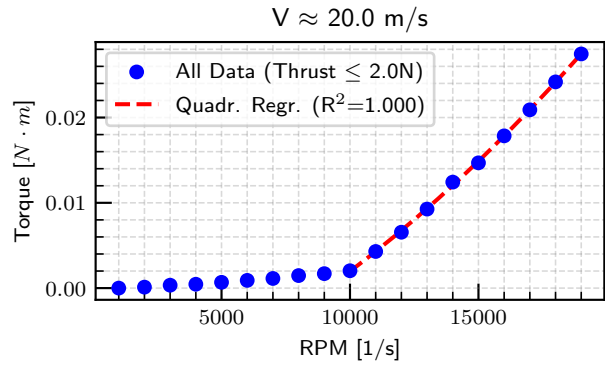


Figure 9.19: Torque vs. RPM (APC 4.1x4.1E,  $V \approx 20$  m/s).

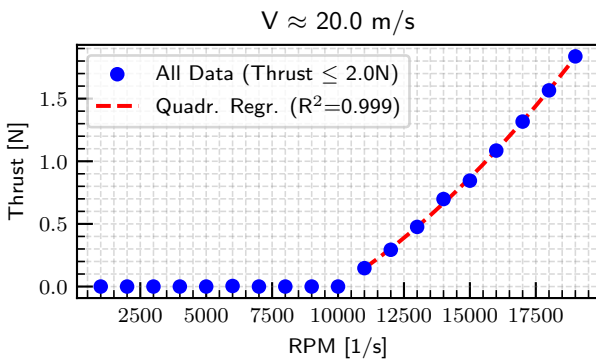


Figure 9.20: Thrust vs. RPM (APC 4.1x4.1E,  $V \approx 20$  m/s).

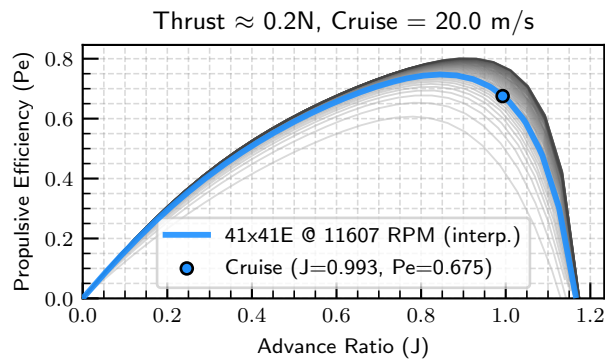


Figure 9.21: Propulsive Efficiency vs. Advance Ratio (APC 4.1x4.1E). Cruise at 0.3 N thrust per prop is marked.

Interpolation of datasheet values (provided in 1000 RPM steps) yields the cruise performance metrics in Table 9.4.

Table 9.4: APC 4.1x4.1E Performance Summary and General Parameters (Cruise at 0.3 N/prop, 20 m/s)

Parameter	Value	Unit	Parameter	Value	Unit
Type	Two-Blade	-	Est. Propeller RPM	10,400	RPM
Diameter	4.10	inch	Shaft Power	6.5	W
Pitch	4.10	inch	Torque	0.0061	N·m
Hub Diameter	12.7	mm	Advance Ratio (J)	0.993	-
Hub Thickness	7.62	mm	Propulsive Efficiency ( $\eta_p$ )	0.675	-
Weight	3.11	g	Thrust (per prop)	0.3	N

Note: Total commanded motor RPM = Est. Propeller RPM + body spin rate (420 RPM), resulting in 10,820 RPM.

### 9.2.2. Motor Selection

With the APC 4.1x4.1E propellers and their cruise operating point established, the E-flite Park 250 motor (approx. 2200 RPM/V KV rating) was identified as a prime candidate.

#### Key Motor Requirements

The chosen motor must satisfy the criteria in Table 9.5.

Table 9.5: Key Motor Requirements

Criteria	Specification
2S LiPo Compatibility	Efficient and reliable operation within 7.0 V to 8.4 V (nominal 7.4 V).

Continued on next page...

Table 9.5: Key Motor Requirements - Continued

Criteria	Specification
Cruise Performance	Drive APC 4.1x4.1E at 10,820 RPM to deliver 6.5 W mechanical shaft power per motor.
Takeoff / Spin-Up	One motor capable of max torque (within safe limits) for rapid annular wing spin-up.
Weight and Size	Suitably sized and lightweight for airframe integration.
Reversibility	Standard BLDC motor inherently reversible (swapping two phase wires) for contra-rotating configuration.

E-flite Park 250 Performance Analysis

Cruise Operation:

The target 10,820 RPM implies a theoretical no-load voltage of ~4.92 V (10,820 RPM/2200 KV). At a nominal 7.4 V, this is ~66% throttle. Using manufacturer efficiency data<sup>2</sup> (Figure 9.26, 7.2 V curve), an iterative process for 6.5 W shaft power yields an estimated motor efficiency ( $\eta_{motor}$ ) of ~55%. This results in: Electrical Power:  $P_{elec,cruise} = P_{shaft,cruise} / \eta_{motor} = 6.5 \text{ W} / 0.55 \approx 11.8 \text{ W}$  per motor. Current Draw:  $I_{cruise} = P_{elec,cruise} / 7.4 \text{ V} \approx 1.6 \text{ A}$  per motor. This current is well below the motor's 8 A continuous limit, indicating a good operational margin. Total propulsion power: ~23.6 W.



Figure 9.22: E-flite Park 250 motor.

**Launch Performance (Spin-Up):** During spin-up, one motor operates at max burst current (8 A for 15 s per manufacturer<sup>3</sup>). At 8 A and 7.4 V, electrical input is 59.2 W. From Figure 9.26, motor efficiency is ~45%. Max mechanical shaft power:  $P_{shaft,max} = 59.2 \text{ W} \cdot 0.45 \approx 26.6 \text{ W}$ . Using APC 4.1x4.1E static data (Figure 9.23, Figure 9.24, Figure 9.25), 26.6 W shaft power yields:

- Thrust: ~1.615 N
- Torque: ~0.0158 N·m
- Propeller RPM: ~16,110 RPM (motor RPM, as drone is initially non-spinning)

This static torque is crucial for spin-up dynamics (section 9.4).

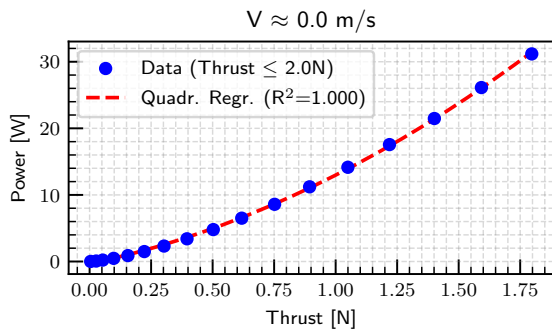


Figure 9.23: Shaft Power vs. Thrust (APC 4.1x4.1E, static V = 0).

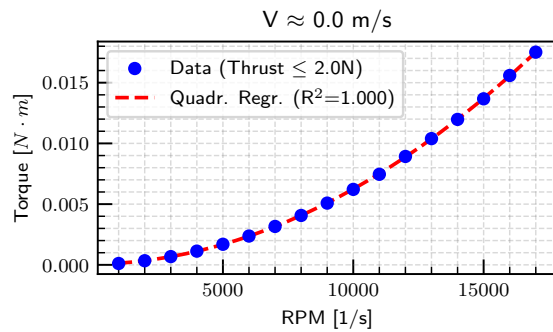


Figure 9.24: Torque vs. RPM (APC 4.1x4.1E, static V = 0).

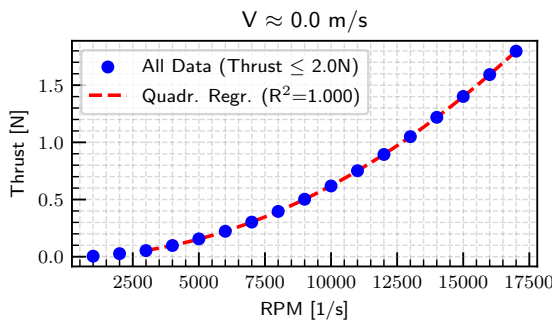


Figure 9.25: Thrust vs. RPM (APC 4.1x4.1E, static V = 0).

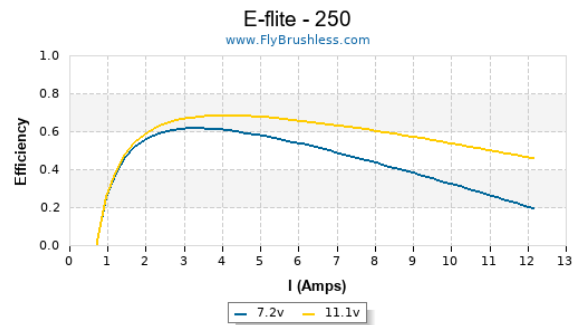


Figure 9.26: E-flite Park 250 Efficiency vs. Current

<sup>2</sup>FlyBrushless.com, E-flite Park 250 Performance Data, 2024. Available at: <https://www.flybrushless.com/motor/view/238> (accessed 12/06/2025).

<sup>3</sup>E-flite, E-flite Park 250 Brushless Outrunner Motor, 2024. Available at: <https://www.e-fliterc.com/product/park-250-brushless-outrunner-motor-2200kv-2mm-bullet/EFLM1130.html> (accessed 12/06/2025).

**Manoeuvre Performance:**

For manoeuvres like spin reversal, one motor provides max continuous power under cruise conditions (20 m/s airspeed). At 26.6 W shaft power:

- Thrust:  $\sim 1.12$  N
- Torque:  $\sim 0.0164$  N·m
- Propeller RPM (relative to air):  $\sim 14,960$  RPM; Total motor RPM:  $\sim 15,380$  RPM.

**Overall Suitability of the E-flite Park 250**

The E-flite Park 250 meets the L.O.R.A.X. demands: good cruise efficiency, ample current margin, and necessary peak power/torque for spin-up. Its KV rating matches 2S LiPo operation with the selected 4.1-inch propellers. While lighter motors exist (e.g., 1404-class), the Park 250's proven capability with 4-inch propellers offers confidence for this application, especially considering spin-up stresses. Performance is summarized in [Table 9.6](#) and general parameters in [Table 9.7](#).

*Table 9.6: E-flite 250 Performance Summary (per motor)*

Parameter	Cruise (Avg)	Takeoff/Spin-up	Manoeuvre	Unit
Operating Mode	Dual Motor	Single Motor	Single Motor	-
Target Prop Thrust	$\sim \frac{1}{2}$ Cr. Drag Force	Max Static	Max Cruise	N
Est. Prop Thrust	0.3	1.615	1.12	N
Est. Prop Torque	0.0061	0.0158	0.0164	N·m
Est. Motor RPM	10,820	16,110	15,380	RPM
Est. Shaft Power ( $P_{\text{shaft}}$ )	6.5	26.6	26.6	W
Est. Electrical Current ( $I_{\text{elec}}$ )	1.6	8.0	8.0	A
Est. Electrical Power ( $P_{\text{elec}}$ )	11.8	59.2	59.2	W
Est. Motor Efficiency	58%	45%	45%	-

*Table 9.7: E-flite Park 250 General Parameters*

Parameter	Value	Unit
Type	Outrunner	-
Length	23.00	mm
Diameter	22.00	mm
Weight	14.00	g
Max Burst Current (15 s)	8.00	A
KV	2200	RPM/V
Idle Current	0.45	A
Internal Resistance	0.25	$\Omega$

**9.2.3. Propeller Model**

To compute propeller thrust and torque, coefficients  $C_T$  and  $C_Q$  are used. These depend on the advance ratio  $J = V/(n \cdot D)$  ([Equation 9.6](#)) [12], where  $V$  is inlet airspeed,  $n$  is propeller frequency (rev/s), and  $D$  is diameter. The simulation ([chapter 8](#)) uses lookup tables for  $C_T$  and  $C_Q$  versus  $J$  and  $n$ . Thrust ( $T$ ) and torque ( $Q$ ) are then:

$$J = \frac{V}{n \cdot D} \quad (9.6)$$

$$T = C_T \cdot \rho \cdot n^2 \cdot D^4 \quad (9.7)$$

$$Q = C_Q \cdot \rho \cdot n^2 \cdot D^5 \quad (9.8)$$

For contra-rotating propellers, the rear propeller's inlet airspeed is slightly higher. The general thrust equation ([Equation 9.9](#)) [24] assumes  $V_0$  (front prop inlet) and  $V_e$  (exit). For this model,  $V_{\text{inlet, rear}} = V_{\text{exit, front}}$ , leading to different coefficients for the rear prop.

$$F = \frac{1}{2} \cdot \rho \cdot A \cdot (V_e^2 - V_0^2) \quad (9.9)$$

### 9.2.4. Propulsion Simulation Model

The propulsion system simulation includes:

#### Motor & Electronic Speed Controller

The Motor & ESC are modelled using a Simscape Motor & Drive block<sup>4</sup> and a PI controller, taking a 0 to 5 V reference (full throttle at 5 V). This allows future integration with a Power Management module.

## 9.3. Power Subsystem

The power subsystem is crucial for the L.O.R.A.X. drone, dictating its endurance and influencing mass and packaging. This section outlines the process of defining power needs, selecting battery technology, and verifying its suitability for the mission, considering the drone's unique CG-shifting mechanism and annular wing integration.

### 9.3.1. Initial Power Architecture Considerations

The L.O.R.A.X.'s novel design, with limited internal volume and initial uncertainties in aerodynamic performance, posed challenges for power system design and battery selection.

#### Battery Integration Concept and Physical Constraints

A key design feature is the mass-shifting mechanism for flight control: the central motor assembly and batteries move along linear rails within the annular wing. Batteries are housed in voids on carriages on these rails (Figure 9.27), imposing strict dimensional constraints, especially on cell thickness, to maximize travel within the curved wing profile.

Optimizing control authority requires maximizing both the movable mass (motors, batteries, struts) and its travel distance ( $d_{\text{travel}}$ ) along the rails. A trade-off emerges: more battery cells increase movable mass but also pack length ( $L_{\text{pack}}$ ), reducing  $d_{\text{travel}}$  (as  $d_{\text{travel}} = L_{\text{rails}} - L_{\text{pack}}$ ). Prioritizing  $d_{\text{travel}}$  (given motors are a significant movable mass component) led to the 2S3P (6 cells) configuration. This balances sufficient battery mass for CG shift with a compact pack for greater  $d_{\text{travel}}$ , aiming to maximize  $m_{\text{movable}} \cdot d_{\text{travel}}$  for effective control.

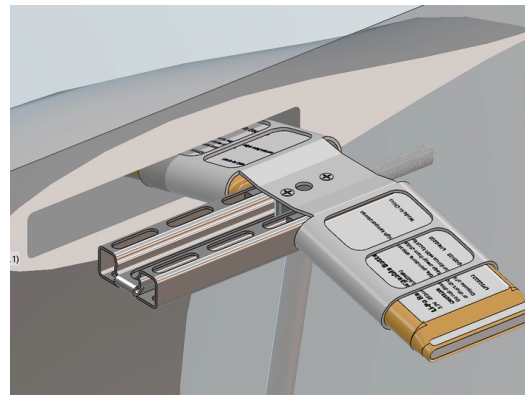


Figure 9.27: 3D Section View: linear rail, 2S battery pack, and strut within annular wing void.

### 9.3.2. Battery Cell Selection and Configuration

Suitable LiPo pouch cells were sought based on the 2S voltage architecture and integration constraints.

Candidate Cell: LPHD4525035

The LPHD4525035 LiPo cell (see Table 9.8) was chosen for its suitable performance and dimensions.

Table 9.8: LPHD4525035 LiPo Cell General Parameters

Parameter	Value	Unit
Chemistry	Lithium Polymer (LiPo)	-
Nominal Voltage	3.7	V
Capacity	250	mA·h
Max Cont. Discharge	15	C
Max Burst Current (15 s)	8.00	A
Thickness	4.5	mm
Dimensions (L x W)	35 x 25	mm
Approx. Mass	5	g

#### Battery Pack Configuration

L.O.R.A.X.'s three 120°-spaced struts suit a distributed battery arrangement, aiding MMOI for gyroscopic stiffness and CG alignment with the annulus axis to reduce vibration. Two LPHD4525035 cells fit per strut/rail (one each side of the carriage, Figure 9.27), totaling 6 cells. A 2S3P (7.4 V nominal, 750 mA·h) configuration was

<sup>4</sup>Simscape Motor & Drive Block, 2025. Available at: <https://www.mathworks.com/help/sps/ref/motordrivesystemlevel.html> (accessed 17/06/2025)

chosen over a potential 3S2P (11.1 V, 500 mA·h) as the latter could not meet the required peak current (9.03 A needed vs. 7.5 A available from 3S2P with 15C cells, as  $0.5Ah \times 15C = 7.5A$ ).

- **2S3P Configuration:** Three parallel strings, each string consisting of two 250 mA·h cells in series (2S1P, 7.4 V).

Final pack specifications are in [Table 9.9](#).

*Table 9.9: L.O.R.A.X. 2S3P Battery Pack Specifications*

Parameter	Value	Unit
Nominal Voltage	7.4	V
Total Capacity	750	mA·h
Total Energy	5.55	W·h
Total Max Cont. Discharge Current	11.25	A
Total Pack Mass	30	g

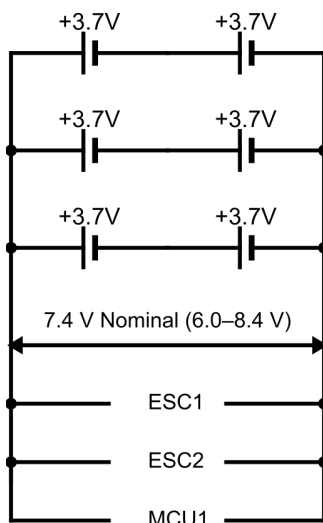


*Figure 9.28: Battery pack wiring concept.*

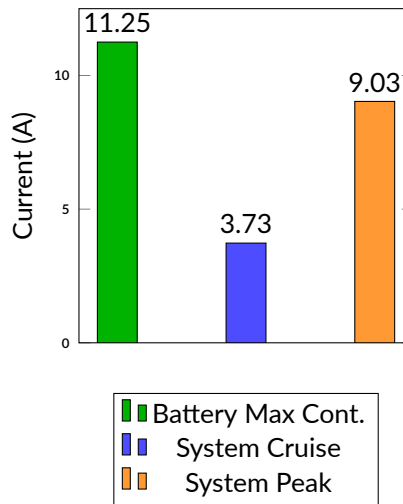


*Figure 9.29: Battery current capability vs. system demands.*

### 9.3.3. Verification of Power Subsystem Adequacy

The defined battery pack’s ability to meet power and energy demands is assessed, assuming an additional 4 W peak power for auxiliary systems (controller, sensors, comms, payload) on top of propulsion needs from [section 9.2](#).

#### Estimated Total Power and Current Demands

Key system power demands are summarized in [Table 9.11](#).

*Table 9.11: Summary of Estimated System Power and Current Demands*

Parameter	Cruise Condition	Peak Demand (Launch/Spin-up)
Propulsion Power (Total)	~23.6 W	~59.2 W (Single Motor Peak)
Auxiliary & Payload Power	~4.0 W	~4.0 W
<b>Total System Power (<math>P_{tot}</math>)</b>	<b>27.6 W</b>	<b>63.2 W</b>
Total System Current ( $I_{tot}$ )	~3.73 A (at 7.4 V)	~9.03 A (at sagged ~7.0 V)

#### Flight Duration Calculation

- Total Stored Energy (2S3P Pack):  $E_{tot\_pack} = 5.55 \text{ W} \cdot \text{h}$
- Usable Energy (90% Depth of Discharge):  $E_{usable} = 4.995 \text{ W} \cdot \text{h}$

- Estimated Flight Time at Cruise Power ( $P_{\text{tot}_{\text{crz}}} = 27.6 \text{ W}$ ):  $\text{Time} = E_{\text{usable}}/P_{\text{tot}_{\text{crz}}} \cdot 60 \approx 10.86 \text{ min}$

This exceeds the 10 min endurance requirement. Real-life endurance may be higher due to conservative drag estimates.

#### C-Rating and Current Delivery Verification

The battery pack must safely deliver peak current (Figure 9.29):

- Max Continuous Discharge of Pack: 11.25 A (2S3P, 15C cells).
- Peak System Demand (Spin-up):  $\sim 9.03 \text{ A}$  ( $\approx 12.04 \text{ C}$  for a 0.75 A-h pack).

This peak is within the 15C continuous limit, indicating safe operation.



Figure 9.30: Energy Budget for Target 10-Minute Cruise Flight. Total Usable Battery Energy: 4.995 W-h

#### Power System Interfaces and Considerations

The battery connects to the FlexPCB, which includes voltage regulators (5 V BEC for payload, 3.3 V BEC for avionics) and directly to the ESCs. The FlexPCB integrates voltage monitoring and safety features (fuse, reverse polarity protection). While significant heating is not expected in a 10 min flight, small air intakes on the FlexPCB and potentially battery compartments can provide cooling if tests indicate a need.

#### 9.3.4. Conclusion on Power Subsystem Design

The LPHD4525035 LiPo cell in a 2S3P (7.4 V, 750 mA-h) configuration meets L.O.R.A.X.'s structural integration and endurance needs. It was selected for its suitable form factor for embedding in the CG-shifting mechanism's mobile carriages, aligning with the three-strut architecture for distributed mass. Analysis confirms it provides sufficient energy for >10 min flight and can safely deliver cruise and peak launch currents. The  $\sim 30 \text{ g}$  pack mass is a reasonable contribution to the drone's total mass.

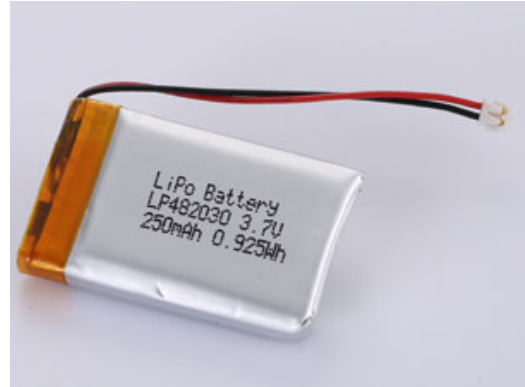


Figure 9.31: Similar LiPo cell (LPHD4525035 image unavailable).

## 9.4. Stability & Control

Due to its spin, the L.O.R.A.X. drone has peculiar flight dynamics. This section will cover the gyroscopic principles that govern the stability and precession of the drone. As well as the Stability & Control subsystem that ensures the drone can fly under stable conditions.

### 9.4.1. Gyroscopic Stabilisation & Precession

The L.O.R.A.X. drone experiences gyroscopic stabilisation. That is the tendency of the spinning object to resist torques that change its angular momentum. Unlike traditional aircraft that receive all their stabilisation effects from aerodynamic forces, the L.O.R.A.X. receives a significant amount of stability from its gyroscopic stabilisation.

The behaviour of gyroscopes, including their tendency to stabilise and precess, is fundamentally governed by Newton's second law for rotation, given in Equation 9.10:

$$\vec{\tau} = \frac{d\vec{L}}{dt} \quad (9.10)$$

Here,  $\vec{\tau}$  is the net external torque applied to the system, and  $\frac{d\vec{L}}{dt}$  is the rate of change of its angular momentum  $\vec{L}$ .

Consider a gyroscope, like the cylinder in Figure 9.32, spinning rapidly with an angular velocity  $\vec{\omega}_s$  about its spin axis. This gives it a spin angular momentum  $\vec{L}_s$ , where  $L_s = I_s \omega_s$ , with  $I_s$  being the moment of inertia about the

spin axis. If an external torque  $\vec{\tau}$  is applied to the gyroscope, Equation 9.10 dictates that the angular momentum vector  $\vec{L}_s$  must change. The change  $d\vec{L}$  occurs in the direction of the applied torque  $\vec{\tau}$ .

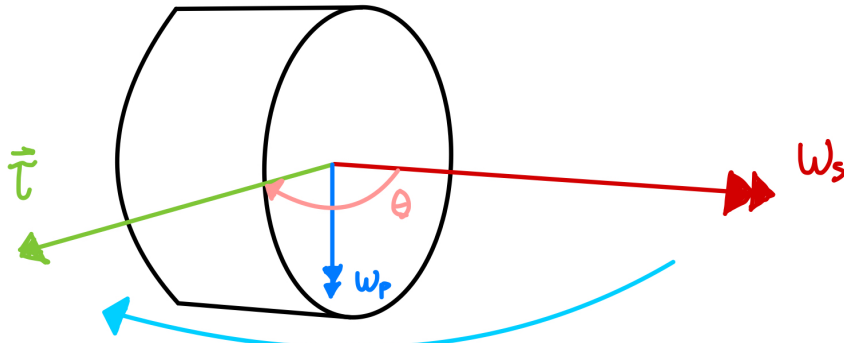


**Figure 9.32:** The figure illustrates the principle of gyroscopic precession. A cylinder spins with an angular velocity  $\vec{\omega}_s$  (red arrow) about its longitudinal axis (the spin axis), giving it an angular momentum  $\vec{L}_s = I_s \vec{\omega}_s$  along this axis. When an external torque  $\vec{\tau}$  (green arrow) is applied, the spin axis itself begins to rotate. This rotation is not a simple tilting in the direction of the torque but a precession around a precession axis. The angular velocity of this precession is  $\vec{\omega}_p$  (blue arrow), shown here along the vertical axis.

Instead of the gyroscope simply toppling over in the direction one might intuitively expect from the torque, the spin axis itself begins to rotate about a different axis, called the precession axis. This rotational motion of the spin axis is known as precession, and its angular velocity is  $\vec{\omega}_p$ . The relationship between these quantities for steady precession is given by Equation 9.11 [28].

$$\omega_p = \frac{\tau}{I_s \omega_s \sin \theta} \quad (9.11)$$

Where  $\tau$  is the torque applied. And the angle  $\theta$  is between the spin axis (the direction of  $\vec{L}_s$  or  $\vec{\omega}_s$ ) and the precession axis (the direction of  $\vec{\omega}_p$ ).

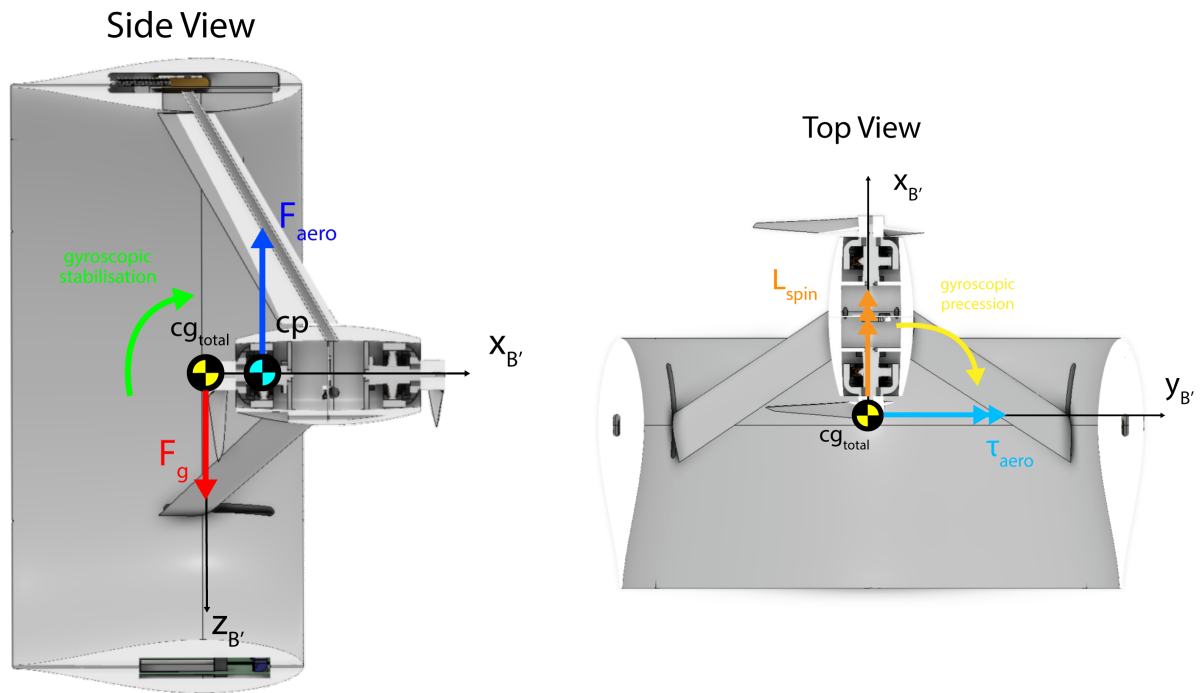
Gyroscopic stabilisation is a direct consequence of this behaviour. A large spin angular momentum  $L_s$  (achieved by a large  $I_s$  and/or a high  $\omega_s$ ) means that for a given disturbing torque  $\tau$ , the precession rate  $\omega_p$  will be small. This makes the gyroscope resist rapid changes in the orientation of its spin axis, giving it a stable characteristic. The only other parameter that changes gyroscopic stability is the moment of inertia along the spin axis. So, this gyroscopic precession is not unique to any of the concepts, as all concepts spin along their longitudinal axis.

### 9.4.2. Flight Stability

For most conventional fixed-wing aircraft to be inherently stable, the CG must be located ahead of the CP. This is known as longitudinal static stability. If such an aircraft's nose pitches up (increasing the angle of attack), the lift force (acting at the CP) increases. Since the CP is behind the CG, this increased lift creates a nose-down pitching moment, which tends to restore the aircraft to its original attitude. This is a self-correcting, stable behaviour. Conversely, if the CP is ahead of the CG, the system is aerodynamically unstable. If the nose pitches up, the increased lift at the CP (now ahead of the CG) would create a nose-up pitching moment, further exacerbating the initial disturbance and causing the aircraft to tumble or stall. Conventional aircraft are generally not designed to fly in this configuration without active control.

However, the L.O.R.A.X. drone presents a unique case. While the precise CP location varies with angle of attack, it is possible that the L.O.R.A.X. can fly even if its CP is, or shifts to be, ahead of its CG [36]. This would normally lead to aerodynamic instability. However, the gyroscopic stabilisation provided by its rapid spin is strong enough to counteract the destabilising aerodynamic moments. Essentially, the gyroscopic effect "overpowers" the aerodynamic tendency to tumble, allowing the L.O.R.A.X. drone to keep stable flight even in configurations that would be unstable for a non-spinning or slowly spinning object. This allows for unique flight characteristics and a broad range of stable flight attitudes.

The L.O.R.A.X. drone leverages this in combination with the principle of gyroscopic precession. By mounting the propeller on a spring-connected carriage, the CG's location dynamically shifts with thrust. This clever design deliberately creates an arm between the propeller's CP and the CG. The resulting torque first pitches the drone, but also leverages gyroscopic precession to induce a yawing moment around its  $z_B$  axis. This allows a single actuator to control both the pitch and the yaw, although coupled.



(a) Illustrates the aerodynamic force ( $\vec{F}_{aero}$ ) acting at the center of pressure (CP) and the gravitational force ( $\vec{F}_g$ ) acting at the total centre of gravity (CG). The green arrow indicates the gyroscopic stabilisation effect due to the drone's spin, counteracting potential aerodynamic instability if the CP is ahead of the CG.

(b) Shows the aerodynamic torque ( $\vec{\tau}_{aero}$ ) acting about the CG (due to  $\vec{F}_{aero}$  and the CP-CG offset) and the spin angular momentum ( $\vec{L}_{spin}$ ) along the  $X_{B'}$  axis. The yellow arrow depicts the resulting gyroscopic precession, which manifests as a yawing motion.

Figure 9.33: This figure shows the behaviour of gyroscopic stabilisation and precession in the L.O.R.A.X.

### 9.4.3. Control

Controlling the L.O.R.A.X. drone is quite complex due to this inherent coupling. Moreover, as the drone pitches forward, the effect of gravity on the movable carriage can exacerbate instability, potentially leading to an uncontrollable state. Because of these, the system necessitates active control for stable flight, especially when dealing with external disturbances like wind.

#### Control Strategy

To be precise, the reason why the L.O.R.A.X. drone is hard to control is that it is a Multiple-Input Multiple-Output (MIMO) system. This is because there are two inputs (the throttles of the two contra-rotating motors) and multiple interacting outputs (pitch, yaw, roll, airspeed, and altitude).

To manage this complexity, a contra-rotating propeller system was chosen. A key benefit of this configuration is its ability to decouple the drone's spin rate from its overall thrust level. Based on recommendations from Dr. Ir. E.J.J. Smeur<sup>5</sup> and N.P. Stebbins Dahl<sup>6</sup>, our control strategy focuses on achieving this decoupling by first implementing a roll rate regulator. Maintaining a constant roll then significantly simplifies the control of pitch.

While more advanced control algorithms like Model Predictive Control (MPC), LQR, or robust control were considered, the decision was made to keep the system as simple as possible by using basic PID controllers. Given the very limited time available and the team's current expertise, this approach offered the most reasonable path to a working solution. Attempts were also made to linearise the system for deeper control analysis, but due to time and experience constraints, this has been deferred to future development. For now, the primary focus remains on developing a proof-of-concept controller to demonstrate the L.O.R.A.X. drone's flight behaviour.

#### Input Mixer

The input mixer is used to translate flight commands into individual motor controls for the contra-rotating propellers. The primary purpose of the input mixer is to decouple the torque control (for modulating spin rate) from the thrust control (for modulating airspeed and pitch). A simple algorithm was designed to perform this task.

The input mixer takes in a throttle command and a differential command. The Throttle Command (ranging from 0 to 1) directly influences both motor commands, acting as a base thrust. The Differential Command (ranging from -1 to 1) introduces differential thrust, with a positive roll increasing forward motor command and decreasing the rearward motor command, and vice-versa, scaled by  $k_{roll}$ . An important function is the saturation handling: if the

<sup>5</sup>Dr.ir. E.J.J. Smeur <https://www.tudelft.nl/staff/e.j.j.smeur/>

<sup>6</sup>N.P. Stebbins Dahl <https://www.stebbinsdahl.com/>

initial calculated motor commands ( $P1\_Raw$ ,  $P2\_Raw$ ) exceed a value of 1, both commands are proportionally scaled down to ensure the maximum output remains 1 while preserving their relative difference. Finally, both motor commands are clipped at a minimum of 0. The logic diagram for the mixer can be seen in Algorithm Figure 9.34. The outputs of the mixer can be seen in Figure 9.35.

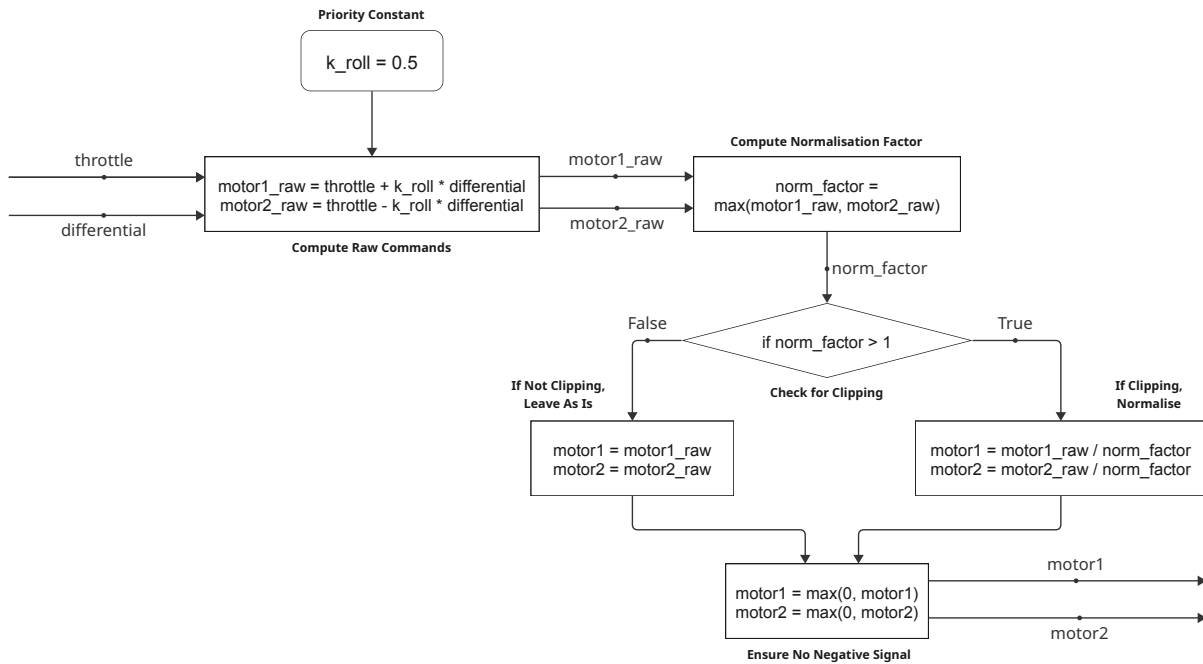
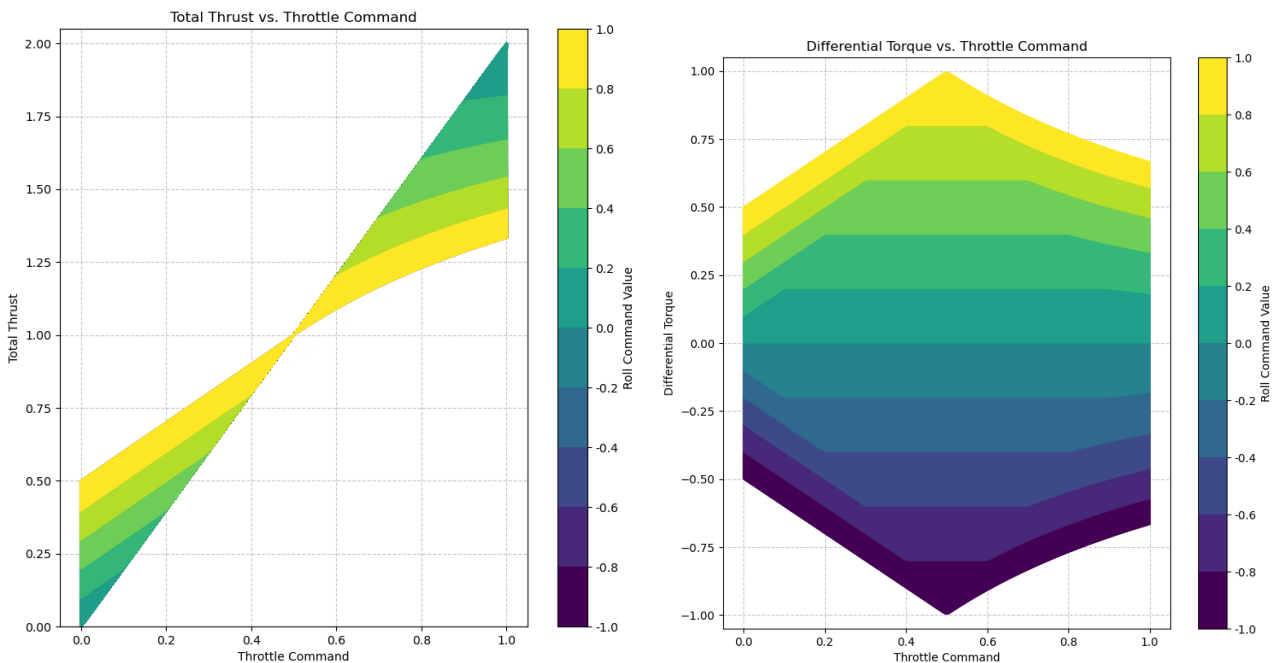


Figure 9.34: This diagram shows the logic of the mixer. The mixer is crucial in decoupling the spin rate control from the throttle. It mixes the throttle and differential signal together whilst respecting clipping.



(a) This figure shows the total thrust for the throttle command. It can be seen that for a roll command of zero, the total thrust is perfectly linear. However, increasing the throttle command clips the total thrust to prioritise providing torque, this can be seen in the . It must be noted that negative roll commands are not shown as in this plot; they are mirrored from the positive roll commands. So -0.6 has the same result as positive 0.6.

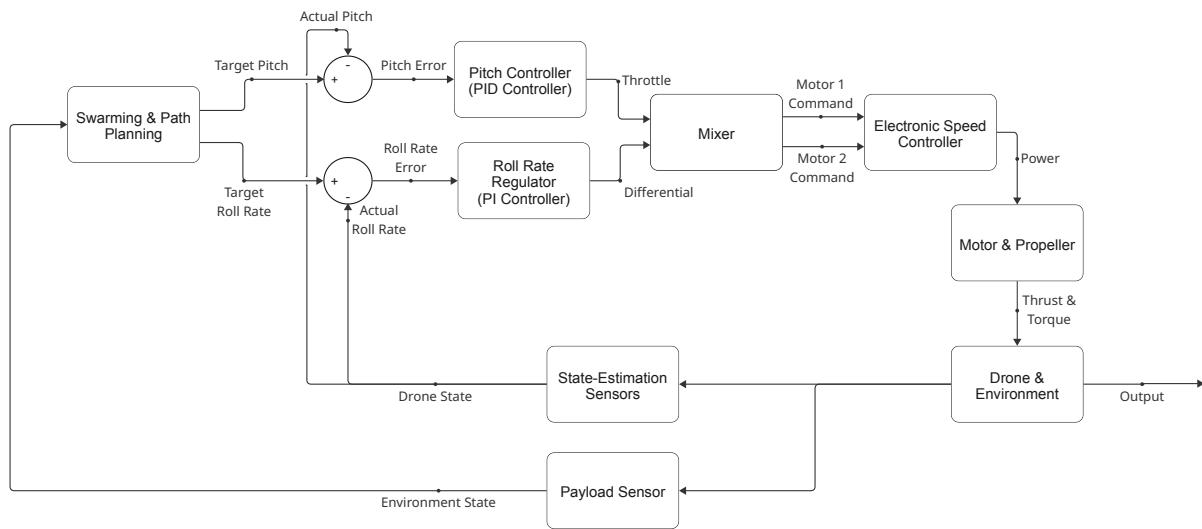
(b) This figure shows the total differential torque for various throttle commands. When the roll command is zero, there is also zero differential torque, no matter the throttle. However, when more roll is added, high and low values of throttle result in limited differential torques.

Figure 9.35: This figure shows the output of the mixer for various inputs, especially highlighting the saturation properties. The total thrust is calculated as the sum of the signals sent to each motor. The differential torque is calculated by subtracting the signal of the front motor from the back. In essence, the mixer translates a desired throttle and roll into individual motor commands, prioritising the maintenance of roll authority even at high throttle settings by potentially sacrificing overall thrust.

### Controller Architecture

The L.O.R.A.X. drone’s control system is implemented with a cascaded loop architecture. This design incorporates an inner-loop controller for roll rate regulation and an outer-loop controller primarily responsible for pitch rate control. This specific variable selection for the outer loop was determined through iterative experimentation, where controlling parameters such as the CG location, airspeed, altitude, and yaw rate were tested. Ultimately, controlling the pitch rate proved to be the most effective and direct means of achieving stable and predictable flight behaviour.

The inner-loop controller, dedicated to regulating the drone’s roll rate, utilises a Proportional-Integral (PI) control law. A derivative (D) term was not incorporated, as initial experimental results indicated that it did not significantly improve performance or stability for this specific loop. The outer-loop controller, responsible for managing the drone’s pitch rate, used a Proportional-Integral-Derivative (PID) controller. The final architecture of the control system can be seen in [Figure 9.36](#).



**Figure 9.36:** This illustrates the multi-loop control system responsible for flight control. The high-level Swarming & Path Planning module generates target trajectory, which are translated into setpoints for Target Pitch and Target Roll Rate. These setpoints feed two PID controllers, where an outer loop corrects for pitch angle error and an inner loop regulates the roll rate. The controller outputs are combined in a Mixer to produce individual motor commands, which are sent to the Electronic Speed Controllers (ESCs) to drive the motors. The resulting drone state is measured by State-Estimation Sensors and fed back to the controllers, while the Payload Sensor provides environmental state information back to the path planner.

### Controller Tuning

Due to the non-linear nature of the system and the project’s scope limitations, the roll rate regulator’s gains were determined through a heuristic tuning methodology. This process involved iterative adjustments based on observed system responses, specifically targeting stable behaviour at a nominal throttle setting of 50%. While a more optimal result can be achieved using an analytical approach (e.g., frequency response analysis, root locus), the empirically derived parameters provided sufficiently stable performance for a proof-of-concept demonstration, which was deemed sufficient within the scope of this project.

Similar to the inner-loop, the gains for this PID controller were established using a heuristic tuning method. The primary objective during tuning was to achieve stable control around a target pitch angle. For experimenting, a target pitch of 5° was selected, and the PID gains were adjusted to ensure the drone exhibited stable and acceptable transient response characteristics at this operating point. The gains for both controllers can be found in [Table 9.12](#).

**Table 9.12:** Empirically Tuned Controller Gains

Gain	Roll Rate Regulator	Pitch Controller
P	100	0.04
I	2	0.03
D	0	0.01

### 9.4.4. Manoeuvring

Now that the active control of the drone is established, its manoeuvring capabilities can be analysed. It was identified that the drone needs to carry out two main manoeuvres: going straight and turning. Because of the coupled nature of the pitch and yaw of the drone, this is not an easy feat. In this subsection, the proposed manoeuvres are discussed.

#### Straight Flight

When flying in a straight line, the L.O.R.A.X. drone will find a point at which the CG is almost exactly in the same location as the CP. To fly in a steady state, a moment equilibrium must be established. However, it can be observed that the drone's yaw rate remains constant over time. This is attributed to the aerodynamic moment around the CG generated by the annular wing. The control algorithm will find a small moment arm between the CG and CP that compensates for this aerodynamic moment. However, because of this, the drone can never fly in a completely straight line; there will always be some precession and non-zero yaw rate. One option is to accept this and take this into account when planning a path. However, for longer distances, this might not always be an option.

One option is to use the contra-rotating propeller property of the drone and to switch the spin direction mid-flight. By switching the direction of spin, the direction of the angular momentum vector is reversed, and the precession will happen in the mirrored direction. The downside of this manoeuvre is that the drone will go through a phase of very low spin, meaning it will almost not be stabilised. This is a potentially risky move as this would be prone to disturbances, resulting in loss of control. This manoeuvre is shown in [Figure 9.37](#). Another option is to repeatedly perform a rotation manoeuvre to correct the heading. The benefit of this is that the spin rate and stability will be maintained. However, more time and endurance would be wasted on turning. This manoeuvre is shown in [Figure 9.38](#). It must be noted that increasing the spin rate also reduces the yaw rate.

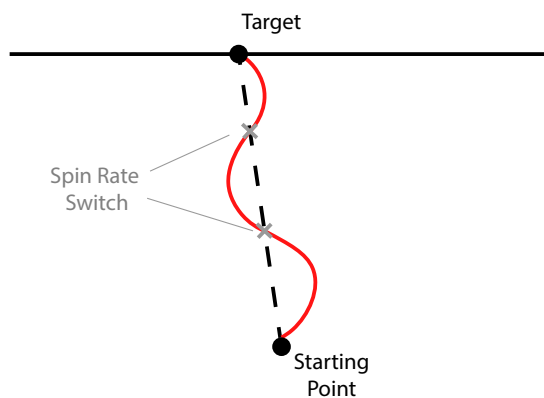


**Figure 9.37:** The red line indicates flight path followed by the L.O.R.A.X. with spin rate switches. By switching the spin rate direction mid-flight, it would be possible to fly a zig-zag pattern. However, at the spin rate switch, the drone is prone to disturbances. This concept will be added to the recommendations for further research.

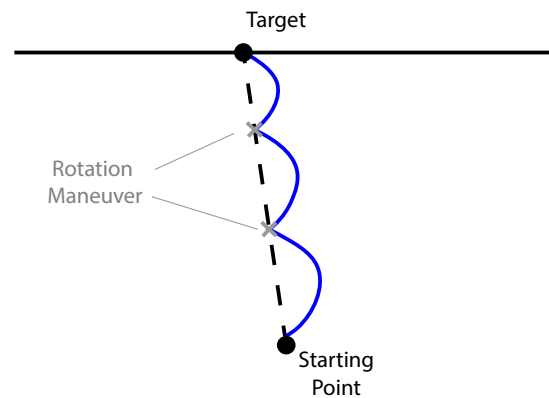


**Figure 9.38:** The blue line indicates flight path followed by the L.O.R.A.X. with rotation manoeuvres. By applying a rotation manoeuvre, which involves rotating left until the new desired heading is reached, it is possible to fly to a target a long distance away. These manoeuvres come with the downside that they require wasting more time on turning and hence reducing the effective area covered by the drone in operation.

Further analysis is required to assess whether switching mid-flight is a feasible possibility and will be added to the recommendations. In [chapter 10](#), where swarming behaviour and path planning are discussed, no corrective manoeuvres for going in a straight line will be used.

#### Rotation Manoeuvre

The most effective turning manoeuvres are performed when the carriage is at either its front or rearward limits. This maximises the shift in CG, which results in maximum yaw rate. However, shifting the CG far forward will result in a rapid pitch down, which results in an unrecoverable pitch down movement. Hence, for making a turning manoeuvre, it is preferred to move the CG backwards, which will cause the drone to stall.

In conventional aircraft, the vehicle becomes unstable when stalling. However, for the L.O.R.A.X. drone, this is not the case as it is spin-stabilised. Due to the aerodynamics of the stall, the moment arm between the CG and the CP stays large, which results in an increased yaw rate. One important note is that this manoeuvre follows the same direction of yaw as the yaw rate in straight line speed. This means that depending on whether the drone flies with a clockwise (CW) or counter-clockwise (CCW) spin, the drone will yaw right or left, respectively. This is suboptimal as this means the straight line flight cannot easily be corrected.

This can be solved by rotating the long way around. Rotating left 3 times also results in a right rotation. This can be seen in [Figure 9.39](#). A big downside is that during the manoeuvre, altitude is lost; this means that it might be necessary to climb during the straight-line manoeuvre and lose altitude during the rotation manoeuvre.

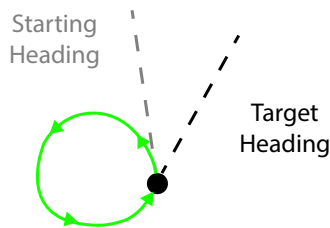


**Figure 9.39:** This image shows a rotating manoeuvre which results in a heading to the right for a normally left-precessing drone. This manoeuvre is useful for spiralling around a detected hotspot or for applying the straight-line manoeuvre in [Figure 9.38](#).

## 9.5. Flight Dynamics

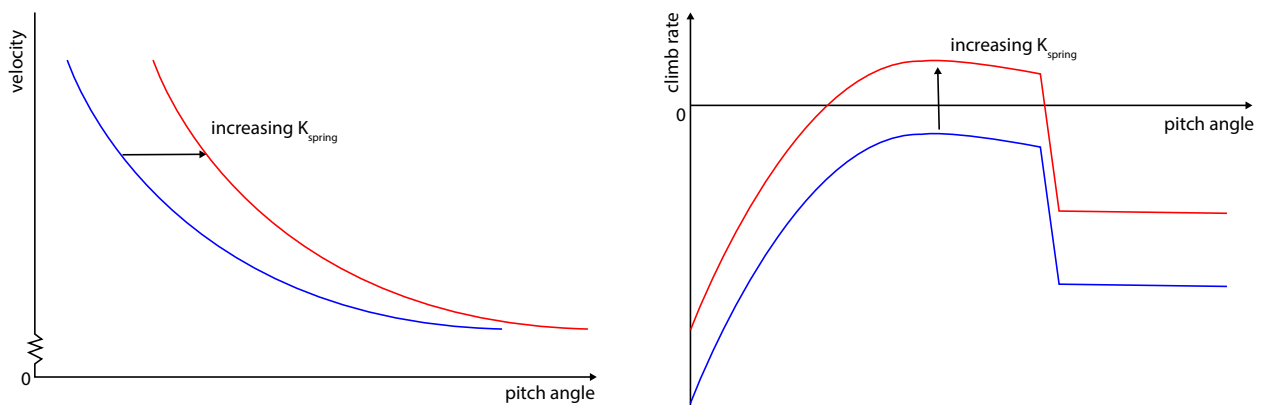
Now that the main physical elements of the L.O.R.A.X. drone have been discussed, the flight characteristics can be analysed.

### 9.5.1. Spring Tuning

Because the drone throttle control system is a Single-Input Multiple-Output (SIMO) system, and only one output is controlled, the remaining variables are a result of the pitch angle. After performing an analysis on the flight characteristics using the flight simulation module, it was established that for a constant pitch angle, the rest of the outputs also achieve a stable state.

An important factor in the equilibrium state achieved is dependent on the spring coefficient of the carriage. A stiffer spring means that the throttle level needs to be higher to ensure the Centre of Gravity (CG) is in the Centre of Pressure (CP). This means that the flight speed also increases, which then in turn results in a larger lift. This essentially means that the airspeed and climb rate of the drone are dependent on pitch, but can be tuned using the spring coefficient.

The maximum lift over drag (L/D) of the drone is found at an angle of attack of  $10^\circ$ . This also means that the maximum climb rate is found at this angle of attack. And depending on the spring coefficient, this maximum climb rate is negative, zero or positive. Considering that being able to increase altitude is crucial for manoeuvrability, this climb rate needs to be tuned such that it is positive. However, the drone also flies most efficiently at this angle of attack, which means endurance is maximised at this point. To fly in horizontal, non-climbing flight, a less optimal angle of attack needs to be used. This results in a performance trade-off between the climb rate and endurance. This behaviour can be seen in [Figure 9.40](#).



**(a)** Increasing the spring coefficient increases the equilibrium flight velocity at the same pitch angle.

**(b)** Increasing the spring coefficient increases the climb rate. Depending on the stiffness of the spring, enough speed is reached to provide a positive climb rate.

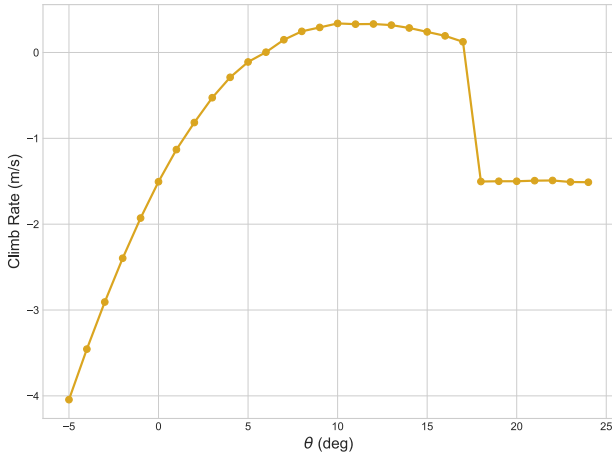
**Figure 9.40:** These two plots show the typical behaviour of the L.O.R.A.X. drone in steady state configuration. It sweeps the climb rate and velocity vs the pitch angle  $\theta$ . It shows how increasing the spring changes flight characteristics and how the spring coefficient can be tuned.

A decision was made to trim the spring to have zero climb rate at  $6^\circ$ , which provides a sufficient amount of climb rate in a straight line and allows the drone to fly level flight at this pitch angle. Further investigation should be

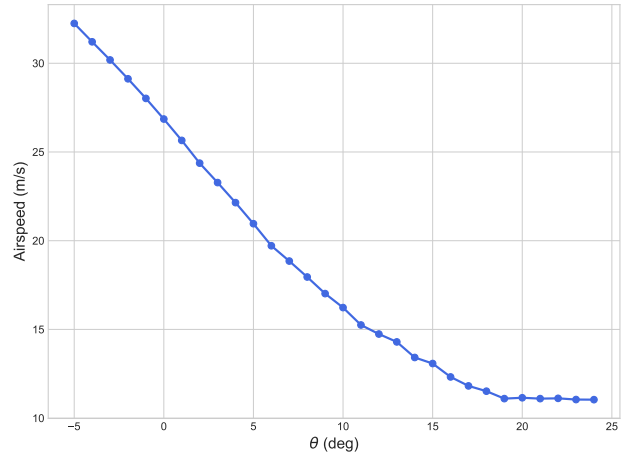
done into optimising this. However, because the spring is quite easily swappable in the drone, it will also be possible to adjust this depending on the mission requirements. For now, this value was used in simulations to show general behaviour.

### 9.5.2. Steady State Flight

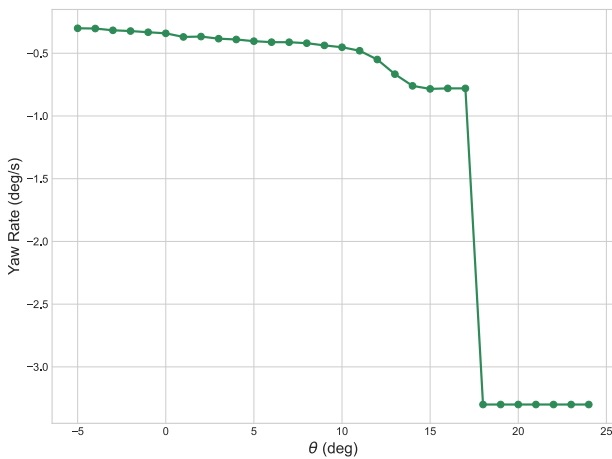
A parameter study was performed, sweeping the pitch angle target. The observed steady states indicate that the velocities are not zero, but the rate of change is zero in the parameters. An overview of the parameter study can be seen in Figure 9.41.



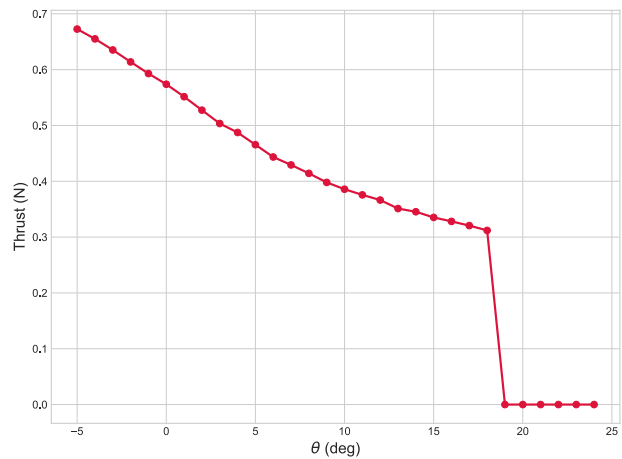
(a) Climb rate vs. pitch angle  $\theta$ . A climb rate of 0 m/s is achieved at  $\theta = 6^\circ$ . The maximum climb rate is 0.34 m/s at a pitch angle of  $10^\circ$ . Stall is seen at  $17^\circ$ .



(b) Velocity vs. pitch angle  $\theta$ . It can be observed that to reach a steady state, velocity must increase at lower pitch angles. Steady state here does not mean that altitude is constant, but rather that the rates are constant.



(c) Yaw rate vs. pitch angle  $\theta$ . It can be seen that at lower pitch angles, the yaw rate is almost constant and rather low. This is beneficial for flying in a straight line. At higher angles of attack, the yaw rate increases; finally, after stall, the yaw rate significantly increases. This property is used in a rotation manoeuvre. The yaw rate at a pitch angle of  $6^\circ$  is  $-0.425^\circ/\text{s}$ . The yaw rate in stall is approximately  $-3.3^\circ$ , however, this value is quite oscillatory, and this is just the median. Initially, when moving to this angle of attack, the yaw rate can go up to  $-6^\circ$ . It must also be noted that the yaw rates could be significantly increased by reducing the spin rate; however, this also makes the drone more susceptible to deviations.



(d) Thrust vs. pitch angle  $\theta$ . This plot shows that increasing the pitch angle decreases the thrust requirement. This might seem counterintuitive, but this is due to the airspeed at this trim point. Increasing the thrust also compresses the spring further and thus results in a lower pitch angle. At high angles of attack where a stall occurs, the drone simply glides down.

Figure 9.41: These figures show the performance of the L.O.R.A.X. under steady state conditions with a controlled pitch angle  $\theta$ . These results were acquired by letting the simulation run between pitch angles  $-5^\circ$  and  $25^\circ$  in steps of  $1^\circ$ . Each simulation was 50 s long, and the steady state was then recorded for this parameter study.

### 9.5.3. Rotation Manoeuvre

To perform a rotation manoeuvre, the target theta gets set to a stall angle, for example  $18^\circ$ . The drone will start rotating whilst spiralling down. Figure 9.42 shows the behaviour of this manoeuvre.

### 9.5.4. Requirement Deviation

As can be seen from the flight behaviour, the manoeuvring requirement of  $30^\circ/\text{s}$  is not met for either the pitch or yaw movement, only a steady state yaw rate of  $-3.3^\circ/\text{s}$  is reached (in a dynamic manoeuvre this can be higher, but not close to  $30^\circ/\text{s}$ ). This was already predicted, as it was classified as a killer requirement. The current concept is limited to a limited manoeuvrability, and there are no easy ways to improve this.

That this concept would not meet this requirement was already predicted in the midterm report. However, the worked-out concept performs worse in manoeuvrability compared to what was predicted in the midterm report. This is mostly to be attributed to the fact that it was assumed that the maximum moment arm could be maintained over an extended time. In reality, the main limitation is losing too much pitch if this is done. Whilst the drone can achieve larger rates than steady state in small peaks by moving the pitch angle up or down, this design will not be able to achieve the desired manoeuvring rates.

The question then arises on whether this requirement is required. After discussion with the tutor, it was established that this requirement was put in place due to the expected performance required for wind disturbances. In the midterm report, it was established that as long as the drone can maintain stability under strong gusts, it is acceptable to have a lower manoeuvrability.

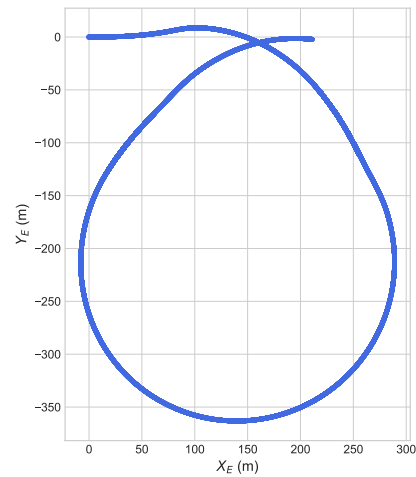


**Figure 9.42:** This figure shows the flight path when performing a rotation manoeuvre. It takes the drone 92.4 s to perform the full rotation. The turning radius is roughly 170 m. During this manoeuvre, 160 m of altitude is lost.

## 10 Swarming Performance

The main objective is to enable the L.O.R.A.X. Drone to operate effectively as part of a swarm to monitor and map a  $10\text{ km}^2$  forest area, as the square in [Figure 10.1](#). Although this is not a large area, it is crucial for initial mapping and spotting potential wildfires at an early stage. Satellite imagery, while useful for monitoring vast territories [15], often lacks adequate temporal resolution for real-time detection of small, early-stage fires, as it may only sweep the same area once every several hours and can be expensive [3]. Drone swarms, on the other hand, can provide a cost-effective solution with enhanced spatial and temporal resolution [22] [41].

While the detection and mapping of nascent wildfires are gaining increasing attention, as evidenced by projects like the Bronco Ember initiative focusing on autonomous detection using short-wave infrared (SWIR) cameras and AI [16], this early phase remains comparatively under-represented in research when contrasted with methods concentrating on fire growth and spread once established [30] [42]. Significant advancements continue in improving the aerial detection accuracy of nascent wildfires. However, a critical research gap persists concerning rapid deployment strategies for drone swarms to ensure timely and comprehensive initial coverage of at-risk areas. Our approach directly addresses this challenge through the capability for rapid deployment of ten drone nodes from a compact system, facilitating immediate, wide-area assessment. Furthermore, our proposed sensor strategy diverges by combining visual cameras with machine learning and thermal infrared (IR) cameras, as opposed to the primary reliance on short-wave infrared (SWIR) and machine learning detailed in the aforementioned NASA project. The key information required by firefighting teams includes the location and size of so-called “hotspots,” which are represented by separate ignitions, and the direction and speed at which the fire is spreading.



**Figure 10.1:** Map of an area in Noord-Holland showing  $10\text{ km}^2$  square in orange of wildland coverage area next to Amsterdam to illustrate scale of scanning area. Note that this area is not representative of an environment prone to forest fires. Source: Google Maps, © Google 2025.

To achieve this, a mothership will transport two types of drones into the mapping area: detector drones and confirmator nodes. The mapping and monitoring consists of three phases shown in [Figure 10.2](#). The detector drones, equipped with visible spectrum cameras, will perform an initial sweep of the area and produce combined risk and uncertainty maps. These maps will then guide the infrared (IR) confirmator nodes to investigate potential ignition points more accurately and efficiently. After confirming a hotspot, the drones continue to monitor the fire front for the rest of the available flight time. The result is a more efficient, flexible, and scalable way to monitor forests in real time and respond quickly to the earliest signs of a wildfire.

Several factors need to be optimised to maximise the system’s resources. E.g. the number of detectors and confirmation drones and their spacing amongst others. The objective is to minimise total energy and time while improving coverage and accuracy.

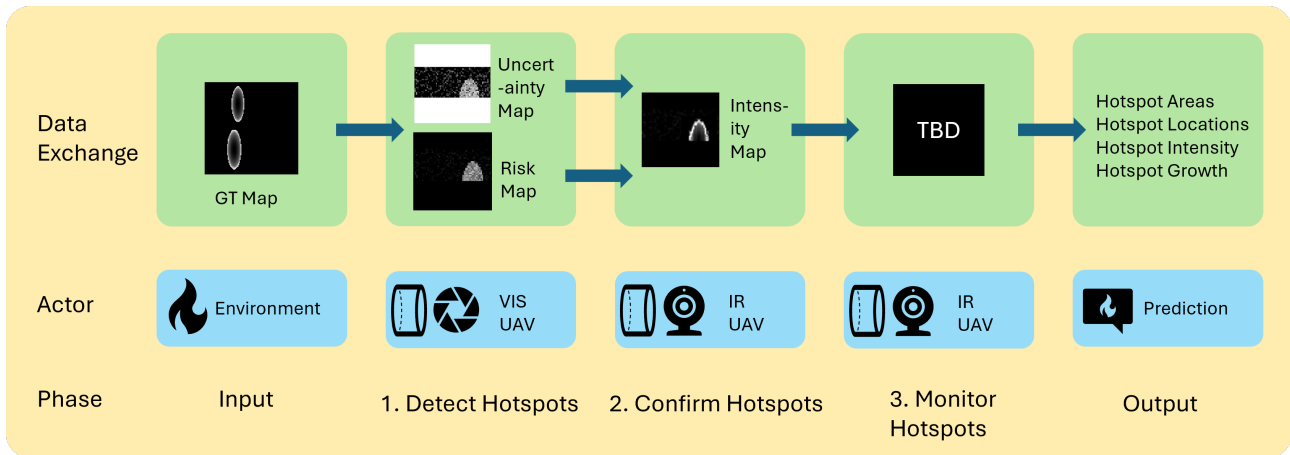


**Figure 10.2:** Three phases of the swarming approach. First, drones with visible cameras sweep the area to detect hotspots. Next, UAVs with infrared sensors move in to confirm detections. Finally, the same infrared drones circle the hotspot to track its growth. Growth tracking is still left to be implemented

The following chapter covers the L.O.R.A.X. mission swarming approach, simulation, data collection and data transmission. [section 10.1](#) covers the approach of modelling the wildfire hotspots and their dynamic behaviour. Then [section 10.2](#) covers the selected payload and its characteristics. Subsequently [section 10.3](#) covers the approach to path planning for each of the drone node types and performs a parameter study to optimise the swarm for the current mission. Finally, [section 10.4](#) elaborates on the communication architecture used by the system.

## 10.1. Map Modelling of Forest Fires

For the purposes of this simulation, two active hotspots were modelled within the 10 km<sup>2</sup> grid. Each hotspot covers between 10 and 20 acres, reflecting the early, free-burning stage of a wildfire: large enough to be detectable and to show spreading behaviour, but small enough to be considered an initial outbreak rather than a fully developed fire. The choice to use two separate ignitions aligns with a high-risk scenario, reflecting conditions typically experienced during peak wildfire season in California, when multiple ignitions can break out nearly simultaneously due to a combination of lightning, human activity, and elevated vegetation dryness.

Determining the number and size of initial hotspots for a small area is challenging due to the scarcity of granular data and the variability of conditions across landscapes. While regional averages for a fire-prone temperate or boreal region (where extreme fire behaviour is worsening [10] [6] [38]) indicate 0.1–0.5 significant hotspot events per year in a 10 km<sup>2</sup> area, this estimate remains highly conservative and appropriate for worst-case simulations. For example, an analysis of China (2003–2016) reported up to  $1.7 \times 10^5$  yearly fires, equivalent to merely 0.18 fires/year in a 10 km<sup>2</sup> grid [38]. Meanwhile, the Global Fire Atlas identified 13.3 million individual fires globally ( $\geq 0.21$  km<sup>2</sup> each) between 2003–2016, averaging about 0.95 million fires per year, and reaffirming how rare ignition events are on small scales [5].

Nonetheless, placing two growing 10–20-acre fires within the grid is a reasonable way to stress-test the capabilities of a swarming strategy under elevated-risk conditions. It falls within a plausible range for small, free-burning wildfires and highlights a scenario where resources may need to track and respond to more than a single incident at once.

### 10.1.1. Hotspot Temperature Intensity Modelling

The map is represented by a 10 km<sup>2</sup> grid in which each cell corresponds to a 10 m × 10 m patch of ground. Each cell holds a temperature “intensity” value on a scale from 0 to 1, reflecting the level of heating at that point. This approach was chosen to enable efficient simulations by employing a Boolean data type when appropriate.

The simulation’s 0–1 intensity scale can be directly mapped to realistic flame and smouldering temperatures. Empirical measurements show that the base of an active wildfire flame typically reaches about 1000–1500°C, dropping toward about 300°C at the flame tip [39]. Smouldering combustion — deeper within the fire — occurs at much lower temperatures, typically between 500°C and 700°C [37]. To translate a cell’s 0–1 intensity ( $I$ ) into a physical temperature, a simple linear scaling is applied:

$$T = T_{ambient} + I \cdot (T_{flame,peak} - T_{ambient}), \quad (10.1)$$

with  $T_{ambient}$  set to 25°C and the conceptual elliptical fire shape where the outermost edge, corresponding to the flame tip, is assigned the maximum intensity of 1.0 at 1100°C ( $T_{flame,peak}$ ). Just inside this main flaming region, a

"smouldering" zone is modelled with a lower peak intensity, specified by 0.4. The intensity then decreases further towards the centre of the active fire area. In the model, the thickness of this main flaming front is controlled by a factor of the normalised square distance set to 0.3. This value marks the boundary between the "smouldering" interior and the "main" flaming front.

Once the flame front passes, temperatures drop rapidly. Field measurements show the main flaming front typically lasts about 30–40 seconds at a given location [39]. During this brief period, temperatures spike as the flame consumes available fuel; afterwards, the area cools quickly by radiation and convection. Within about a minute, temperatures typically fall to a few hundred degrees or lower, and after roughly 10 minutes, the area often approaches ambient conditions.

This cooling process is represented in the simulation by applying an exponential decay to all cell intensities at each time step, reflecting Newton's law of cooling. The resulting decrease in intensity is illustrated for two hotspots within a 10 km<sup>2</sup> area in Figure 10.3. The decay factor is calibrated to bring a smouldering cell back toward ambient within 10 minutes. Intensities that diminish below a small threshold are set to zero, indicating complete cool down.

The model assumes a uniform cooling rate across all cells, applying the same exponential decay regardless of actual temperature and terrain conditions. As a result, a peak-intensity cell (1.0) and a lower-intensity cell (0.4) diminish at the same proportional rate, even though in reality the physical mechanisms at 1100°C and 500°C would differ. Additionally, each cell cools independently, ignoring radiative or convective transfer to adjacent areas. While this approach disregards the complex, non-linear, and interactive nature of real-world cooling, it is sufficient for a proof of concept.

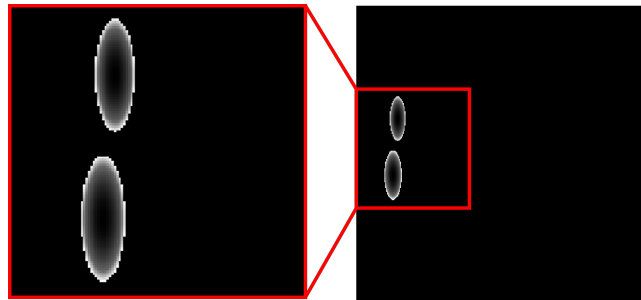


**Figure 10.3:** Example of initial ground truth for the 10 km<sup>2</sup> simulation grid. Black indicates no fire (intensity 0, ambient conditions), while white denotes active flame (intensity 1, ≈ 1100°C). The grid shows two separate hotspots, each covering roughly 10–20 acres, reflecting a realistic scenario of multiple ignitions during a high-risk period.

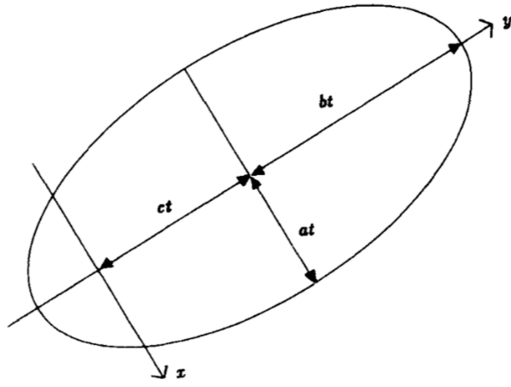
### 10.1.2. Fire Shape and Spread Modelling

Wildfire propagation has been represented by a range of models over the years, ranging from simple ellipses to more sophisticated egg- and fan-shaped formations. Initial approaches often assumed uniform terrain and vegetation, ignoring factors such as wind and slope that strongly influence a fire's forward spread. Modern models combine these earlier ellipsoidal concepts with Huygens' Principle to treat the flame perimeter as a continually expanding polygon, allowing for more realistic simulations of fire growth under changing conditions [27].

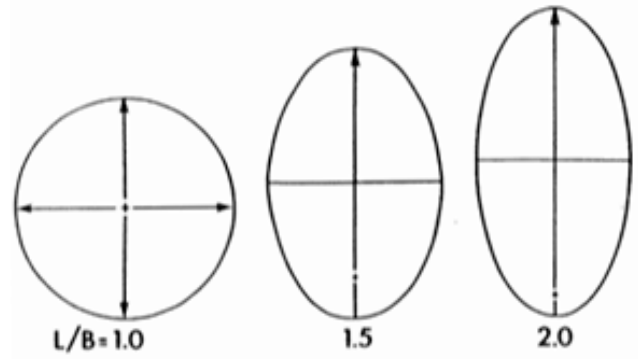
For demonstration purposes, a simple ellipsoidal model suffices. The ellipse is defined by its semi-minor axis ( $a$ ) perpendicular to the wind direction, semi-major axis ( $b$ ) aligned with the wind, and centre offset ( $c$ ) representing the forward shift of the ellipse's centre from the point of ignition in the direction of the wind (see Figure 10.4a). Furthermore, it has been observed that, within certain limits, the ratio of  $a$  to  $b$  depends predominantly on wind speed [2]. To determine this length-to-breadth ( $L/B$ ) ratio ( $b/a$ ), an empirical formula by Dr. Martin Alexander [2] is applied, which was derived by fitting a power-law curve to Initial Spread Index calculations:

$$L/B = a/b = 1.0 + 0.00120 \cdot W^{2.154}, \quad W < 50, \quad (10.2)$$

$W$  denotes wind speed in km/h. The formula applies to standing timber, reflecting conditions analogous to our scenario. As the  $L/B$  ratio increases, the fire's shape becomes more elongated in the direction of the wind, which is illustrated in Figure 10.4b.



(a) Fire front at time  $t$ , showing semi-minor axis  $a$ , semi-major-axis  $b$  and offset from ignition  $c$ . Wind is in the direction of the  $y$ -axis. Figure adapted from Richards [27].



(b) Ellipse length to breadth ratio as a function of increasing wind speed. Figure adapted from Alexander[2].

Figure 10.4: Illustrations of ellipse-based fire spread.

Then, the fire’s point of origin is assumed to be located at the focus of the ellipse [2]. Based on the geometric relationship between the centre of the ellipse and its focus, the ratio of the semi-major axis  $b$  to the centre offset  $c$  can be expressed as:

$$\frac{b}{c} = \sqrt{1 - \frac{1}{(L/B)^2}} \tag{10.3}$$

The forward rate of spread (ROS) represents the rate at which the furthest point of the fire (the “head”) moves away from its ignition point. The ROS is based on a range of factors, including fuel type, moisture, wind, and slope [2].

In practice, the rate of spread varies considerably depending on these conditions. As a rough rule of thumb, under dry conditions and strong winds, the forward rate of spread in forests is about 10% of the 10 m wind speed [9]. Furthermore, this rule performs reasonably well under high-risk conditions, yielding reduced bias and mean relative errors lower than 50%, making it a useful approximation [9].

In the context of the L.O.R.A.X. model, where the ignition point is placed at a focus of the ellipse, the forward rate of spread (ROS) corresponds to the time derivative of the sum of the ellipse’s semi-major axis  $b$  and the distance from its centre to the ignition point  $c$ . Rearranging this relationship allows us to compute the growth rate of  $a$  directly and then determine the corresponding growth of  $b$  and  $c$  based on their geometric ratios:

$$\frac{da}{dt} = \frac{ROS \cdot a}{b + c} \tag{10.4a}$$

$$\frac{db}{dt} = \frac{da}{dt} \cdot \frac{b}{a} \tag{10.4b}$$

$$\frac{dc}{dt} = \frac{db}{dt} \cdot \frac{c}{b} \tag{10.4c}$$

A wind speed of 30 km/h was applied in the model, yielding a ROS of 0.3. As a result, a 15-acre fire grows to 57 acres within 10 minutes of simulation time. This growth is illustrated in Figure 10.5, which shows five minutes of simulation time to highlight the more pronounced fire spread furthest from the ignition point in the direction of the wind.

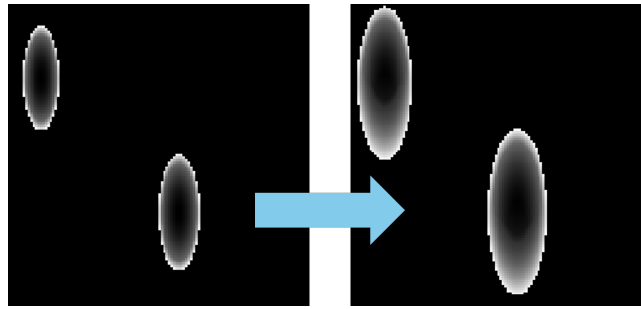


Figure 10.5: Growth of the fire front over five minutes of simulation. White areas represent hotter ground, reflecting greater fire intensity. The wind direction is downward, contributing to a more pronounced spread at the base of the ellipses.

## 10.2. Payload

The need for quick detection has led to a detect-confirm approach. To most optimally achieve this approach, the L.O.R.A.X. uses two different drone types, both carrying different payload sensors. A visual camera is used in combination with a machine learning image detection model to generate a global map of the fire, then an IR photodiode is used to finely map the areas of interest and their intensities.

### 10.2.1. Visual Camera

The visual camera chosen is the Teledyne BFS board level <sup>1</sup>, which is a global shutter camera with an extra short exposure time. This allows the making of blur-free images, and the frame rate of 78 fps enables continuous measurements without gapping caused by the spin rate. The lens selected for the visual camera is the TS-2709G-A08 <sup>2</sup>. The lens was selected to minimise the field of view without introducing gaps in the measurements, while being able to fit the entire module in the space of the airfoil. The full configuration of the camera is given in Table 10.1:

Table 10.1: Visual camera sensor specifications and performance parameters during flight

Parameter	Value	Units
Detection altitude	270	m
Cruise velocity	20	m/s
Detection capability area	10800	m <sup>2</sup> /s
Horizontal FOV	62	degrees
Vertical FOV	46.5	degrees
Horizontal resolution	1440	pixels
Vertical resolution	1080	pixels
Sweep FOV	90	degrees
L1	0.276	m
L2	0.410	m
Maximum pixel area	0.113	m <sup>2</sup>
Spin rate	7	Hz
Exposure time	21	μs
Blur ratio	0.0107	–

The camera performs sweeps in it's vertical direction. L1 and L2 refer to the physical size of the most distorted pixel of the frame, which occurs at the far corners of the frame. The effective FOV has been selected to be 90 degrees to limit the projection distortion of the pixels. and also corresponds to slightly less than the area covered by 3 consecutive frames. To ensure a symmetrical swath and to reduce unnecessary data rate, the timing of the frames of the visual camera has to be carefully coordinated using state-estimation sensor data.

<sup>1</sup>Teledyne Vision Solutions. *Blackfly S Board Level*. Available at: <https://www.teledynevisionsolutions.com/en-150/products/blackfly-s-board-level/?vertical=machine+vision&segment=iis>. Accessed June 18, 2025.

<sup>2</sup>TeSooOptical *Tesoo 4.5mm Lens*. Available at: <https://www.tesoooptical.com/products/4.5-mm-lens/>. Accessed June 18, 2025.

### 10.2.2. IR photodiode

The IR sensor chosen is the HAMAMATSU G7151-16<sup>3</sup>, which is an InGaAs linear IR photodiode, has a light intensity detection range in the LWIR to MWIR that is favourable for forest fire detection. Since the IR photodiode is an analogue sensor, the field of view of the selected lens can be far lower since the limiting factor is now the response time. For the IR lens, the CIL857-F3.0-M08ANIR<sup>4</sup> was selected. The final sensor properties can be found in Table 10.2:

Table 10.2: Infrared sensor and flight parameters

Parameter	Value	Units
Detection altitude	70	m
Cruise velocity	20	m/s
Detection capability area	2800	m <sup>2</sup> /s
Horizontal FOV	8	degrees
Vertical FOV	0.5	degrees
Horizontal resolution	16	pixels
Vertical resolution	1	pixels
Effective FOV	90	degrees
L1	0.61	m
L2	1.22	m
Area	0.74	m <sup>2</sup>
Spin rate	22	rad/s
Response time	$3.33 \times 10^{-9}$	s
Blur ratio	$6.67 \times 10^{-7}$	—

The flight altitude was selected to be as low as possible while still providing clearance above a large amount of maximum tree heights. The field of view was selected to achieve the 1 m<sup>2</sup> with a 33% margin, while still achieving at least 3 repeated measurements per point.

The IR is to be used as a state-estimation sensor to determine the rotation and roll rate of the drone body at a given moment in time. By using the periodical changes in the measured intensity caused by the difference in received IR intensity between the sky and ground. Depending on the result of the parameter study, an alternative IR photodiode might be selected for the visual camera nodes to measure the rotation rate at a lower cost.

### 10.2.3. Simulation of Detection with VIS Camera and ML Model

The drones with visual cameras will survey the ground and take pictures which will be analysed by a ML detection algorithm. Detection is done with an enhanced YOLO model by Shi, Pei et al [31]. The enhanced YOLOv5 algorithm integrates Switchable Atrous Convolution, Polarised Self-Attention, and Soft Non-Maximum Suppression for accurate forest fire detection. The swath covers a length of 540 m when flying at an altitude of 270 m. This length is determined based on the geometry illustrated in Figure 10.6.

<sup>3</sup>Hamamatsu Photonics K.K. G7151-16 InGaAs PIN photodiode array. Available at: <https://www.hamamatsu.com/jp/en/product/optical-sensors/infrared-detector/ingaas-photodiode-array/ingaas-photodiode-array/G7151-16.html>. Accessed June 18, 2025.

<sup>4</sup>Commonlands Small 6mm Lens. Available at: <https://commonlands.com/products/small-6mm-lens-cil857?variant=40275566329974>. Accessed June 18, 2025.

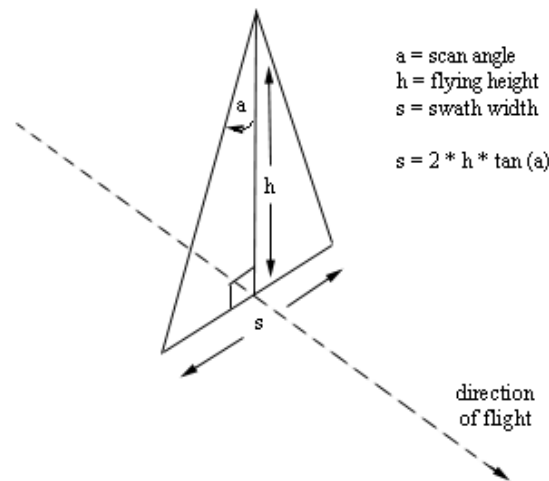


Figure 10.6: Swath width as a function of instrument FOV and UAV altitude. Image from Lim [20].

To simulate and demonstrate a proof of concept for wildfire detection with a L.O.R.A.X. drone swarm, the machine learning (ML) detection process is modelled in Simulink. Instead of deploying a full ML pipeline, the model simulates detections and confidence scores based on ML model performance parameters and ground truth data. This approach is useful for identifying trends in detections. Importantly, while the method highlights capabilities and trends, the exact values should be further calibrated and validated to reflect true conditions accurately.

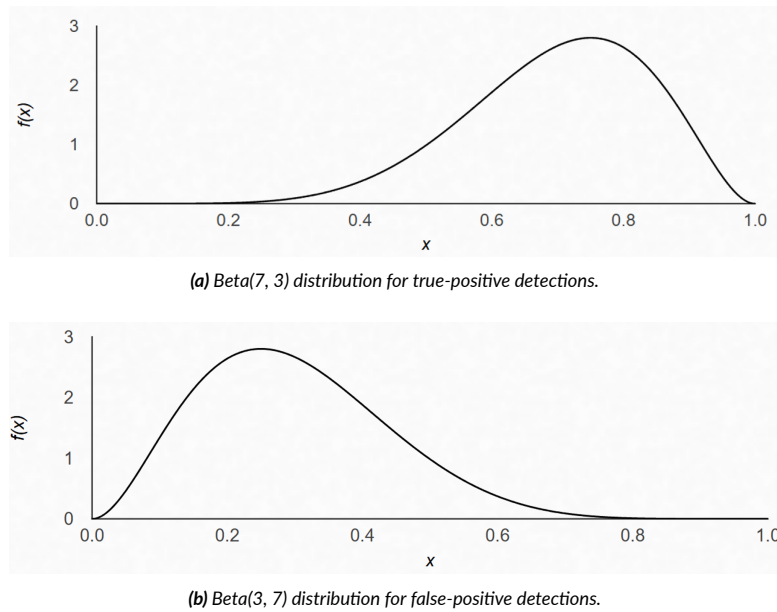
Each drone surveys its assigned area and generates a local risk map by assigning a confidence score to each  $10 \times 10$  meter grid cell. These scores represent the likelihood of fire presence, with values ranging from 0 (low risk) to 1 (high risk). The ground track image of each UAV is used to simulate detections, with the ML algorithm producing bounding boxes, each representing a potential fire detection within a cell. An example of three local risk map patches is shown in Figure 10.7:



Figure 10.7: Example of camera view for illustrative purposes, with assigned risk scores for three  $10 \times 10$  m example patches. Aspect ratio (AR) does not represent the actual AR of the visual camera,

To incorporate uncertainty and variability in detections, the ML model is simulated probabilistically. For each grid cell within the sensor's field of view, a detection is generated depending on whether the cell contains a true hotspot (i.e., ground truth intensity  $> 0.1$ ). If it does, the model samples a confidence score from a Beta distribution tailored for true positives, with a detection probability matching the recall of the enhanced YOLO model (0.743, as reported by Shi et al. [31]). If the cell is not a hotspot, it may still trigger a false alarm with a small probability (5%), and the confidence score is drawn from a separate Beta distribution representing false positives.

Since the visual cameras-ML combination can detect the presence of fire but not accurately measure fire intensity, confidence scores are interpreted solely as risk indicators, not absolute intensity values. In contrast, infrared (IR) cameras are capable of quantifying fire intensity and offer more accurate ground truth mapping.



**Figure 10.8:** Probability density functions (PDFs) of Beta distributions used to simulate detection confidence scores. (a) True positives generate higher confidence scores, skewed toward 1. (b) False positives tend to produce lower confidence values, concentrated below 0.5. These curves reflect the expected behaviour of a visual sensor’s detection certainty.

The parameters used to model false positives and the Beta distributions were heuristically selected, as precise empirical data for these distributions are not currently available. For true-positive detections, confidence scores typically fall between 0.45 and 0.85, modelled using a Beta(7, 3) distribution as shown in Figure 10.8a. False positives usually produce lower confidence values, predominantly below 0.5, modelled with a Beta(3, 7) distribution (Figure 10.8b). Cells outside the sensor’s field of view are marked as undefined. The algorithm in Figure 10.9 outlines this simulation process.

Each UAV produces a localised risk map based on its individual detections. These maps are then aggregated to form a global risk map of the surveyed area (Figure 10.10c). To consolidate detections and mitigate the effect of noise or outliers, an averaging approach is applied.

In addition, an uncertainty map is made on a 0-1 scale as shown in Figure 10.10d. Uncertain areas should be prioritised in (re)visiting. The level of uncertainty is based on how many risk measurements are made. When there is no risk level in a cell, maximum uncertainty of 1 is assigned.

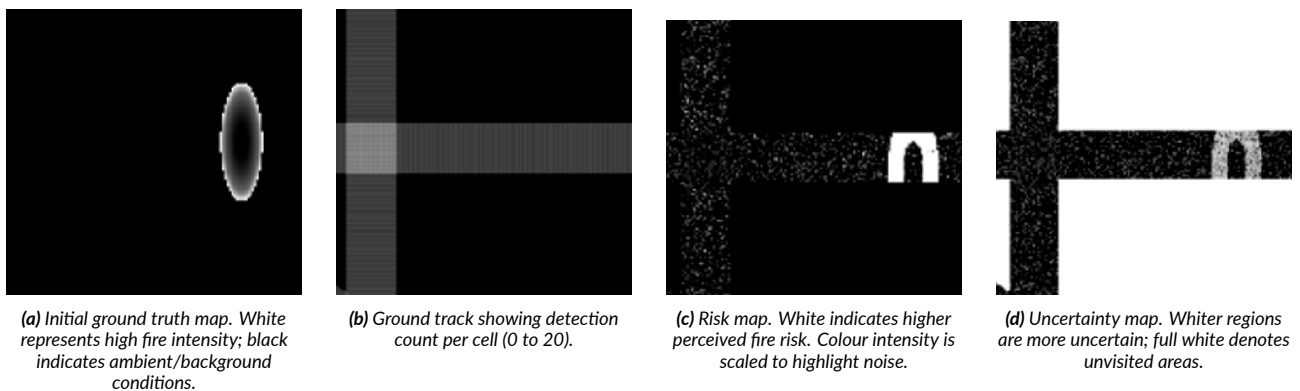


**Figure 10.10:** Visual summary of the simulated fire detection scenario over a zoomed-in region of the full map. (a) shows the initial fire intensity ground truth; (b) presents the UAV ground track with detection counts per cell; (c) illustrates the aggregated risk map based on detection confidence; (d) highlights spatial uncertainty, with brighter areas reflecting greater uncertainty due to limited or absent coverage.

When a grid cell has multiple observations, the algorithm assesses its uncertainty by first computing the standard deviation of all the risk scores for that cell; this measures how much the observations diverge from their average. It then normalises this variability by dividing it by the maximum standard deviation of 0.5 (for the case of 0 and 1 measured).

For cells with only a single observation, uncertainty cannot be directly measured from variance. Instead, heuristic values are assigned to reflect confidence based on the observation’s context. For a non-detection (risk level 0), the uncertainty is set to 0.85, reflecting greater uncertainty because the absence of detection may be a false

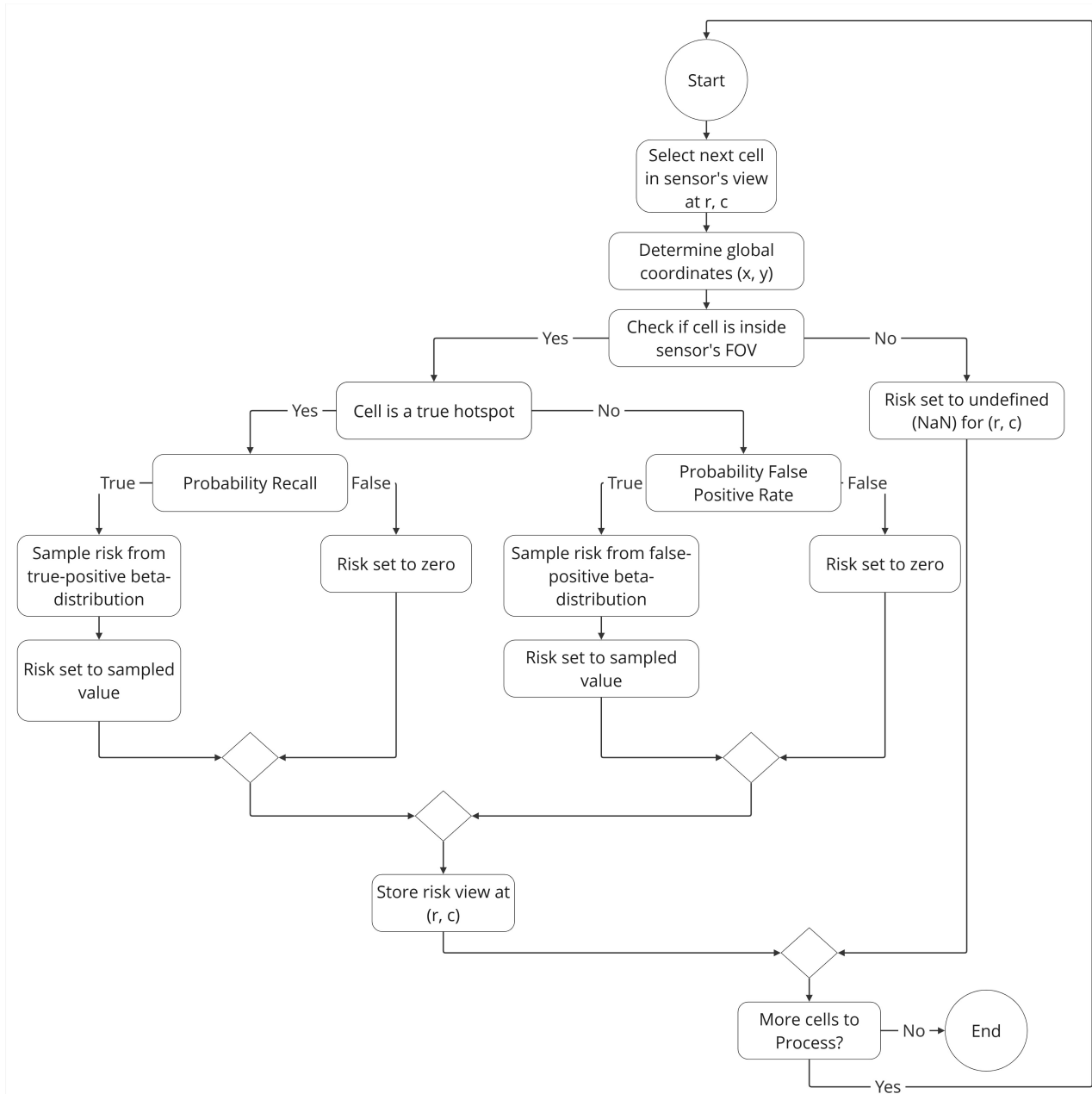


Figure 10.9: Logic diagram for simulating risk map generation using visual camera input and machine learning-based object detection.

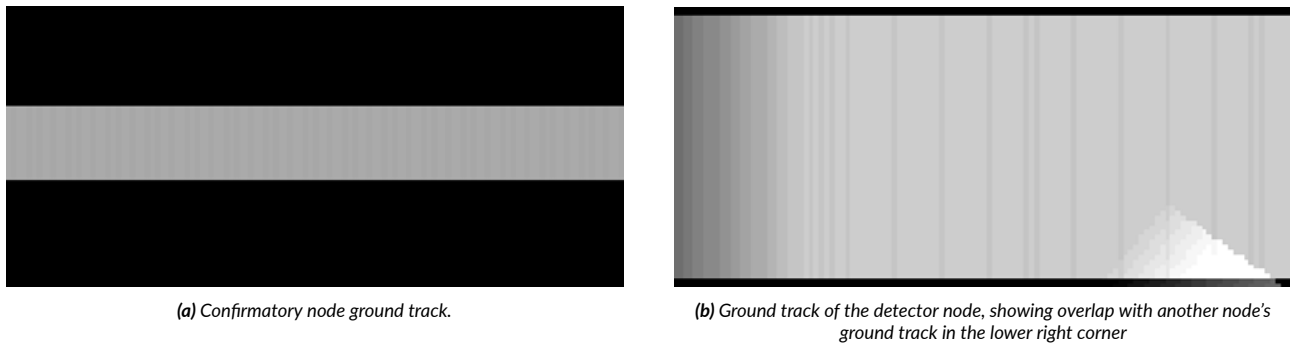
negative. For a single detection, the uncertainty is set to 0.75, indicating high uncertainty, but with greater confidence because something was observed. The values are summarised in Table 10.3:

Table 10.3: Values used to compute uncertainty in grid cells.

Max theoretical STD dev	Uncertainty no data	Uncertainty > 1 data point	Uncertainty 1 valid obs.	Uncertainty 1 zero obs.
0.5	1.0	SD/Max. SD	0.75	0.85

### 10.2.4. Simulation of Confirmation with IR Sensor

The IR photodiode uses a similar approach to the VIS camera, projecting a detection range on the grid as can be seen in Figure 10.11a. However, unlike the VIS-ML system, the IR photodiode directly measures the wavelengths of the thermal radiation emitted by the fire, and is therefore modelled to observe the ground truth temperature distribution.



**Figure 10.11:** Ground tracks of confirmatory (a) and detector (b) nodes over approximately 1000 m of flight, with intensity indicating relative detection density. Note: intensities are not scaled between node types. Visualisation is intended to highlight the difference in swath width coverage.

Because the IR sensor provides accurate thermal readings, its measurements are used to overwrite the corresponding values in the risk map, improving fidelity in confirmed fire regions. In contrast, the VIS-ML combination can only indicate the presence of hotspots without quantifying their temperature.

Due to the narrow ground track of the IR sensor, it is crucial for the system to guide it precisely based on preliminary detections from the wide-field VIS camera. This coordination ensures high-resolution confirmation where it is most needed.

As with the VIS-based detections, the IR-based intensity updates are aggregated into a final global risk map, referred to as the global intensity map. This map, intended for situational awareness, is ultimately delivered to fire management authorities as illustrated in [Figure 10.2](#).

### 10.3. Path Planning

This section outlines the path-planning strategies employed throughout the mission. It covers the initial deployment of the drone swarm during detection, confirmation of hotspots, and subsequent monitoring. The aim is to maximise efficiency and coverage while respecting operational constraints.

#### 10.3.1. Mothership and deployment

To optimise performance, the mothership path needs to be able to launch the drones to their different paths as fast as possible. Afterwards, the mothership needs to keep a distance of no greater than 2 km from each drone node. The deployment of the drone nodes should be done in a straight line across the coverage area to minimise the mission time. Using a mothership cruise velocity of 20 m/s, all detector drones are launched within 150 s of the mothership reaching the coverage area. After deployment, the mothership employs a path optimisation algorithm to reduce its distance from the furthest drone node.

#### 10.3.2. Detection

The drone's path needs to be planned for every stage of the mission. Path planning requires additional attention due to the flight characteristics of the drone. The drone nodes have been shown in [section 9.5](#) to have a cruise yaw rate of  $0.4^\circ/\text{s}$  at a cruise velocity of 20 m/s. This translates to a passive turn radius of approximately 2850 m. The drone nodes can use stall behaviour to achieve a turn rate of  $4^\circ/\text{s}$  at a flight velocity of 10 m/s, resulting in a turn radius of 170 m.

During turn manoeuvres, the drone nodes lose 1.5 m/s of altitude; the altitude lost is approximately 67.5 m for a 180-degree turn. So, a climb manoeuvre is required when initiating a turn, which negatively affects the resolution of measurements in the region of the turn.

The degree of control over the yaw rate is minimal for most of the range of pitch angles, except for when the drone enters the stall regime. However, it rapidly loses altitude in this regime, so the drone can't spend a significant amount of the flight time performing manoeuvres. All these factors cause a large number of conventional coverage strategies [17] to become unfeasible, since they rely on the free manoeuvrability of the drone. Finally, the distance between the mothership and drones is not allowed to exceed 2 km due to communication link concerns.

This specific coverage problem is not yet studied, so it would be best optimised using a reinforcement learning optimisation model. However, this is left for future work. This work focuses on optimising a known feasible coverage strategy for a varying number of detector and confirmation nodes.

The strategy being considered is an outward-segmented Archimedes spiral. The overlapping coverage area is minimised, optimising the area covered per second and reducing altitude loss during flight by minimising the

absolute turn angle. The coverage strategy is shown in [Figure 10.12](#).

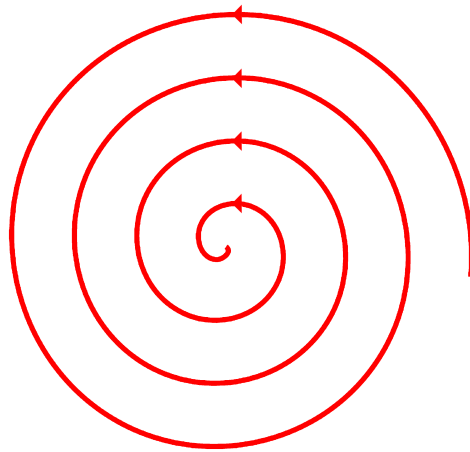


**Figure 10.12:** Coverage pattern considered, drone paths are indicated with red lines, with direction indicated by the arrows.

Using discrete turning points, a spiral coverage pattern can be achieved. For this pattern, the distance between the drones and the mothership would need to be investigated, since the drones will quickly get out of phase. This will be further investigated in [subsection 10.3.5](#).

### 10.3.3. Confirmation

The confirmation drones need to visit each hotspot location to produce a high-confidence measurement of a hotspot. Simulations of the ML model have shown that the number of false detections is limited enough for the problem to be modelled as a Travelling Salesman Problem. Various methods exist to solve this problem with multiple agents. The approach taken was based on a k-means clustering combined with a Mixed integer linear programming path optimisation model based on Chethan. R [7]. [Figure 10.13](#) shows the coverage path of the confirmation drones for a scenario of 6 confirmation drones and 6 hotspots.

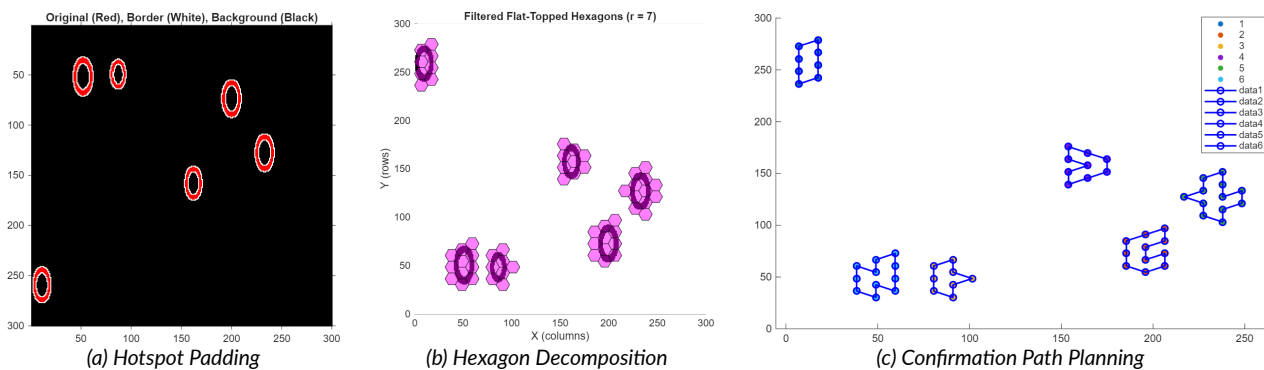


**Figure 10.13:** Confirmation path planning algorithm: Firstly, the intensity of the hotspots is compared to a threshold case; the area above this threshold is padded. The padded area is decomposed into regular hexagons with a diameter equal to the swath-width of the sensor. Finally, the centroids of the hexagons are distributed to each drone as waypoints using a k-means clustering algorithm, and their paths through the waypoints are optimised using an MILP formulation.

### 10.3.4. Active Monitoring

After all the fires have been visited by the confirmation drones, the remaining mission time is spent actively monitoring the spread of the fire. This means that the drone should follow a path around the fire front. Which dynamically adjusts. This can be done by running the same clustering algorithm as for the confirmation stage with the updated hotspot map. This algorithm can be continually run to dynamically update the drone paths for the remainder of the mission.

### 10.3.5. Optimal Swarming Configuration

For the swarm, the main design choice was the relative number of detector drones to confirmator drones. The path planning has been integrated with the sensor simulation to create a unified simulation to investigate the optimal configuration. An overview of the simulation architecture is given in [Figure 10.14](#)

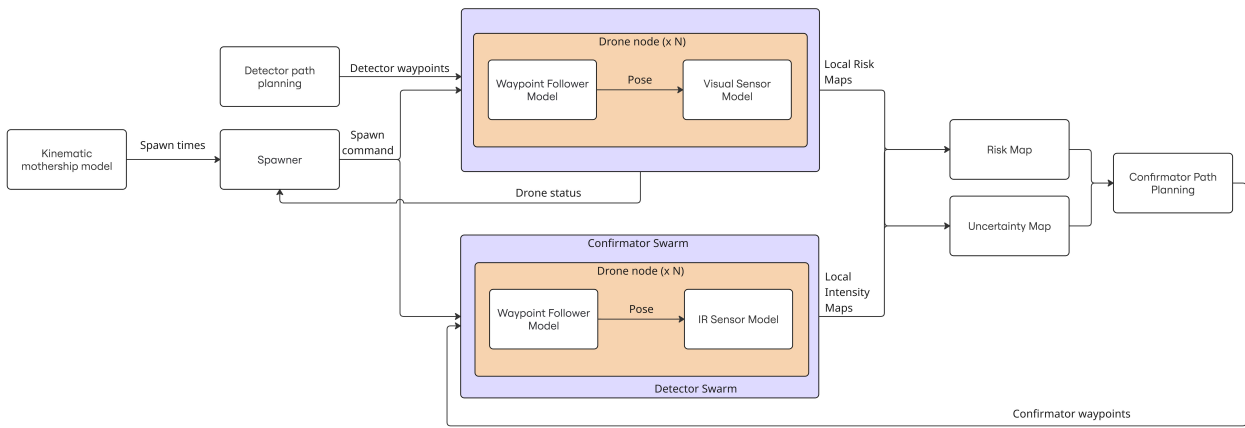


Figure 10.14: Simulation flow diagram showing the integration of the map and sensor models with the path planning and path following UAV model.

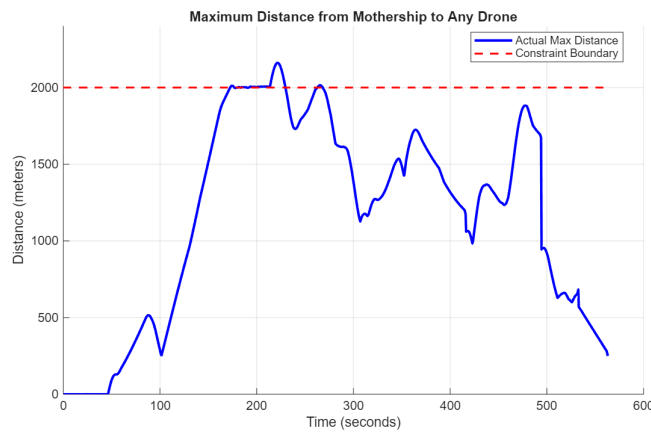


Figure 10.16: Maximum mothership distance for 6 detector drones

Before the simulation can produce results, the launch times of the drones need to be determined. The mothership path has been modelled in the spiral coverage to optimise for total mission time while ensuring the mothership remains within 2 km from the furthest drone node. The launch times were then taken from this path and used for the integrated model. The generated path and distance from the mothership to the drone are given in Figure 10.15 and Figure 10.16, respectively.

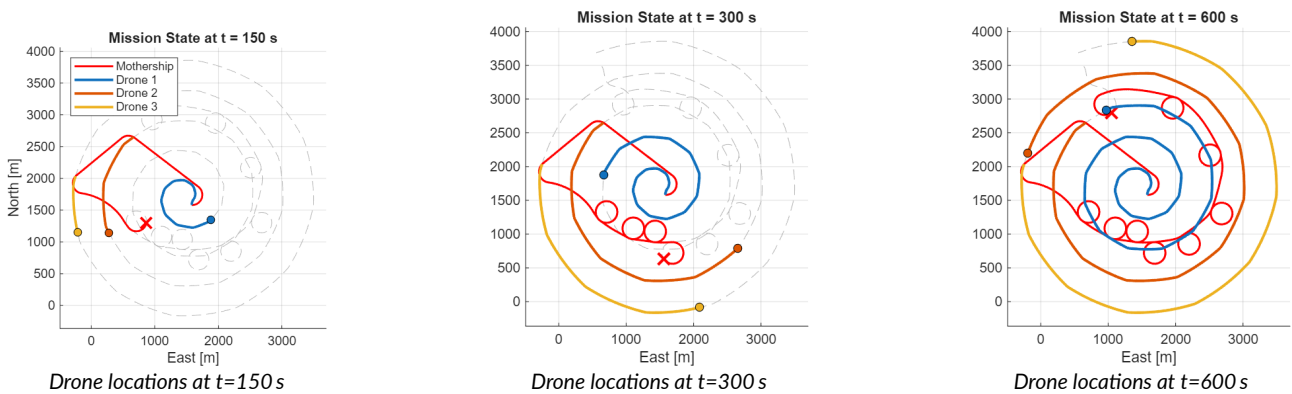


Figure 10.15: Drone node locations for 3 detector drones

The mothership has been assumed to have a flight velocity of 30 m/s and a turning radius of 150 m.

As is shown in Figure 10.16, the path presented meets the distance requirement for almost the entire mission; however, there is a small point where the maximum distance is exceeded. This can be accounted for by making one of the detector nodes diverge from its path to cover the area. Alternatively, the path is partially redundant in configurations with more than 4 detector nodes. The spiral coverage pattern allows the drones to continue the spiral to cover any potential gaps in the coverage due to external factors.

The confirmation drones were modelled to be launched from the centre of the coverage area, at offsets of 5 seconds to account for the delay between launches. Per configuration, 5 trials were run to account for the random hotspot location. It was found that increasing the number of confirmation nodes did not reduce maximum mission time since the mission time is driven by the travel time to far-away hotspots. It was found that increasing the number of detector nodes past the number of hotspots did not reduce mission time, which would lead to a 2 confirmation drone configuration for the L.O.R.A.X. system; however, for the system to be adaptable, it needs to handle a various number of hotspots. When the number of hotspots increases, for a low number of drone nodes, the mission time increases significantly. For 2 confirmator drones and 4 hotspots mission time increases by 107 seconds compared to 2 hotspots.

Using the launch times and the integrated model, the total mission time was evaluated using various configurations in [Figure 10.17](#).

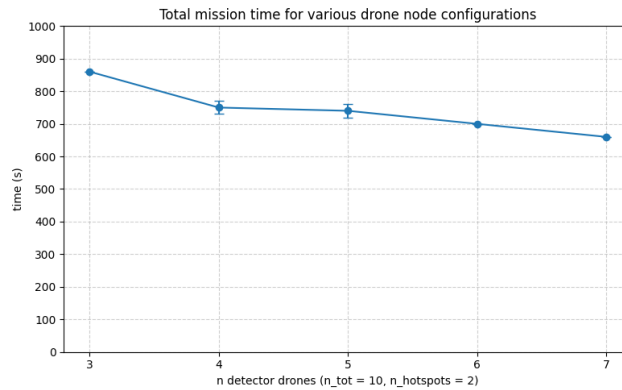


**Figure 10.17:** Total mission time for various drone node configurations, for 10 total drones and 2 hotspots.

The configuration that was selected was a 6-detector, 4-confirmator configuration. This configuration offers quick coverage of the area while being capable of operating in various hotspot conditions. The final parameters of the selected configuration are given in [Table 10.4](#)

**Table 10.4:** Final swarming configuration parameters

Parameter	Value	Unit
Detector drones	6	-
Confirmator drones	4	-
Detector phase time	604.8	s
Avg. detector flight time	381.1	s
Confirmator phase time	107.2	s
Total mission time	712.0	s

## 10.4. Communications

Communication performance is a key driver for both swarm coordination and payload effectiveness. It directly constrains the volume and rate at which imagery can be transferred for fire detection. This section presents the final design of the communication system, including data flow, link budget analysis, and component selection.

### 10.4.1. Data Flow

The data flow for the L.O.R.A.X. mission is divided into two parts. The first is the internal data flow, which illustrates the data paths used within the drone. The second is the external data flow, which describes the data streams between the drone, the mothership, and the ground station.

[Figure 10.18](#) presents the external communications architecture. It shows the high-level data streams which will be transmitted between the various units. The internal data flow within each drone node is discussed in [section 11.2](#).

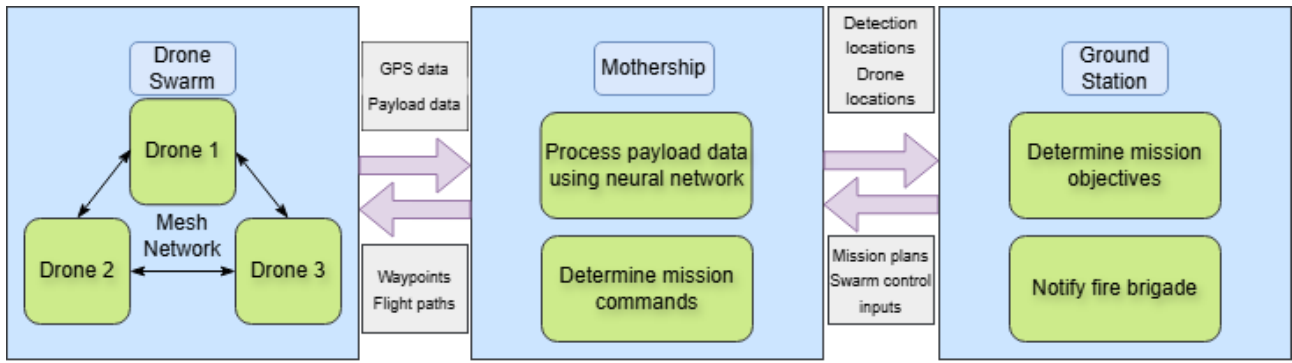


Figure 10.18: External data flow diagram for the L.O.R.A.X. mission

Each drone collects payload and GPS data via onboard sensors. This data is transmitted to the mothership to be processed. In case the mothership is not within connection range of the drone, a mesh network between drones can be used to relay the data connection. The mothership uses GPS to track the individual drone nodes, which is essential for geolocating detected fires.

The payload data is used to obtain these detections. Detector drones transmit swath images to the mothership via Wi-Fi. This information is then processed on board the mothership to detect fire signatures using artificial-intelligence-based object recognition. The computationally intense computer vision models required for this are operated on a dedicated core processing unit. Combining the processed GPS and Payload data enables the generation of a fire detection map.

Based on this map, the mothership determines the optimal swarming strategy for the confirmator drones. This strategy is translated into waypoints and flight paths, which are sent back to the drone swarm to guide their movement.

Simultaneously, the mothership transmits both the detection locations and real-time drone positions to the ground station. This enables mission operators to monitor swarm activity and, if necessary, alert emergency services such as the fire brigade.

### 10.4.2. Link budget

The proposed communication system shall be able to perform all the above-stated tasks in the mission environment. For this, the most limiting data link is the transmission of the payload data to the mothership, at a range of at least 1000 m.

The payload generates a vast number of images, of which a few are concatenated and sent to the mothership. To image every ground location at least four times, a frame rate of 0.283 Hz is required. At a pixel depth of 12 bits, and a resolution of 1440x3240, this leads to a required data rate of per connection, 15.85 Mbps.

$$Datarate = \frac{1440 \cdot 3240 \cdot 12 \cdot 0.283}{10^6} = 15.85 \text{ Mbit/s.} \tag{10.5}$$

This data rate is required when transferring the raw image data, and can be significantly reduced by down-sampling. The images are thus downsampled to 720x1660. This leads to a final data rate requirement of 3.96 Mbit/sec. To reach the required performance, Wi-Fi was chosen as the ideal protocol to use due to its high data rate capabilities. Table 10.5 shows the total link budget generated for this link, to quantify the link margin achievable.

Table 10.5: Communication Link Budget Parameters

Parameter	Value	Unit
Transmitter Power	18.1	dBm
Transmitter Antenna Gain	1	dBi
Receiver Antenna Gain	0	dBi
Free Space Path Loss (1 km)	100.1	dB
Atmospheric Loss	0.00386	dB

Continued on next page...

Table 10.5: Communication Link Budget Parameters – Continued

Parameter	Value	Unit
Receiver Sensitivity	-91	dBm
System Losses	2	dB
Link Margin	10	dB
Operating Frequency	2.4	GHz
Bitrate	11	Mbit/s

With a margin of 10 dB, this link budget is closing. This means that the connection can reliably transfer the 3.95 Mbit/sec required.

This data rate is sufficient for the required rate of 3.6 Mbit/sec, including margin for intermittent connection losses and mesh overhead.

The use of mesh networking also allows for a drone-mothership distance of over 1 km, as drones could use each other as relays.

### 10.4.3. Communications component selection

The communications subsystem consists of three main components integrated into the final mission design:

- Drone Antenna
- Mothership receiver
- Wi-Fi module

#### Drone Antenna

The chosen antenna for the drone is the TBS Tracer Flex Dipole<sup>5</sup>. As a dipole, it does not radiate in its longitudinal direction. This causes some problems regarding link reliability. However, as the data rate available far exceeds the required rate, momentary downtime due to radiation pattern mismatch can be overcome. The antenna is flexible and will be mounted on the back of the drone, connected to the FlexPCB using its U.FL connector.

#### Mothership receiver

While the drones use the same antenna for both transmitting and receiving data, the mothership shall employ a larger dedicated receiver to improve the link characteristics and range. The receiver chosen for this is Siretta Tango 23<sup>6</sup>. This antenna provides an omnidirectional gain of approximately 5 dB, potentially increasing the link range by almost 1000 m.

#### Wi-Fi module

As part of the FlexPCB, a Wi-Fi module is selected to handle the conversion from a digital signal to RF waves. This is achieved using a single ESP-WROOM-02D<sup>7</sup> per drone. This module allows for the required 11 Mbit/s using CCK, at a sensitivity of -91 dB

### 10.4.4. Design recommendations

While the current system design demonstrates basic feasibility, it is far from optimal. This section outlines key areas where targeted redesigns could significantly improve the design.

#### Antenna design

The current configuration uses a commercial off-the-shelf antenna commonly found in conventional drones. However, due to the unconventional shape and the rotation of the L.O.R.A.X., a more novel antenna design should be investigated. A proposed concept is a circular antenna wrapped around the trailing edge of the drone to allow for spin-independent radio communication.

<sup>5</sup>Team Blacksheep, TBS Tracer Flex Dipole RX Antenna, 2025. Available at: [https://www.team-blacksheep.com/products/prod:tracer\\_flexant](https://www.team-blacksheep.com/products/prod:tracer_flexant) (accessed 17/06/2025).

<sup>6</sup>RS Components Netherlands, "Wi-Fi Antenna, Omni-directional, 2.4GHz/5GHz" product page, 2025. Available at: <https://nl.rs-online.com/web/p/wifi-antennas/1408057> (accessed 17/06/2025).

<sup>7</sup>Espressif Systems, "ESP-WROOM-02D/02U Datasheet", Version 2.2, June 2023. Available at: [https://www.espressif.com/sites/default/files/documentation/esp-wroom-02u\\_esp-wroom-02d\\_datasheet\\_en.pdf](https://www.espressif.com/sites/default/files/documentation/esp-wroom-02u_esp-wroom-02d_datasheet_en.pdf) (accessed 17/06/2025).

Furthermore, the current design assumes that the dipole antenna's signal can propagate through the drone's structure with negligible attenuation. This assumption also needs further investigation. For example, by use of electromagnetic simulation or physical testing.

#### **Image compression methods**

The downscaling of the images from the visual camera is a very rudimentary compression method. A more tailored compression scheme could allow for better image recognition after transmission, while potentially further reducing data rates. For this design, the idea of on-board image processing was discarded due to technical limitations. However, with future advancements, it might be possible to run the object recognition algorithms on board the drone.

# 11 Detailed Design

This chapter outlines the detailed implementation of the technical components of the L.O.R.A.X. drone. It begins by highlighting the development of the structural design, comprised of the design of the outer body and the struts connecting to the motor hub. Next, the electronics architecture is presented by going over data flow, sensor selection and data filtering. This part also contains a detailed overview of the PCB layouts that were constructed. Additionally, an investigation into the drone noise is performed, based on numerical methods. Finally, the launching system to be used aboard the mothership is described, allowing for in-air release of the drone swarm.

## 11.1. Structural Characteristics

To design the structure of the L.O.R.A.X., first, the loads introduced on the airframe during flight had to be analysed. For this, the point loads caused by batteries positioned in the shell were determined, as well as the loads introduced in the struts connecting the motors to the wing. Furthermore, the hoop stresses, accounting for rotation, were computed. For the airframe analysis, the dimensions presented in [Figure 11.1](#) were used.

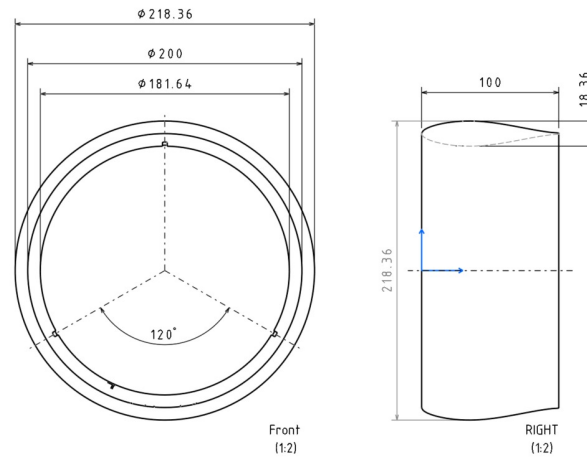


**Figure 11.1:** Airframe geometry including dimensions in [mm]

### 11.1.1. Airframe Analysis

To find the maximum shear stress on the airframe, the load that the batteries exert on the frame was calculated. It was assumed that three sets of two battery cells were equally spaced and that the mass of two cells was concentrated at one point. Furthermore, it was assumed that in this case, the frame is spinning at 10 Hz, which is the saturation limit for the sensors. In this case, the cells experience a 40 g acceleration and weigh 5 grams each (not taking into account the mass of the frame itself), leading to a shear force of 3.95 N on the frame. The shear stress introduced on the airframe by the struts is computed using the maximum torque exerted by the motor, which is further detailed in [subsection 11.1.2](#).

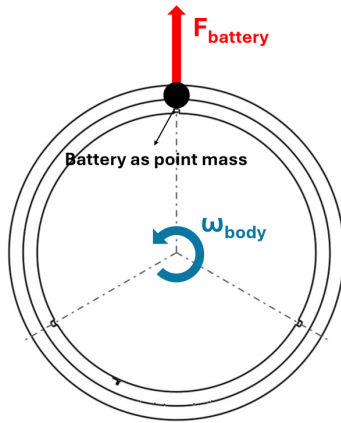


Figure 11.2: Free-body diagram of extreme load case caused by acceleration of batteries, represented as a point mass.

Table 11.1: Calculated Stresses on the Structure. Assuming the frame takes the entire load from the strut,  $\tau_{strut}$  is taken from subsection 11.1.2.

Maximum Shear Stresses		
$\tau_{battery}$	0.018	MPa
$\tau_{strut}$	0.072	MPa

After finding the limiting load cases of the drone during flight, suitable materials for the airframe were compared and are shown in Table 11.3. For each material, the mass of the airframe was calculated since minimising the weight of the airframe is essential to comply with the weight requirement.

The materials presented in the table are all sufficiently strong to absorb the loads during flight. A few things had to be considered when choosing the best material, with the main considerations being the weight and manufacturability. It was found that 3D printable materials are preferred in terms of manufacturability due to their efficiency and cost. However, materials such as PLA<sup>1</sup> and PP<sup>2</sup> turned out to be too heavy, even at a wall thickness of 0.8 mm. Balsa wood<sup>3</sup> was considered because of its sustainable nature; however, manufacturing the annular wing shape turned out to be unfeasible. Carbon Fibre<sup>4</sup> and Aluminium<sup>5</sup> were considered for comparison, though these materials were deemed to be too heavy. Finally, two foams were considered, namely Ethylene-vinyl acetate (EVA)<sup>6</sup> and expanded polystyrene<sup>7</sup>. Both materials are lightweight and relatively easy to shape. EVA was chosen as the most suitable material for the airframe over polystyrene, as polystyrene is more brittle due to its grain structure.

Table 11.2: Material Comparison including estimated mass for the airframe per material. The material in blue indicates the selected material for the airframe.

Material	$\rho$ (kg/m <sup>3</sup> )	E Modulus (GPa)	$\tau_{max}$ (MPa)	Mass (g)	$t_{wall}$ (mm)	Benefit
PLA	1250	4.20	27.58	<b>126.10</b>	0.8mm	Easier manufacturing
PP	900	1.69	17.32	<b>90.79</b>	0.8mm	Easier manufacturing
Balsa wood	160	3.00	4.04	<b>69.36</b>	1 mm	Sustainable
Expanded Polystyrene	30	0.03	0.09	<b>21.08</b>	entire cross section	Lightweight
EVA CF65	65	0.07	2.78	<b>45.67</b>	entire cross section	Lightweight
Carbon Fibre Epoxy	1600	70	90.00	<b>161.41</b>	0.8mm	High strength

<sup>1</sup>JuggerBot3D, Polyactic Acid (PLA) 3D Printing Filament Review. Available at: <https://juggerbot3d.com/pla-filament-review/> (accessed 11/06/2025).

<sup>2</sup>MatWeb, Overview of materials for Polypropylene. Available at: <https://www.matweb.com/search/datasheet.aspx?MatGUID=08fb0f47ef7e454fbf7092517b2264b2&ckck=1> (accessed 11/06/2025).

<sup>3</sup>MakeltForm.com, Balsa. Available at: <https://www.makeitfrom.com/material-properties/Balsa> (accessed 11/06/2025).

<sup>4</sup>AZO materials, Carbon/Epoxy Composite Materials Properties - Supplier Data by Goodfellow. Available at: <https://www.azom.com/article.aspx?ArticleID=1995> (accessed 11/06/2025).

<sup>5</sup>ASM Aerospace Specification Metals Inc., Aluminum 6061-T6; 6061-T651. Available at: <https://asm.matweb.com/search/specificmaterial.asp?bassnum=ma6061t6> (accessed 11/06/2025).

<sup>6</sup>MakeltForm.com, Ethylene Vinyl Acetate (EVA). Available at: <https://www.makeitfrom.com/material-properties/Ethylene-Vinyl-Acetate-EVA> (accessed 11/06/2025).

<sup>7</sup>MatWeb, Overview of materials for Expanded Polystyrene (EPS). Available at: <https://www.matweb.com/search/DataSheet.aspx?MatGUID=5f099f2b5eeb41c8a804ca0bc64fa62f> (accessed 11/06/2025).

Aluminium 6061	2700	68.9	207.00	272.38	0.8mm	High strength
----------------	------	------	--------	--------	-------	---------------

After selecting the material, the hoop stresses were computed using stress equations from Timoshenko’s elasticity theory [32], as they account for the rotation of the shape. Since the airframe is axis-symmetric, the equations were slightly simplified, resulting in Equation 11.1 and 11.2.

$$\sigma_r = \rho\omega^2 \left[ \frac{3+\nu}{8}(r^2 - (r-t)^2) + \frac{\nu(1+\nu)}{6(1-\nu)} \left(\frac{c}{2}\right)^2 \right] \tag{11.1}$$

$$\sigma_\theta = \rho\omega^2 \left[ \frac{3+\nu}{8}r^2 - \frac{1+3\nu}{8}(r-t)^2 + \frac{\nu(1+\nu)}{6(1-\nu)} \left(\frac{c}{2}\right)^2 \right] \tag{11.2}$$

Where  $\rho$  is the material density,  $\nu$  is the Poisson ratio,  $\omega$  is the spin rate,  $r$  is the radius of the annular wing, and  $t$  is the maximum thickness. For EVA,  $\sigma_r$  and  $\sigma_\theta$  were found to be approximately 512 Pa and 736 Pa respectively, well below the yield stress of the material.

### 11.1.2. Strut Analysis & Design

To connect the motor mount to the airframe, a set of struts had to be sized. These struts were designed to serve two purposes, namely, to withstand the torque of the motor on the airframe and to guide the cables from the wing to the motor mount and vice versa. To fulfil these purposes, off-the-shelf carbon fibre rods<sup>8</sup> with a 4 mm diameter were used, as they can be very thin and hollow, while maintaining structural rigidity and keeping a minimal frontal area (lower drag).

The maximum torque the motor exerts 0.016 N·m, from which, using simple shear and bending calculations, the maximum stresses on the rods can be calculated. To make sure the EVA foam is still sufficiently strong, the maximum load case assumed is when the maximum shear stress is fully transferred to the foam. The 0.057 MPa shear stress leads to a maximum deformation of 1 mm of the foam. In reality, the load from the strut will be transferred to the aluminium rail. This distributes the load over a larger surface on the airframe, reducing the stress experienced by the airframe.

Table 11.3: Strut geometry parameters and calculated stress for maximum torque applied (0.016 N·m)

Geometry		
Material	Carbon Fibre Epoxy	
Density	1600	kg/m <sup>3</sup>
Length	102.8	mm
Outer Radius	2	mm
Thickness	0.5	mm
Yield Strength	400	MPa
Shear Strength	50	MPa
Mass	0.8	g
Computed Stresses		
Bending Stress	3.83	MPa
Shear Stress	0.057	MPa



Figure 11.3: 3D Drawing of a single strut. The black pipe represents the carbon fibre rod, the blue shape indicates the EVA airfoil.

To reduce the drag from these struts, a non-load-bearing EVA airfoil shape is added, depicted in Figure 11.3.

<sup>8</sup>Easy composites, 4mm (3mm) Pultruded Carbon Fibre Tube. Available at: <https://www.easycomposites.eu/4mm-pultruded-carbon-fibre-tube> (accessed 11/06/2025).

As mentioned in [section 9.1](#), the Eppler 863<sup>9</sup> airfoil is used. This airfoil was chosen because it is specifically designed to minimise the drag over a strut, without producing lift. The "wing" shape has a twist of  $14.6^\circ$  at the tip such that the flow vector is aligned with the chord line. To be able to shift the CG further, the struts also have a forward sweep  $30^\circ$  to move the motor mount further forward. Finally, in total, three struts are added to connect the motor to the airframe, as this will aid the balancing the batteries.

## 11.2. Electronics

With the airframe and structural considerations of the design covered, this section focuses on the internal workings, specifically the electronics. It explores the electronics by first discussing the data flow diagram. Then, the selection of the sensors is highlighted. This is followed by how the sensor interprets the data and filters it. Finally, the PCB design is shown.

### 11.2.1. Data/power flow diagram

In addition to the high-level architecture of the external data flow provided in [Figure 10.18](#), a detailed visualisation of the internal data is shown in [Figure 11.4](#). It shows the data and power connections between the different subsystems. The system is centred around two MCUs, MCU\_1, which is responsible for the IMU-based state estimation. And MCU\_2, which is responsible for managing system peripherals, motor control, and external communications. The internal link budget can be found later in [Table 11.4](#).

---

<sup>9</sup>Airfoil Tools, *Eppler 863 Strut Airfoil*. Available at: <http://airfoiltools.com/airfoil/details?airfoil=e863-il> (accessed 11/06/2025).

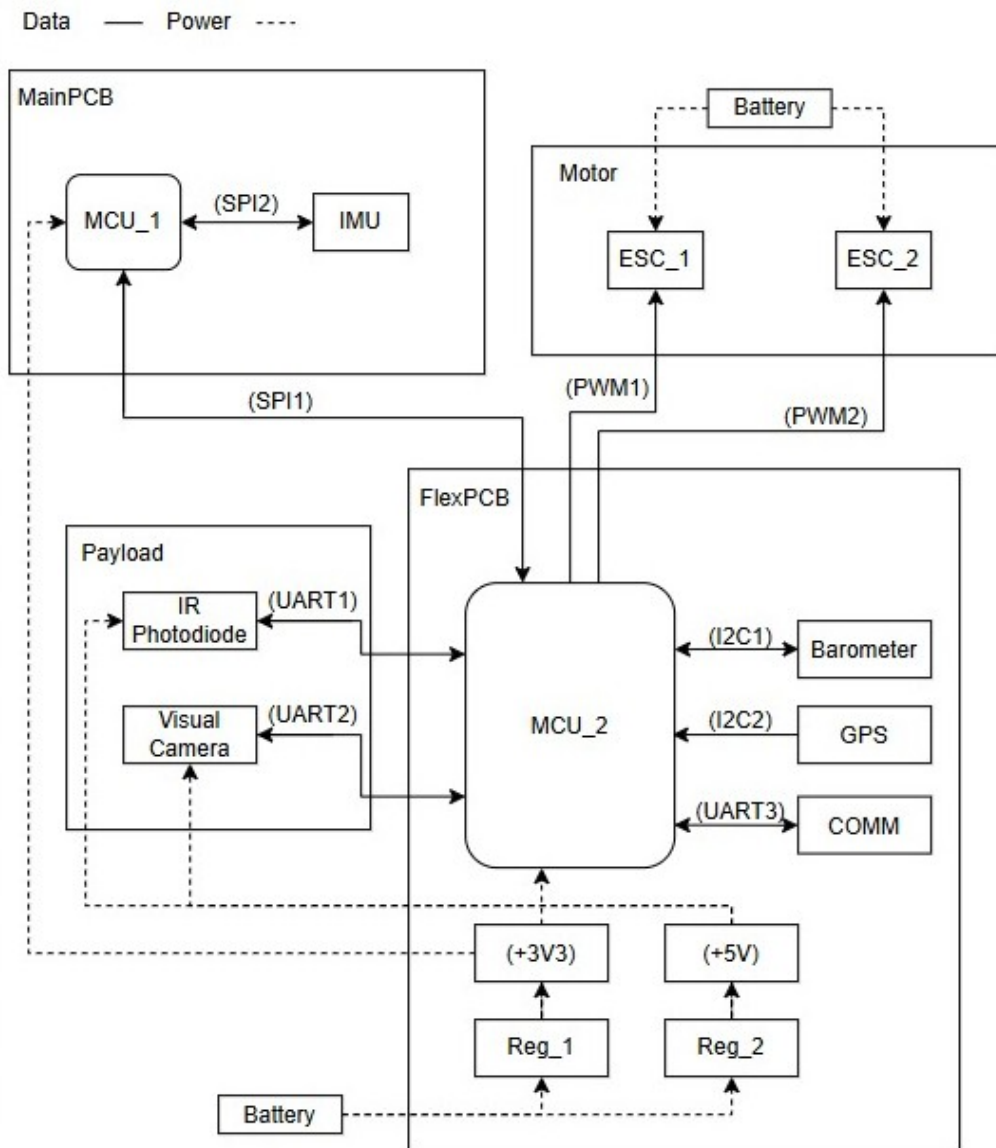


Figure 11.4: Data and power flow diagram, this diagram highlights the connections between the different subsystems involved in the electrical design in terms of both data flow and power flow.

### 11.2.2. Component selection

An accurate state estimation of the L.O.R.A.X. drone relies on carefully selected components. Therefore, four different subsystems were examined and matched with components that best meet the drone's performance requirements and environmental constraints.

#### MCU

As seen in Figure 11.4, a dual-microcontroller architecture was selected to distribute processing tasks and optimise peripheral access. The Main PCB features an STM32F411CEU6, chosen for its efficient Cortex-M4 core, suitable for dedicated high-frequency IMU data acquisition via SPI and serving as an SPI slave to the primary flight controller (FlexPCB). The FlexPCB integrates a more powerful STM32F405RGT6, selected for its richer peripheral set, higher performance capabilities (including FPU), and greater pin count necessary to manage overall flight control, sensor fusion (GPS, barometer, IR array), Wi-Fi communications (ESP8266), ESC control, and multiple payload interfaces. This division allows each MCU to focus on specialised tasks effectively.

#### IMU

The IMU selected was the TDK ICM20948.<sup>10</sup> This is motivated by the fact that a 9-axis IMU was necessary to get accurate state estimation of the body, as it would be difficult to measure the dynamics of the states of such a high-spin body with a simpler configuration. The refresh rate for the gyroscope and accelerometer configurable

<sup>10</sup>TDK InvenSense, ICM-20948 Datasheet. Available at: <https://invensense.tdk.com/wp-content/uploads/2016/06/DS-000189-ICM-20948-v1.3.pdf> (accessed 05/06/2025)

up to 1125 Hz is beneficial for the high spin context. The magnetometer has a 100 Hz refresh rate. It also boasts a low power consumption of 2.5 mW.

Of course, the use of sensors brings noise and biases into a system that need to be taken into account. These were modelled using MATLAB, specifically with aid from the documentation and functions available in the Navigation toolbox.<sup>11</sup> The implementation is discussed in subsection 11.2.3.

### GPS module+ Antenna

The GPS system chosen consists of the RXM-GPS-SR module together with the ANT-GNFPC-SHL1 Flexible Omnidirectional Antenna. The omnidirectional antenna was chosen as with consistent gain in all three axes, which will show strong reception during the full revolution of the body, whereas a typical patch antenna would exhibit signal dropout at points in the revolution facing downwards when placed on a rotating body. It also has the benefit of only weighing 0.4 g. The module has an update rate of 1 Hz.

### Barometer

A BMP180 digital barometric pressure sensor is integrated onto the Flex PCB to provide crucial altitude data for flight stabilisation and navigation. Selected for its small footprint, low power consumption, and I2C interface, it allows the STM32F405 flight controller to accurately measure atmospheric pressure. This data is then processed to estimate relative altitude changes and can be fused with GPS and IMU readings for enhanced vertical position hold and altitude-dependent flight manoeuvres. The sensor is locally decoupled and interfaced via the I2C1 bus. Note that due to the fact that the BMP180 is obsolete, its successor, BMP390, should be integrated in the next revision.

### 11.2.3. Sensor Fusion & Filtering

To model sensor data, the IMU is modelled using the 'imuSensor' function in MATLAB, where specifications of the gyroscope, accelerometer and magnetometer in the IMU could then be defined (e.g. Measurement range, Constant Bias, Noise Density, Axes misalignment).

A trajectory is then constructed, defined according to the flight conditions to be expected for the drone. Integration with the main drone simulation, including the flight controller, was not possible due to time constraints. Therefore, two trajectories are considered to mimic expected scenarios during flight, shown in Figure 9.41:

- Straight horizontal flight ran for 60s.  $V = 20$  m/s, Spin rate = 7 Hz, Pitch =  $6^\circ$ . The cruise velocity is selected from Table 9.1
- Turning flight. A constant radius turn is assumed with Yaw rate =  $2.5^\circ$ /sec for a full 360-degree revolution. Spin rate = 7 Hz, Pitch =  $8^\circ$ . The drone is also simulated with a constant rate of climb (RoC) of 0.3m/s. (Note: The yaw rate simulated is not the same as that to be expected for  $8^\circ$  pitch in Figure 9.41, as the simulation was ran with older steady state conditions. The updated rate is smaller ( $\approx 0.4^\circ$ /sec than the  $2.5^\circ$ /sec simulated, which should not be an issue for the state estimation sensors+filter as the dynamics of the drone are changing at a slower rate.)

The IMU function takes acceleration, angular velocity, and orientation inputs of the ground-truth defined trajectory and 'corrupts' it, applying its noise, biases, etc.

Sensor filtering is then performed with the 'insfilterAsync', the basis of which is an Extended Kalman Filter (EKF) fusing sensor data asynchronously (accelerometer and gyroscope @1125Hz, magnetometer @ 100Hz, and GPS data @1Hz) to estimate position and orientation. ted, such as a complementary filter, but proved insufficient for state estimation of our high-spin system. The EKF that the insfilterAsync uses performs better as it is a much more effective and configurable way of combining dynamic models with multiple sensors. It can capture non-linear dynamics via local linearization and keeps track of a lot more states<sup>12</sup>, but the exact details of why it performs better are beyond the scope of this report.

### Filter Tuning

In the implementation of the EKF, key tunable parameters include the process noise and the measurement noise. These parameters significantly influence the filter's responsiveness and stability. Measurement noise is defined from the specification of the ICM 20948, whilst the process noise was manually tuned. The general approach involved iterative adjustments based on qualitative feedback from the Pose Viewer. By observing the response of the estimated versus actual orientation in the drone's trajectory, the parameters could be tuned accordingly,

<sup>11</sup>Mathworks, Navigation Toolbox. Available at: [https://nl.mathworks.com/help/nav/index.html?s\\_tid=CRUX\\_topnav](https://nl.mathworks.com/help/nav/index.html?s_tid=CRUX_topnav) (accessed 05/06/2025)

<sup>12</sup>Phil's Lab, Sensor Fusion and Kalman Filters Explained - Part 3. Available at: <https://www.youtube.com/watch?v=hQUkiC5o0JI&list=PLoaD3DF6-tZl1trEfsVW9tx4CO0SMSMKg&index=3> (accessed 05/06/2025)

depending on what the discrepancy was, such as high noise or drift: basically striking a balance between responsiveness to dynamics and robustness against sensor noise. Due to time constraints, a proper automated tuning method using, for example, a gradient descent algorithm was not implemented.

Additionally, a 1-second trailing moving average is applied to the sensor data, as even after post-filtering, the data remained highly noisy. This will be stored in memory on the onboard MCU.

## Results

The results for two trajectories are shown below in [Figure 11.7](#) and [Figure 11.8](#). The error is plotted both raw (as in post-filter) over time and smoothed, using a 1-second trailing moving average, shown in [Figure 11.7a](#) and [Figure 11.7b](#). The smoothed error is also represented as a Gaussian distribution in figures [Figure 11.7c](#) and [Figure 11.7e](#) with corresponding  $\mu$  and  $\sigma$ .

To assess whether the selected sensor system is sufficient, we should better analyse the Gaussian distribution errors. Pitch angle during straight flight shows a very low mean error with  $\mu = -0.0143^\circ$  as well as during turning flight  $\mu = -0.3665^\circ$ , suggesting that the estimation error is purely due to noise, still not fully captured by the EKF. It should be noted though, that the filter struggled at some points in the turning simulation shown in [Figure 11.8a](#), specifically around  $\approx 40$  s and  $\approx 110$  s, suggesting a need for better tuning of the EKF.

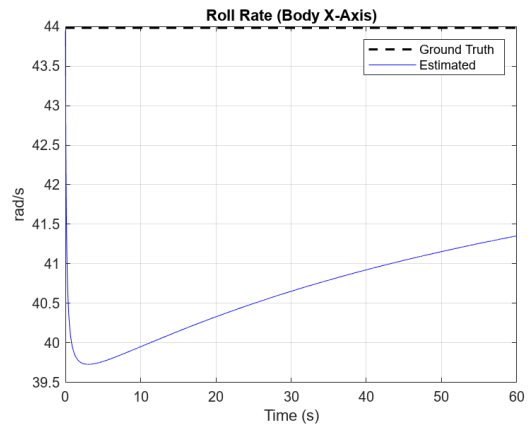
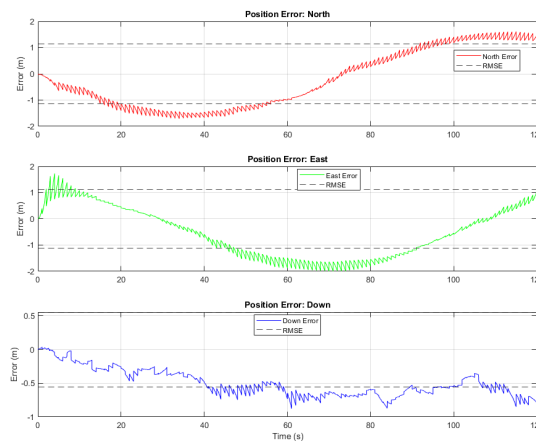


Figure 11.5: Roll rate estimate



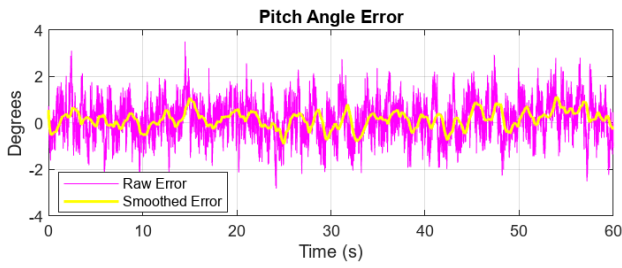
Position error

Figure 11.6: Position error during turning flight (limiting case).

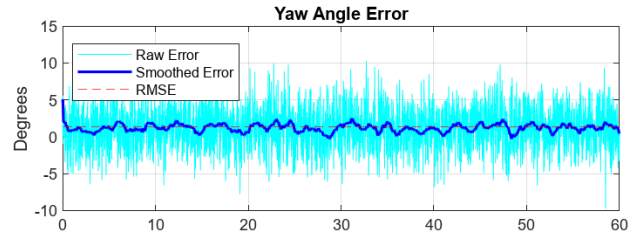
The yaw angle also exhibits relatively low error. However, a small constant bias is seen in both straight and turning simulations, with  $\mu = 1.0804^\circ$  and  $\mu = 1.0474^\circ$  respectively. This suggests a small but constant bias that is prevalent but not captured by the EKF. Again, further tuning is required to remove this, most likely tuning the magnetometer, although it is not a big error. An error in yaw estimation is also less important for the flight control algorithm, as pitch is the primary attitude angle determining the dynamic evolution of states during flight (changing pitch = changing lift).

The last important state that the sensors must accurately estimate for flight performance and stability of the drone is the spin rate. The computed spin rate during the simulation is shown in [Figure 11.5](#). The current IMU + filtering setup is not sufficient, most likely due to gyroscope saturation, as it is only rated for 34.9 rad/s. The estimate is slowly recovering to the actual  $\approx 44$  rad/s spin rate; however, over 60 seconds of flight, the estimate is still around 6% off. This suggests a need to modify the current setup, which will be discussed in the Limitations and Recommendations subsection.

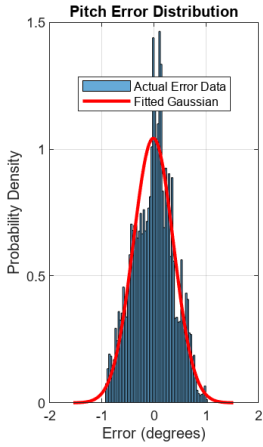
The position + velocity estimate was found to be sufficient with just the GPS + IMU configuration, with North/East error very slowly oscillating between  $\pm 2$  m and altitude error drifting by 1 metre over 2 minutes. It should be noted that the EKF is currently fusing without measurements from the barometer, giving an absolute altitude reading that would correct for the drift. These results are also shown in [Figure 11.6](#).



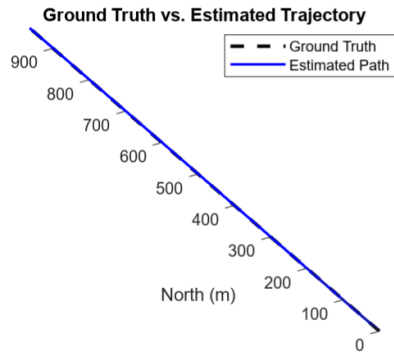
(a) Pitch angle estimation error for a horizontal straight path with constant pitch angle = 8°. The raw error is plotted after filtering, as well as a smoothed 1-second (1125 samples @ 1125 Hz) trailing moving average line.



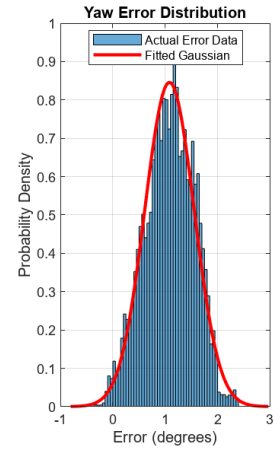
(b) Yaw angle estimation error for the same horizontal straight path with constant pitch angle = 8° and no sideslip. The raw error is plotted after filtering, as well as a smoothed moving average line.



(c) Pitch error distribution straight flight:  $\mu = -0.0143^\circ$ ,  $\sigma = 0.3826^\circ$

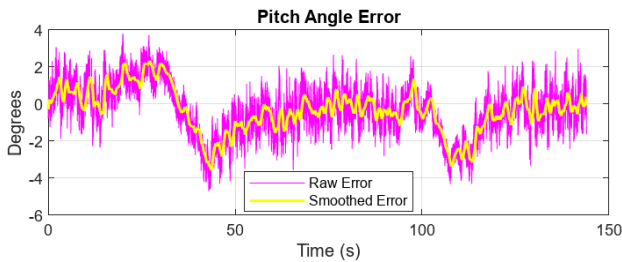


(d) Straight Path trajectory versus estimated (via GPS and accelerometer fusion)

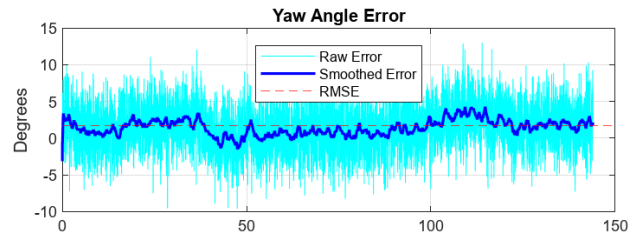


(e) Yaw error distribution straight flight:  $\mu = 1.0804^\circ$ ,  $\sigma = 0.4717^\circ$

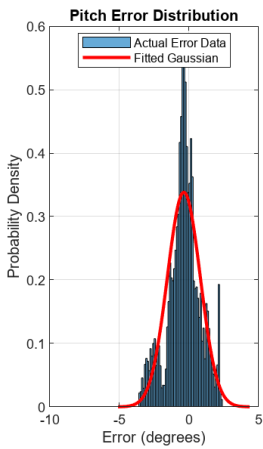
Figure 11.7: Straight-path orientation estimation errors (top) and corresponding error distributions + trajectory visualization (bottom).



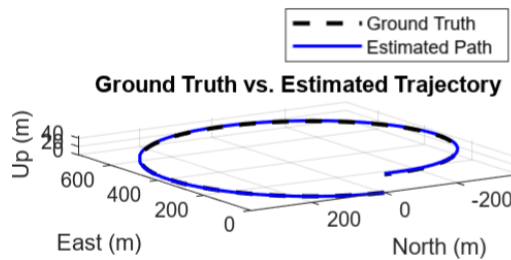
(a) Pitch angle estimation error for a 2.5°/s path with constant pitch angle = 8°. Raw error as well as a smoothed 1-second (1125 samples @ 1125 Hz) trailing moving average line are plotted.



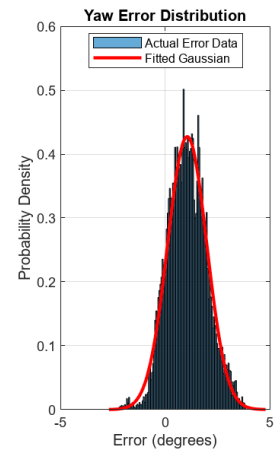
(b) Yaw angle estimation error for the turning flight. The raw error is plotted after filtering, as well as a smoothed moving average line.



(c) Pitch error distribution turning flight:  $\mu = -0.3665^\circ$ ,  $\sigma = 1.1797^\circ$



(d) Turning path trajectory versus estimated (via GPS and accelerometer fusion)



(e) Yaw error distribution turning flight:  $\mu = 1.0474^\circ$ ,  $\sigma = 0.9338^\circ$

Figure 11.8: Turning-maneuvre orientation estimation errors (top) and corresponding error distributions + trajectory visualization (bottom).

### Limitations and Recommendations

As mentioned before, a better estimation of the spinning motion is required. This can be done via a gyroscope with greater range, although almost all light-weight COTS IMUs are only rated for a maximum of 34.9 rad/sec. Another possible option is to incorporate the use of the infrared payload sensor for attitude estimation, specifically for spin estimation. This approach has been taken by Xu et al. for a spinning projectile's attitude measurement with LW infrared radiation under sea-sky background[40]. The implementation of this in a forest wildfire context may be more complex, though, as there is not a mostly constant signal from the sea surface but a highly varying signal due to thermal variation in wildfire.

Moreover, in order to get a definitive answer on whether the selected sensors and filter combination are sufficient to keep the drone in stable flight along its desired trajectory, a proper implementation of the model, together with the flight controller, is necessary. Due to the limited time and resources available, we were, however, not able to fuse these two. Combining the two models would show whether the control inputs given due to slightly inaccurate sensor readings could lead to pushing the drone off-course and/or into unstable flight. This could be done by sampling the Gaussian error distributions onto the true system state orientation (figures 11.7c, 11.7e, 11.8c and 11.8e) into the flight controller and seeing whether the drone is pushed off course.

Another recommendation is the implementation of a more representative temperature during the mission, which affects the sensitivity and biases of the accelerometer and gyroscope. Proper modelling of this would be performed by combining the sensor fusion simulation with the current temperature at drone altitude as modelled by the generated wildfire map. The current assumption of ambient temperature at the cruise height is considered valid for the scope of the project, justified by the high cruise altitude of around 270m for detector nodes. The effect of varying temperature may need proper modelling for confirmation of nodes flying closer to hotspots.

The model also assumes ideal sensor placement, so at the CG and therefore the centre of rotation of the drone. The effect of centripetal acceleration on the accelerometer is therefore not modelled. In reality, the IMU is placed on the PCB at the centre of the drone, so the offset is still very small ( $\approx 5mm$ ), but present. Potential magnetic disturbances caused by the brushless motors are also not considered on the magnetometer. Therefore during testing the magnetic field inside the drone should be mapped such that this effect can be compensated for to properly tune the filter.

### 11.2.4. PCB design

As outlined in the data/power flow diagram, three customised PCBs are made being referred to as the MainPCB, FlexPCB and IrPCB. Note that due to space constraints posed by the thickness of the airfoil, the camera module chosen would not fit and therefore, a customised camera module is necessary, but it would rather be just a modified version and not included in the current iteration.

#### FlexPCB

The Flex PCB (FPC) is the drone's core avionics board, designed for a compact, curved fit as shown in Figure 11.9. It hosts an STM32F405 MCU for flight control and sensor processing. Power management includes LiPo input protection, a 3.3V buck converter, a 5V LDO, and battery sensing. Integrated sensors comprise a GPS and a barometer. An ESP8266 enables Wi-Fi telemetry. The FPC directly controls two ESCs and interfaces with the main MCU/IMU board via SPI. Modular payload connectors support an external InGaAs photodiode array (requiring off-board TIA/MUX) and other sensors. Design emphasises component survivability under 20g and robust power/signal integrity.

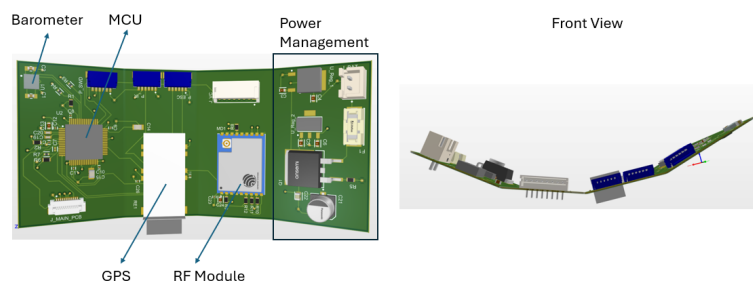


**Figure 11.9:** Top and front view of the FlexPCB, which serves as the core PCB of the drone and houses the majority of the avionics. The schematic could be found in section 17.2. The FlexPCB has a 2D dimension of 10cm x 4.5cm, and an accumulated curvature of 180 degrees posed by the space constraint of the airframe.

The connectors' pin specifications could be seen in Figure 11.10. And Figure 11.11 shows the layer stack structure of the flex-rigid PCBs.

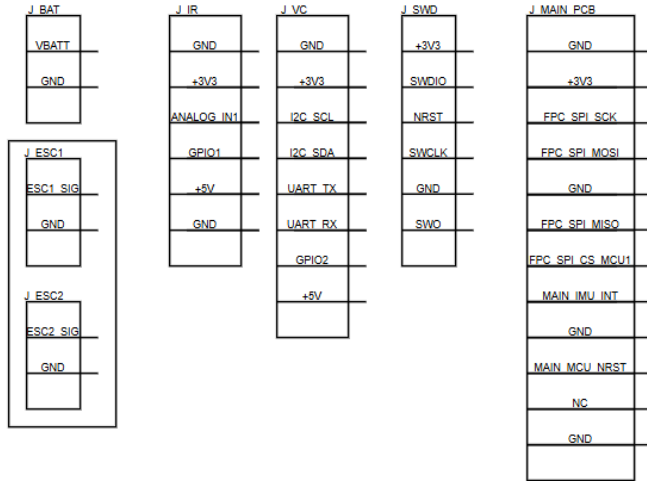


**Figure 11.10:** Connector pins of the FlexPCB. Each block represents a connector on the FlexPCB. Wires must be connected to the designated pins. J\_BAT connects to the battery terminal; J\_ESC connects to the ESC board; J\_VC connects to the visual camera board; J\_SWD is for debugging and programming; J\_MAIN\_PCB is to connect to the MainPCB.

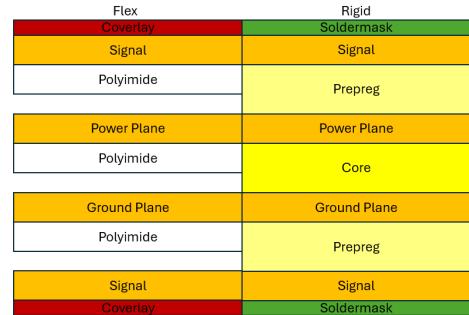


**Figure 11.11:** Layer stack of the rigid-flex PCB, the flex and rigid sections both contain four layers with different insulation materials.

**MainPCB**

The Main PCB is a compact, rigid board serving as the drone’s primary inertial sensing and co-processing unit, centrally located for optimal IMU performance. It features an STM32F411CEU6 microcontroller dedicated to processing data from the onboard ICM-20948 9-axis IMU. This processed inertial data is then transmitted to the Flex PCB’s main flight controller via a dedicated high-speed SPI link. The Main PCB receives its +3.3V power and ground from the Flex PCB through a board-to-board connector, ensuring a tightly integrated system for robust flight stabilisation and navigation.

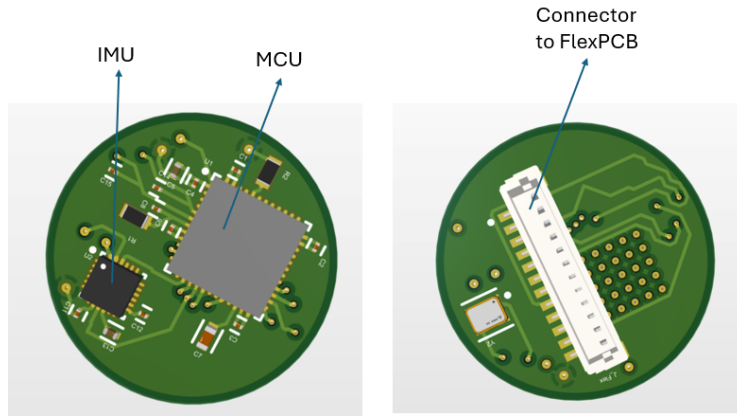


**Figure 11.12:** Front and back view of the MainPCB, this serves solely as a processor of the IMU information. The schematic could be found in section 17.2. The MainPCB has a 2D dimension of 2 cm in diameter.

**IrPCB**

The IrPCB is a demonstration module for the proposed 16-pin InGaAs linear IR photodiode (Only 8 pins demonstrated on the board). Signals from these photodiodes are managed onboard by two analogue multiplexers, which route selected channels to two dedicated transimpedance amplifier (TIA) circuits. This configuration provides two amplified analogue outputs, representing sequential pairs of the photodiode array, to the FlexPCB via a connector.

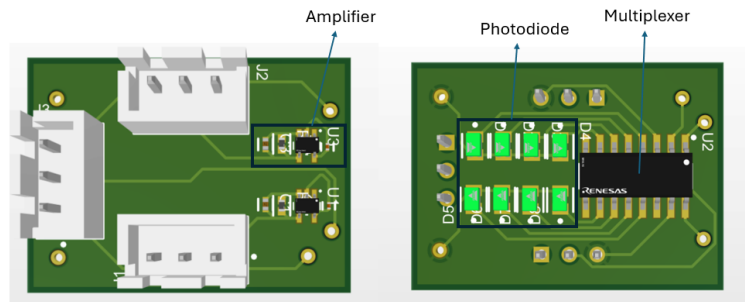


**Figure 11.13:** Front and back view of the demonstration board of the IrPCB, which serves as a potential board for the IR photodiode. The schematic could be found in [section 17.2](#). The IrPCB has a 2D dimension of 1cm x 2cm.

### Internal Link Budget

[Table 11.4](#) presents the internal link budget, showing the communication setup between each master and slave in the system. It is clearly seen that all chosen protocols provide data rates well above the minimum required for their respective connections. Synchronous protocols like SPI and I2C, which use a dedicated clock line, offer very high margins because they operate at high clock frequencies relative to the data they need to transfer. In contrast, asynchronous protocols like UART, which rely on internal timing and include overhead bits, show more moderate margins, but still sufficient to ensure stable communication. This confirms that all internal links are appropriately configured with safe bandwidth headroom.

**Table 11.4:** Final Internal Link Budget, showing protocols used, configured speed and required data rate. Margin on required data rate is given to show feasibility (should be above 1).

Final Internal Link Budget					
Master	Slave	Protocol	Configured Speed	Data Rate (kbps)	Margin
MCU1	IMU	SPI	5 MHz	128	39x
MCU2	MCU1	SPI	5 MHz	160	31x
MCU2	GPS	UART	57,600 bit/s	30	1.9x
MCU2	ESP8266	UART	115,200 bit/s	64	1.8x
MCU2	BMP180	I2C	400 kHz	3	133x
MCU2	ESC	Dshot	600,000 bit/s	256	2.3x
MCU2	TIA	ADC	1 MSPS	768	10x

### Recommendations for PCB

The three customised PCBs are all in their second version, and the layout is still far from perfect. Thus, a list of actions is proposed to be taken before the PCBs can be fully functional and sent for fabrication. A common improvement that should be implemented first is to establish a more detailed and specific Design Rule Check (DRC) profile in Altium, tailored to the FPC/Rigid-Flex manufacturing process and ensuring all component footprint and clearance requirements are met. This comprehensive DRC validation is not fully completed in the current version. Meanwhile, some unused pins are still unconnected, as there may still be improvements or adjustments to the pin assignment. Therefore, the unconnected pins must be addressed according to their specific data sheet in the fabrication version. And it would be nice to spend some time rearranging the net labels and component designators to make it clearer. A last recommendation is to check the strain relief of all connectors to ensure the wire doesn't fall out during operation.

For the MainPCB, first review the necessity of both the HSE and the LSE crystals for the MCU1. It is possible to omit the LSE if precise RTC or USB functionality is not required on this MCU, and omit the HSE if running on HSI of the STM32 itself suffices. And consider adding test pads for key signals to facilitate debugging and verifications in hardware revisions. Meanwhile, there has been no mechanical analysis performed on the rigidity of the PCB and the strain relief of the connectors at the moment, which might be useful to consider.

For the FlexPCB, once the camera PCB design is made or known, it is recommended to check if the LDO would still reliably supply power or if a switching back converter should be used instead. Note that in further iterations, if the capacitor is to be changed for whatever reason, a ceramic capacitor must be used instead of an electrolytic bulk capacitor; this is due to the high-G environment of the FlexPCB. Since this PCB is flexible, it would be crucial to discuss the detailed design with the manufacturer and improve the design based on their production

requirements. Also, the current antenna is a patch antenna, which is an integrated part of the chosen GPS modules; this might be replaced if another antenna is to be used (Which might mean replacing the entire antenna module). Lastly, the current flexible part has four copper layers exactly like the rigid part, which leads to a maximum static bend angle of around 6 degrees and a dynamic bend angle of around 4 degrees. It would be a good improvement to reduce the number of layers of the flexible section, which would allow a higher degree of flexibility. The potential layers to be removed are the two power layers, but then there have to be connections established to pass the power source between sections of rigid parts.

For the IrPCB, the next step is to obtain the footprint from the manufacturer and finish the real schematic, and investigate how many amplifier circuits are necessary and choose the right multiplexer. For the camera module, the current one is not directly compatible with the MCU. This shall be taken into account when making or requesting modifications to the current selected camera module.

### 11.3. Noise Estimation

To comply with STK02-MIS19-SYS29, the noise level emitted by the drone must be investigated. For the purposes of this design, a simplified analysis based on numerical methods developed by NASA[19] is used. For this investigation, it is assumed that the propellers are the dominant noise source in the system.

The generated noise is assessed in three parts. First, harmonic noise sources, including *thickness noise*, which is caused by the physical displacement of air as the propeller blades rotate, and *steady loading noise*, which results from the constant aerodynamic forces acting on the blades. Second, unsteady noise, which is divided into *unsteady loading noise* due to time-varying inflow conditions, and *broadband noise* produced by turbulent interactions near the blade surfaces. Lastly, the effects on propagation due to shielding and other effects are assessed.

Due to the contra-rotating propeller setup, the investigation of the noise becomes more complex, as the second propeller experiences interference from the first. This effect is not taken into account in these calculations. So the SPL is only modelled as two independent propellers.

This numerical method can be reduced to the following formulae:

$$\text{SPL} = 20 \log_{10} \left[ \frac{538\,673 \cdot m_B \cdot M_x \cdot \sin \theta}{y \cdot D \cdot (1 - M_x \cos \theta)} \left( \frac{\cos \theta}{1 - M_x \cos \theta} T - \frac{550}{z_{\text{eff}}^2 M_c^2 C_0} W \right) \Psi_L J_{m_B} \right] \quad (11.3)$$

$$\text{OASPL} = 10 \log_{10} \left( M^5 \cdot \frac{\delta^* s}{r_e^2} \cdot D \right) + K_1 \quad (11.4)$$

$$\text{SPL}_{1/3} = \text{OASPL} + 10 \log_{10} \left\{ 0.613 \left( \frac{\tilde{\omega}}{\tilde{\omega}_{\text{max}}} \right)^4 \left[ \left( \frac{\tilde{\omega}}{\tilde{\omega}_{\text{max}}} \right)^{3/2} + 0.5 \right]^{-4} \right\} \quad (11.5)$$

The equations presented above provide a structured breakdown of the drone's propeller noise emissions. Equation 11.3 estimates the sound pressure level (SPL) resulting from harmonic noise mechanisms, combining contributions from blade loading, thickness effects, and observer geometry. Key parameters include the blade passage frequency harmonic  $m_B$ , Mach numbers  $M_x$  and  $M_c$ , and the directivity function  $\Psi_L$ . The Bessel function  $J_{m_B}$  accounts for tonal content at specific frequencies.

Equation 11.4 provides the Overall Sound Pressure Level (OASPL), which integrates all broadband and tonal contributions into a single scalar value. It captures the dependency on propeller tip Mach number, source strength, and distance to the observer, with  $K_1$  as an empirical offset based on fitting. Finally, Equation 11.5 takes the OASPL and adds a contribution as a function of the normalised rotational frequency.

The requirement specifies a maximum noise intensity of 35 dB at a distance of 150 m. This translates to, at 1 m, a noise intensity of 78.5 dB. Table 11.5 shows the results of the investigations using Equation 11.3, 11.5 and 11.4.

Table 11.5: Sound Pressure Level Breakdown for Each Noise Component and Total SPL

Configuration	Harmonic Eq. (11.3) [dB]	OASPL Eq. (11.4) [dB]	1/3 Octave Eq. (11.5) [dB]	Total SPL [dB]	Reference Limit [dB]
Noise intensity	60.9	45.2	22.8	61	78.5

As can clearly be seen in Table 11.5, the total SPL found is far below the reference limit imposed by requirement STK02-MIS19-SYS29. This number is also largely conservative, as the propeller noise is shielded by the outside

body of the drone. This means that in practice, at 150 m, the noise level will be below 35 dB. With the margin of 17.5 dB, the assumption of discarding the noise contribution of the interference between the two counter-rotating propellers is deemed valid for the purpose of meeting the noise requirement.

## 11.4. Launching System

In addition to the drone node design, as referred to by requirement **STK01-MIS24** given in [chapter 5](#), the drone nodes shall be deployed from an In-Air Launch Unit. Hence, in this section, the complete design of the launching system is provided.

The launching system is required to be able to deploy each drone with a rotational speed of 7 Hz, to ensure gyroscopic stability already from the launch state. Moreover, the drones are launched along the airspeed with no initial side-slip or angle of attack. However, because the design of the mother-ship is out of the scope of the project and the cruise speed is unknown, the swarm of cylinders are launched in line, one after the other and in the opposite direction to the flight of the mother-ship. This ensures that the drones do not collide with the mother ship.

The main design consists of a launching tube with an inner diameter of 220 mm and 2 mm of thickness. This tube has a length of 1100 mm, as to fit a swarm of 10 drones longitudinally, allowing for a margin of 1 cm of space between each drone, which can be visualised in [Figure 11.14](#). To achieve the nominal spin rate of each drone, each drone is accelerated sequentially, by using its respective propulsive system at maximum thrust and torque, shown in [subsection 9.2.2](#). After one of the drones is launched, the next one is accelerated and translated to the launching point (i.e. the fixed point before the deployment and separation from the mother-ship). However, whilst the drone accelerates to get to its target rotational velocity, its position shall be fixed at the launching point. Hence, a system of 6 wheels is implemented, which will constrain the translational motion of any drone located at the front of the launching system, but it will allow the cylinder to spin freely, rolling without slip with respect to the wheel system. Such a system can be appreciated in [Figure 11.14](#). Moreover, by making use of wheels, we comply with the requirement that there will be no friction from the tube that would remove material from the drone, which would decrease its reliability.

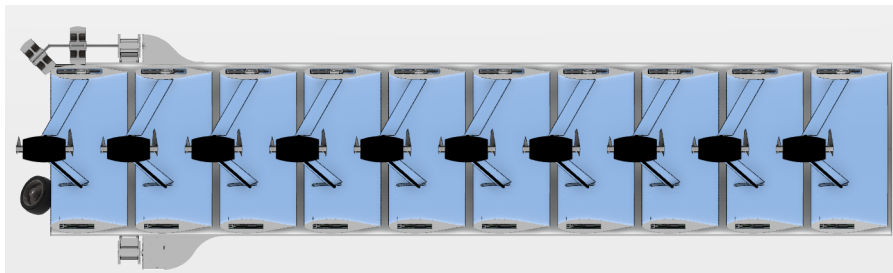


**Figure 11.14:** Cross-section visualisation of the launch system with a swarm of 10 drones, showing 1 cm of space between each node. From this reference, the left side of the tube is the launching point from which each drone is deployed sequentially. A system of wheels is also shown, which is used to fix the position of the launching drone without limiting its rotation.

### 11.4.1. Wheel System Design

3 sets of castor wheel systems allow the drone to rotate while constraining its motion. Each set has 2 wheels, one with its rotational axis being parallel to the longitudinal axis of the cylinder and the other wheel at a 45° angle, as seen in [Figure 11.15](#). The angled wheel has the function of blocking the translational motion of the cylindrical body without constraining its rotation, while the wheel that has its longitudinal axis parallel to the tube allows the drone to rotate without causing friction with the launch tube. Each set of wheels is separated by 120° from the other. The wheels used are 50 mm in diameter and 19 mm wide<sup>13</sup> and have 4mm x 8mm x 3mm ball bearings with a pressure fit connection, one at each edge of the wheel<sup>14</sup>.

To ensure that the drone could accelerate by using its torque. The static friction was computed for the ball bearing systems by using [Equation 11.6](#). A conservative static friction coefficient of 0.02 is considered, taking into account that most ball bearings have a friction of one order of magnitude lower<sup>15</sup>.

<sup>13</sup>50mm x 19mm Industrial Castor Wheels - Dark Grey Synthetic Rubber. Available at: <https://www.accu.co.uk/industrial-castor-wheels/588462-HICW-50-19-8-R-GR> (accessed 16/06/2025)

<sup>14</sup>Axial 4mm x 8mm x 3mm Ball Bearing (2) - AXI237003. Available at: <https://www.toemen.nl/product/axial-4mm-x-8mm-x-3mm-ball-bearing-2-axi237003?gQT=1> (accessed 16/06/2025)

<sup>15</sup>TOC of Basic Bearing Knowledge. Available at: <https://koyo.jtekt.co.jp/en/support/bearing-knowledge/8-4000.html> (accessed 16/06/2025)

$$M = \mu \cdot P \cdot \frac{d}{2} \quad (11.6)$$

Whereby  $\mu$ ,  $P$ ,  $d$  are the static friction, normal load on the bearing and bore diameter of the bearing, respectively, and  $M$  is the moment friction. For the wheels that are at an angle, the load applied on the bearing is the normal component of the take-off thrust of the drone (which is being held in place), which is  $\cos(45) \cdot 1.615 = 1.142$  N. For the non-angled wheels, the maximum conservative load is the weight force of the drone, resulting in  $0.250 \cdot 9.81 = 2.4525$  N (Note that the limit mass of 250 grams established in the requirements is assumed, which is a conservative approach). Thus, by adding these two components, a total friction of  $-4.313 \cdot 10^{-4}$  N·m.

Furthermore, by assuming a no-slip roll condition of the wheels and the wing body, and knowing the mass moments of inertia of the components computed in the 3D model in CATIA, it is known that for a take-off torque of 0.158 N·m (which is retrieved from subsection 9.2.2), a torque of  $3.618 \cdot 10^{-3}$  N·m is induced on the wheels. With that being said, the total launch torque of the drone is  $3.186 \cdot 10^{-3}$  N·m. This means that the system can be launched solely using the maximum propulsive thrust and torque from the drone, resulting in an angular acceleration of 13.916 rad/s. This means that each drone would take at least 3.16 s. Assuming that, on average, each drone takes time from when it turns on the propeller until it reaches the launch point, and rounding the time to 5 seconds per drone, the total time for the system to launch the complete swarm is 50 seconds, allowing for a wide operational margin, taking into account that requirement SUB-LAU-2 establishes a maximum of 150 seconds for the total launch time (as stated in chapter 5).

Additionally, the thrust force of the drone generates a bending moment on the angled section of the rod. Taking into account that the rod diameter is equal to the bore diameter of the bearings (which is 4 mm) as they have a tight fit connection, and retrieving the length of the angled section of the rod from Figure 11.15, the problem was simplified to the free body diagram shown in Figure 11.16. The blue arrow force has previously been calculated to be  $\cos(45) \cdot 1.615 = 1.142$  N. With that being said, the maximum bending moment of the rod was computed, and hence, by using the flexure formula, a total bending moment of 3.99 MPa was computed. Note that the rods are made of Aluminium Alloy 6061, and from section 11.1 it is known that the maximum yield stress is approximately 330 MPa. Hence, it is safe to say that the current dimensions of the rod can withstand the bending with a significantly wide margin.

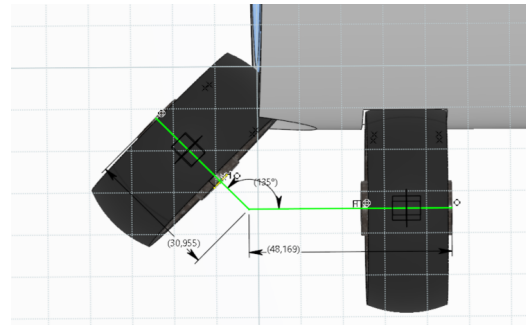


Figure 11.15: Wheel system visualisation and dimensions of one out of the 3 arms. Each wheel is rounded at the edge and has a normal contact with the wing body surface. The length of each rod is given in mm.

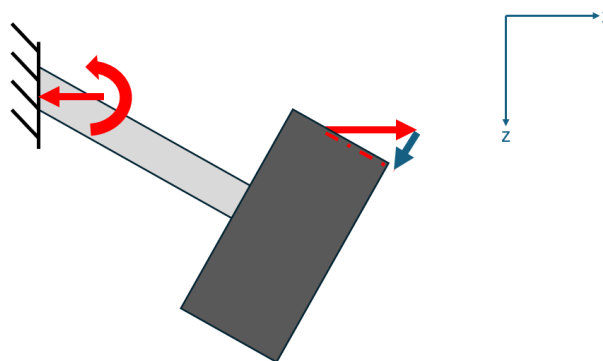


Figure 11.16: Freebody diagram of the thrust of the drone applied to the angled wheel. The red arrows show the applied forces and the reaction forces and moment, while the blue arrow represents the normal component of the thrust force applied by the drone.

#### 11.4.2. Gear System Design and Servomotor Selection

The wheel systems must be able to rotate about the central axis to deploy the launched drone. To do so, each wheel system is attached to a small pulley gear of 24.4 mm in diameter. These are connected to a ring gear of 243.96 mm in diameter pitch. Finally, a torque must be provided to the central gear with the use of a servo motor clamped on top of the tube and attached to another 24.4 mm in diameter pulley gear. The gear system can be seen in Figure 11.17. By using a gear system, the total cost can be decreased as only one servomotor will be necessary to rotate the three arms. These dimensions were chosen in order for the sum of both pitch radii to

be equal to the radius at which the rotation axis of each wheel system is located. Moreover, a 0.1 ratio between both radii was chosen, and thus, by using Equation 11.7, 120 teeth were selected for the ring gear and 12 teeth were chosen for the smaller pulley gears.

$$\frac{N_1}{N_2} = \frac{r_1}{r_2} \quad (11.7)$$

Note that the central ring gear is not in contact with the tube, as it must be free to rotate. The use of 3 small pulley gears constrains the ring gear's position, allowing it only to rotate. Figure 11.18a and Figure 11.18b show rendered visualisations of the gear-wheel system for the deployed and disengaged wheels, respectively. Each of the pulley gears that are attached to a wheel arm system is tight-fitted to a ball bearing<sup>16</sup>, mounted on the launch tube.

The torque required by the servomotor to actuate the gear system was computed by first calculating the acceleration  $a$  of the cylinder, provided by the maximum thrust (resulting in  $6.46\text{m/s}^2$ ). The distance  $s$  required by the cylinder to leave the launch point was computed to be  $0.0439\text{m}$ , from geometry using CATIA V6. In addition, the angle  $\theta$  required by the wheels to retract from the path of the drone was geometrically determined to be  $106.688^\circ$  (view Figure 11.19). With that being said, the minimum angular acceleration  $\alpha$  that the wheels must perform was computed by using Equation 11.8, resulting in  $274,250\text{rad/s}$ . From the geometry, the mass moment of inertia of the wheel system was calculated about the rotation axis of the arm (resulting in  $2 \cdot 10^{-5}\text{kgm}^2$ ), and hence, the minimum torque was determined to be  $5.5 \cdot 10^{-3}\text{N}\cdot\text{m}$ . Nevertheless, because there are three pulley gears attached to a bearing, the friction caused by the ball bearings was computed using Equation 11.6. The maximum load on these bearings is equal to the weight of the PLA central ring gear, which is  $0.156\text{kg}$ , leading to a friction of  $1.18 \cdot 10^{-3}\text{N}\cdot\text{m}$ . Finally, the total net torque after adding the effects of the bearing friction resulted in  $6.68 \cdot 10^{-3}\text{N}\cdot\text{m}$ .

$$\frac{s}{a} = \frac{\theta}{\alpha} \quad (11.8)$$

### Servo Motor Selection

By knowing the nominal torque of  $6.68 \cdot 10^{-3}\text{N}\cdot\text{m}$ , the servomotor could be sized, such that it could provide a higher nominal torque. In the end, the MS4005 V2 Servo Motor from the company SMC Powers. Table 11.6 shows the main specifications of the motor. Finally, to be able to actuate this motor, a Raspberry Pi Zero will be used<sup>17</sup>, as the code required to actuate the gear is a simple and timed servo control, so only a few amount of available RAM is required.

Table 11.6: Specifications of MS4005 V2 Servo Motor<sup>18</sup>

Nominal Voltage [V]	12
Nominal Current [A]	0.79
Nominal Torque [N·m]	0.08
Stall Torque [N·m]	0.11
Motor Weight [kg]	0.065

<sup>16</sup>Axial 4mm x 8mm x 3mm Ball Bearing (2) - AXI237003. Available at: <https://www.toemen.nl/product/axial-4mm-x-8mm-x-3mm-ball-bearing-2-axi237003?gQT=1> (accessed 16/06/2025)

<sup>17</sup>Raspberry Pi Zero - 512MB RAM. Available at: <https://www.raspberrypi.com/products/raspberry-pi-zero/>, (Accessed 15/06/2025)

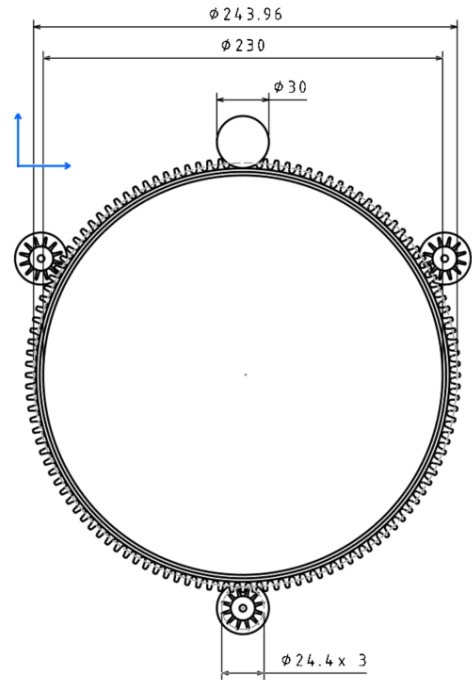
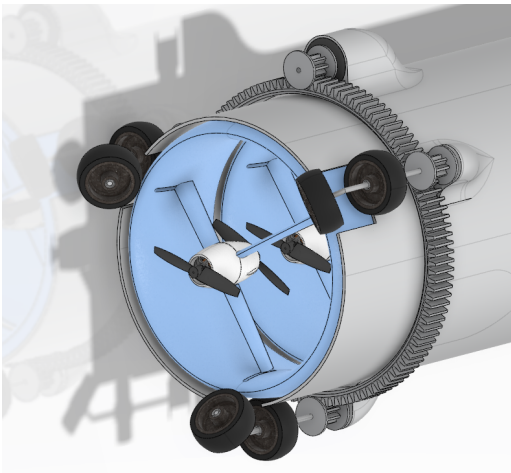
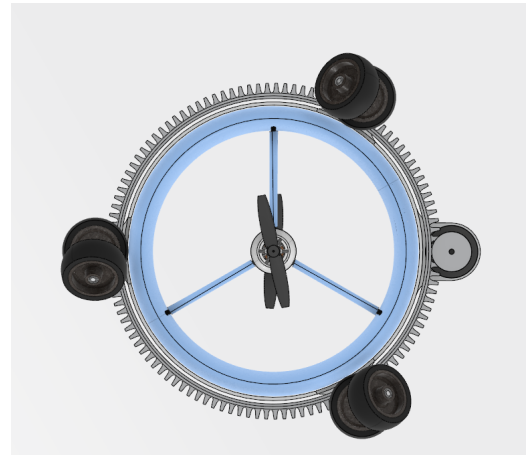


Figure 11.17: Technical Drawing of the gear system, in which a servo motor is clamped to the launching tube. There is one big ring gear centred around the tube. For the remaining small gears, 1 of them rotates about the servo motor, while the others spin about a ball bearing mounted on top of the tube.



(a) Rendered visualisation of deployed wheel system, constraining the motion of the drone.



(b) Rendered visualisation of retracted wheel arms, allowing for the drone to be launched.

Figure 11.18: Rendered visualisations of the wheel-gear system for the launch system.

### Further Recommendations

Although this design has been theoretically proven to be feasible, certain assumptions have been made. The non-angled wheels are assumed to have a low enough friction with the main wing body will be deployed in the axial direction of the tube without having any orientation disturbance, once the angled wheels are retracted. However, there could be asymmetries depending on the normal load of the wheels on the wing body and the friction coefficient of both surfaces. Hence, a recommendation for a further design stage is to implement a design that would slightly retract the non-angled wheels as well. This would ensure a completely free path for the drone at the launch point. Additionally, the code for the Raspberry Pi Zero could be further developed in a subsequent update, and a more detailed study could be conducted on the RAM required.

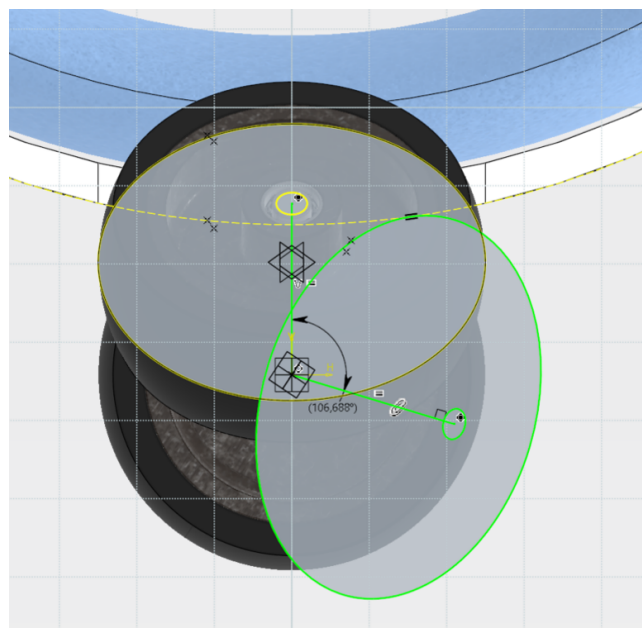


Figure 11.19: Geometrical angle computation for the wheels to fully retract from obstructing the path of the drone.

<sup>18</sup>MS4005 V2 Servo Motor RS485 Driver 2A 15bit 0.08Nm 65g 91KV. Available at: <http://shop.smc-powers.com/MS4005-V2-RS485-15.html?search=MS4005>, (Accessed 11/06/2025)

## 12 Final Design

Having considered all the previous information, the final design of the system is presented in the following chapter. [Appendix F](#) presents the final technical drawing for a single drone node, which includes an exploded view showing all its components. By contrast, [Appendix G](#) shows the final technical drawing for the launching system, with its relevant components marked with balloons as well. Hence, the following chapter covers in detail how each of these components is assembled, referring to [Appendix F](#) and [Appendix G](#). Note that for this final design, the drone node is assumed to include both an infrared and a visual camera; however, due to the modular property, depending on the nodes, they do not need to include both payload components.

Having said that, the final mass for one single drone node resulted in 237 g. This leaves a margin of 5.2% which is used for all cables, screws and nuts. The total mass of the Launcher resulted in 3.52 kg. [Table 12.1](#) and [Table 12.2](#) provide the information for the bill of material and weights for a single and complete drone node, and the launching system, respectively. The ID for each of these tables is the balloon identification within its respective technical drawing, as shown in [Appendix F](#) and [Appendix G](#).

*Table 12.1: Bill of Material for LORAX*

ID	Description	Quantity	Material	Weight [kg]
1	Leading edge airframe (up to maximum thickness)	1	EVA CF65 Foam	0.015
2	Propeller 4x4.5x2	2	Laminate Glass Fibre	0.003
3	Motor E-flight 250	2	N/A	0.014
4	Front motor mount	1	PLA	0.013
5	MainPCB to process and provide IMU information data	1	N/A	0.002
6	Back motor mount	1	PLA	0.013
7	Trailing edge airframe (from maximum thickness of the airfoil)	1	EVA CF65 Foam	0.023
8	Visual Camera	1	N/A	0.015
9	Infrared Camera	1	N/A	0.005
10	FlexPCB to control the motors	1	N/A	0.023
11	Electronic Speed Controller for the motors	2	N/A	0.009
12	Strut connecting motor mount to airframe	3	Carbon Fibre Epoxy	$7.777 \cdot 10^{-4}$
13	Airfoil strut coverage	3	EVA CF65 Foam	$2.834e-4$
14	Sheet metal rail system for the carriage to move along	3	Aluminium Alloy 6061	0.001
15	Carriage connecting the strut to the rail	3	Aluminium Alloy 6061	$4.667e-4$
16	Spring for the carriage to go front and back	3	Spring Steel	$1.467 \cdot 10^{-4}$
17	Battery LPHD4525035	6	N/A	0.008
18	Battery mount	3	Aluminium Alloy 6061	0.002
19	Counterweight to correct the centre of gravity	1	AISI Type 316L stainless steel	0.014

*Table 12.2: Bill of Material for LORAX Launcher*

ID	Description	Quantity	Material	Weight [kg]
1	MS4005 V2 servo motor	1	N/A	0.065
2	Central ring gear	1	PLA	0.156
3	Exterior pulley gear	3	PLA	0.008
4	Rod for with torque control	3	Aluminium alloy 6061	0.005

5	Castor wheel	6	Synthetic rubber and plastic	0.051
6	Ball bearing	15	Stainless steel	$2 \cdot 10^{-4}$
7	Raspberry Pi	1	N/A	0.023
8	Launch tube	1	PVC and glued PLA for mounts	3.066

## 12.1. Drone Final Assembly

### Airframe Group

The main airframe is divided into two main wing sections, the first part goes from the leading edge to the maximum thickness of the NACA63(3)018, while the second section extends to the trailing edge. For each half, there are cutouts to fit in the FlexPCB, the 2 ESCs, the infrared camera, and the visual camera (view the exploded view in [Appendix F](#)). Furthermore, note that the team designed a groove cutout around the leading edge to put a stainless steel toroid section, which is to be used as a counterweight. This counterweight is dependent on the type of modular configuration for the flying gyroscope. The need for this component is to ensure that the final centre of gravity of the drone is centred along the central axis of the cylinder, which ensures a stable spin rate. For the current design configuration (whereby both payload components are included), the centre of gravity was computed from the CATIA V6 software, and it was concluded that a  $26.648^\circ$  toroid section of 14 grams was required. Assuming it is made of AISI Type 316L stainless steel, the diameter of the cross-section would have to be of 7 mm.

Note that the use of foam in the airframe may cause electronic components to heat up, potentially creating a fire hazard. Nevertheless, a solution was implemented whereby 1 mm holes were made from the leading edge to the trailing edge, allowing for air flow and ventilation that cool the inner components (view [Appendix F](#)).

For further development, the system should undergo accurate thermal tests to design holes that can cool the system with minimal drag interference. However, for the given case, an initial estimate was performed to check whether the current system can cool its electronic components. To do so, a derivation from the heat flow equation was applied for cooling electronics with forced airflow [29]. The International Unit System version of the equation is shown in [Equation 12.1](#).  $Q$  is the airflow required to cool the electronic components (in  $[m^3/s]$ ),  $t_i$  is the inlet temperature in [K],  $P_{diss}$  is the dissipated power in [kW],  $\Delta t$  is the temperature difference between the airflow and the electronics systems [K], and  $P_t$  is the total pressure of the air in [Pa].

$$Q = \frac{285.57 \cdot t_i \cdot P_{diss}}{\Delta t \cdot P_t} \quad (12.1)$$

Sea level conditions are considered (assuming it flies at a maximum altitude of 150 m), which implies that the inlet air temperature is 288.15 K, the density is 1.225 kg/m and the static pressure is 101,325 Pa. The total pressure is the sum of the static pressure at sea level and the dynamic pressure, as shown in [Equation 12.2](#) (whereby  $\rho$  and  $V$  are the density and velocity, respectively). The velocity of the free-stream is 20 m/s, as stated in [section 9.1](#). The maximum temperature that the EVA foam can withstand is assumed for the electronics temperature, which is  $65^\circ\text{C}$  [34].

$$P_t = P_s + \frac{1}{2} \cdot \rho \cdot V^2 \quad (12.2)$$

The internal heating power generated in the battery due to resistive losses can be estimated using the following equation:

$$P = I^2 R$$

where  $P$  is the power in watts,  $I$  is the discharge current in amperes, and  $R$  is the internal resistance in ohms.

In this case, the battery is discharging at 11 A, and the internal resistance is 10 m $\Omega$ . A safety margin of 20% is applied to account for variations in resistance or operating conditions. Substituting the values and applying the margin, the estimated heating power becomes approximately 1.45 W. For each cutout section, there are 2 batteries, so a total of 2.9 W is assumed to be dissipated by the airflow.

It is important to note that the battery is the primary source of internal heat generation and represents the most significant risk of overheating within the system. This is especially critical in enclosed environments with poor thermal dissipation, such as foam insulation.

With all of these assumptions, a final airflow of  $1.246 \cdot 10^{-4} \text{ m/s}^3$  is required. Assuming that the air flows into the hole at 20 m/s, it would require a hole of 0.9 mm in diameter. Hence, the current design is sufficient to cool down the electronics systems.

### Motor Mount Group

The motor mount system assembly consists of a front motor mount, a back motor mount, each with its motor and propeller screwed, and in between there is the MainPCB. Figure 12.1 shows a detailed technical drawing of the back motor mount, revealing the thick metric pitch M2 thread holes for screwing the motor on the mount and for screwing the mount through the MainPCB and onto the front motor mount. Note that to ensure the least amount of drag disturbance caused by this assembly, the motor mount is screwed with a self-supported screw, screwed from the back to the front. Moreover, the thread hole has been designed such that the screw head can fit inside the mount and not cause any further disturbance.

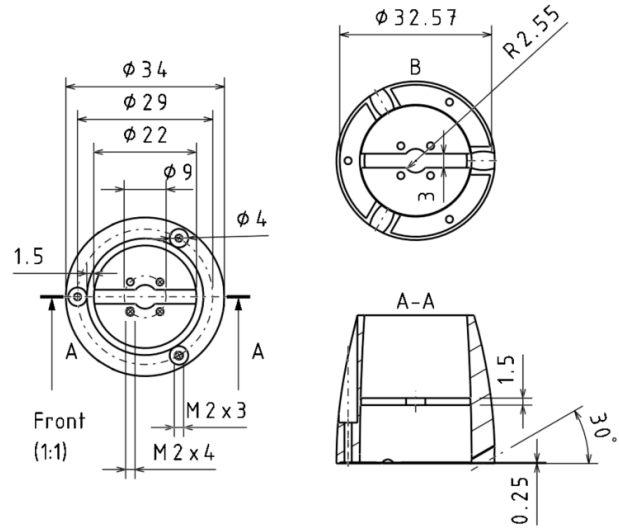


Figure 12.1: Detailed technical drawing of the back motor mount, whereby the metric dimensions are expressed in [mm].

### Carriage Group

The carriage system consists of the motor mount assembly attached to the 3 struts, together with the carriage and mounted batteries. A final sweep angle of 30° was used for the struts, to ensure that the shift of the centre of gravity was centred at the front, near the average centre of pressure location (which is 19.89% at 6° of angle of attack, as stated in subsection 9.1.4).

Furthermore, the rail system, allows the carriage to be displaced from 46.264% from the leading edge to 11.764%, resulting in a total shift of 34.5%, as seen in Figure 12.2. Table 12.3 reveals the final CG shift and location data for the furthest carriage configuration and the most aft configuration.

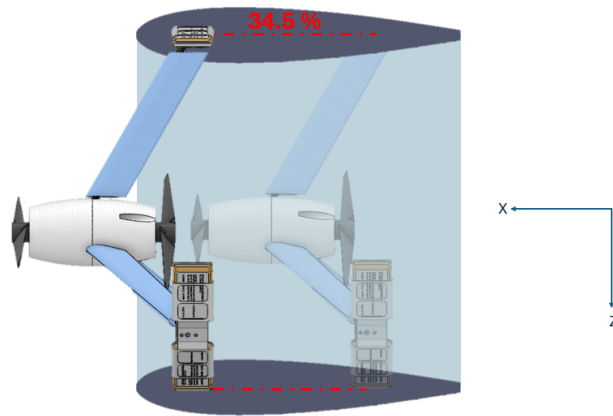


Figure 12.2: Visualisation of the shift of the carriage along the wing body.

Table 12.3: CG shift data for the carriage system

Component	Mass [kg]	Most fore CG position relative to the chored]	Most aft CG position relative to the chord	Total CG shift
Moving Carriage System	0.120	-13.10%	21.40%	34.50%
Fixed Wing Body	0.117	41.76%	41.76%	0%
Complete Assembly	0.237	13.98%	31.45%	17.47%

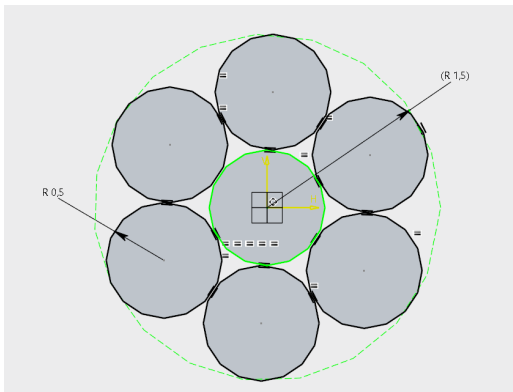
Knowing that the cruise throttle configuration produces a 0.365 N at 6 degrees (as discussed in chapter 8), and by assuming that during a cruise flight, the centre of gravity shall be located approximately at the same location

as the centre of pressure, it was concluded that the spring constant required for the carriage is 21.218 N/m.

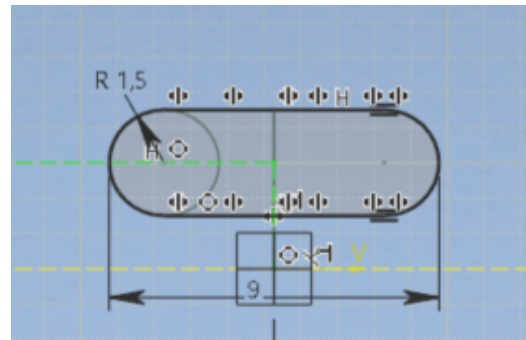
## Cabling System

Having all of the components fitted and designed, it was necessary to ensure that all cables were managed. To compute how wide the wires will be, a source voltage of 7.4 V with an allowable voltage from the battery drop of 3%, and a constant current drawn from the motors of approximately 6 were assumed (view [section 9.3](#)). Furthermore, by assuming an approximate maximum wire temperature of 50° [35], and knowing that the maximum wire length can be equal to the circumference of the airframe (for the wires between the batteries), the maximum diameter of these wires resulted in 0.9345 mm.

Taking into account that each strut has an inner diameter of 3 mm (as shown in [subsection 11.1.2](#)), and assuming that the maximum diameter for each cable, including insulation is of 1 mm, it was proven that a maximum of 7 cables could fit in each strut (as shown in [Figure 12.3a](#)). Moreover, for the airframe, a groove cutout was made such that at least 21 cables could go through the airframe simultaneously at any given location (view [Figure 12.3b](#)).



(a) Sketch of a pack of 7 cables inside a 3 mm in diameter hole, shows each strut can fit a maximum of 7 cables.



(b) Visualisation of the groove cut-out for cabling, ensuring that at least 21 cables can go through at a specific location of the LORAX at a given point in the airframe.

Figure 12.3: Visualisations for the spacing of the cables

Finally, [Figure 12.4](#), shows the cable distribution diagram for one drone node. As seen, the motor wires complete a full circumference around the cylinder, as they must connect each pack of 2 batteries in series, in parallel, and then connect to the PCB. The wires connecting from the ESC to the motor go through the same strut, and there are 6 cables for that. There are 11 cables going from the FlexPCB to the MainPCB, and hence, they are split into 5 cables for one strut and 6 for the other. From this figure, it can be concluded that the location where the maximum cables go through in the airframe is between the FlexPCB and the strut on the left of the figure, resulting in a total of 15 cables: 6 wires connecting from the FlexPCB to the MainPCB, 6 wires connecting from the FlexPCB to the Visual Camera, 2 wires connecting from the FlexPCB to the ESC and 1 connecting from the FlexPCB to one of the battery packs. This means that the current configuration and design are feasible to fit all batteries.



**Figure 12.4:** Cable distribution diagram for one single drone node. The red cables resemble the connection of the batteries within the system, in which the two batteries at each carriage are connected in series, and each of these battery groups is connected in parallel, and the cables are then connected to the FlexPCB. The purple wires are 2 groups of 6 wires each going from the FlexPCB to the infrared and the camera payload. The blue wires refer to the 11 wires that connect from the FlexPCB to the MainPCB. The yellow wires are 2 groups of 2 wires that connect from the FlexPCB to the ESC, and the green wires are 2 groups of 3 wires that connect from each ESC to their respective motor.

## 12.2. Hardware/Software Diagram

Figure 12.5 is the hardware/software diagram of LORAX. LORAX uses two motors with contra-rotating propellers for flying. These spinning propellers not only push the drone forward but also press against a spring. This action shifts the drone's center of gravity, which helps control its movement. The control also uses gyroscopic forces caused by the spinning propellers.

The main body of the drone includes the carriage, airframe, motor mount, struts, and a counterweight. These make up the physical structure and keep the drone balanced. The power system has a battery that connects to two electronic speed controllers, which power the motors.

LORAX has several sensors, including a 9-axis IMU, GPS, and barometer. These sensors send data to a sensor fusion system, where an Extended Kalman Filter is used to estimate the drone's orientation and movement.

At the heart of LORAX is the flight controller. It handles pitch and roll using control loops. It also uses aerodynamic models, like VSPAero, to decide how the drone should move. A mixer combines these outputs and sends commands to the motors.

LORAX carries a visual camera and an infrared photodiode as its payload. These are used to find and track forest fires. The drones work in a swarm. It uses tools including FFT transform, neural networks, object detection (YOLO v5), spatial mapping, and path planning to fly together with other drones, guided by a mothership.

Communication is done through a WiFi module and antenna. This allows LORAX to send and receive data from other drones or a ground station. All the parts are connected through either mechanical or signal lines, working together as one complete system.

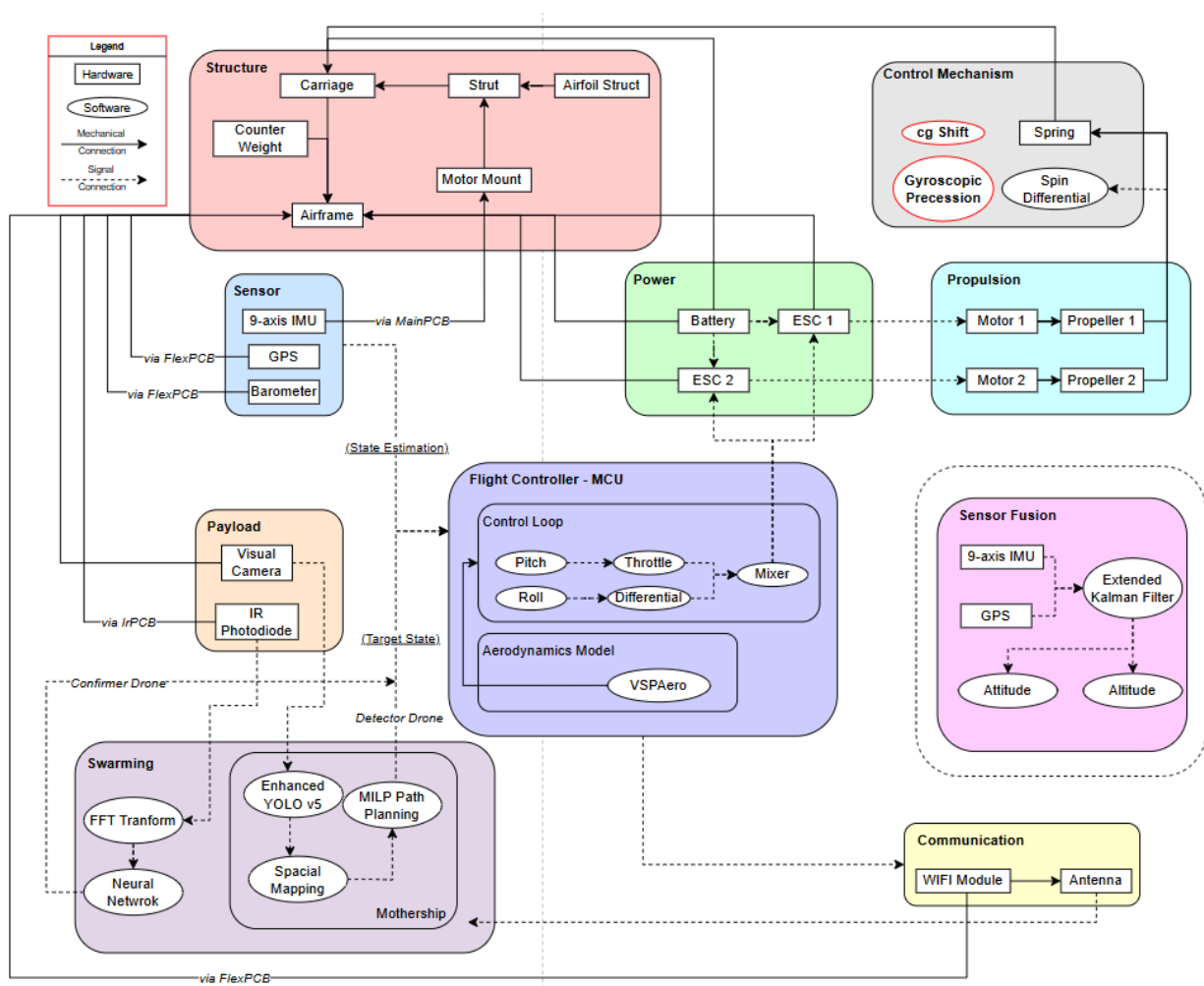


Figure 12.5: Hardware/Software Diagram

### 12.3. Final Budgets

#### Mass Budget

The final mass budget is presented in Table 12.4 and shows the approximate mass of each subsystem. The values were found using the bill of material in Table 12.1. The propulsion subsystem includes the mass of the motors, propellers, and motor mounts. The electronics contain the PCBs, ESCs, the batteries, and a 5.2% margin on the total weight for cables (~ 2 g). The payload contains the mass of the visual camera and infrared sensor. Finally, the airframe contains the remaining components.

Table 12.4: Final Mass Budget computed from the BOM (12.1), ordered per subsystem.

Final Mass Budget	
Subsystem	Value (grams)
Airframe	64.62
Propulsion	60.00
Electronics & Power	92.23
Payload	20.00
<b>Total Mass</b>	<b>236.85</b>

#### Power Budget

The final power budget is mainly driven by the power drawn by the motors, which is estimated to be around 27.6 W for both motors operating in cruise. The visual camera draws 2.8 W when operating. Table 12.5 includes the power draw from other components as well, and presents the estimated total power draw of the drone during operations.

*Table 12.5: Final Power Budget, containing all main power consuming components*

Final Power Budget	
Component	Typical Value (Watts)
MCU1	0.198
IMU	0.0025
MCU2	0.396
GPS	0.046
WiFi module	0.264
Visual Camera	2.8
Motor (2x)	27.6
<b>Total Power</b>	<b>31.31</b>

## Contingencies

Now that the initial design phase is being wrapped up, it is important to update the contingencies on the engineering budgets for the upcoming phase. According to NASA [25], the contingencies taken into account vary per phase. Since the upcoming design iteration should end with a critical design review (CDR), the margins taken into account for mass and power should be 5% and 10% respectively. Applying these contingencies to the budgets discussed above, the estimated mass and power budget range is shown in Table 12.6.

*Table 12.6: Estimated budgets are presented with a contingency margin added according to NASA[25].*

Budget	Contingency	Range
Estimated Mass (grams)	5%	225.01 - 248.69
Estimated Power Use (Watts)	10%	28.18 - 34.44

# 13 Operations

In this chapter, several topics related to operations are discussed. First, a concept of the operations and logistics of the L.O.R.A.X. is presented. This concept will present the different phases throughout a typical mission. After, the operational characteristics will be discussed, particularly, the section will present the reliability and maintainability of the L.O.R.A.X. drones. Finally, the sustainability of the project is considered.

## 13.1. Operations and Logistics

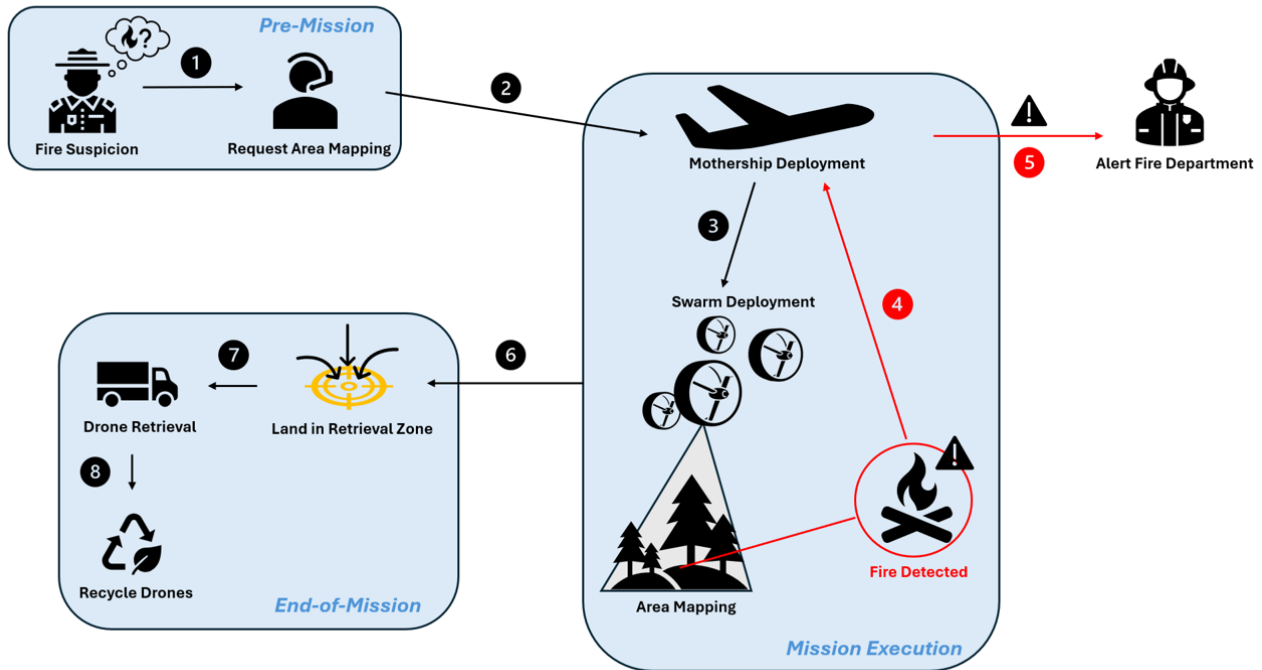


Figure 13.1: Conceptual Operations Diagram

In Figure 13.1, a conceptual operations diagram is presented. This diagram shows how the potential sequence of a typical mission, performed by the L.O.R.A.X., would look. Below, each of the phases is described and linked to the numbers on the figure.

### Pre-Mission:

- *Phase 1:* When a fire is suspected in the forest, an area mapping can be requested to an emergency service that is linked to the drone swarm operator.
- *Phase 2:* The emergency service puts the request through to the swarm operator, who sends out the mothership to the desired area.

### Mission Execution

- *Phase 3:* Once the mothership is in the area, the detector nodes are sent out to scan the area, followed by the confirmator nodes.
- *Phase 4:* If a fire is detected, the swarm sends the location of the fire back to the mothership.
- *Phase 5:* If the mothership receives a signal of a detected fire, it sends a distress signal to the local fire department along with the location of detection.
- *Phase 6:* After mapping the area, regardless of whether a fire is detected or not, the swarm proceeds towards a designated retrieval zone.

### End-of-Mission

- *Phase 7:* Once the swarm has touched down in the retrieval zone, the drones can be brought back to the operator.

- *Phase 8:* When the drones are back at the operator, they can be maintained and reused.

## 13.2. Operational Characteristics

### Reliability

To assess how useful the final product is, it is important to quantify the reliability of both the individual drones and the swarm as a whole. STK03-MIS16 and STK03-MIS17 state that the drone and the swarm network shall have minimum reliability of 95% and 99% respectively. Since the L.O.R.A.X. has a novel design and uses flight principles that are different from standard quadcopters or fixed-wings, it is difficult to get representative numbers on reliability. To quantify the reliability or failure rates, extensive testing has to be done, as it is currently impossible to predict this by simulation. One of the aspects that makes the L.O.R.A.X. unique is that it only uses one actuator for propulsion, stability and control. This results in mechanical simplicity and can increase reliability compared to existing drone types. However, this idea can only be proven once a prototype is actually built and tested.

### Maintainability

As mentioned previously the drone only has a single actuator, which is particularly good for maintainability, as there are fewer components to be monitored. Furthermore, the drone nodes are designed to be modular, which implies that components can be changed and/or replaced. This makes the drone more attractive from a maintainability perspective.

## 13.3. Sustainability

In this section, the sustainability considerations taken during the L.O.R.A.X. project are discussed. Furthermore, an outlook on operational sustainability and the potential impact on society is given.

### Project Sustainability

**Material Selection:** During the design phase, the team put strived to use as many biodegradable/sustainable materials that come from recycling or reusing. Due to technical disadvantages, biodegradable materials were not an option. Instead, materials that have the potential to be recycled were chosen to try and contribute to the circular economy <sup>1</sup> as much as possible. Adopting a circular economy philosophy was made a priority during the design phase; a schematic of this philosophy is presented in [Figure 13.2](#). To minimise waste, different manufacturing processes were considered. However, due to budget constraints, minimal waste options became unfeasible.

**Energy Efficiency:** During the design of the drone, the team has aimed to design for minimum drag and mass to reduce power consumption. Not only is this attractive to customers, but it also increases the life span of the product, making it more sustainable.

**Design for EoL:** Since the goal is to contribute to a circular economy, the end-of-life phase has been taken into account already during the design phase. To ease the recycling of the product, the method of Design for Disassembly (DfD) <sup>2</sup> is implemented. It has been designed such that it is relatively accessible to disassemble individual components of the drone to individually recycle. The end goal is to produce less waste and work towards a circular economy.



**Figure 13.2:** A visual representation of a circular economy made by the European Parliament

### Operational Sustainability

During the design phase of the L.O.R.A.X., some thought has been put in the sustainability of the operations. The main considerations being the post-mission retrieval and the End-of-Life of the drone nodes. **Post-Mission:** Though none of the requirements specify anything about being able to retrieve the drone after a mission, circular economy principles suggest the drones should not be left as waste. Therefore, during the design of the swarming algorithm, it was decided that after scanning the area, the drones should all be directed to a "retrieval zone", where they can safely be picked up by the operator for reuse.

<sup>1</sup>European Parliament, Circular economy: definition, importance and benefits, last updated May 2023. Available at: [https://www.europarl.europa.eu/pdfs/news/expert/2023/5/story/20151201ST005603/20151201ST005603\\_en.pdf](https://www.europarl.europa.eu/pdfs/news/expert/2023/5/story/20151201ST005603/20151201ST005603_en.pdf) (accessed 01/05/2025)

<sup>2</sup>Dassault Systèmes (Corporate author), Design for Disassembly (DfD), 2025. Available at: <https://www.3ds.com/sustainability/circular-economy/design-for-disassembly> (accessed 01/05/2025)

**End-of-Life:**

Once the drones are at the end of their lifespan or broken, they will be disassembled, and the components will be reused or recycled where possible. An effort to increase the drone's lifespan can be made by regularly replacing components such as the batteries.

**Social Sustainability**

During operations, it is important that the L.O.R.A.X. drones do not harm any people or any wildlife. Once again, the retrievability of the drones can reduce the chances of wildlife getting harmed. Since the drones are not designed to fly in urban areas, the risk of harming people is minimal. Assessing how dangerous the product can be on for example, impact when crash, is relatively hard during the early design phases; therefore, during further development, more effort should be put into fully mitigating the risk of harming any life.

**Workplace Environment:**

Aligned with LCSP principles [33], the manufacturing partner should ensure a safe workplace by eliminating physical, chemical, biological, and ergonomic hazards [1]. This includes using safe chemicals or robotic automation to reduce employee physical hazards. Prioritising a safe, environmentally conscious workplace is critical for minimising the drone's ecological footprint and maximising social responsibility during production.

# 14 Cost Breakdown

In this chapter, an estimate of the project's cost is presented. First, the cost is broken down for each subsystem, with an estimate of the cost per drone node per system. Furthermore, a prediction of the variable costs is given. Finally, the total cost for a single swarm is presented.

## 14.1. Materials

In [Table 14.1](#), each of the materials used in the drone is listed along with their cost per kilogram or per metre. The values for the cost were found on Alibaba<sup>1</sup>, Foamatelier<sup>2</sup>, and Easycomposites<sup>3</sup>. Assuming the weights from the Bill of Material in [Table 12.1](#), and including a 100% margin for potential waste, the total cost for a single node summed to approximately 4 euros.

*Table 14.1: Cost Budget for Materials*

Material	Cost [€ FY25]	Per
EVA CF65 Foam	€ 27.68	kg
PLA	€ 3.46	kg
Aluminium	€ 3.52	kg
Carbon fibre rods	€ 2.60	m
Cost for 1 node	€ 4.00	-

## 14.2. Propulsion

Similar to the materials discussed previously, the costs of the propulsion system components are listed in [Table 14.2](#). All components shown in the table are commercially off-the-shelf available. The motor is provided by E-flite RC, and the propellers are provided by APC propellers, as discussed in [section 9.2](#). Estimates for the price of the ball bearings and springs were found on Alibaba. Since there are 2 motors, 2 propellers, 3 springs, and approximately 100 ball bearings per node, the price of the propulsion system is estimated to be € 84.09 per node.

*Table 14.2: Cost Budget for Propulsion System*

Component	Cost [€ FY25]	Per
Motor	€ 38.76	pc
Propeller	€ 2.20	pc
Spring	€ 0.50	pc
Bearing Balls	€ 0.67	100 pc
Cost for 1 node	€ 84.09	-

## 14.3. Electronics & Power

The cost breakdown of the electronics and power subsystem is presented in [Table 14.3](#). The cost of the PCBs were determined by taking components from Mouser Electronics<sup>4</sup> and adding € 50 for assembly costs. The batteries and ESCs are discussed in [section 9.2](#). For one node, the cost comes down to € 274.99, for a two-ESC and six-battery configuration.

*Table 14.3: Cost Budget for Electronics & Power System*

<sup>1</sup>Alibaba. Available at: <https://www.alibaba.com/> (accessed 17/06/2025).

<sup>2</sup>Foamatelier, *Eva Craft Foam | CF 65 | 10mm | 1x2m | Wit | Med. Density*. Available at: <https://www.foamatelier.nl/nl/foam-en-foamboard/eva-foam/eva-foam-10-mm/eva-craft-foam-cf-65-10mm-1x2m-wit-med-density-per-stuk/a-91335-20000695> (accessed 17/06/2025).

<sup>3</sup>Easy composites, *4mm (3mm) Pultruded Carbon Fibre Tube*. Available at: <https://www.easycomposites.eu/4mm-pultruded-carbon-fibre-tube> (accessed 11/06/2025).

<sup>4</sup>Mouser Electronics. Available at: <https://nl.mouser.com/> (accessed 17/06/2025).

Component	Cost [€ FY25]	Per
Flex PCB	€ 76.15	-
Main PCB	€ 19.00	-
IR PCB	€ 29.72	-
ESC	€ 18.95	-
Batteries	€ 10.37	-
Assembly	€ 50.00	-
Total cost for 1 node	€ 274.99	-

## 14.4. Payload

The cost of the payload components is summarised in Table 14.4. The payload components are discussed in section 10.2, however due to trouble obtaining a quote for the IR photodiode, the price of a similar model was taken. Assuming only half of the drones in the swarm have a visual camera, the total payload cost per node was estimated to be € 502.80.

Table 14.4: Cost Budget for Payload components

Component	Cost [€ FY25]	Per
IR photodiode	€ 291.00	pc
Visual Camera	€ 423.60	pc
Cost for 1 node	€ 502.80	-

## 14.5. Launch System

The components of the launching system were discussed in section 11.4. The launch tube is taken to be a COTS PVC tube, while the gears will all be 3d printed with PLA. The prices of the PVC tube and PLA were found on Alibaba. The total cost of the launching system was estimated to be € 132.57

Table 14.5: Cost Budget for Launch System components.

Component	Cost [€ FY25]	Per
PVC Pipe	€ 1.24	pc
Wheel Bearings	€ 8.29	2 pcs
Servo Motor	€ 51.66	pc
Wheels	€ 2.12	pc
PLA	€ 3.46	kg
Cost for the launching system	€ 132.57	-

## 14.6. Variable Costs

Finally, the breakdown also accounts for variable costs such as labour<sup>5</sup>, machine costs<sup>6</sup>, and a margin included for unforeseen costs and potential legal fees. For the labour, it was assumed that an aerospace engineer spends around 10 hours total on one drone. Furthermore, it was assumed that one node needs around two hours of machine operations. The unforeseen cost is assumed to be approximately 10% of the cost of a node without variable costs, which rounds up to € 100. In total, variable cost for a single node is assumed to be € 790.

Table 14.6: Budget for Variable Costs such as hiring personnel and unforeseen costs.

<sup>5</sup>Salary Expert, Aerospace Project Engineer. Available at: <https://www.salaryexpert.com/salary/job/aerospace-project-engineer/netherlands/amsterdam> (accessed 17/06/2025).

<sup>6</sup>Yijin Hardware, CNC Machining Cost: How to Calculate & Reduce its Cost?. Available at: <https://yijinsolution.com/cnc-guides/cnc-machining-cost/> (accessed 17/06/2025).

Type	Cost [€ FY25]	Per
Labour	€ 39	hr
Machine Costs	€ 150.00	hr
Unforeseen Costs/Legal Fees	€ 100	node
Cost for 1 node	€ 790.00	-

## 14.7. Total Cost Budget

The total cost breakdown is summarised in [Table 14.7](#), and shows the cost for a single node and the total cost for a swarm of 10 drones. The available budget for the development of one L.O.R.A.X. swarm with a minimum of 10 nodes is € 20k. The estimated development cost is € 16.6k, leaving a margin for unexpected costs. Note that due to time constraints, more effort has been put into the design of the drones and less on the further development after the DSE. This meant that there were limited resources available to properly estimate the variable costs. Mainly, it is hard to predict how much personnel is needed to develop a swarm. To account for this uncertainty, a 30% margin is added to the variable costs and on top of that, a 10% contingency is added to the other components.

*Table 14.7: Total Cost Budget*

Subsystem	Cost [€ FY25]	Contingency	Range
Materials	€ 4.00	10%	€ 3.60 - € 4.40
Propulsion	€ 84.09	10%	€ 73.28 - € 89.57
Electronics & Power	€ 274.99	10%	€ 247.49 - € 302.49
Payload	€ 502.80	10%	€ 452.52 - € 553.08
Launch System	€ 132.57	10%	€ 119.32 - € 145.83
Variable Cost	€ 790	30%	€ 718.90 - € 1,027.00
<b>Total Cost of 1 Node</b>	<b>€ 1,653.22</b>	-	€ 1,495.80 - € 1,976.54
<b>Total Cost of 10 Node Swarm</b>	<b>€ 16,664.75</b>	-	€ 15,077.27 - € 19,911.22
<i>Available Budget</i>			€ 20,000.00

## 14.8. Operational Costs

STK05-MIS26 states that the operational cost should be lower than € 1k an hour. From this early stage, it is hard to predict the exact operational cost. The team predicted the operational costs to include the wage of the drone operator(s), the cost of retrieval and the cost of replacing a drone depending on the failure rate. Since it is not yet decided how many operators there are and how the retrieval is done specifically, it is impossible to get a good estimate for the operational cost. Therefore, the operational cost is left as TBD for the further development phase.

# 15 Verification & Validation

## 15.1. Requirements Compliance Matrix

This section details the Requirements Compliance Matrix (Table 15.1), listing each stakeholder and mission requirement alongside its priority, compliance status, chosen verification method, and justification. The matrix serves as a comprehensive reference to assess whether the design meets the defined objectives and constraints of the project.

Table 15.1: Stakeholder and Mission Requirements Compliance Matrix

ID	Requirement Text	Prio.	Comp. Status	Verif. Method	Value Achieved/Expl.
<b>STK Level (Stakeholder Requirements)</b>					
STK01	The system shall provide the primary customer (e.g., Firefighting Agencies) with a more effective and rapidly deployable wildfire monitoring solution compared to current methods.	Ky	Pass	Analysis	[section 3.4]
STK02	The system shall operate with minimal negative environmental impact, addressing societal and regulatory expectations.	Ky	Pass	Analysis	Derived from STK02-MIS04
STK03	The system shall operate safely and in full compliance with applicable airspace and drone regulations (e.g., EASA).	D	Fail	Analysis, Inspection	Derived from STK03-MIS-03
STK04	The project shall be developed successfully within the academic, time, and resource constraints defined by the Design Synthesis Exercise.	D	Pass	Inspection	N/A
STK05	The system shall represent a cost-effective solution in terms of acquisition and operation for potential end-users.	D	Pass	Analysis	Derived from STK05-MIS25
STK06	The system shall be designed so it can be easily adapted for uses beyond wildfire mapping.	Ky	Pass	Analysis	Derived from STK06-MIS29
<b>MIS Level (Mission Requirements)</b>					
<i>High-Level Mission Goals</i>					
STK01-MIS01	The Swarm System shall perform effective autonomous wildfire mapping over a designated area.	Ky	Pass	Sim./Mod., Demonstration	[chapter 10]
STK05-MIS02	The Swarm System shall operate within defined economic constraints.	D	Pass	Analysis	Verified by STK05-MIS25

Continued on next page...

Table 15.1: Stakeholder and Mission Requirements Compliance Matrix – Continued

ID	Requirement Text	Prio.	Comp. Status	Verif. Method	Value Achieved/Expl.
STK03-MIS03	The Swarm System shall operate safely according to regulations.	D	Fail	Analysis, Inspection	Derived from STK03-MIS15
STK02-MIS04	The Swarm System shall meet sustainability goals addressing societal and regulatory expectations.	Ky	Pass	Analysis, Test, Insp.	N/A [section 13.3]
STK04-MIS05	The Swarm System development shall adhere to specified DSE process constraints.	D	Pass	Inspection, Analysis	N/A
STK06-MIS29	The Swarm System Mission shall support operational scenarios utilising different, interchangeable sensor payloads.	Ky	Pass	Analysis, Demonstration	Interchangeable Payload [chapter 12]
<i>Detailed Mission Capabilities &amp; Constraints (Original User Req. Mapping)</i>					
STK01-MIS06	Each drone node shall have a minimum flight time of 10 [min].	D	Pass	Test, Simulation	10.86min [subsection 9.3.3]
STK01-MIS07	The mission shall utilise a main mother-ship for drone node launch.	Ky	Pass	Inspection	[section 11.4]
STK01-MIS89	Each drone shall not stall due to a gust of 5 m/s	D	Pass	Sim./Mod., Test	section 9.5
STK01-MIS10	The system shall provide a mothership-drone communication range of at least 1 [km] line of sight.	D	Pass	Test, Analysis	>1km [subsection 10.4.2]
STK01-MIS11	The swarm shall scan an area of at least 10 [km <sup>2</sup> ].	D	Pass	S, A	>10 km <sup>2</sup> (exact value TBD)
STK01-MIS12	Each drone node shall detect hotspots of at least 1 [m <sup>2</sup> ].	D	Pass	Sim./Mod., Test	0.9m <sup>2</sup> [section 10.2]
STK01-MIS13	Each drone node shall determine an average hotspot temperature of at least 110 [°C].	Ky	TBD	TBD	[section 10.2]
STK01-MIS14	Each drone node actuator shall provide thrust, control, and torque.	D	Pass	Analysis, Inspection	[chapter 12]
STK03-MIS15	The system shall comply with EASA Open Category A1/C0 regulations for civil drones.	D	Fail	Inspection, Analysis	200m Altitude. [Cannot comply with C0 altitude limit of 120m]
STK03-MIS16	Each drone node shall have a minimum reliability of 95 [%] for a mission.	Ky	TBD	TBD	Requires production& testing
STK03-MIS17	The integrated swarm network shall have a minimum reliability of at least 99 [%].	Ky	TBD	TBD	Requires production& testing
STK02-MIS18	Each drone node shall produce zero nitrogen oxide emissions during operation.	Ky	Pass	Analysis, Inspection	0 [section 13.3]

Continued on next page...

Table 15.1: Stakeholder and Mission Requirements Compliance Matrix – Continued

ID	Requirement Text	Prio.	Comp. Status	Verif. Method	Value Achieved/Expl.
STK02-MIS19	Each drone node flying over 150 [m] shall emit a maximum noise level of 35 [dB] at ground level.	Ky	Pass	Analysis, Test	17.5 dB @ 150m [Table 11.5, 61dB @ 1m]
STK02-MIS20	Each drone node operating above 150 [m] altitude shall not be spotted by civilians.	Ky	Pass	Analysis, Inspection	4.6 arcminutes is the drone, 1 arcminute can be seen by the human eye. With the light blue colour, this is deemed sufficient.
STK03-MIS21	Each drone node weight shall not exceed 250 [g].	D	Pass	Inspection, Test	248.69 [Table 12.4]
STK03-MIS22	The system communication shall comply with European datalink requirements (EASA Art. TCO.205).	D	Pass	Inspection, Analysis	Wi-Fi [section 10.4]
STK05-MIS23	The drone node design shall be suitable for mass production.	D	Pass	Analysis, Inspection	[chapter 16]
STK01-MIS24	The swarm shall be launched from an in-air launch unit.	D	Pass	Analysis, Inspection	[section 11.4]
STK05-MIS25	The mission total acquisition cost (10 nodes + launch unit) shall be under 20,000 [€].	D	Pass	Analysis	€ 16,664.75 [Table 14.7]
STK05-MIS26	The mission operational cost shall be lower than 1000 [€/hour].	Ky	TBD	Analysis	section 14.8

## Feasibility Analysis

As some of the requirements are not compliant in Table 15.1, a feasibility analysis was conducted to ensure the proposed design can still function as intended, or if not, what steps and/or modifications must be made to have a feasible design for the mission.

- **STK03:** This requirement, more specifically detailed by STK03-MIS03 and STK03-MIS15 is not compliant with the design. This is both due to cruise altitude being above the specified maximum 120m, as well as the 20m/s cruise speed being above 19m/s limit specified for open category C0 class drones<sup>1</sup>. Therefore, drones will be required to apply in the 'specific' category for drones<sup>2</sup>, also due to their autonomous operation and Beyond Visual Line of Sight (BVLOS) intended use. The drone will be subject to a prior risk analysis using SORA to determine whether it is a Low, Medium, or High risk operation (and therefore whether Operational Authorisation will be required). To make the proposed design feasible the requirement must be adjusted to be 'EASA Specific Category Compliant'.
- **STK03-MIS16 & STK03-MIS17:** The following requirements are based respectively on the individual node and integrated swarm reliability of: 95% and 99%. These cannot currently be classified as compliant as they require production and testing. This reliability will be quantified as the ratio of successful trialed missions to total trial attempts under representative conditions in testing.
- **STK01-MIS89** This requirement on not stalling under a 5m/s gust was proposed and approved by the tutor in place of the original STK01-MIS8 and STK01-MIS9 requirements on 30°/s pitch and yaw rate respectively. This modification was made as the requirement was primarily established to ensure the drone could actively control against gusts in case they destabilised the drone, but this was shown to not be necessary due to the high gyroscopic stability of the spinning drone in simulation (section 9.4). The initial rate requirements were infeasible for our gyroscopically stabilised drone design, as determined by achieved

<sup>1</sup>Certification Requirements for C0 Drones, EU Drone Port: <https://eudroneport.com/blog/certification-requirements-c0-drones/>

<sup>2</sup>Flying Drones in the Specific Category, EU Drone Port: <https://eudroneport.com/blog/specific-category/>

simulation results in [section 9.5](#). This lower turning rate did not impact the ability to adequately map terrain, defined by STK01-MIS01 and STK01-MIS11.

## 15.2. Sensitivity Analysis

A sensitivity analysis is performed on the change in performance and whether the design remains feasible and requirement compliant to changing system parameters. As the design still needs to be developed and tested, there is still uncertainty in certain structural and flight parameters. A sensitivity analysis is crucial to ensure robustness. Identifying sensitive parameters and ensuring their target is met reduces the risk of needing to fully redesign systems at a later stage.

### Mass Sensitivity

With the current budgeted mass shown in [Table 12.4](#), the main component subject to higher uncertainty is the airframe mass, as this needs to be produced, whilst other components are primarily COTS and therefore have exact masses. As a result, the mass sensitivity study is only conducted on parameters affecting airframe structural mass.

### Changing Aspect Ratio

The aspect ratio is the main parameter defining the geometry of the airframe. The airfoil geometry chosen was not changed for the sensitivity study, as it was precisely selected because it contained enough volume to house the moving battery components inside the frame. The aspect ratio was varied between 1 and 3 from the nominal value  $AR=2$ , chosen at 0.1 intervals, which were then interpolated. The result on airframe mass is shown in [Figure 15.1](#). It can be seen that the variation in airframe mass is not very sensitive to changing AR due to changing chord (orange line), whilst a changing diameter (blue line), exceeds the allowable limit at  $AR \approx 2.4$ . This allows for little freedom in the variation of the airframe geometry in case of redesign before production, especially as the total projected mass is already at 236.85g (248.69g with 5% final design contingency), unless the aspect ratio is decreased via reducing diameter. This however, decreases the lift-to-drag ratio, leading to worse efficiency, but this aspect is not analysed for mass sensitivity.

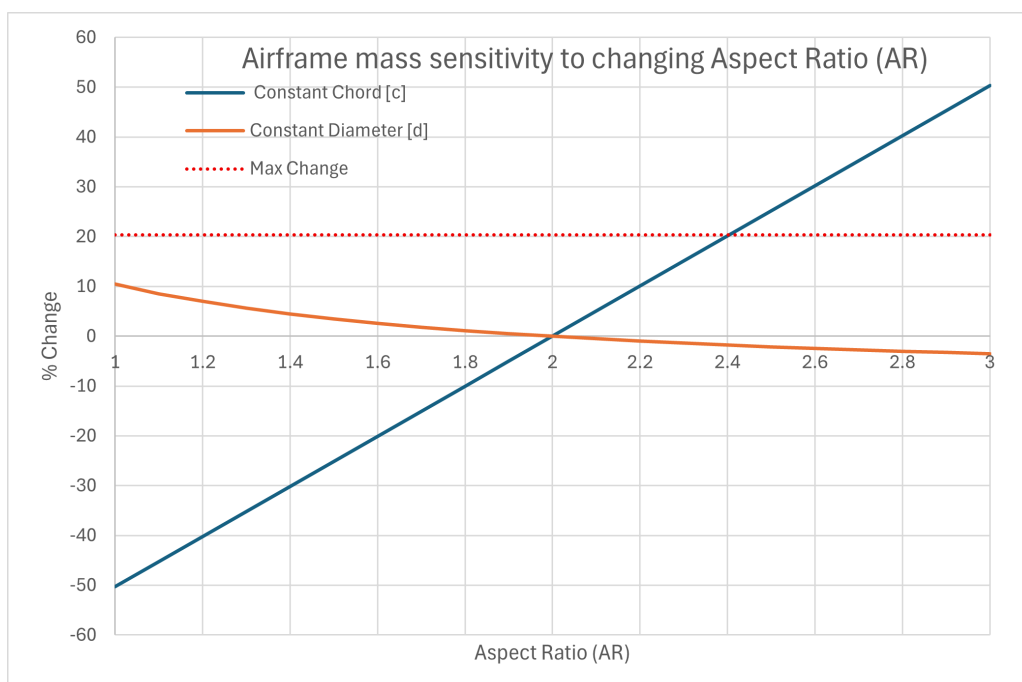


**Figure 15.1:** Sensitivity of Airframe mass with changing Aspect ratio. The maximum variation allowed to meet the 250g requirement of total mass is +20.35%

### Flight performance Sensitivity

The sensitivity of flight performance with varying flight parameters is discussed in [section 9.5](#). Specifically, the main parameter that is used is the varying pitch angle to compare flight performance. [Figure 9.41](#) shows how changing pitch affects Climb rate, Airspeed, Yaw rate and Thrust required. A high sensitivity in flight performance with varying pitch is desired to tweak flight conditions depending on whether we want to climb/descend, turn faster or cruise at a different speed according to the path planning. The main issue, shown in [Figure 9.41c](#), is

the very low sensitivity in yaw rate with changing pitch, varying only between approximately 0.3-0.8 °/sec (not considering stalling rates). This makes manoeuvring very difficult, limiting the path planning options discussed in [chapter 10](#).

An analysis on the effect of flight performance with varying spring stiffness was also performed in [section 9.5](#). [Figure 9.40](#) shows specifically the sensitivity in velocity and climb rate with varying spring stiffness. Further investigation is still required to optimise the stiffness based on mission requirements.

### Cost Sensitivity

The only costs that have proven to make the system less robust are the variable cost, as depending on the manufacturing method, the machinery supplier, the country of manufacturing, and the usage of outsourcing methods, the labour costs, the number of hours taken to, machine costs and legal or unforeseen costs may all vary. Assuming that the time taken for manufacturing each drone node, or the labour cost, were doubled, the total cost would increase by 50 %, making these the most sensitive costs in the system.

## 15.3. Software Verification & Validation

The successful development of the L.O.R.A.X. drone swarm relies on the thorough verification & validation of the software that is used to evaluate the drone's performance and characteristics. The software that is used consists of the OpenVSP program and RANS software used for the aerodynamic analysis, and the Simulink environment to provide the simulations of the L.O.R.A.X. drone. In [Table 15.2](#), the verification and validation procedure of the OpenVSP software is discussed.

*Table 15.2: OpenVSP Verification and Validation Plan*

Test	Explanation	Resources
<b>Verification</b>		
Geometric Model Generation	Confirm generation of shapes (cylinders, airfoils, annular wing, propulsion system). Check parameters displayed in the API match the input. Ensure complex structures are watertight and well-integrated. Check total wetted surface area.	OpenVSP API, Visual Inspection
VSPAERO Solver (Finite Wing)	Compare lift and drag predictions for a simple finite wing with Lifting Line Theory results and trusted software like XFOIL.	Lifting Line Theory, XFOIL
VSPAERO Propeller Modelling	Compare isolated propeller thrust and torque predictions against Blade Element Momentum Theory calculations or available manufacturer data.	Blade Element Momentum Theory, Manufacturer Data
Python Script Unit Tests	Unit test Python scripts developed to interface with OpenVSP/VSPAERO using the unittest framework to ensure correctness and reliability.	Python 'unittest' framework
<b>Validation</b>		
Geometric Model Export	Export assembly to a different meshing tool and have it run geometry diagnostics to confirm the measurements	Alternative Meshing Software
Geometric Model Manufacturing	Manufacturing the geometry and then measuring the geometry of the drone to ensure correctness.	Manufacturing capability, Measurement tools
VSPAERO Panel Method Comparison	Continue validation by comparing other aerodynamic coefficients (pitching moment, centre of pressure) against experimental data (e.g., Fletcher <a href="#">[14]</a> ).	Experimental Data (e.g., Fletcher <a href="#">[14]</a> )

*Continued on next page*

Table 15.2: OpenVSP Verification and Validation Plan – Continued

Test	Explanation	Resources
Propeller Performance	Use experimental data to validate the results of the OpenVSP software for the propeller.	Experimental Data
Propeller-Airframe Interference	Use experimental data to validate results for propeller-airframe aerodynamic interference.	Experimental Data

From the validation of the OpenVSP software that has already been performed in [subsection 9.1.3](#), error bounds were established to ensure correctness in the predictions of the VSPAero solver. In [Table 15.3](#), the verification & validation plan of the RANS simulation is discussed.

Table 15.3: RANS Validation Plan Considerations

Test/Method	Explanation	Resources
<b>Verification</b>		
Setup Correctness	Verify the computational domain size is adequate, boundary conditions (inlet, outlet, walls, symmetry) are correctly applied, and appropriate physical models (e.g., turbulence model, fluid properties) are selected.	RANS Software Documentation, Guidelines
Grid Sensitivity Study	Perform simulations on a series of systematically refined meshes to ensure that key results (e.g., lift, drag coefficients) are independent of mesh resolution, achieving grid convergence.	Multiple Meshes, RANS Solver, Post-processing tools
Residual Convergence	Monitor the solver residuals for all transport equations (continuity, momentum, turbulence quantities) to ensure they decrease by several orders of magnitude (typically 3-5) and reach a steady or acceptably low level.	RANS Solver Output, Convergence Plots
Physical Quantity Convergence	Monitor key physical quantities of interest (e.g., lift, drag, moment coefficients, surface pressures) over solver iterations/time to ensure they stabilise and reach a converged steady-state or statistically steady periodic solution.	RANS Solver Output, Force/Moment Monitors, Post-processing tools
<b>Validation (Ideal/Future Work)</b>		
Wind Tunnel Experiments	Replicate the simulated setup in a wind tunnel and compare experimental data with simulation outputs.	Wind Tunnel, Measurement Equipment
Benchmark Case Modelling	Model a benchmark case with reliable experimental data and compare simulation predictions against this dataset. Ensure close correspondence of defining characteristics (Re, length scales, etc.).	Published Benchmark Experimental Data
<b>Validation (Current Project Scope)</b>		
Trend Analysis	Observe behaviour of RANS results for qualitative trends (e.g., effect of rotation on lift/drag) while acknowledging limitations in precise numerical accuracy due to lack of full validation.	RANS Simulation Results

As the actual validation of the RANS simulation is beyond the scope of the project, this is left as a suggestion to

improve the validity of the simulation. The verification & validation of the Flight Dynamics Model can be found in [Table 15.4](#).

*Table 15.4: Flight Dynamics Model Verification and Validation Plan*

Test	Explanation	Resources
<b>Verification</b>		
Simulink Implementation Correctness	Ensure Simulink implementation correctly executes the algorithm and accurately models desired behaviour. Use tools like Simulink Design Verifier.	Simulink, Simulink Design Verifier
Extreme Value Tests	Input very low or high (plausible) values for state variables (velocity, rotational velocity, pitch, height) to observe predictable model behaviour.	Simulink Model
Small Disturbance Stability	Apply small, impulsive disturbances to simulated state (angular rates, translational velocities) and analyze response for convergence to steady-state.	Simulink Model
Long-Duration Simulation Stability	Perform long-duration simulations to identify potential instabilities or drift.	Simulink Model
Gyroscopic Stability (Spin-up)	Simulate spin-up manoeuvres from various initial rotation states to target axial rotation rate.	Simulink Model
Gyroscopic Stability (Maintenance)	Test controller's ability to maintain steady target rotation in presence of external disturbances or during concurrent translational manoeuvres.	Simulink Model
<b>Validation</b>		
Comparison with Wagner [36]	Model initial conditions from N. Wagner's X-ZyLo launch setup and compare model output with his experimental results.	Simulink Model, Wagner [36] study data

## 15.4. Subsystem Verification & Validation

Due to the novelty of the L.O.R.A.X. drone design, it is key for the subsystems to operate as desired and required. Therefore, a complete Verification & Validation plan is established to ensure that the design meets the requirements. The subsystems consist of the payload, swarming control, structure and propulsion. Numerous verification & validation methods are discussed in [Table 15.5](#).

*Table 15.5: System Level Verification and Validation Plan*

Test	Explanation	Resources
<b>Functional Feasibility (Thermal Sensor)</b>		
<i>Verification</i>		
Sensor Specification Check	Verify manufacturer's sensor specifications meet requirements (detection of 1 m <sup>2</sup> hotspot at 110 °C from >150 m).	Manufacturer's Datasheet
Sensor Initialization	Power on sensor and verify it initialises correctly.	Thermal Sensor, Power Supply
Sensor Data Capture	Verify sensor can capture data by performing a reading; manually check reading.	Thermal Sensor, Test setup

*Continued on next page*

Table 15.5: System Level Verification and Validation Plan – Continued

Test	Explanation	Resources
<i>Validation</i>		
Comparison with Existing Detection Methods	Simulate wildfire detection scenarios and compare L.O.R.A.X. performance (probability of detection, time-to-detect) with data from existing systems (poles, aircraft, satellites).	Simulation Environment, Data on Existing Systems
Real-Life Hotspot Detection Test	Detect a real-life hotspot (>110 °C, heated material) from >150 m. Measure actual hotspot temperature and compare with sensor reading.	Thermal Sensor, Heated material, Heat measuring gun (approx. 20 EUR)
<b>Visual Data Pipeline (Camera to YOLOv5)</b>		
<i>Verification</i>		
Camera Specification Check	Verify visual camera specifications (resolution, frame rate, field of view, low-light performance) meet the requirements for providing adequate data to the YOLOv5 model.	Camera Manufacturer's Datasheet, System Requirements
Camera Initialisation	Power on the visual camera and verify it initialises correctly, is recognised by the onboard processing unit, and can be commanded.	Visual Camera, Drone's Onboard Computer/Microcontroller
Data Stream Integrity (Drone to Mothership)	Verify that the visual data stream from the drone's camera to the mothership (where YOLOv5 runs) is established correctly, maintains an acceptable frame rate, and has minimal latency and data corruption under various communication conditions (e.g., range, interference).	Visual Camera, Drone, Mothership Communication Link, Network Monitoring Tools
Image Quality Check	Capture sample images/video under various expected operational lighting conditions (day, dusk, varied backgrounds) and different rotational velocities, and verify that image quality (clarity, focus, exposure, lack of excessive noise/blur) is suitable for YOLOv5 processing.	Visual Camera, Test Scenarios/Environments, Spin Rig
YOLOv5 Model Input Compatibility	Verify that the image format, resolution, and pre-processing steps (if any, e.g., resizing, normalisation) applied to the camera data before feeding it to YOLOv5 are correctly implemented and compatible with the model's input requirements.	Camera Output, Pre-processing Scripts, YOLOv5 Model Documentation
<i>Validation</i>		
End-to-End Object Detection Test (Simulated/Lab)	Test the entire pipeline: capture images with the drone's camera, transmit to mothership, process with YOLOv5. Use known objects/targets in a controlled lab environment and verify correct detection and classification by YOLOv5. Assess accuracy, precision, and recall.	Drone with Camera, Mothership with YOLOv5, Test Objects, Ground Truth Annotations
Real-World Object Detection Performance	Conduct tests in representative outdoor environments. Evaluate the YOLOv5 model's performance on detecting and classifying hotspots using the live camera feed from the L.O.R.A.X. drone.	L.O.R.A.X. Drone, Mothership with YOLOv5, Real-world Environment, Performance Metrics

Continued on next page

Table 15.5: System Level Verification and Validation Plan – Continued

Test	Explanation	Resources
Latency Measurement	Measure the end-to-end latency from image capture on the drone to object detection output from YOLOv5 on the mothership to ensure it meets operational requirements (e.g., for timely obstacle avoidance).	Timestamping at Capture and Detection, Synchronised Clocks (if possible)
Robustness to Environmental Conditions	Evaluate the performance of the visual pipeline and YOLOv5 detection under various environmental conditions (e.g., changing light, weather, if applicable, cluttered backgrounds, changing rotational velocity) expected during operation.	L.O.R.A.X. Drone, Mothership, Varied Environmental Test Conditions, Spin Rig
<b>Flight Time (&gt; 10 minutes)</b>		
<i>Verification</i>		
Energy Budget Analysis	Calculate expected flight time based on drone's total power consumption and onboard power source capacity under typical operational conditions.	Drone specifications, Power source specifications, Analytical tools
Stationary Current Draw Test	Measure the total current draw of the drone in a stationary, powered-on state (motors idle or at minimum operational RPM) to verify it aligns with the sum of individual component datasheets and the energy budget assumptions.	L.O.R.A.X. Prototype, Precision Multimeter (ammeter function), Power Supply/Battery
<i>Validation</i>		
Physical Flight Endurance Test	Fly a fully operational L.O.R.A.X. prototype until power depletion; measure actual flight duration.	L.O.R.A.X. Prototype, Timer
<b>Swarm Control</b>		
<i>Verification</i>		
Individual Drone Path Following	Test individual drone control algorithms in simulation across diverse trajectories (curves, altitude changes) for tracking and stability.	Simulink Environment
Inter-Drone Communication & Coordination	Simulate and verify inter-drone communication protocols and coordination logic (e.g., commanding multiple drones to a common waypoint simultaneously or sequentially).	Simulink Environment
<i>Validation</i>		
Scenario-Based Swarm Behaviour Testing	Simulate the drone swarm operating in various mission scenarios (e.g., area search patterns, N amount of hotspots, cooperative hotspot investigation, response to detected hotspots, dynamic re-tasking) to validate overall swarm effectiveness, coordination, and robustness.	Simulink Environment, Defined Mission Scenarios
<b>Structure (Max Take-Off Weight 250 g)</b>		
<i>Verification</i>		
Critical Load Case Analysis	Define critical flight/landing load cases, apply to structure in simulation, calculate stresses and deflections.	CAD Model, FEA Software (if used)

Continued on next page

Table 15.5: System Level Verification and Validation Plan – Continued

Test	Explanation	Resources
Weight Budget Management	Maintain a detailed weight budget, cross-referenced with 3D CAD model's mass calculations.	CAD Model, Spreadsheet
<i>Validation</i>		
Static Load Test	Perform a simplified static load test applying representative loads to the physical structure to assess its ability to withstand critical loads.	Physical Prototype, Test Rig, Weights
Prototype Weighing	Weigh the complete, flight-ready L.O.R.A.X. prototype using a precision laboratory scale.	L.O.R.A.X. Prototype, Precision Scale (TU Delft Aerospace Faculty)
<b>Propulsion (Thrust and Noise &lt; 35 dB)</b>		
<i>Validation</i>		
Thrust Generation (Manufacturer Specs)	Compare manufacturer's specifications of propulsion unit (motor + propeller) with desired performance for L.O.R.A.X.	Manufacturer Datasheets
Thrust Stand Test	Confirm propulsion unit performance using a thrust stand.	Thrust Stand (approx. 1000 EUR - Tyto Robotics Series 1585 or similar)
Wind Tunnel Performance Test	Validate propulsion unit performance under realistic flight conditions using a portable wind tunnel (if feasible).	Portable Wind Tunnel
Noise Emission Test	Measure noise emission level with a sound level meter to ensure it stays below 35 dB.	Sound Level Meter

# 16 Development

After finalising the initial design phase, it is important to get an outlook on the future of the L.O.R.A.X. project. This chapter presents a conceptual development plan that outlines the next logical phases of the project. Next to that, the chapter presents a more detailed manufacturing and integration plan, discussing the manufacturing strategies and outlining the sequence for the subsystem assembly.

## 16.1. Project Design and Development Plan

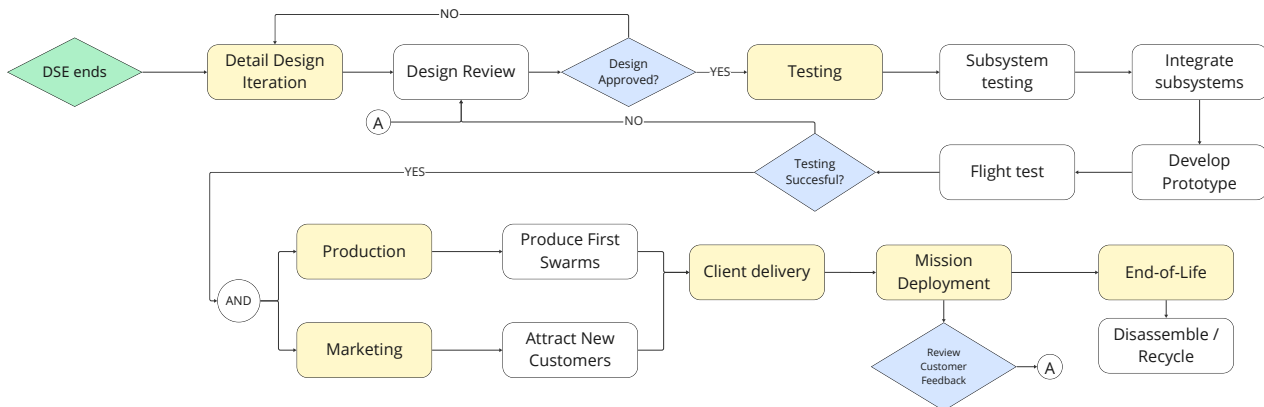


**Figure 16.1:** Project design and development logic diagram. After receiving customer feedback, the flow returns to the design review stage, iterating from Block A back to Block A.

A design and development flow diagram for the continuation of the L.O.R.A.X. project is shown in [Figure 16.1](#). The diagram starts right at the end of the DSE and shows the different (sub)phases that would be applicable when the project is continued. It starts with an iteration on the detailed design that came out of the DSE itself and ends with the end-of-life phase. In [Appendix C](#), an estimated timeline of these phases is presented in the form of a Gantt chart.

## 16.2. Manufacturing and Integration Plan

In this section, the manufacturing processes of each part from the final design will be discussed for both the drone and the launching system. Note that this is a conceptual approach to how the drone can be manufactured. However, since there was little time to optimise the production process, some processes might be subject to change in future phases.

### Drone Node Manufacturing and Integration Plan

#### Manufacturing of Parts

- **Annular Wing:** The annular wings will be manufactured in two separate parts, a leading edge section and a trailing edge section (as shown in [Appendix F](#)). The manufacturing process being considered is to lathe an EVA CF65 foam block using a CNC machine, since this allows for precisely cutting the annular wing shape. To fit the internal components, the designated volumes will be cut out after the annular wings have been shaped.
- **Motor Fairings:** The motor fairings will be 3D-printed with PLA filaments using the CAD model as reference. This method is chosen since it is cost-friendly compared to other machining methods.
- **Strut Fairings:** The fairings that fit around the carbon fibre struts will be wire cut from an EVA CF65 foam block. This method does not require expensive machines and is much more efficient and precise compared to cutting by hand.
- **Rail System:** The rail system will be made from aluminium sheets. These sheets can be stamped into the desired shape. Each of the three rail systems consists of three separate aluminium parts, namely, the guide rail, carriage, and battery holder. All of these will use the same manufacturing method which is a commonly used method and can reach the required tolerances.

The remaining components shown in [Appendix F](#) are COTS components, chosen specifically to fit the current design. Once the COTS components have arrived, they can be fitted inside the trailing edge section along with

the carriage system. After that, the leading edge section of the airframe can be glued to the trailing edge.

### **Launching System Manufacturing and Integration Plan**

For the launching system, only the gears and gear attachment points have to be manufactured by 3D printing. The wheels, rods, bearings, servo, and PVC tube are COTS available. To integrate the components, first, the PVC tube has to be cut to the correct length. After that, the 3D printed gears can be glued to the pipe. Finally, the rods with the wheels attached have to be connected to the gears. For more detailed information on the components, see [Appendix F](#).

# 17 Conclusion & Recommendations

The goal of the L.O.R.A.X. project was to design a swarm of rotating cylindrical wing drones for effective aerial wildfire detection and mapping. This resulted in a unique and novel design that features a rotating cylindrical wing that shifts its centre of gravity to pitch and yaw. The drone is significantly more power efficient than quadcopter alternatives featuring similar endurance to fixed-wing aircraft, but in a much smaller form factor.

By extending the single-drone concept to an optimized 10-node swarm, this project demonstrates a solution for a critical real-world problem. The L.O.R.A.X. system strikes a unique balance between fast area coverage (10 km<sup>2</sup>), high-resolution data, and a dramatically lower cost (€16,705) than traditional methods, directly addressing the urgent market need for real-time, early-stage fire detection.

## 17.1. Achievements

The results of this project is built upon a few achievements that prove the viability of the L.O.R.A.X. concept.

Firstly, a revolutionary new drone concept was presented which utilises a rotating cylindrical wing which steers by moving its centre of gravity inducing gyroscopic precession. Driven by the manoeuvrability of the drone, a contra-rotating propeller configuration was chosen. This concept satisfied the critical requirement that each actuator should provide thrust, spin and control, resulting in a very simple drone that can work in powered, controlled flight.

### Concept Feasibility and Flight Dynamics

A new methodology was established to analyse its unique aerodynamics. Moving beyond simplified models, to qualitatively assess the aerodynamic effects of the L.O.R.A.X. drone, RANS simulations were used. These effects were then implemented into a simplified Panel Method. This analysis established the fundamental design parameters—an aspect ratio of 2 and a NACA63(3)018 airfoil.

Using these aerodynamics, a flight dynamics module was added to the simulation. This uncovered the core flight characteristic of the system. Among the very important trade-off between gyroscopic stability and manoeuvrability. A proof-of-concept cascaded PID controller was developed, proving that despite the coupled dynamics, the drone's roll and pitch can be effectively regulated to maintain stable flight using a mixer.

### Integrated System Design

A complete physical design was developed in significant detail, successfully integrating all mechanical, power, and electronic components within a 250 g mass constraint, achieving a final assembly mass of just 237 g. This makes this drone very light and provides good performance. Furthermore, various subsystems were developed in really high detail:

- **Propulsion and Power:** The selection of contra-rotating propellers and E-flite Park 250 motors, paired with a custom 2S3P LiPo battery configuration, ensures a flight endurance exceeding 10 minutes while providing the necessary torque for spin-up and the control authority for flight.
- **Structure and Materials:** The use of EVA CF65 foam and carbon fibre struts provides a lightweight and robust structure. A clear emphasis on Design for Disassembly (DfD) aligns the project with sustainability principles.
- **Electronics:** A highly detailed, custom dual-MCU electronics architecture was designed to manage high-frequency state estimation, flight control, and communications, demonstrating a clear path to hardware implementation. This included the design of multiple custom PCBs.

Due to its high detail, the system is very close to first prototypes right after DSE ends.

### Mission Capability & Swarming

The project successfully designed a complete mission architecture, from launch to data delivery. A feasible in-air launch system was designed to deploy the drones with immediate gyroscopic stability.

Additionally, the swarming of the drone was analysed. The 'detect-confirm' payload strategy, combining visual and IR sensors, was verified to provide effective detection over a 10 km<sup>2</sup> area. Finally, the communications system was proven capable of handling the required data rates for swarm coordination and data transmission to a mothership and ground station.

All in all, this project presents a solution to early- detection effective aerial wildfire detection in a unique, very-lightweight and affordable solution.

## 17.2. Recommendations

Despite these achievements, certain limitations and areas for future development were identified. The drone's manoeuvrability, particularly its yaw rate, remains limited, not fully meeting initial performance expectations. However, it was shown that there would always be a trade-off between strong gyroscopic stability and manoeuvrability, making it an acceptable for this mission application.

Compliance with EASA Open Category A1/C0 regulations presents a challenge, requiring the system to operate under the 'specific' category due to flight altitude and speed parameters. The robustness of the simulation models, particularly for RANS aerodynamic predictions and overall system reliability, necessitates further extensive physical testing, including wind tunnel experiments and flight trials, for comprehensive validation and quantification.

To reduce the risk associated with development of the L.O.R.A.X. drone, a derisking roadmap was created. The recommendations will be divided into three categories detailing how critical they are for the feasibility and uncertainty of this concept.

**Critical Priority:** These recommendations should be the first steps taken into further development of the drone as they are critical to see whether the concept of the drone is feasible. These recommendations are roughly equivalent to a Technology Readiness Level (TRL) of 3-4.

1. Conduct wind tunnel tests on a full-scale model to validate the baseline aerodynamic ( $L/D$ ,  $C_m$ ) and control (CP location) models. This is critical as the entire design relies on this.
2. Investigate the Magnus effect on flight performance of the drone. Evaluate if the drone can still fly with a side wind.
3. Validate the flight dynamics module of the simulation. A very large part of the feasibility assessment of the drone is based on this simulation, so it is critical it is as accurate as possible.
4. Investigate and optimise control algorithms further. The current control algorithms are just a proof-of-concept design. Investigations into making the controllers more robust and tuned to the real life hardware are critical for successful flight.

**High Priority:** These recommendations should be covered after the critical priority recommendations as they are important for the design of the drone. These recommendations fall under a TRL of 4.

1. Build a Hardware-in-the-Loop simulation to test the flight controller with the real MCUs against the unverified flight dynamics model. This verifies the control logic and sensor fusion implementation before the first flight.
2. Develop advanced image compression methods to ensure onboard processing of the image data is possible. At the current moment, these algorithms have not yet been sufficiently researched and implemented. These are critical for the swarming and communication systems.
3. Investigate the potential problem of overheating of batteries due to foam isolation. For now, holes have been added to the leading edge but further analysis should be done on whether this is sufficient.
4. Optimise the design for the in-air unit launcher, to ensure that the current wheel arm systems do not obstruct the drone's orientation during launch. This could potentially be an issue reducing the reliability of the launching system.
5. Design a mothership drone that carries the launch system and required communication and computation hardware. This would provide a further insight in the total costs of the solution.
6. Investigate launching statically from a tower or from another aircraft such as an airplane or helicopter. This would improve the versatility of the system.
7. Investigate compliance with the EASA Open Category A1/C0 regulations. Due to the specifications of the drone, the system is required to operate under the 'specific' category due to flight altitude and speed parameters. Besides that, this category is required if you want to fly autonomous and beyond line-of-sight. Further investigation should be done into what would be required to license the drone and whether this would have any further impact on the design.
8. Conduct physical flight tests to validate the integrated system's performance (stability in gusts, actual power consumption, and maneuverability)

**Medium Priority:** These recommendations are important to evaluate longer term to improve performance and market attractiveness of the system. These recommendations fall under a Technology Readiness Level (TRL) of 4-5.

1. After gathering more data, perform a reiteration on the design using Multidisciplinary Design Optimisation (MDO). This will improve the performance of the drone.
2. Investigate reversing spin direction mid-flight, as this would significantly improve manoeuvring capabilities. This could make swarming algorithms a lot easier and generally improves mission performance of the drone.
3. Exploring novel spin-independent antenna designs to overcome current radiation pattern limitations.
4. Investigate precise operational costs, as these are still rather uncertain at the moment. This is very important for the market analysis of the project. Additionally, investigation needs to be done into upscaling production, potentially reducing costs even further.
5. Investigating increasing the swarm size. This could potentially increase the capabilities of the swarm, and as the concept is very scalable this could be an easy way to increase the effectiveness of the system.
6. Perform a thorough Verification & Validation of the entire system.

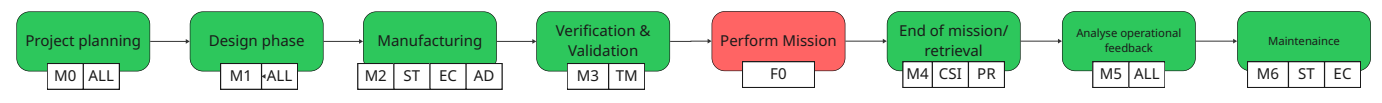
These recommendations are critical to advance the L.O.R.A.X. project from a proof-of-concept to a robust and deployable solution.

# Bibliography

- [1] C. Alayón, K. Säfsten, and G. Johansson. "Conceptual sustainable production principles in practice: Do they reflect what companies do?" In: *Journal of Cleaner Production* 141 (Jan. 2017), pp. 693–701. ISSN: 09596526. DOI: [10.1016/j.jclepro.2016.09.079](https://doi.org/10.1016/j.jclepro.2016.09.079).
- [2] Martin Edward Alexander. *Estimating the length-to-breadth ratio of elliptical forest fire patterns*. Tech. rep. 1985. URL: <https://www.researchgate.net/publication/284389352>.
- [3] Ahmad A.A. Alkhatib. *A review on forest fire detection techniques*. 2014. DOI: [10.1155/2014/597368](https://doi.org/10.1155/2014/597368).
- [4] Yunes Alqudsi and Murat Makaraci. "UAV swarms: research, challenges, and future directions". In: *Journal of Engineering and Applied Science* 72 (1 Dec. 2025). ISSN: 25369512. DOI: [10.1186/s44147-025-00582-3](https://doi.org/10.1186/s44147-025-00582-3).
- [5] Niels Andela et al. "The Global Fire Atlas of individual fire size, duration, speed and direction". In: *Earth System Science Data* 11.2 (Apr. 2019), pp. 529–552. ISSN: 18663516. DOI: [10.5194/essd-11-529-2019](https://doi.org/10.5194/essd-11-529-2019).
- [6] Jennifer K Balch et al. *The fastest-growing and most destructive fires in the US (2001 to 2020)*. Tech. rep. 2020. URL: <https://www.science.org>.
- [7] Ragala Chethan and Indrani Kar. "Multi-Agent Coverage Path Planning using a Swarm of Unmanned Aerial Vehicles". In: *INDICON 2022 - 2022 IEEE 19th India Council International Conference*. Institute of Electrical and Electronics Engineers Inc., 2022. ISBN: 9781665473507. DOI: [10.1109/INDICON56171.2022.10039853](https://doi.org/10.1109/INDICON56171.2022.10039853).
- [8] Peter R. N. Childs. "Rotating Flow". In: *Rotating Flow*. Ed. by Peter R. N. Childs. Elsevier Inc., 2011. Chap. 6, pp. 177–247. DOI: [10.1016/B978-0-12-382098-3.00006-8](https://doi.org/10.1016/B978-0-12-382098-3.00006-8).
- [9] Miguel G. Cruz and Martin E. Alexander. "The 10% wind speed rule of thumb for estimating a wildfire's forward rate of spread in forests and shrublands". In: *Annals of Forest Science* 76.2 (June 2019). ISSN: 1297966X. DOI: [10.1007/s13595-019-0829-8](https://doi.org/10.1007/s13595-019-0829-8).
- [10] Calum X. Cunningham, Grant J. Williamson, and David M.J.S. Bowman. "Increasing frequency and intensity of the most extreme wildfires on Earth". In: *Nature Ecology and Evolution* 8.8 (Aug. 2024), pp. 1420–1425. ISSN: 2397334X. DOI: [10.1038/s41559-024-02452-2](https://doi.org/10.1038/s41559-024-02452-2).
- [11] Z. Czyż et al. "Wind Tunnel Performance Tests of the Propellers with Different Pitch for the Electric Propulsion System". In: *Sensors* 22.1 (2021). Basel, Switzerland, p. 2. DOI: [10.3390/s22010002](https://doi.org/10.3390/s22010002).
- [12] Mark Drela and Michael Selig. *UIUC Airfoil Coordinates Database*. Accessed: 2025-06-17. 1996. URL: <https://m-selig.ae.illinois.edu/props/propDB.html>.
- [13] N.A.P. Even. "Parametric Study of Aerodynamic Interference on Global Propeller Performance Using OpenVSP". PhD thesis. Twente: University of Twente, 2024. URL: [https://essay.utwente.nl/104738/1/Even\\_MA\\_ET\\_EFD.pdf](https://essay.utwente.nl/104738/1/Even_MA_ET_EFD.pdf).
- [14] Herman S. Fletcher. *Experimental Investigation Of Lift, Drag, and Pitching Moment Of Five Annular Airfoils*. English. Tech. rep. NACA TN 4117. Washington: NACA, Oct. 1957. URL: <https://ntrs.nasa.gov/citations/19930084906>.
- [15] Masami Fukuda et al. *Forest fire detection based on MODIS satellite imagery, and Comparison of NOA A satellite imagery with fire fighters' information*. Tech. rep. URL: <https://www.researchgate.net/publication/251764783>.
- [16] Zachary Gaines, Maximum Wilder-Smith, and Cristian Rodriguez. *Bronco Ember an Edge Computing Acceleration Platform with Computer Vision*. Tech. rep.
- [17] Enric Galceran and Marc Carreras. "A survey on coverage path planning for robotics". In: *Robotics and Autonomous Systems* 61 (12 Dec. 2013), pp. 1258–1276. ISSN: 09218890. DOI: [10.1016/j.robot.2013.09.004](https://doi.org/10.1016/j.robot.2013.09.004).
- [18] S Hoerner. *Fluid-Dynamic Drag*. -, 1965.
- [19] Harvey H. (Editor) Hubbard. *Aeroacoustics of Flight Vehicles: Theory and Practice, Volume 1: Noise Sources*. Reference Publication NASA RP-1258, Vol. 1. Washington, D.C.: National Aeronautics and Space Administration, 1991.
- [20] Kevin Lim. *Lidar Remote Sensing of Forest Canopy and Stand Structure*. Accessed on ResearchGate. 2006. URL: <https://www.researchgate.net/publication/252766380>.
- [21] Mathworks. *Simulink*. 2024. URL: <https://www.mathworks.com/products/simulink.html> (visited on 04/25/2025).
- [22] Dimitrios Meimetis et al. "An Architecture for Early Wildfire Detection and Spread Estimation Using Unmanned Aerial Vehicles, Base Stations, and Space Assets". In: *Drones and Autonomous Vehicles* 1.3 (2024), pp. 10006–10006. ISSN: 2958-7689. DOI: [10.35534/dav.2024.10006](https://doi.org/10.35534/dav.2024.10006).
- [23] D. C. Mikkelson, G. A. Mitchell, and L. J. Bober. "Summary of Recent NASA Propeller Research". In: *AGARD Fluid Dynamics Panel Meeting on Aerodynamics and Acoustics of Propellers*. NASA Technical Memorandum NASA-TM-83733, Report Number: E-2216, NAS 1.15:83733. Toronto, Canada: NASA Lewis Research Center, Oct. 1984. URL: <https://ntrs.nasa.gov/citations/19840024274>.
- [24] NASA Glenn Research Center. *Propeller Thrust*. <https://www1.grc.nasa.gov/beginners-guide-to-aeronautics/propeller-thrust/>. Accessed: 2025-06-17. 2023. URL: <https://www1.grc.nasa.gov/beginners-guide-to-aeronautics/propeller-thrust/>.
- [25] NASA Goddard Space Flight Center. *Rules for the Design, Development, Verification, and Operation of Flight Systems*. NASA Goddard Space Flight Center. 2023.
- [26] P. Rajeevalochanam et al. "Comparative Study of Two and Three Blade Mini Propellers Aerodynamic Performance". In: *Proceedings of ASME Turbo Expo 2016: Turbomachinery Technical Conference and Exposition*. Seoul, South Korea: ASME, June 2016, V001T01A007. DOI: [10.1115/GT2016-56174](https://doi.org/10.1115/GT2016-56174).
- [27] Gwynfor D Richards. *AN ELLIPTICAL GROWTH MODEL OF FOREST FIRE FRONTS AND ITS NUMERICAL SOLUTION*. Tech. rep. Department of Mathematics and Computer Science, Brandon University, 1990, pp. 1163–1164.
- [28] Jeff Sanny and Samuel Ling. *University Physics Volume 1*. Houston, Texas: OpenStax, 2016. Chap. 11.
- [29] Allen W. Scott. *Cooling of Electronic Equipment*. New York, NY: John Wiley & Sons, 1974.

- [30] Bryan Shaddy et al. "Generative Algorithms for Fusion of Physics-Based Wildfire Spread Models with Satellite Data for Initializing Wildfire Forecasts". In: *Artificial Intelligence for the Earth Systems* 3.3 (Apr. 2024). DOI: [10.1175/aies-d-23-0087.1](https://doi.org/10.1175/aies-d-23-0087.1).
- [31] Pei Shi et al. "An Efficient Forest Fire Detection Algorithm Using Improved YOLOv5". In: *Forests* 14.12 (Dec. 2023). ISSN: 1999-4907. DOI: [10.3390/f14122440](https://doi.org/10.3390/f14122440).
- [32] S. Timoshenko and J. N. Goodier. *Theory of Elasticity*. 2nd. Engineering Societies Monographs. New York, Toronto, London: McGraw-Hill Book Company, Inc., 1951.
- [33] Vesela Veleva and Michael Ellenbecker. "Indicators of sustainable production: framework and methodology". In: *Journal of Cleaner Production* 9.6 (Dec. 2001), pp. 519–549. ISSN: 09596526. DOI: [10.1016/S0959-6526\(01\)00010-5](https://doi.org/10.1016/S0959-6526(01)00010-5).
- [34] Vinyl Acetate. <https://www.sciencedirect.com/topics/chemistry/vinyl-acetate>. Accessed: 2025-06-24.
- [35] W. L. Gore & Associates. *Tethered Drone Cables: Achieving Long-Term Power and Signal Transmission*. Tech. rep. White paper. W. L. Gore & Associates, 2019. URL: [https://www.gore.com/system/files/2021-04/GORE-Tethered-Drone-Cables-WhitePaper\\_031319.pdf](https://www.gore.com/system/files/2021-04/GORE-Tethered-Drone-Cables-WhitePaper_031319.pdf).
- [36] Nils Wagner. *Theoretical and Experimental Investigation into the flight of an X-Zylo*. Tech. rep. arXiv, 2021. arXiv: [2102.02647v1](https://arxiv.org/abs/2102.02647v1) [physics.flu-dyn].
- [37] Adam C. Watts and Leda N. Kobziar. "Smoldering combustion and ground fires: Ecological effects and multi-scale significance". In: *Fire Ecology* 9.1 (2013), pp. 124–132. ISSN: 19339747. DOI: [10.4996/fireecology.0901124](https://doi.org/10.4996/fireecology.0901124).
- [38] Xikun Wei et al. "A spatio-temporal analysis of active fires over China during 2003-2016". In: *Remote Sensing* 12.11 (June 2020). ISSN: 20724292. DOI: [10.3390/rs12111787](https://doi.org/10.3390/rs12111787).
- [39] B. Mike Wotton et al. "Flame temperature and residence time of fires in dry eucalypt forest". In: *International Journal of Wildland Fire* 21.3 (2012), pp. 270–281. ISSN: 10498001. DOI: [10.1071/WF10127](https://doi.org/10.1071/WF10127).
- [40] Miaomiao Xu et al. "Spinning projectile's attitude measurement with LW infrared radiation under sea-sky background". In: *Infrared Physics & Technology* 90 (May 2018), pp. 214–220. ISSN: 1350-4495. DOI: [10.1016/J.INFRARED.2018.03.017](https://doi.org/10.1016/J.INFRARED.2018.03.017). URL: [https://www.sciencedirect.com/science/article/pii/S1350449517308654?ref=pdf\\_download&fr=RR-2&rr=9510bd0048e4fba7#f0020](https://www.sciencedirect.com/science/article/pii/S1350449517308654?ref=pdf_download&fr=RR-2&rr=9510bd0048e4fba7#f0020).
- [41] Huang Yao, Rongjun Qin, and Xiaoyu Chen. *Unmanned aerial vehicle for remote sensing applications - A review*. June 2019. DOI: [10.3390/rs11121443](https://doi.org/10.3390/rs11121443).
- [42] Long Zhang, Changjiang Shi, and Fuquan Zhang. "Predicting Forest Fire Area Growth Rate Using an Ensemble Algorithm". In: *Forests* 15.9 (Aug. 2024), p. 1493. ISSN: 19994907. DOI: [10.3390/f15091493](https://doi.org/10.3390/f15091493).
- [43] Peter H. Zipfel. *Modeling and simulation of aerospace vehicle dynamics*. Reston, Virginia: American Institute of Aeronautics and Astronautics, 2000. ISBN: 1-56347-456-5. DOI: <https://doi.org/10.2514/5.9781624102509.0000.0000>.

# Functional Flow Diagram

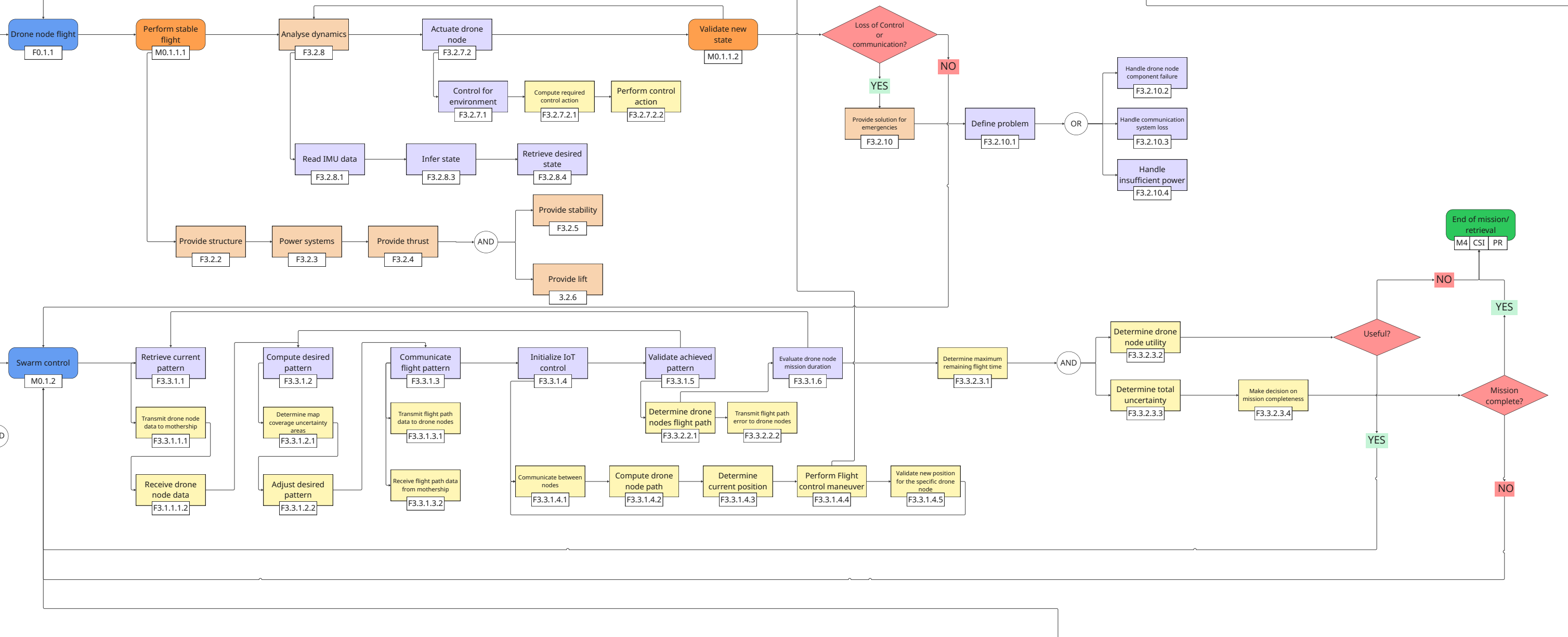
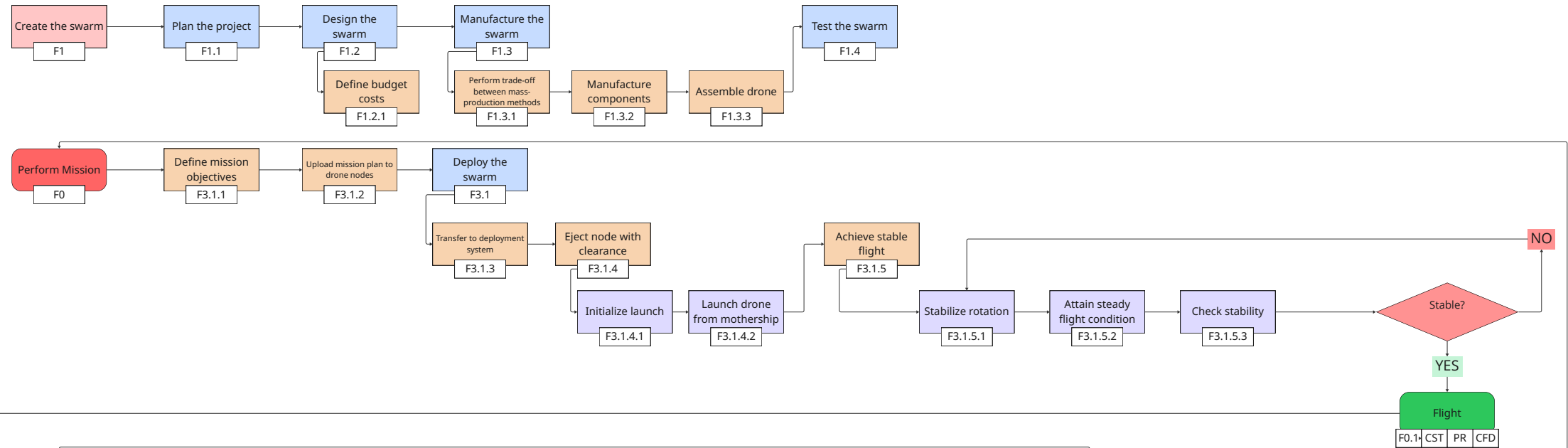


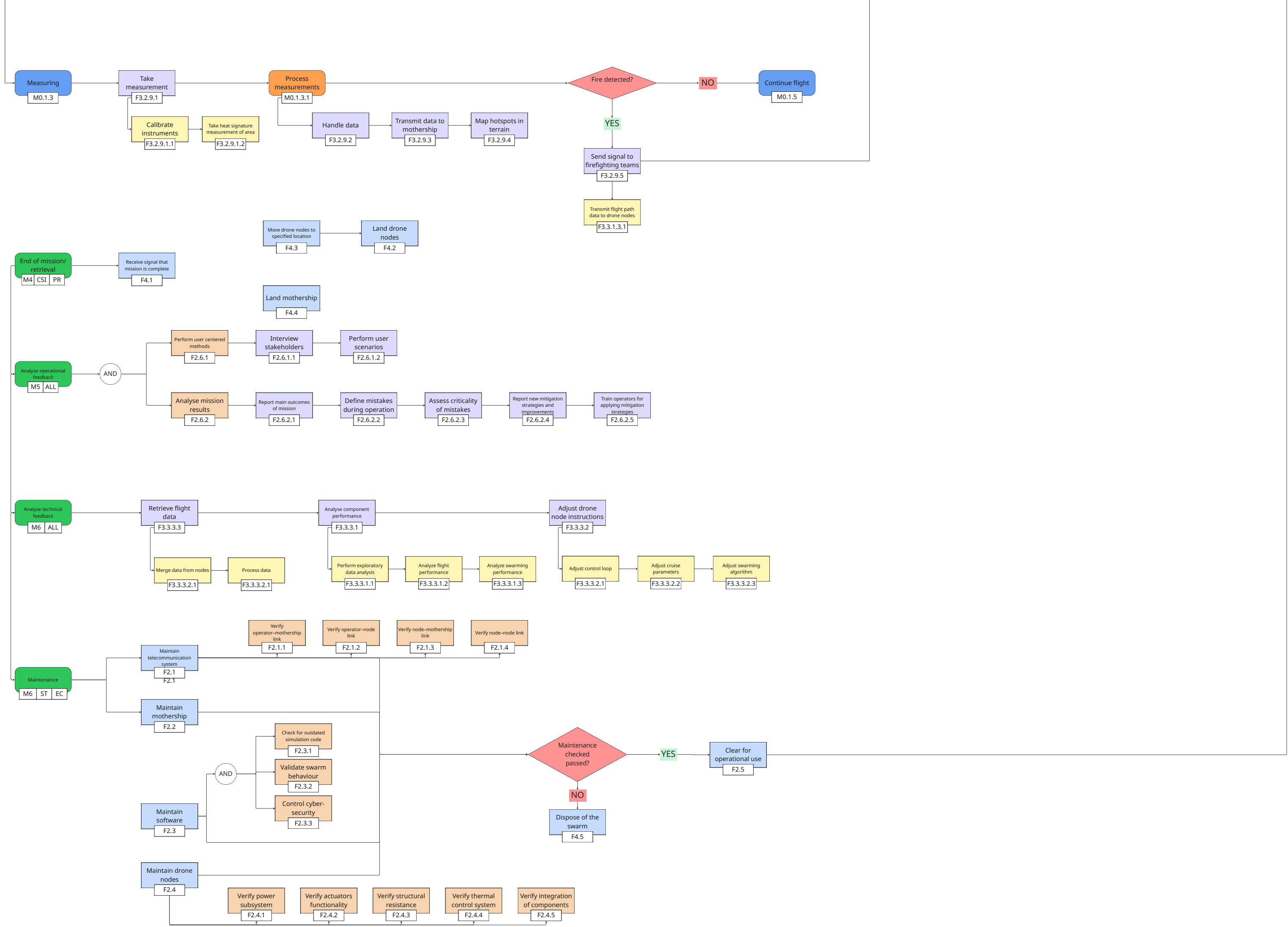
**Legend**

Identifier	Name
TM	Technical Manager
AH	Aerodynamics Head
CST	Control & Stability Head
SW	Swarming Head
ST	Structures Head
CFD	CFD Engineer
AD	Aerodynamic Design Engineer
CSI	Control & Simulation Engineer
EC	Electrical Control Engineer
PR	Propulsion Engineer
ALL	All Members

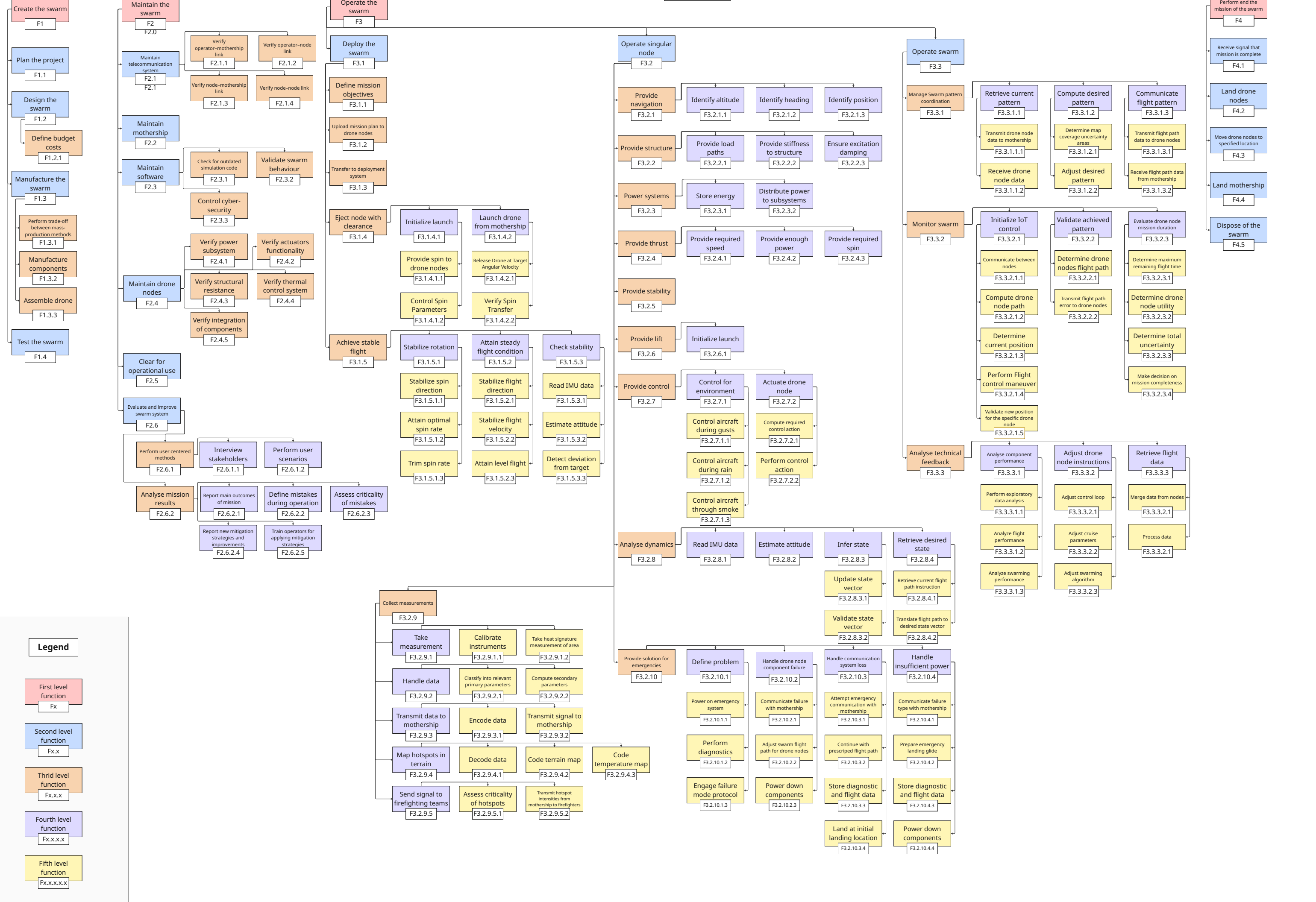
  

<b>Mission</b>	First level function
<b>First level mission function</b>	Second level function
<b>Second level mission function</b>	Third level function
<b>Third level mission function</b>	Fourth level function
<b>Conditionals</b>	Fifth level function





# Perform Mission



## Legend

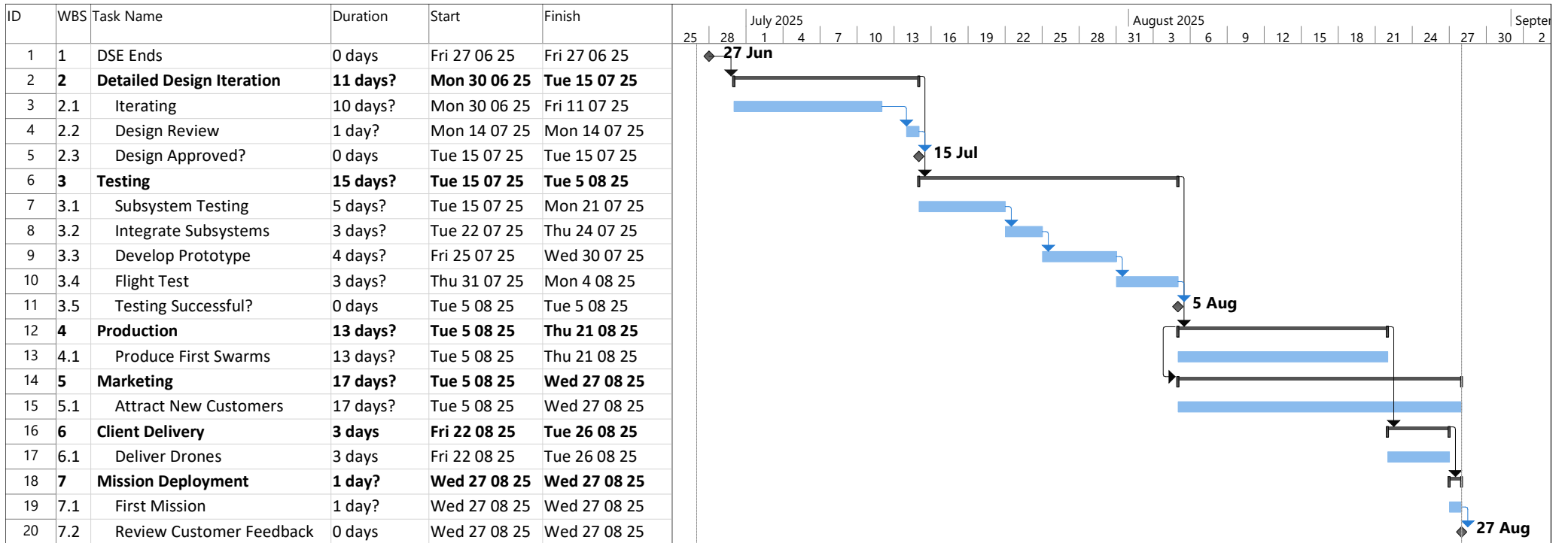
First level function  
Fx

Second level function  
Fx.x

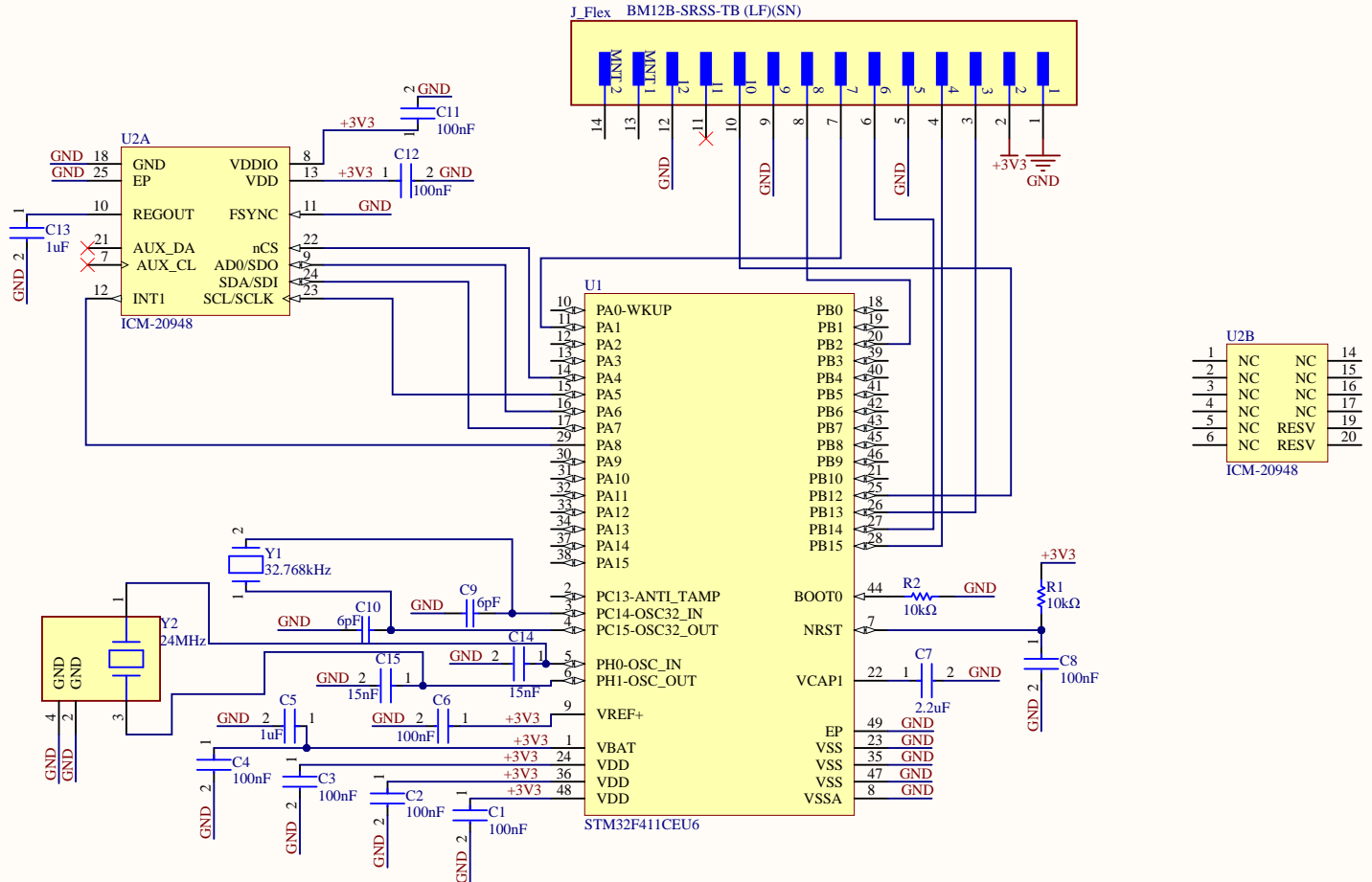
Thrid level function  
Fx.x.x

Fourth level function  
Fx.x.x.x

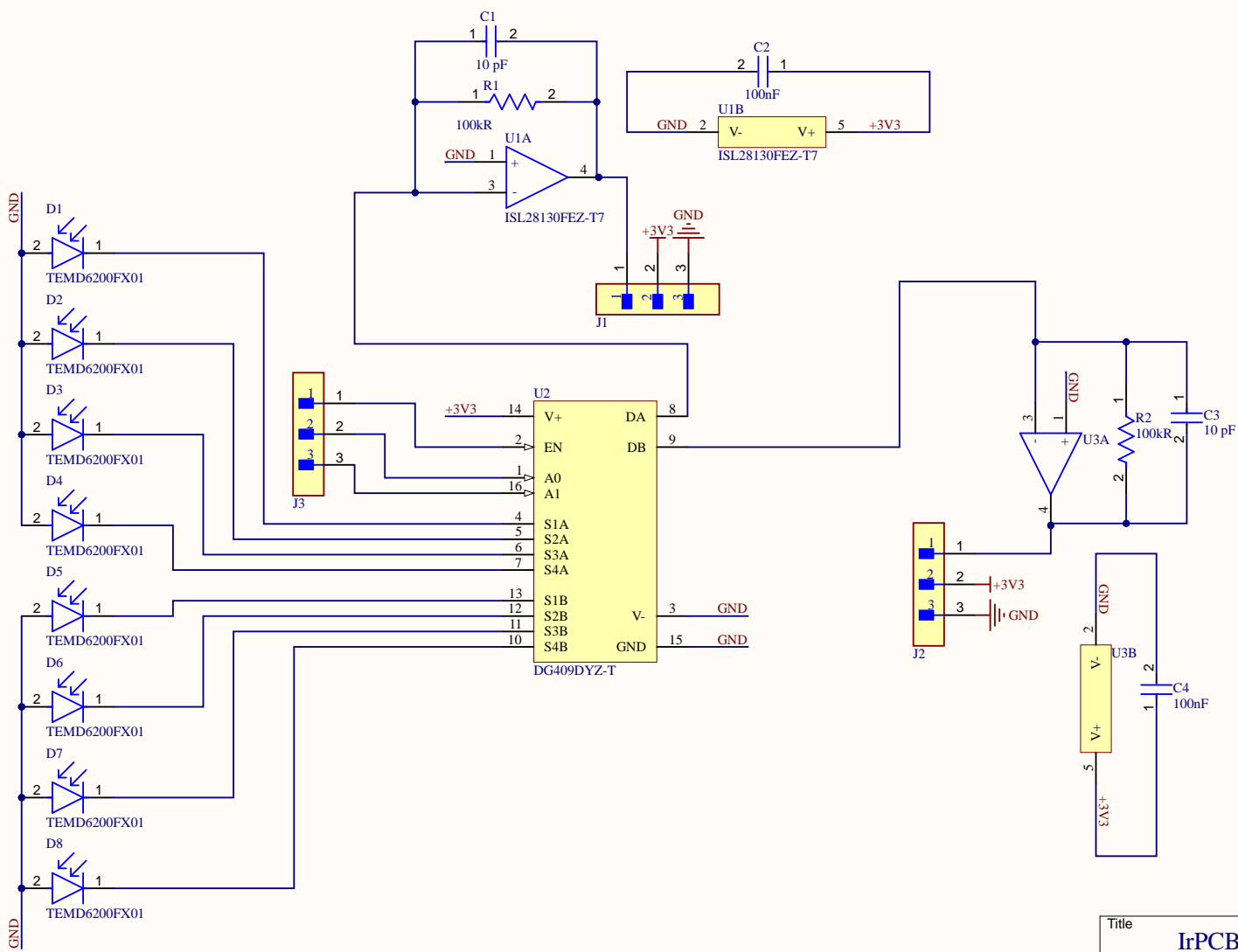
Fifth level function  
Fx.x.x.x.x



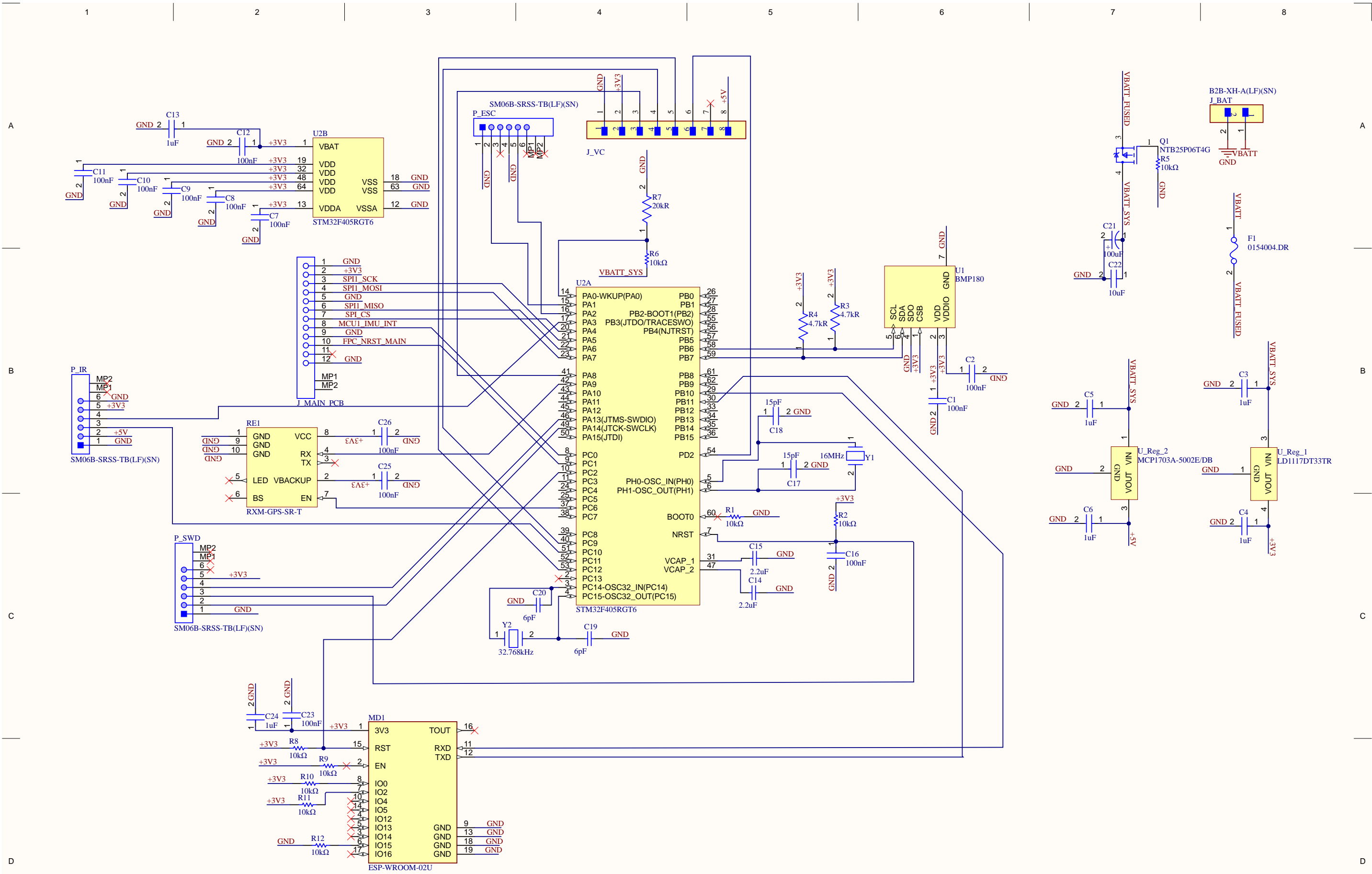
Project: Project Gantt Date: Tue 17 06 25	Task		Inactive Task		Manual Summary Rollup		External Milestone	
	Split		Inactive Milestone		Manual Summary		Deadline	
	Milestone		Inactive Summary		Start-only		Progress	
	Summary		Manual Task		Finish-only		Manual Progress	
	Project Summary		Duration-only		External Tasks			



Title		
<b>MainPCB</b>		
Size	Number	Revision v2.1
A4		
Date:	6/13/2025	Sheet of 1 of 1
File:	C:\Users\...\MainPCBv2.SchDoc	Drawn By: LORAX

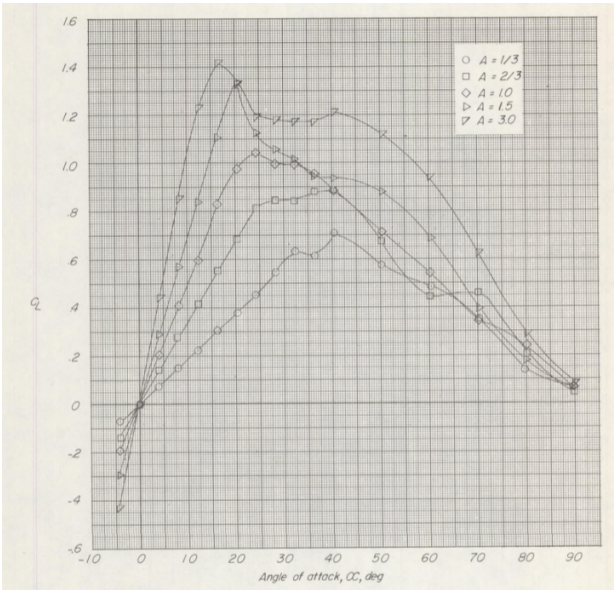


Title		
<b>IrPCB</b>		
Size	Number	Revision
A4		v1.1
Date:	6/13/2025	Sheet of
File:	C:\Users\...IrPCB.SchDoc	1 of 1
		Drawn By:
		LORAX

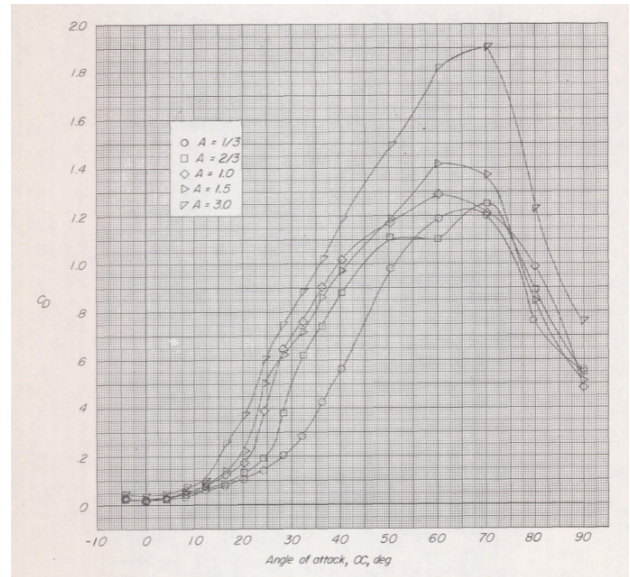


Title		
FlexPCB		
Size	Number	Revision v2.1
A3		
Date:	6/13/2025	Sheet of 1 of 1
File:	C:\Users\...\FlexPCB.SchDoc	Drawn By: LORAX

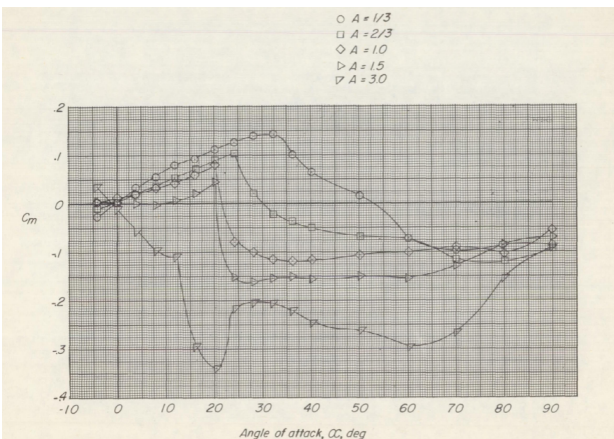
# Appendix E



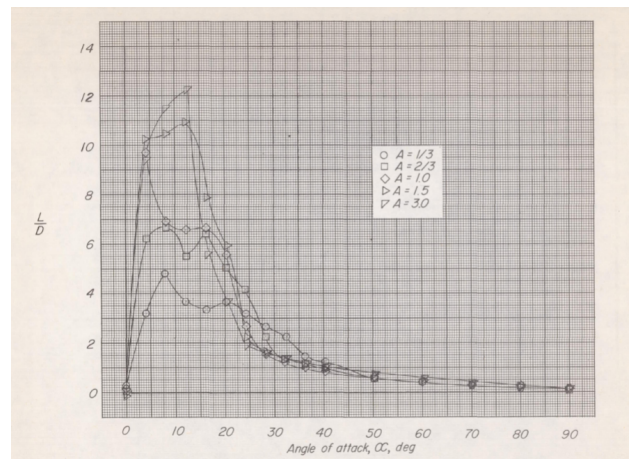
(a) Experimental data from Fletcher [14], showing the lift-to-drag ratio for annular wings with different aspect ratios (diameter/chord).



(b)  $C_L$  vs. angle of attack for five annular wings with different aspect ratios, ranging from 1/3 to 3.0.

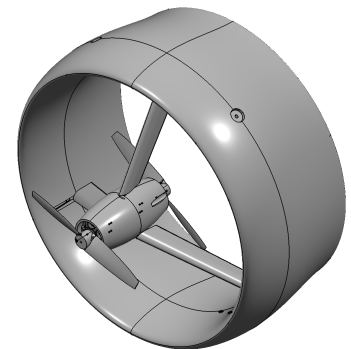


(c)  $C_D$  vs. angle of attack for five annular wings with different aspect ratios, ranging from 1/3 to 3.0.

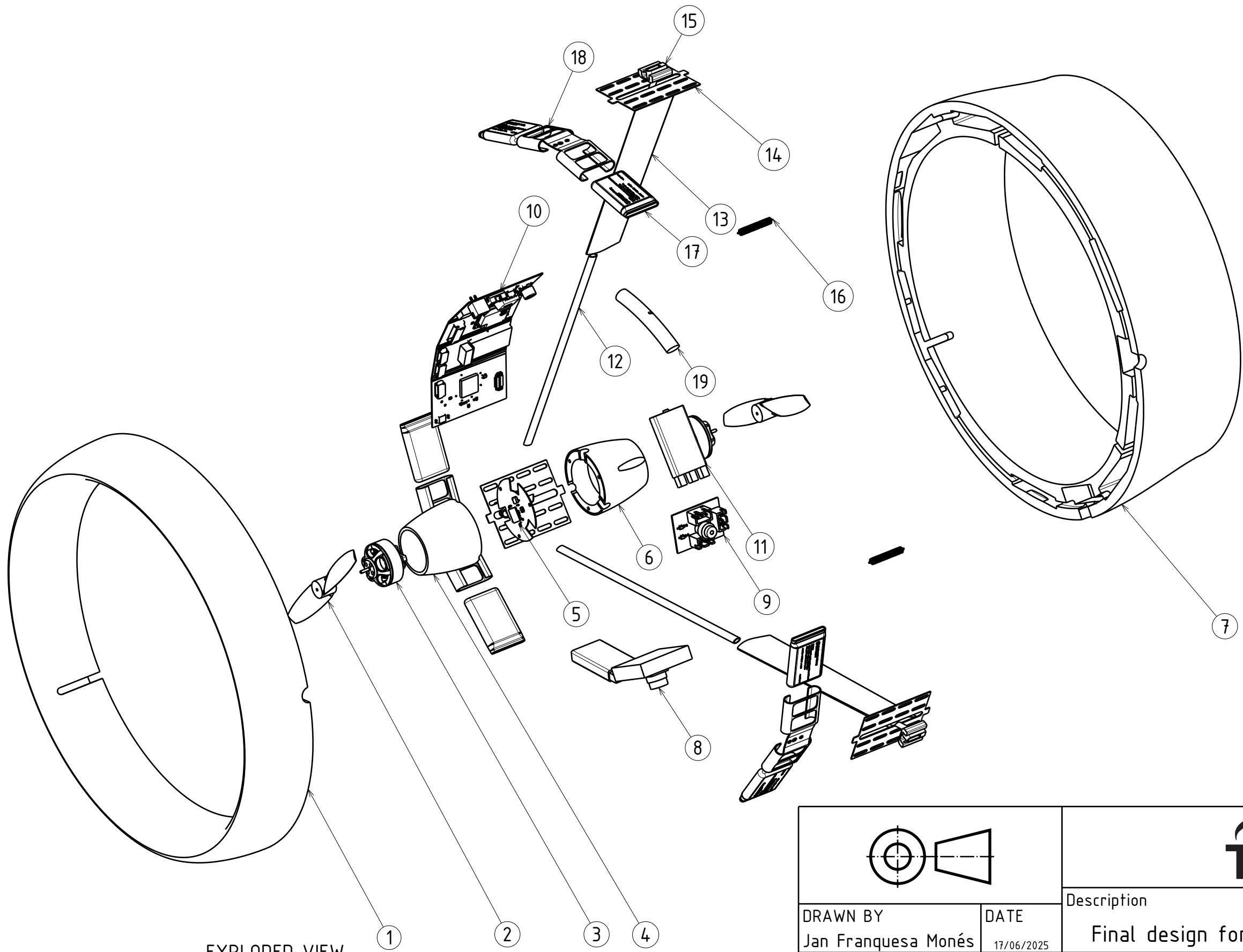


(d)  $C_M$  vs. angle of attack for five annular wings with different aspect ratios, ranging from 1/3 to 3.0.

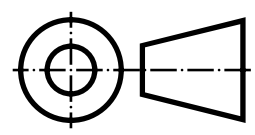
Figure 1: Wind tunnel experiment data obtained by Fletcher [14].



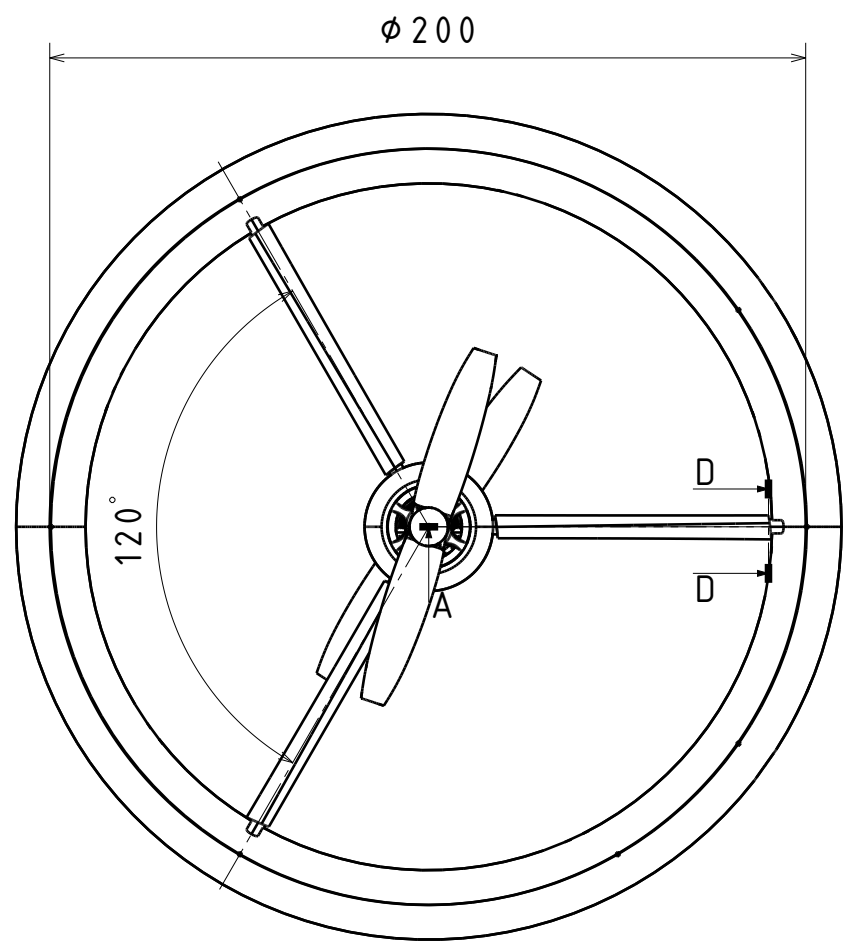
ISOMETRIC VIEW (1:5)



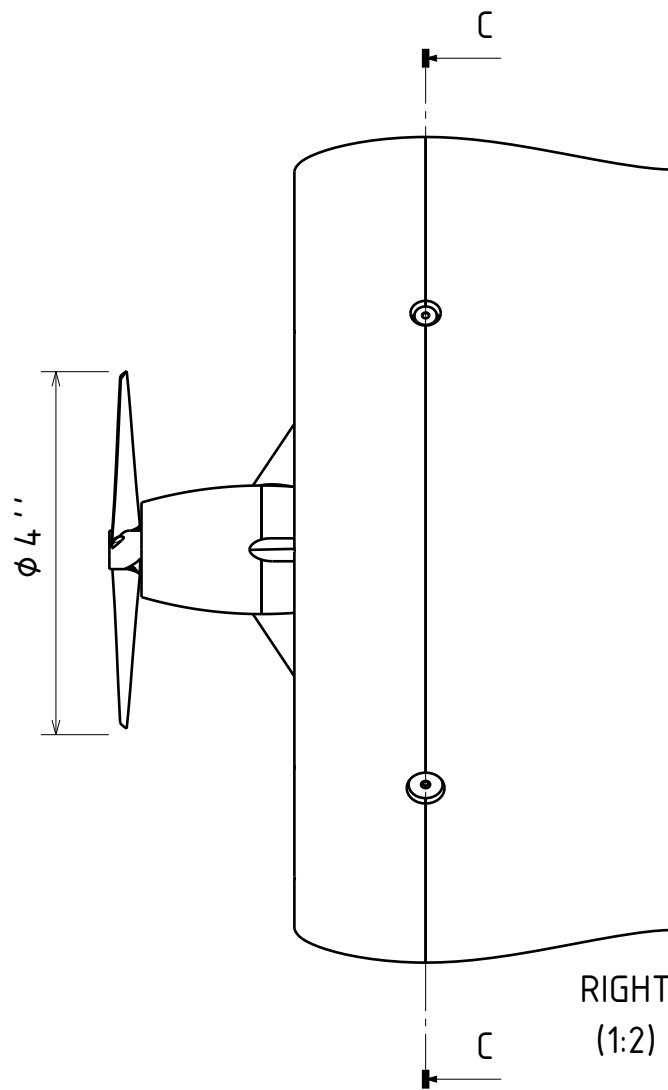
EXPLODED VIEW (1:2)



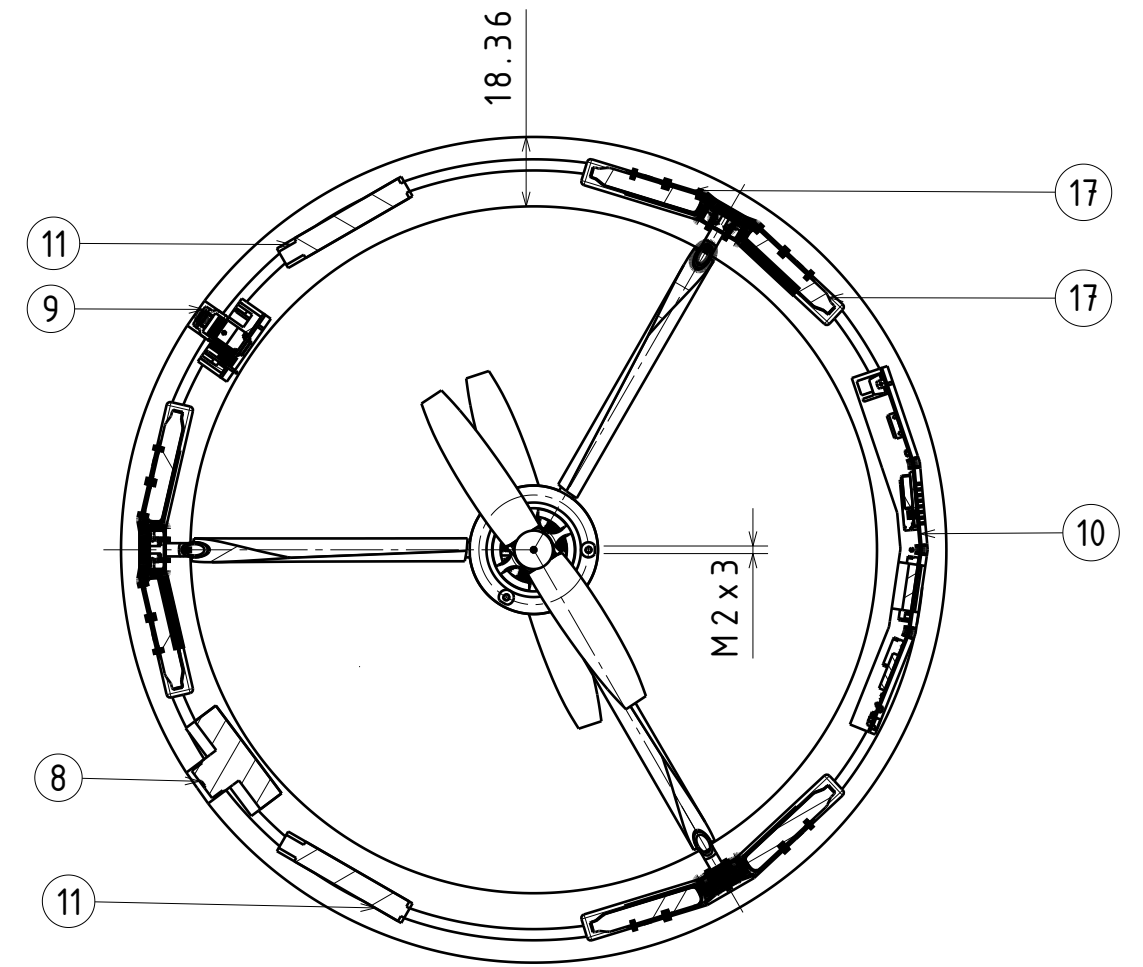
DRAWN BY Jan Franquesa Monés		DATE 17/06/2025		Description Final design for a rotating gyroscopic drone		
CHECKED BY Django van der Plas		DATE 17/06/2025		SIZE A3	Title L.O.R.A.X.	REV A.1
DESIGNED BY DSE Group 13		DATE 17/06/2025		SCALE 1:1	WEIGHT(kg) 0.237	SHEET 1/1



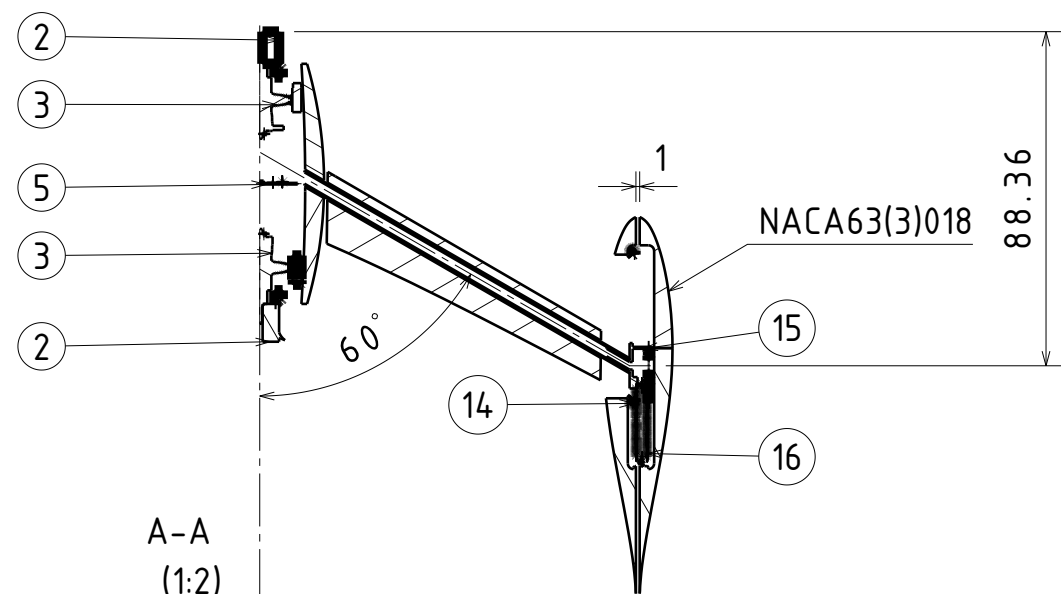
FRONT  
(1:2)



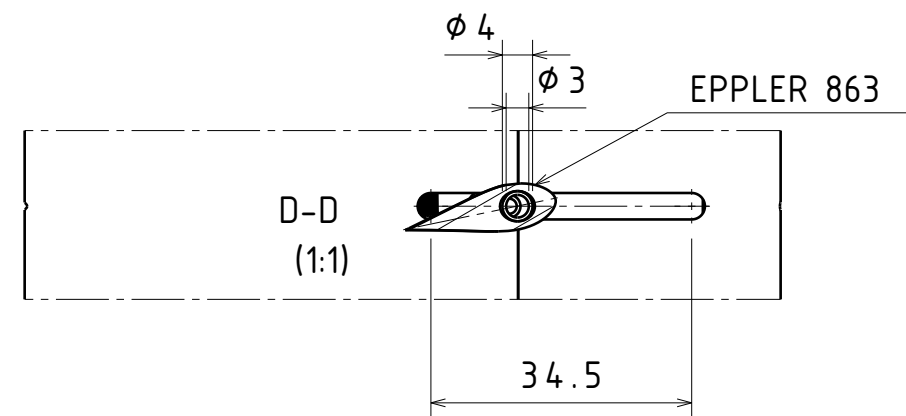
RIGHT  
(1:2)



C-C  
(1:2)

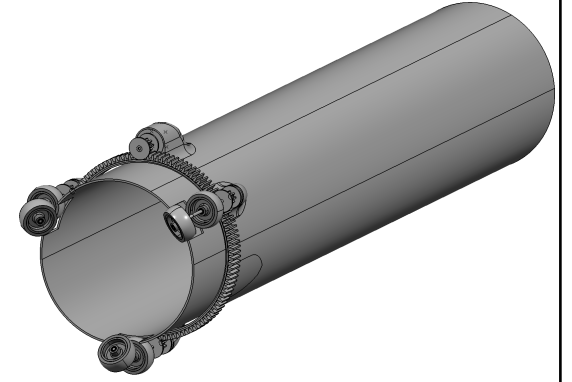
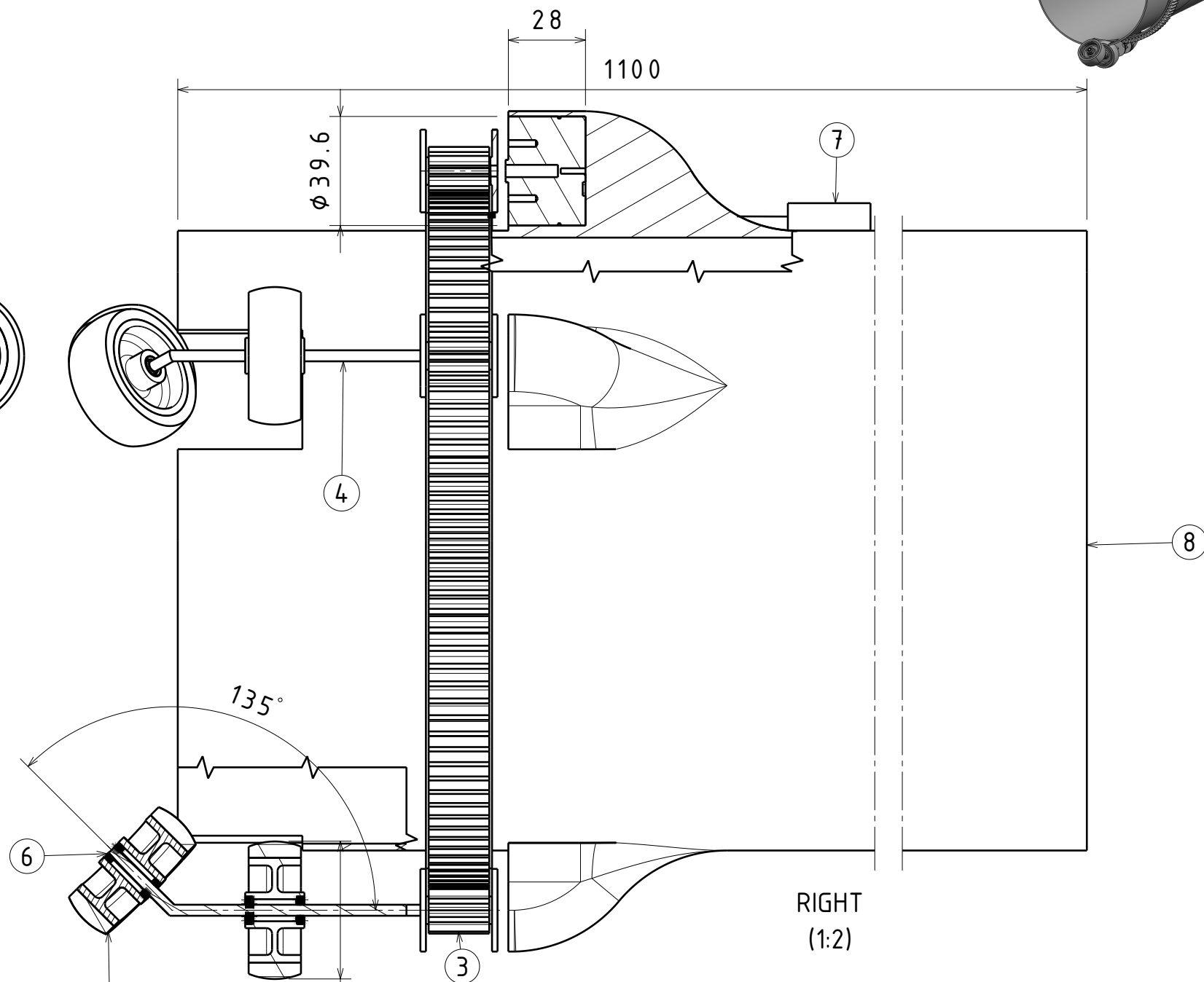
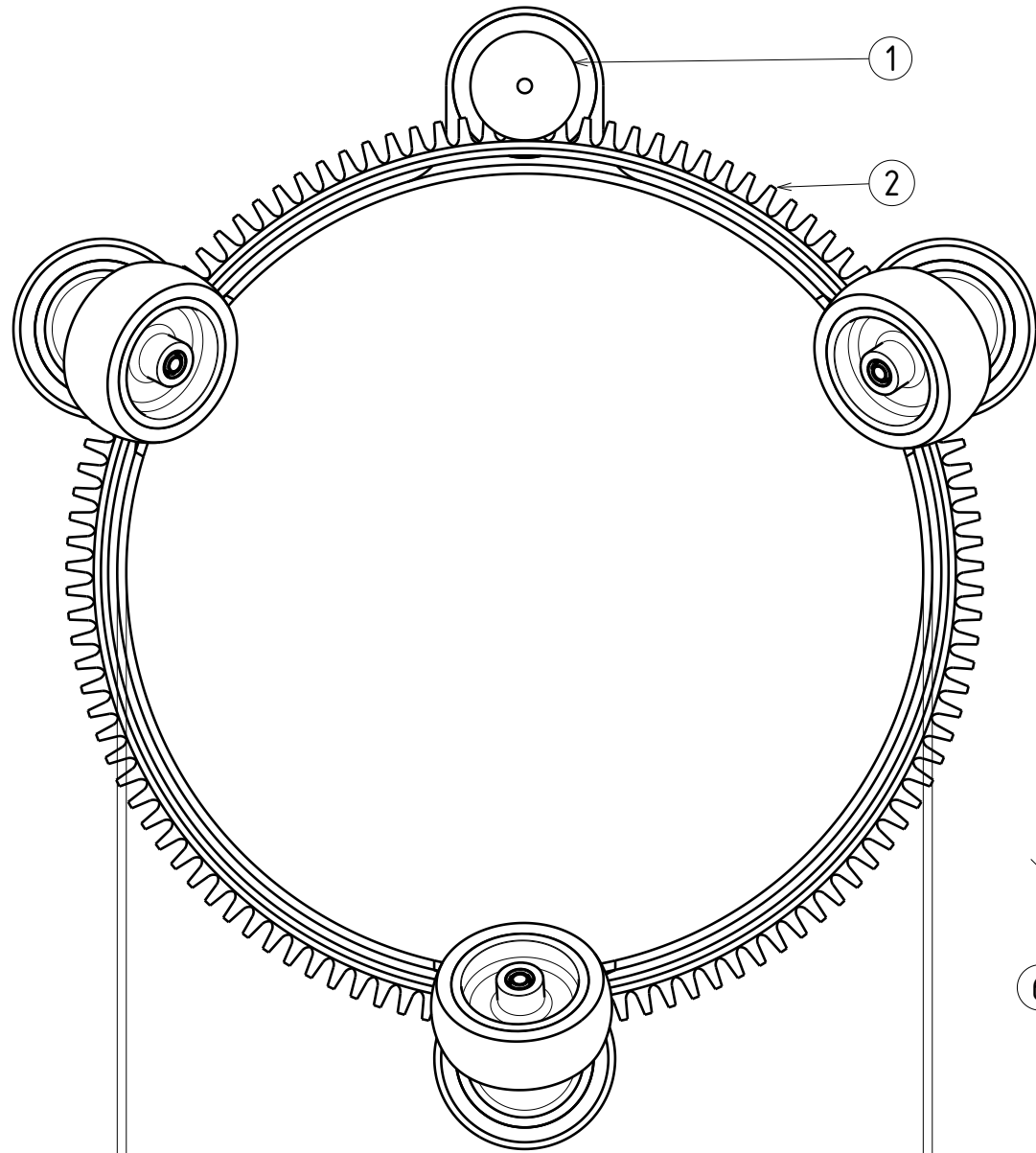


A-A  
(1:2)



D-D  
(1:1)

		Description			
		Final design for a rotating gyroscopic drone			
DRAWN BY Jan Franquesa Monés	DATE 17/06/2025	SIZE A3	Title L.O.R.A.X.	REV A.1	
CHECKED BY Django van der Plas	DATE 17/06/2025	SCALE 1:1	WEIGHT(kg) 0.237	SHEET 1/2	
DESIGNED BY DSE Group 13	DATE 17/06/2025				



		Description Launch system final design concept for swarm of cylindrical drones			
DRAWN BY Jan Franquesa Monés	DATE 17/06/2025	SIZE A3	Title LaunchSystemL.O.R.A.X.	REV A.1	
CHECKED BY Django van der Plas	DATE 17/06/2025	SCALE 1:1	WEIGHT(kg) 3.52	SHEET 1/1	
DESIGNED BY DSE Group 13	DATE 17/06/2025				